

Prediction of sound transmission in elongated or compact acoustic cavities

Thesis submitted in accordance with the requirements of the
University of Liverpool for the degree of Doctor in Philosophy

by

Hyoseon Jang

May 2017

Abstract

The ability to predict sound fields in coupled volumes is important for noise control and acoustic quality with buildings, cars, aircraft and trains. This thesis investigates methods to assess the diffusivity of sound fields in rooms and the prediction of sound transmission between coupled volumes using statistical approaches.

Sound fields in a box-shaped room were assessed using ray tracing with the spatial correlation coefficient for instantaneous sound pressure. The results were compared with the theory for a three-dimensional diffuse field and propagating plane waves. Three different options were considered for the measurement lines: (1) pairs of points formed by one fixed point when the other point varies along the same line, (2) pairs of points with fixed spacing and (3) all permutations of points with variable spacing. The general conclusion is that option (1) can lead to conclusions that seem inappropriate. Options (2) and (3) were found to have potential as assessment procedures, but definitively characterising a sound field as diffuse was not possible.

Sound transmission between coupled volumes was investigated using an empty cuboid, a cuboid with staggered barriers and a car cabin model based on Statistical Energy Analysis (SEA) and Experimental SEA (ESEA). Experimental work on corridors was used to validate the ray tracing models. For sound transmission along an empty cuboid, the direct field was significant with highly absorptive surfaces such that a propagating two-dimensional model overestimated transmission for low absorption, and underestimated it for high absorption. SEA incorporating coupling loss factors from the general form of ESEA gave improved agreement with ray tracing and showed the importance of indirect coupling between subsystems. For a corridor with staggered barriers, source locations for the Power Injection Method used in ESEA were assessed to ensure accurate predictions of sound transmission along the corridor. For the corridor and car cabin, the general form of ESEA tends to always result in a working SEA model and be more accurate when a source position (point or surface) used for the power injection process is similar to the actual source position. This tends to be more apparent when using a single source rather than multiple sources.

Acknowledgements

This is for people who helped me psychologically, educationally and in all manner of ways throughout the duration of my PhD study.

I would like to express my sincere gratitude to my supervisor Professor Carl Hopkins for arranging financial support for the study, valuable advice to overcome difficulties and precious experiences with his honourable guidance and encouragement over the four years. These memories will be a foundation for me to grow in the academic area.

Dr. Gary Seiffert is unparalleled to deserve my appreciation for his aid throughout everything about ARU from the moment I started. I could smile with his warm cares and humorous jokes. I also appreciate Professor Barry Gibbs for enjoyable short conversation at odd times. He is a warmhearted man taking care of all staff and students in the ARU indeed. I would like to extend my thanks to Dr. Pyoung-jik Lee for giving me smiles and helpful advices on my research work.

I am grateful to all members of the ARU, in particular, Dr Xing Wang, Nuno Ferreira, Marios Filippopolitis, Sanghee Park, Susumu Hirakawa, Yicheng Yu and Dr Simone Graetzer for easing my life during the PhD.

Last but not least, I would like to express many thanks to my family for their support, trust and unconditional love even when they have been through a hard time without me, and to say I love them very much. I would also not like to forget to thank all my friends for always standing by me.

Contents

Abstract.....	iii
Acknowledgements.....	v
Contents.....	vii
List of Figures.....	xi
List of Tables	xxiii
List of Symbols	xxv
Chapter 1 Introduction.....	1
1.1 Background and motivation	1
1.2 Literature review	2
1.2.1 Spatial correlation	2
1.2.2 Statistical Energy Analysis (SEA)	3
1.2.2.1 Definition of subsystems.....	3
1.2.2.2 ‘Weakly’ or ‘strongly’ coupled subsystems.....	4
1.2.3 Experimental SEA.....	5
1.2.4 Clustering analysis	6
1.2.5 Prediction of sound transmission between coupled volumes in buildings..	7
1.2.6 Prediction of sound transmission between coupled volumes in cars, aircraft and trains.....	8
1.3 Aims	9
1.4 Thesis layout	10
Chapter 2 Theory, modelling and experimental work	12
2.1 Introduction	12
2.2 Ray tracing model	12
2.2.1 RAYNOISE	13

2.2.2 ODEON.....	13
2.3 Propagating 2D diffuse field.....	14
2.4 Statistical Energy Analysis (SEA).....	16
2.4.1 Classical SEA.....	16
2.4.1.1 General matrix	17
2.4.1.2 Path analysis.....	19
2.4.2 Experimental SEA (ESEA).....	20
2.4.2.1 General ESEA.....	20
2.4.2.2 Alternative ESEA.....	22
2.4.3 Clustering analysis	25
2.5 Finite Element Method (FEM).....	28
2.6 Experimental work.....	30
2.6.1 Empty corridor	30
2.6.2 Corridor with staggered partitions	32
2.6.3 Absorption coefficient of the partition.....	33

Chapter 3 Characterization of sound field using spatial correlation

.....36

3.1 Introduction.....	36
3.2 Spatial correlation for instantaneous sound pressure in a free-field and a diffuse field	36
3.3 Numerical experiments to determine R using ray tracing.....	39
3.3.1 Spatial correlation for a propagating plane wave in a free-field.....	40
3.3.2 Spatial correlation in a reverberant field - distribution of individual R values	48
3.4 Average spatial correlation in different reverberation rooms	50
3.4.1 One fixed point with variable points (Option (1) used by Cook et al)	50
3.4.2 Pair of points with fixed spacing (Option (2)).....	62

3.4.3 Pair of points with variable spacings (Option (3))	69
3.5 Conclusions	87
Chapter 4 Measurements and prediction of sound transmission along an elongated cuboid	88
4.1 Introduction	88
4.2 Direct field	89
4.3 Propagating 2D diffuse field	90
4.3.1 Decrease in sound pressure level along a corridor	90
4.3.2 Incorporating the direct field in the propagating 2D diffuse field model	93
4.3.3 Comparison of measurements and propagating 2D diffuse field model	95
4.4 SEA model	101
4.4.1 Consideration of open-ended spaces as SEA subsystems	101
4.4.1.1 Modal response of open-ended space subsystems using FEM	102
4.4.1.2 Clustering approach to define open-ended subsystems	107
4.4.2 SEA	110
4.4.3 Forced SEA	114
4.4.4 SEA with direct field and forward propagation	119
4.5 SEA using ESEA	122
4.6 Case study: Experimental work on an empty corridor	124
4.7 Conclusions	132
Chapter 5 Measurements and prediction of sound transmission along an elongated cuboid with staggered barriers	135
5.1 Introduction	135
5.2 Ray tracing with and without diffraction around a barrier	135
5.3 SEA model	136
5.4 SEA using ESEA	137
5.5 SEA/ESEA model with sources located in other subsystems	147

5.5.1 Point source in subsystem 2	147
5.5.2 Multiple sources	148
5.6 Case study: Corridor with staggered partitions	149
5.7 Conclusions	157
Chapter 6 Prediction of sound transmission in a compact cavity ..	159
6.1 Introduction	159
6.2 Numerical experiments with rectangular cuboid space representing an idealised car cabin	159
6.2.1 Division into two subsystems	161
6.2.2 Division into four subsystems	165
6.2.3 Division into eight subsystems	169
6.3 Numerical experiments based on real car cabin geometry	174
6.3.1 Car cabin model	175
6.3.2 SEA using ESEA with single point source	176
6.3.2.1 Three subsystems	178
6.3.2.2 Five subsystems with horizontal subdivision	180
6.3.2.3 Five subsystems with vertical subdivision	182
6.3.2.4 Nine subsystems	184
6.3.3 SEA using ESEA with surface source	188
6.3.4 ESEA results	188
6.4 Conclusions	204
Chapter 7 Conclusions	206
7.1 Future research	209
Appendix A. Modified CLFs and TLFs	210
Appendix B. Negative ILFs	222
References	228

List of Figures

Figure 2-1.	Triangular Beam Method.	13
Figure 2-2.	Corridor divided into narrow sections of width dL .	15
Figure 2-3.	Schematic diagram of a six-subsystem SEA model showing only direct coupling.	17
Figure 2-4.	Schematic diagram of a three-subsystem SEA model showing only direct coupling.	23
Figure 2-5.	Hierarchical cell clustering process.	27
Figure 2-6.	Comparison of FEM with NMM for sound pressure level at the corner position.	29
Figure 2-7.	Schematic diagram of the corridor used for measurements.	30
Figure 2-8.	Measurement setup on a real corridor.	32
Figure 2-9.	Measurement for the sound pressure along the empty corridor.	32
Figure 2-10.	Schematic diagram of the corridor with partitions.	32
Figure 2-11.	Measurements for the sound pressure at each subspace divided by partitions along the corridor.	33
Figure 2-12.	Partition used for the measurements.	34
Figure 2-13.	Measurement setup for the absorption coefficient of the partition used for the real corridor experiment in the reverberation chamber at two different position of the omnidirectional power source and with two partitions.	35
Figure 3-1.	Plane wave propagating past points i and j at an angle θ .	37
Figure 3-2.	Sound wave incident from all possible angles in spherical coordinate system.	38
Figure 3-3.	Spatial correlation as a function of kd in a three-dimensional diffuse field and a two-dimensional diffuse field.	39
Figure 3-4.	Schematic diagram of room used for ray tracing with measurement lines along x- and z-directions.	39
Figure 3-5.	Two different source positions in an anechoic space. (a) A point source aligned with the measurement line along the x-axis and (b) a point source positioned at an angle to the measurement line.	41

- Figure 3-6. Spatial correlation for plane wave in a free field for source position (A) with (a) option (2) considering adjacent pairs of points along the line and with (b) option (3) considering all permutation pairs of points along the line. 42
- Figure 3-7. Approximation of spherical wave to plane wave. Dashed lines represent the plane wave and the solid arc represents the spherical wave front. 43
- Figure 3-8. Spatial correlation for plane wave in a free field for source position (B) with option (2) considering adjacent pairs of points ($d=0.1\text{m}$) along the line (a) individual points and (b) average values using Eq. (3.2.9) and (3.2.10). 44
- Figure 3-9. Spatial correlation for a point source in a free field for source position (B) with option (3) considering all permutations of points along the line for (left) individual points and (right) average values (Eq. (3.2.9) and (3.2.10)). Individual pairs of points are accepted on the following basis (a) >0 , (b) >0.9 , (c) >0.95 and (d) >0.99 . 45
- Figure 3-10. Spatial correlation for a point source in a free field for source position (B) with option (3) considering all permutations of points along the line for (left) average R values for each kd value from ray tracing and plane wave theory and (right) percentage difference between ray tracing and plane wave theory. Individual pairs of points are accepted on the following basis (a) >0 , (b) >0.9 , (c) >0.95 and (d) >0.99 . 47
- Figure 3-11. Individual spatial correlation coefficients for each pair of points calculated from adjacent pairs of points that are at least $\lambda/2$ away from the boundary, and that lie along each measurement line up to a distance that is $\lambda/2$ away from the opposite boundary in 50m^3 room. (a) Ten measurement lines along the x-direction for comparison with three-dimensional diffuse field theory, (b) Distribution of individual coefficients from x-direction lines. 49
- Figure 3-12. Individual spatial correlation coefficients for each pair of points calculated from adjacent pairs of points that are at least $\lambda/2$ away from the boundary, and that lie along each measurement

line up to a distance that is $\lambda/2$ away from the opposite boundary.

(a) Ten measurement lines along the z-direction for comparison with three-dimensional diffuse field theory, (b) Distribution of individual coefficients from z-direction lines.

49

Figure 3-13. Average spatial correlation in 30m^3 room ($\alpha=0.01$) along x- and z-axis ten measurement lines using option (1) compared with plane wave and diffuse field theory in one-third octave frequency.

53

Figure 3-14. Average spatial correlation in 30m^3 room ($\alpha=0.1$) along x- and z-axis ten measurement lines using option (1) compared with plane wave and diffuse field theory in one-third octave frequency.

55

Figure 3-15. Average spatial correlation in 50m^3 room ($\alpha=0.02$) along x- and z-axis ten measurement lines using option (1) compared with plane wave and diffuse field theory in one-third octave frequency.

57

Figure 3-16. Average spatial correlation in 50m^3 room ($\alpha=0.3$) along x- and z-axis ten measurement lines using option (1) compared with plane wave and diffuse field theory in one-third octave frequency.

59

Figure 3-17. Average spatial correlation in 120m^3 room ($\alpha=0.3$) along x- and z-axis ten measurement lines using option (1) compared with plane wave and diffuse field theory in one-third octave frequency.

61

Figure 3-18. Average spatial correlation in 30m^3 room ($\alpha=0.01$) along x- and z-axis ten measurement lines with option (2) pairs of points with a fixed spacing, average plane wave and diffuse field theory. All measurement points are at least $\lambda/2$ away from the boundary, and that lie along each measurement line up to a distance that is $\lambda/2$ away from the opposite boundary. Fixed spacing with 0.1m, 0.2m, 0.4m, 0.6m and 0.8m.

64

Figure 3-19. Average spatial correlation in 30m^3 room ($\alpha=0.1$) along x- and z-axis ten measurement lines with option (2) pairs of points with a fixed spacing, average plane wave and diffuse field theory. All

measurement points are at least $\lambda/2$ away from the boundary, and that lie along each measurement line up to a distance that is $\lambda/2$ away from the opposite boundary. Fixed spacing with 0.1m, 0.2m, 0.4m, 0.6m and 0.8m. 65

Figure 3-20. Average spatial correlation in 50m^3 room ($\alpha=0.02$) along x- and z-axis ten measurement lines with option (2) pairs of points with a fixed spacing, average plane wave and diffuse field theory. All measurement points are at least $\lambda/2$ away from the boundary, and that lie along each measurement line up to a distance that is $\lambda/2$ away from the opposite boundary. Fixed spacing with 0.1m, 0.2m, 0.4m, 0.6m and 0.8m. 66

Figure 3-21. Average spatial correlation in 50m^3 room ($\alpha=0.3$) along x- and z-axis ten measurement lines with option (2) pairs of points with a fixed spacing, average plane wave and diffuse field theory. All measurement points are at least $\lambda/2$ away from the boundary, and that lie along each measurement line up to a distance that is $\lambda/2$ away from the opposite boundary. Fixed spacing with 0.1m, 0.2m, 0.4m, 0.6m and 0.8m. 67

Figure 3-22. Average spatial correlation in 120m^3 room ($\alpha=0.3$) along x- and z-axis ten measurement lines with option (2) pairs of points with a fixed spacing, average plane wave and diffuse field theory. All measurement points are at least $\lambda/2$ away from the boundary, and that lie along each measurement line up to a distance that is $\lambda/2$ away from the opposite boundary. Fixed spacing with 0.1m, 0.2m, 0.4m, 0.6m and 0.8m. 68

Figure 3-23. Average spatial correlation in 30m^3 room ($\alpha=0.01$) along x- and z-axis ten measurement lines with option (3) all permutations of pairs, plane wave and diffuse field theory. 72

Figure 3-24. Average spatial correlation in 30m^3 room ($\alpha=0.1$) along x- and z-axis ten measurement lines with option (3) all permutations of pairs, plane wave and diffuse field theory. 73

Figure 3-25. Average spatial correlation in 50m^3 room ($\alpha=0.02$) along x- and z-axis ten measurement lines with option (3) all permutations of pairs, plane wave and diffuse field theory. 74

Figure 3-26. Average spatial correlation in 50m ³ room ($\alpha=0.3$) along x- and z-axis ten measurement lines with option (3) all permutations of pairs, plane wave and diffuse field theory.	75
Figure 3-27. Average spatial correlation in 120m ³ room ($\alpha=0.3$) along x- and z-axis ten measurement lines with option (3) all permutations of pairs, plane wave and diffuse field theory.	76
Figure 3-28. Average spatial correlation in 30m ³ room ($\alpha=0.01$) along x- and z-axis ten measurement lines with option (3) all permutations of pairs, plane wave and diffuse field theory in terms of frequency.	78
Figure 3-29. Average spatial correlation in 30m ³ room ($\alpha=0.1$) along x- and z-axis ten measurement lines with option (3) all permutations of pairs, plane wave and diffuse field theory in terms of frequency.	80
Figure 3-30. Average spatial correlation in 50m ³ room ($\alpha=0.02$) along x- and z-axis ten measurement lines with option (3) all permutations of pairs, plane wave and diffuse field theory in terms of frequency.	82
Figure 3-31. Average spatial correlation in 50m ³ room ($\alpha=0.3$) along x- and z-axis ten measurement lines with option (3) all permutations of pairs, plane wave and diffuse field theory in terms of frequency.	84
Figure 3-32. Average spatial correlation in 120m ³ room ($\alpha=0.3$) along x- and z-axis ten measurement lines with option (3) all permutations of pairs, plane wave and diffuse field theory in one-third octave frequency.	86
Figure 4-1. Empty cuboid system used for numerical modelling.	88
Figure 4-2. Empty cuboid model: Comparison of direct field with ray tracing models (different absorption coefficients) using (a) specular reflections and (b) diffuse reflections.	90
Figure 4-3. Empty cuboid model: Comparison of the propagating 2D diffuse field model with ray tracing models in terms of the decrease in sound pressure level for (a) $\alpha=0.1$, (b) $\alpha=0.3$ and (c) $\alpha=0.6$.	92
Figure 4-4. Empty cuboid model: Comparison of the propagating 2D diffuse field model incorporating the direct field with the ray tracing model for (a) $\alpha=0.1$, (b) $\alpha=0.3$ and (c) $\alpha=0.6$	94
Figure 4-5. Real corridor: Measured decrease in sound pressure level.	96

Figure 4-6. Real corridor: Curve fitting of measurements including points near the source with the propagating 2D diffuse field models (red line represents measurements and black line represents propagating 2D models).	97
Figure 4-7. Real corridor: Curve fitting of measurements excluding points near the source with the propagating 2D diffuse field models (red line represents measurements and black line represents propagating 2D models).	98
Figure 4-8. Real corridor: Estimated averaged absorption coefficients from curve fitting and the ODEON material database.	100
Figure 4-9. Example SEA model of an empty cuboid composed of four subsystems.	102
Figure 4-10. FEM models for modal responses of cuboids with closed, open or partly open ends (grey colour indicates an open area).	102
Figure 4-11. Modal responses for the five FEM models.	105
Figure 4-12. (a) Mode count and (b) Modal density of different boundary conditions in terms of one-third octave band centre frequency.	106
Figure 4-13. Subsystem lengths defined using the clustering approach using 1.25m, 2.5m and 5m cell sizes for axial, tangential and oblique modes (a=1.25m, b=2.5m, c=3.75m, d=5m, e=10m, f=12.5m, g=15m and h=25m).	109
Figure 4-14. Empty source position and the numbering corridor model indicating the subsystem.	110
Figure 4-15. Empty cuboid model: Decrease in sound pressure level for empty cuboid SEA models with specular reflections and diffuse reflections with different absorption coefficients for the boundaries. (a,b) $\alpha=0.1$, (c,d) $\alpha=0.3$, (e,f) $\alpha=0.6$.	113
Figure 4-16. Forced SEA model: Errors between exact and approximate energy ratio in terms of the energy decrease between adjacent subsystems.	115
Figure 4-17. Empty cuboid model: Decrease in sound pressure level for forced SEA model with absorption coefficient for the boundaries of (a) 0.1, (b) 0.3 and (c) 0.6.	118

Figure 4-18. Three different types of forward propagation in a corridor: (Key: ‘a’ indicates boundaries with the actual absorption coefficient, ‘A’ indicates anechoic boundaries where $\alpha=1$, ‘x’ indicates a grid point in the receiving subsystem).	119
Figure 4-19. Empty cuboid model (all corridor boundaries have $\alpha=0.3$): Comparison of SEA, SEA with direct field and forward propagation and ray tracing with specular reflections and diffuse. (a,b): Type1, (c,d): Type1+Type2, (e,f): Type1+Type2+Type3.	121
Figure 4-20. Empty cuboid model: Point source locations for the power injection method (PIM)	123
Figure 4-21. Comparison of direct coupling loss factors of (a) η_{12} and (b) η_{23} estimated from ESEA with predictive SEA.	123
Figure 4-22. Empty cuboid model: Comparison of SEA using ESEA with ray tracing (a) with specular reflections and (b) with diffuse reflections ($\alpha=0.3$).	124
Figure 4-23. Real corridor: Comparison of measurements with ray tracing using average absorption coefficients estimated by curve fitting with the propagating 2D model.	126
Figure 4-24. Real corridor: Comparison of measurements with the ray tracing using average absorption coefficients of standard material (from ODEON database) in the decrease in SPL along the corridor.	128
Figure 4-25. Real corridor: Comparison of measurements, SEA models, and ray tracing with specular reflection using absorption coefficients for the boundaries from the ODEON material database without windows (in octave bands from 500 to 4000Hz).	131
Figure 4-26. Real corridor: Comparison of measurements, SEA models, and ray tracing with diffuse reflections using absorption coefficients for the boundaries from the ODEON material database without windows for the 8000Hz octave band.	132
Figure 5-1. A cuboid model with staggered barriers.	135
Figure 5-2. Cuboid model with staggered barriers: Comparison of ray tracing with or without diffraction around a barrier using (a) specular reflections and (b) diffuse reflections.	136

Figure 5-3.	Cuboid model with staggered barriers (cuboid boundaries have $\alpha=0.3$): Comparison of SEA and the ray tracing (a) with specular reflections and (b) with diffuse reflections.	137
Figure 5-4.	Point source locations for PIM.	138
Figure 5-5.	Cuboid model with staggered barriers (cuboid boundaries have $\alpha=0.3$): Comparison of SEA using ESEA with ray tracing (1) with specular reflections and (2) with diffuse reflections with respect to different source permutations for cases A, B, C and D.	143
Figure 5-6.	Cuboid model with staggered barriers: Difference in decrease in SPL between ray tracing using the red source (specular reflections) and SEA using GESEA CLFSs with difference sources.	146
Figure 5-7.	Cuboid model with staggered barriers: Comparison of SEA using ESEA with ray tracing using the source in subsystem 2 (a) with specular reflections and (b) with diffuse reflections (cuboid boundaries have $\alpha=0.3$). Case A source distribution is used for SEA model.	148
Figure 5-8.	Cuboid model with staggered barriers (cuboid boundaries have $\alpha=0.3$): Comparison of SPL in each subsystem estimated from SEA, SEA using ESEA and ray tracing (a) with specular reflections and (b) with diffuse reflections using multiple sources.	149
Figure 5-9.	Real corridor with staggered partitions: Standard deviation of measured SPL on the real corridor with partitions in one-third octave band (red line: source subsystem, black line: receiving subsystems).	151
Figure 5-10.	Real corridor with staggered partitions: Comparison of (a) total loss factors (TLFs), (b) coupling loss factors (CLFs) and (c) energy ratio $10\lg(\eta_1/\eta_{12})$ estimated from SEA using ODEON material database with barrier and AESEA based on experimental measurements. NB AESEA results using the full matrix and approximation are nominally identical.	152
Figure 5-11.	Modified propagation 2D diffuse field model (S_{open} : open area, S_{total} : cross-section of corridor).	153

Figure 5-12. Real corridor with staggered partitions: Comparison of measurements with SEA using GESEA CLFs and SEA using AESEA CLFs in the decrease in SPL along the corridor.	156
Figure 6-1. Idealised car cabin: (a) high absorption coefficients (grey: $\alpha=0.9$) and (b) low absorption coefficients (yellow: $\alpha=0.03$).	160
Figure 6-2. Idealised car cabin: Modal density of the rectangular cuboid in octave bands.	160
Figure 6-3. Idealised car cabin: SEA model composed of two subsystems (solid circle: main source position, open circle: additional source position used for PIM).	161
Figure 6-4. Idealised car cabin: Comparisons of SPL in each subsystem from SEA using ESEA with FEM from 63 to 1kHz octave bands. Source: Subsystem 1.	163
Figure 6-5. Idealised car cabin: Comparison of SPL in each subsystem estimated from SEA using ESEA with ray tracing assuming diffuse reflections. Source: Subsystem 1.	164
Figure 6-6. Idealised car cabin: SEA model composed of four subsystems (a) horizontal subdivision and (b) vertical subdivision (solid circle: main source position, open circle: additional source positions used for PIM).	165
Figure 6-7. Idealised car cabin: Four subsystem SEA model showing only direct coupling between subsystems (a) horizontal subdivision and (b) vertical subdivision.	165
Figure 6-8. Idealised car cabin: Comparisons of SPL in each subsystem from SEA using ESEA with FEM from 63 to 1kHz octave bands for four subsystem SEA models ((a),(b),(c),(d) and (e) are with horizontal subdivision and (f),(g),(h),(i) and (j) are with vertical subdivision). Source: Subsystem 1.	167
Figure 6-9. Idealised car cabin: Comparison of SPL in each subsystem estimated from SEA using ESEA with ray tracing assuming diffuse reflections (a) horizontal subdivision and (b) vertical subdivision. Source: Subsystem 1.	168

Figure 6-10. Idealised car cabin: SEA model composed of eight subsystems (solid circle: main source position, open circle: additional source positions used for PIM).	169
Figure 6-11. Idealised car cabin: Eight subsystem SEA model showing only direct coupling between subsystems. Dashed red lines indicated that two subsystems are not directly coupled by an open area because they are diagonally adjacent but coupling is expected to occur.	169
Figure 6-12. Idealised car cabin: Comparisons of SPL in each subsystem from SEA using ESEA with FEM from 63 to 1000Hz octave bands. Source: Subsystem 1.	171
Figure 6-13. Idealised car cabin: Comparison of SPL in each subsystem estimated from SEA using ESEA with ray tracing assuming diffuse reflections. Source: Subsystem 1.	174
Figure 6-14. Car cabin model (a) side view of the car cabin, (b) front view of the car cabin and (c) rear view of the car cabin.	175
Figure 6-15. Car cabin: Mode count in octave bands.	177
Figure 6-16. Car cabin: Subdivisions for SEA subsystems and source positions for PIM.	178
Figure 6-17. Car cabin: Three subsystem model: Ray tracing results in terms of the sound pressure level in each subsystem relative to the source subsystem. Point source in front left subsystem.	179
Figure 6-18. Car cabin: Open area (shaded red) between adjacent subsystems (a) front seat to rear seat and (b) rear seat to boot.	179
Figure 6-19. Car cabin: Five subsystem model with horizontal subdivision: Ray tracing results in terms of the sound pressure level in each subsystem relative to the source subsystem. Point source in front left subsystem.	181
Figure 6-20. Car cabin: Open area (shaded red) between adjacent subsystems (a) Top view of front upper to lower, (b) Top view of rear upper to lower, (c) Cross-section of upper front to rear, (d) Cross-section of lower front to rear and (d) Cross-section of rear to boot.	181

Figure 6-21. Car cabin: Five subsystem model with vertical subdivision: Ray tracing results in terms of the sound pressure level in each subsystem relative to the source subsystem. Point source in front left subsystem.	183
Figure 6-22. Car cabin: Open area (shaded red) between adjacent subsystems (a) front side, (b) rear side, (c) Cross-section of front to rear (left/right) and (d) Cross-section of rear to boot (left/right).	183
Figure 6-23. Car cabin: Nine subsystem model: Ray tracing results in terms of the sound pressure level in each subsystem relative to the source subsystem. Point source in front left subsystem.	185
Figure 6-24. Car cabin: Open area (shaded red) between adjacent subsystems (a) front side upper, (b) rear side upper, (c) front side lower, (d) rear side lower, (e) front upper-lower (left/right), (f) rear upper-lower (left/right), (g) upper front-rear (left/right), (h) lower front-rear (left/right) and (i) rear-boot (left/right).	186
Figure 6-25. Car cabin: Red lines indicate the surface sources.	188
Figure 6-26. Car cabin: 63Hz octave band. Point source in front left subsystem.	189
Figure 6-27. Car cabin: 125Hz octave band. Point source in front left subsystem.	190
Figure 6-28. Car cabin: 250Hz octave band. Point source in front left subsystem.	191
Figure 6-29. Car cabin: 500Hz octave band. Point source in front left subsystem.	192
Figure 6-30. Car cabin: 1kHz octave band. Point source in front left subsystem.	193
Figure 6-31. Car cabin: Eigenmodes within 63Hz octave band	194
Figure 6-32. Car cabin: SPL in each subsystem estimated from SEA using ESEA and ray tracing in terms of (a) three subsystems, (b) five subsystems with horizontal subdivision, (c) five subsystems with vertical subdivision and (d) nine subsystems. Point source in front left subsystem.	196
Figure 6-33. Car cabin: SPL in each subsystem estimated from SEA using ESEA and ray tracing in terms of (a) three subsystems, (b) five	

subsystems with horizontal subdivision, (c) five subsystems with vertical subdivision and (d) nine subsystems. WS surface source in front left and right subsystems. 200

Figure 6-34. Car cabin: SPL in each subsystem estimated from SEA using ESEA and ray tracing in terms of (a) three subsystems, (b) five subsystems with horizontal subdivision, (c) five subsystems with vertical subdivision and (d) nine subsystems. Floor surface source in front left/right and rear left/right subsystems. 201

Figure 6-35. Car cabin: SPL in each subsystem estimated from SEA using ESEA and ray tracing in terms of (a) three subsystems, (b) five subsystems with horizontal subdivision, (c) five subsystems with vertical subdivision and (d) nine subsystems. WS+Floor surface sources in front left/right and rear left/right subsystems. 202

Figure 6-36. Car cabin: SPL in each subsystem estimated from SEA using ESEA and ray tracing in terms of (a) three subsystems, (b) five subsystems with horizontal subdivision, (c) five subsystems with vertical subdivision and (d) nine subsystems. WS+FSW+RSW+Floor surface sources in front left/right and rear left/right subsystems. 203

List of Tables

Table 2-1.	B&K sound power source output.	31
Table 2-2.	Measured absorption coefficient of the partition.	35
Table 4-1.	Real corridor: Absorption coefficients determined from curve fitting in one-third octave bands.	99
Table 4-2.	Real corridor: Absorption coefficients from ODEON material database in octave bands.	99
Table 4-3.	Air absorption in terms of absorption area - calculated according to ISO 9613 (70% RH, 20°C).	100
Table 4-4.	Input parameters for the corridor models.	111
Table 4-5.	Empty cuboid model: Assignment of coupling and internal loss factors for two different SEA models.	111
Table 4-6.	Empty cuboid model: Difference between SEA and diffuse field SPL in the source subsystem.	114
Table 4-7.	Empty cuboid model: Coupling and internal loss factors for two different forced SEA models.	117
Table 5-1.	Cuboid model with staggered barriers: Difference between the direct coupling loss factor, η_{12} determined from GESEA and from predicted SEA in dB with different main sources.	138
Table 5-2.	Cuboid model with staggered barriers: Difference between the direct CLFs determined from ESEA and from predicted SEA in dB (a) specular reflections and (b) diffuse reflections for different source permutations with source 1 (red) and standard deviation (σ) in dB.	141
Table 5-3.	Cuboid model with staggered barriers: Direct CLFs between adjacent subsystems determined using GESEA for different sources and standard deviation (σ) in dB.	145
Table 5-4.	Fundamental modes and frequencies for a closed cuboid space (6m x 2.1m x 2.3m).	151
Table 6-1.	Idealised car cabin: FEM mode shapes in 63Hz and 125Hz octave bands.	161

Table 6-2.	Idealised car cabin: Direct CLFs determined from GESEA and full matrix AESEA at 250Hz, 500 Hz and 1kHz octave bands. NB AESEA results using the full matrix and approximation are nominally identical.	172
Table 6-3.	Idealised car cabin: Indirect CLFs determined from GESEA which are as strong as direct CLFs at 250Hz, 500Hz and 1000Hz octave bands.	172
Table 6-4.	Idealised car cabin: Path analysis (a) between subsystem 1 and 5 and (b) between subsystem 1 and 6 for 250Hz, 500Hz and 1000Hz.	173
Table 6-5.	Absorption coefficient from ODEON material database for window glass in octave bands.	177
Table 6-6.	Car cabin: SPL in each subsystem relative to the source subsystem.	180
Table 6-7.	Car cabin: Three subsystem model: subsystem volumes and open area between adjacent subsystems.	180
Table 6-8.	Car cabin: SPL in each subsystem relative to the source subsystem	182
Table 6-9.	Car cabin: Five subsystem model with horizontal subdivision: subsystem volumes and open area between adjacent subsystems.	182
Table 6-10.	Car cabin: SPL in each subsystem relative to the source subsystem.	184
Table 6-11.	Car cabin: Five subsystem model with vertical subdivision: subsystem volumes and open area between adjacent subsystems.	184
Table 6-12.	Car cabin: SPL in each subsystem relative to the source subsystem.	187
Table 6-13.	Car cabin: Nine subsystem model: subsystem volumes and open area between adjacent subsystems.	187
Table 6-14.	Car cabin: Difference between the direct CLFs determined from ESEA and from predicted SEA in dB and standard deviation (σ) in dB for (a) three subsystems and (b) five subsystems with vertical subdivision.	197

List of Symbols

AESEA	Alternative Experimental Statistical Energy Analysis
CLF	Coupling Loss Factor
ESEA	Experimental Statistical Energy Analysis
FE	Finite Element
FEM	Finite Element Method
FSW	Front Side Window
GESEA	General Experimental Statistical Energy Analysis
ILF	Internal Loss Factor
LF	Loss Factor
MSE	Mean Square Error
NMM	Normal Mode Model
PDE	Partial Differential Equations
PIM	Power Injection Method
rms	root-mean square
RSW	Rear side window
RT	Reverberation Time
SEA	Statistical Energy Analysis
SPL	Sound Pressure Level
TBM	Triangular Beam Method
3D	Three-dimensional
2D	Two-dimensional
WS	Windscreen
c_0	Phase velocity of sound in air (m/s)
d	Distance (m)
d_{mfp}	Mean free path (m)
e	energy density (J/m^3)
f	Frequency (Hz)
$f^{\text{high}}, f^{\text{lower}}$	Higher and Lower limits of a frequency band (Hz)

k	Wave number (radians/m)
l	Arc length (m)
$n(f)$	Modal density
$n_{2D}(f)$	Modal density for a cavity – two-dimensional space (modes per Hz)
$n_{3D}(f)$	Modal density for a cavity – three-dimensional space (modes per Hz)
p	Sound pressure (Pa)
\mathbf{u}	Sound particle velocity (m/s)
w_d	Energy density of the direct field (J/m^3)
\mathbf{x}	Energy vector
B	Bandwidth (Hz)
E	Energy (J)
L_x, L_y, L_z	x-,y-,z-dimensions(m)
ΔL	Decrease in sound pressure level along a corridor (dB)
ΔL_{inf}	Decrease in sound pressure level along an infinite length corridor (dB)
K_t	Bulk modulus (N/m^2)
N_s	Mode counts (-)
R	Spatial correlation coefficient (-)
S	Surface area (m^2)
S_T	Total area of the room surfaces (m^2)
T	Reverberation time (s)
U	Perimeter (m)
V	Volume (m^3)
R	Reflection coefficient (-), Spatial correlation coefficients for instantaneous sound pressure (-)
W_{in}	Input power (W)
α	Absorption coefficient (-)
α_s	Absorption coefficient of the sample (-)
γ	Included angle (radians)
η_{ii}	Internal loss factor for subsystem i (-)

η_{ij}	Coupling loss factor from subsystem i to subsystem j (-)
λ	Wavelength (m)
ρ_0	Density of air (kg/m^3)
τ_{NR}	Non-resonant transmission coefficient (-)
ω	Angular frequency (radians/s)
θ	Incident angle passing through a pair of points
ψ	Local mode shape (eigenvector)

Chapter 1 Introduction

1.1 Background and motivation

This thesis concerns the acoustics of internal spaces in built structures comprised of coupled volumes in terms of describing the diffusivity of sound fields and the prediction of sound transmission between those coupled volumes. In acoustic engineering, an understanding and ability to predict the acoustics of coupled volumes is important when assessing noise control and acoustic quality for buildings, cars, aircraft and trains.

In buildings, one room is often connected via an open area to another room. If these rooms have different volumes and different amounts of absorption, the decay time in one room can be significantly affected by sound returning from the other one [1]. Along elongated spaces such as corridors or between open-plan areas, it is often necessary to predict sound transmission from one space containing a sound source to other connected spaces. There are other elongated spaces such as train carriages or aircraft cabins, and compact spaces such as car cabins where it is also important to be able to predict sound transmission between coupled volumes due to sound radiated by the structure which is excited by mechanical or aerodynamic sources.

The prediction of sound transmission between coupled spaces can be simplified if it is possible to assume that the sound field is diffuse. This assumption is sometimes reasonable for a closed reverberant room where previous research has studied characterisation of the diffusivity of a sound field in a closed reverberant room [e.g. see 2,3]. However, there are still unanswered questions on optimal experimental procedures and the accuracy of indicators that can identify the degree of diffuseness. In room acoustics it is common to use ray tracing [4,5] for coupled volumes to predict reverberation times, speech intelligibility and sound pressure levels. For vibroacoustic problems concerning sound transmission in a built up structure, deterministic models such as Finite Element Methods (FEM) are often used for low-frequency problems [6,7]. However, for airborne sound transmission in the mid- and high-frequency ranges it is possible to consider statistical approaches, such as Statistical Energy Analysis (SEA) [8,9]. This thesis uses ray tracing, SEA and FEM to assess, validate and develop prediction models for coupled volumes.

1.2 Literature review

This section reviews the literature related to the main topics in this thesis.

1.2.1 Spatial correlation

Spatial correlation techniques are primarily used to characterize sound fields to assess the applicability or validity of acoustic measurements.

In the 1950s, Cook et al [2] proposed measurement of the spatial correlation coefficient to assess the diffusivity of random sound fields. This was carried out for instantaneous sound pressure in a three-dimensional diffuse field. Kuttruff [10] showed that measurements of the spatial correlation coefficient for instantaneous sound pressure in an empty reverberation chamber with diffusers gave results similar to the theory for a three-dimensional diffuse field. He also showed that the spatial covariance followed the two-dimensional theory for $0 < kd < 0.5$, and the three-dimensional theory for $0.5 < kd < 1.5$ when a specific absorbent material was laid on the floor. Morrow [11] computed the correlation function in a rectangular reverberation room using a modal approach that was in agreement with Cook's formula under the condition of high modal density so that the bandwidth contained many modes for an undamped reverberant field. This indicated that frequency averaging could replace spatial averaging in a reverberant sound field because the pressure measured at the same position driven with a band of noise in a reverberation room could be assumed to be uncorrelated. Koyasu and Yamasita [12] studied that spatial correlation coefficient in two reverberation chambers (non-rectangular room and rectangular room) to find the dependence of absorption coefficients on the diffusivity index which described a diffuse sound field when $>75\%$. The authors noted that it was important to ascertain the correlation coefficients for all directions in the sound field. Chu [13] experimentally investigated spatial correlation in a reverberation room excited by a pure tone and one-third octave band random noise. Chu showed that there was a coherent sound field with pure tone excitation but with band-limited random noise the sound field could be incoherent due to the large number of excited modes for which any coherent contributions from wave components of individual modes were negligible. In a later paper, Chu [14] provided a derivation of the spatial correlation coefficient for mean-square pressure with pure-

tones in a three-dimensional diffuse field. Nelisse and Nicolas [15] investigated diffuseness of sound field by the use of spatial correlation for narrow-band noise excitation and used spatial uniformity of sound pressure as a second descriptor in a room. Comparisons with theoretical prediction gave close agreement when there are at least 20 to 30 room modes within the frequency bandwidth. This also makes a link to the Schroeder frequency although it is not always sufficient. Rafaely [16] derived generalised correlation coefficient for broadband signals for which the author verified analytical results with diffuse field simulations that gave close agreement. Chun et al [17] experimentally investigated spatial correlation in a reverberation chamber driven by broadband signals and showed that it was in good agreement with theoretical predictions above the Schroeder frequency due to high modal overlap, with poor agreement below the Schroeder frequency. It was suggested that the agreement below the Schroeder frequency could be improved by the using the measured power spectral density.

In the aforementioned works, authors have shown the applicability of characterising sound field using spatial correlations for experimental measurements and theoretical formula. Experimental validation tends only to have been studied at a few frequencies. In this study, spatial correlations are assessed by numerical experiments using ray tracing for wide range of frequencies. In addition, new approaches are used in order to choose a pair of points for calculation of spatial correlation.

1.2.2 Statistical Energy Analysis (SEA)

Since its early development in the 1960's SEA has been proven to be a powerful tool to assess vibro-acoustic behaviour in automotive, aeronautic and building industries. Although classical SEA is based on the assumption of diffuse sound and vibration fields, it is applicable to reverberant sound and vibration fields with sufficient numbers of modes [8].

1.2.2.1 Definition of subsystems

The application of SEA requires defining subsystems by their ability to store modal energy. Lyon [8] defined a subsystem by a group of similar local modes with similar damping.

In this thesis the subsystems are coupled volumes connected via large open areas hence the complete space can be considered to have global modes for which the subdivision into subsystems assumes that analysis of sound transmission can still be modelled based on local mode assumptions.

1.2.2.2 ‘Weakly’ or ‘strongly’ coupled subsystems

Treating coupled volumes as subsystems could potentially violate the assumption of weak coupling in SEA. Therefore, it is necessary to consider the applicability of SEA model with strongly coupled subsystems. SEA assumes that the response of a subsystem is determined by resonant modes and that it can give reliable estimates based on statistical assumptions even though the exact modal properties are not known.

Langley [18] has shown that a theoretical derivation of SEA in response to random excitation is applicable for a variety type of multi-coupled dynamic systems when the coupling between two subsystems is weak in wave approach and modal approach. Mace [19] stated that determination of weak coupling and strong coupling is still not clearly defined yet but two subsystems can be described as being strongly (or weakly) connected if energy can (or cannot) flow freely across the interface between them. The term ‘weakly coupled’ can be interpreted that each subsystem exhibits local mode behaviour with low coherent modal response in other subsystems when it is directly excited. Langley [20] has given a definition of weak coupling by establishing Green function based on the wave approach. Keane and Price [21] showed that the applicability of SEA regardless of coupling strength and low modal overlap factors for multi-coupled subsystem by a point-to-point spring using Green function of uncoupled subsystems. However, they have also described that the reversal of energy flows is possible when frequency or coupling strengths are varied. This can lead to degraded estimate of energy response for SEA and that was verified by Mace [22] using coupling strength parameter for one- and two-dimensional coupled subsystems. Mees and Vermeir [23] showed that one single beam can be treated as strongly coupled two substructures for bending wave and in-plane wave in T-junction beam structure with resilient layer. Zhang and Sainsbury [24] showed that SEA incorporating energy flow method to determine appropriate Coupling Loss

Factors (CLFs) based on FEM models using sandwich plates structures gives good estimate of energy transmission for strongly-coupled subsystem.

1.2.3 Experimental SEA

Predictive SEA requires the prediction of Coupling Loss Factors (CLFs), but this is not always possible with complex coupling conditions and complex subsystems. In addition, when subsystems have low modal overlap predicted CLFs from wave theory are not always accurate [8].

As noted by Lyon [8], when a physical or numerical system exists, Experimental SEA (ESEA) can be used to determine the CLFs. However, the errors involved when inverting a matrix of experimentally determined energies were identified as a significant problem. Bies and Hamid [25] investigated ESEA by focussing on the measurement of the injected power into coupled plates, and were able to gain reasonable estimates of loss factors on plates with at least four modes in each frequency band. Woodhouse [26] highlighted the potential in ESEA and focussed on evaluating the appropriateness of CLFs determined using a ‘hill-climbing computer program’ to deal with errors in the energies giving incorrect or inappropriate CLFs. Woodhouse found that small errors could cause large errors in the loss factors. Hodges et al [27] proposed matrix fitting to obtain optimal CLFs. Lalor [28] also investigated determining loss factors using ESEA and addressed the issue of ill-conditioned energy matrices. He noted that it can be improved by rearranging the SEA power balance matrix. The main focus had been on using experiments to provide subsystem energies whereas Hopkins [29] used ESEA with FEM data. This indicated that ESEA could also work when the subsystems had low modal overlap and low mode counts by making use of an ensemble average approach. Mace [19,30] proved that indirect coupling is not negligible and direct/indirect CLFs are proportional to damping loss factors when modal overlap is low. Borello and Gagliardini [31] applied ESEA on the basis of numerical experiment with FEM for complex automobile structure to estimate subsystem energy. He proposed that an SEA model is able to be identified using predicted structural transfer function. Thite and Mace [32] addressed the issue that CLFs determined from ESEA could change

when subsystem damping was altered, and showed that it was possible to predict the change without a full re-analysis.

ESEA models have been primarily studied for structure borne sound transmission where it is relatively convenient to define subsystems. However, when a single cavity is considered definition of subsystems becomes complicated due to existence of a large open area between subsystems and all subsystems are strongly coupled each other that violates SEA assumptions. For this reason, this thesis investigates applicability of SEA models incorporating CLFs from ESEA to assess sound transmission for elongated space and a car cavity.

1.2.4 Clustering analysis

Choices made to subdivide into subsystems can determine the accuracy of prediction model. Gagliardini et al [33] described a new approach to building an SEA model (“virtual SEA”) using FEA models and an automatic sub-structuring technique based on energy transfer functions. Automatic sub-structuring using energy transfer function was performed by Borello et al [31] that was hierarchically progressed by clustering the elements with lower response than a given energy threshold and that is optimized using minimum entropy in different frequency band.

For automatic partitioning of a single system, many authors have studied finding optimal subdivision. Kovalevsky and Langley [34] proposed clustering for energy models based on Green’s functions. Totaro and Guyader [35] suggested a clustering strategy based on vibratory problem by multiple excitation. They carried out numerical simulations to obtain energy transfer functions on a set and perform principal component analysis before cluster analysis to reduce the data size. The optimal sub-structuring was determined using mutual inertia ratio. Although not linked to SEA, Kassem et al [36] suggested an energy density field approach for the low-mid frequency range. It can provide model simplified and local vibro-acoustic energy model as well. Diaz-Cereceda et al [37] proposed an automatic clustering strategy to identify optimal SEA subsystems based on modal analysis. It was concluded that the resulting dendogram provided information that was clearer than that with the mutual inertia ratio. The approach by Diaz-Cereceda et al is considered in this thesis.

1.2.5 Prediction of sound transmission between coupled volumes in buildings

Decaying sound fields between coupled rooms has been of interest to researchers for many decades [e.g. 1]. In contrast to an enclosed room Kuttruff [38] solved the energy balance equations to show that coupling effects can cause a variety of different slope decay curves using three coupled rooms of equal volumes in a line with a single source in one room. Anderson et al [39] derived two sound energy balance models, a general model for any combination of coupled rooms and an approximate model for specific coupled rooms with a repeated architectural pattern to predict the decay curves. In later work, Anderson & Bratos-Anderson [40] showed that the general model gives reasonable prediction of sound decay through the comparison of experimental results for a St Paul's Cathedral, London. Note that the solution of the energy balance equations during short periods of time is essentially the same approach as used in Transient SEA [e.g. see 8]. Bradley and Wang [41] carried out ray tracing for a concert hall conducting the change of configuration to predict sound decay, reverberation time and clarity index (C_{80}) and the results were compared with measurements. They showed that the parameters obtained from ray tracing were valid at high frequencies, particularly at 1kHz, although C_{80} was less accurately predicted in the low frequency range. Xiang et al [42] investigated sound energy decay applying a diffusion equation on a scale model of coupled rooms.

This thesis is concerned with steady-state sound fields in coupled volumes rather than decaying sound fields. To predict steady-state sound fields in large coupled rooms, Cremer et al [43] noted that general statistical analysis for a reverberant field was not suitable for applying to coupled volumes via a large aperture since sound energy was not uniformly distributed throughout the whole space. Nijs et al [44] validated the use of ray tracing for coupled volumes by comparing with measurements on a scale model. However, ray tracing has an intrinsic drawback of reflection order of absorption coefficient regarding incident angle, which can lead to sometimes inaccurate estimate for coupled volumes.

In buildings, the coupled spaces are not always large. An example of an elongated cuboid which could be considered as relatively small coupled volumes is a corridor. These are required to have fire doors to obey the relevant regulations for fire safety so that in practice most corridors are no longer than 40m between fire doors [45].

Kang [46] reviewed the different prediction models for sound attenuation in long enclosures and concluded that "...it is still necessary to develop a more practical prediction method" although this also considered long enclosures such as underground tunnels and street canyons with line sources but these are not considered in this thesis. Early work by Yamamoto [47] used an image source approach to calculate sound attenuation along a corridor which gave good agreement with measurements and was dependent on the ratio of cross-section and absorption coefficient. Davies [48] tackled the problem of predicting sound transmission along corridors using a modal approach with the practical application of sound insulation being considered through open doors and different types of corridor junctions. However, the experimental validation was only carried out in one corridor at one frequency (2kHz) with all absorption coefficients of the surfaces being estimated. Redmore and Flockton [49] investigated sound attenuation along a corridor based on the assumptions of a corridor consisting of a number of very thin box-shaped sections having a uniform energy density. Redmore [50] extended the formula derived from Redmore and Flockton by carrying out a series of test in a corridor scale model and derived an empirical formula. Kang [46] refers to the formula derived by Redmore as empirical, although it can be derived assuming two-dimensional sound fields [51]. This long space model can be based on a corridor of infinite length that is divided into a number of very thin sections as suggested by Redmore and Flockton [49]. From Hopkins [51] the following derivation results in an equation that differs from that in Redmore and Flockton. However, Hopkins notes that it gives the same equation that was later determined empirically in scale model experiments of corridors by Redmore [50]. Kang also notes that the formula is limited to elongated cuboids representing corridors as the errors tend to increase for long enclosures up to 120m such as occur in underground stations.

1.2.6 Prediction of sound transmission between coupled volumes in cars, aircraft and trains

In cars, there is literature indicating that SEA models often subdivide the car cabin volume into separate subsystems. For example, Dejong [52] determined that road noise and wind noise are dominant noise transmission path to a car interior noise. Fahy [53] considered the subdivision of the air volume in a medium size saloon car

into subsystems in the mid-frequency range (200-800Hz). No numerical or theoretical analysis was carried out, but the qualitative discussion led to the conclusion that subdivision could be justified in some frequency ranges. Musser et al [54] assessed sound pressure level inside a car cavity excited by turbulent layer noise at side windows applying subdivisions based on SEA. They showed that there are level variations in terms of location (3 to 6dB) which suggests that the assessment of noise control is required to be performed at different sub-volumes. Manning et al [55] evaluated the effect of material change on sound transmission in a car cabin using wind noise excitation. Charpentier et al [56] carried out the assessment of airborne noise transmission in a heavy-duty truck cabin applying SEA indicating the effect of trim modification on sound transmission. Wang and Maxon [57] investigated noise control by splitting a wide-body aircraft cabin into coupled volumes to predict the sound pressure levels. They indicated that the influence of different type of noise sources varies in terms of cabin location. Forssen et al [58] investigated sound transmission in a train carriage based on SEA approach and the validation of the statistical model was carried out through comparison with measurements on a scale model of a Swedish Regina train and ray tracing. The sound level at each volume in average is reasonably predicted for high frequency (500-4kHz octave band) due to the limitation of satisfying SEA assumptions (i.e. modal density and modal overlap).

This thesis aims to carry out investigations into subdivision of a car cabin into SEA subsystems using numerical experiments with ray tracing and FEM.

1.3 Aims

The two main aims in this thesis are:

- (1) to investigate and assess approaches to quantify the diffusivity of a sound field using the spatial correlation coefficient.

The spatial correlation coefficient is determined using ray tracing in box-shaped reverberation rooms with different absorptive surfaces. Different procedures to determine the spatial correlation coefficient are assessed and compared with a diffuse field and plane wave theory. Numerical experiments are carried out in 30m³, 50m³ and 120m³ rectangular rooms. An assessment of three sampling

options is made: (1) a fixed point with variable point, (2) a pair of points with fixed spacing and (3) a pair of points with variable spacing.

(2) to develop and validate approaches based on SEA to predict sound transmission between coupled volumes.

SEA and ESEA are used to predict sound transmission with validation through comparison with ray tracing, experiments and FEM. The main aim is to assess whether ray tracing models can be used as a basis on which to build more practical models that are suited to the prediction of sound insulation, or sound transmission with multiple sound sources. The followings are investigated:

- Indirect couplings for coupled volumes with large open area between subsystems.
- Optimal source configuration for ESEA.
- Experimental validation through comparison of measurements.
- Applicability of ESEA for compact volume space

1.4 Thesis layout

The layout of the chapters in this thesis is as follows.

Chapter 2 describes the theory and experimental measurements used in the thesis.

Chapter 3 concerns the characterisation of the diffusivity of a sound field in a regular space using the spatial correlations coefficient with data acquired from ray tracing. Three different approaches are considered to choose a pair of points for computation of spatial correlation.

Chapter 4 applies SEA and ESEA to an empty cuboid model to investigate sound transmission between coupled volumes. Consideration of the direct field and propagating 2D diffuse models is used to give insights into sound propagation along the corridor. A combination of SEA and ESEA model is proposed to compensate for the drawbacks of those predictive approaches.

Chapter 5 applies SEA and ESEA to a corridor with staggered barriers so that the direct field is of less importance. This requires investigations into appropriate source locations for the power injection method (PIM) used in ESEA. The validation is carried out through comparison with measurements on a real corridor with staggered partitions.

Chapter 6 applies ESEA to a car cabin to investigate the subdivision of a compact space into several subsystems with significantly different absorbing surfaces. Approaches to ESEA are investigated using a point source and a radiating surface source. The models considered in this chapter are validated against numerical experiments with FEM in the low- and mid-frequency range and ray tracing for the high-frequency range.

Chapter 7 summarises the main conclusions.

The main areas of novelty in this thesis are the use of ray tracing to determine spatial correlation coefficients and the assessment of different approaches to choose of sampling positions, and the validation of Experimental SEA to build SEA models for volumes coupled via an open area.

Chapter 2 Theory, modelling and experimental work

2.1 Introduction

This chapter describes (a) ray tracing and Statistical Energy Analysis (SEA) as predictive methods of analysis used in this thesis and (b) descriptions of the experimental work in corridors used to validate the predictive approaches in Chapters 4 and 5.

2.2 Ray tracing model

Ray tracing can be used to predict different room acoustic parameters such as sound pressure distribution, reverberation time and speech intelligibility [5]. This technique is based on the principles of geometrical acoustics. It assumes that sound waves from a source travel in straight lines as sound rays in a similar way to light. The rays are partly reflected and partly absorbed when they hit the room boundaries. The method assumes that the energies generated from a point source are distributed into a given space using a discrete number of sound rays which travel at the speed of sound. As the rays hit each surface the energy level of each ray is slowly reduced due to absorption. Sound energy at a chosen receiver position is determined by tracing those rays as each ray contributes to the overall sound pressure level. This method is suited to modelling in the mid- to high-frequency ranges where the effects of individual room modes on the sound field tend to be negligible.

In this research, two commercial ray tracing software models were used: RAYNOISE and ODEON. RAYNOISE has the ability to specify coherent sources which are needed to give complex pressures at any point in space; hence it is used to determine the spatial correlation coefficient. To assess the validity of SEA predictions by predicting steady-state root-mean square (rms) sound pressure, coherent sources are not necessary and ODEON was used due to its more advanced GUI and a reasonable number of reflections to obtain reliable results with a small number of beams [59].

2.2.1 RAYNOISE

RAYNOISE handles complex interactions such as multiple reflections from different surfaces and the effects of coherent and incoherent sources. It is used for the computation of spatial correlation coefficient from complex sound pressure in Chapter 3.

Sound pressure data from RAYNOISE was calculated using the Triangular Beam Method (TBM), which uses a mixture of ray tracing and mirror image source method. Sound rays emitted from a point source are used to construct triangular-based pyramids to discretize the spherical wave front. The advantage that TBM has over other approaches such as the Conical Beam Method (CBM) is that there are no overlapping regions [60].

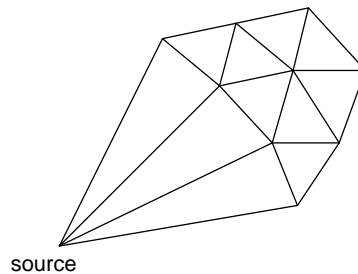


Figure 2-1. Triangular Beam Method.

The following parameters are used in the models: 5000 rays, a reflection order of 200, and a 2s or 5s time window depending upon the room reverberation time. A diffusion coefficient $d=1$ is used for all surfaces to give diffuse reflections (NB $d=0$ would give specular reflections). Harmonic excitation from a point source is used over a frequency range covering one-third octave band centre frequencies from 50 to 5000 Hz. Air absorption is not included in the model.

2.2.2 ODEON

ODEON (v14.01 *combined*) is used to determine spatial distributions of sound pressure levels in corridor-like spaces and car cabins for the purpose of comparison with other modelling approaches such as SEA and analytical models in Chapters 4, 5 and 6. It also combines a mixture of ray tracing and mirror image source method by

defining an early reflection method, early scattering and late reflections [61]. The source used is a point source and the analysis is implemented with specular and diffuse reflections.

The data calculated from this model are used for comparison with SEA models; hence the sound pressure levels are calculated at many positions and spatially averaged over volumes representing SEA subsystems.

An impulse response length of 200ms and 50ms is used for the corridors and car cabins respectively; this was determined by the software based on the Sabine reverberation time.

Air absorption was not included in the model because it was insignificant in the car cabins and only starts to become significant in the elongated cuboids in the 8kHz octave band. To investigate diffraction effect by barriers in the corridor model, screen diffraction was considered. The model uses 320000 rays, transition order of 2, reflection order of 10000 and either specular or diffuse reflections were chosen.

Specular and diffuse reflections are determined as specified by the scattering coefficients and they are vector based scattering method. If scattering is zero then the direction of reflected ray is calculated according to Snell's Law that the reflected angle equals the angle of incidence. If the scattering coefficient is one then the ray is reflected in a completely random direction according to Lambert's Law that the scattered intensity is proportional to the cosine of the scattering angle [61,62].

2.3 Propagating 2D diffuse field

For an irregular elongated room such as a corridor where the length/height and length/width ratios are large, an analytical approach can be used to gain insight into the decrease in sound pressure level with distance.

Assume a cuboid infinite corridor system. Wave propagation down to a corridor of infinite length with rigid boundaries is driven by reflected energy on the surfaces and can be determined by the assumption of two-dimensional coupled sound field. The corridor is simply modelled as the system that a number of very thin box-shaped sections are coupled which is suggested by Redmore and Flockton [49]. This model

is solely or with combination of direct field compared with ray tracing and measurements in following sections.

Sound decrease in the sound pressure level along a corridor can be modelled using a series of coupled spaces with two-dimensional sound fields as shown in Figure 2-2 based on the following assumptions [49,51]:

- 1) There is no explicit consideration of any power source injecting a sound into the corridor in other word and the model therefore does not consider the direct field from the source.
- 2) At $x=0$ the thin corridor section has uniform energy density, w_d which propagates in the positive x direction.
- 3) No interference effects occur between the incident and reflected sound at the receiver.
- 4) Air absorption is ignored (only boundary absorption is considered).
- 5) Absorption coefficient on the boundaries is uniform along a corridor.

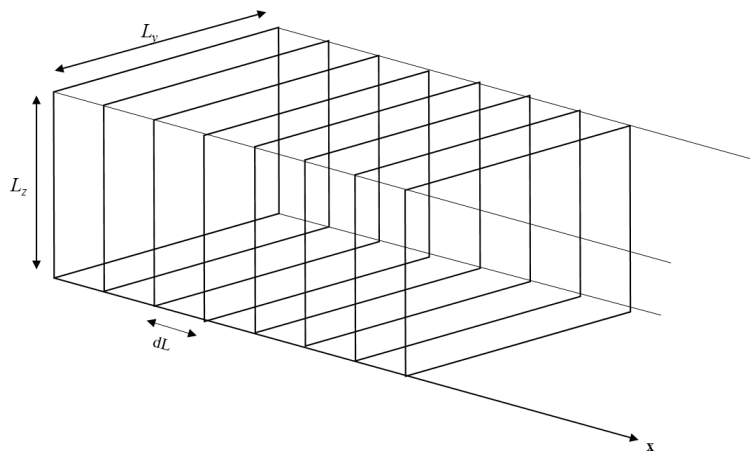


Figure 2-2. Corridor divided into narrow sections of width dL .

The energy, E , in a volume, V , is related to the temporal and spatial average mean-square sound pressure using

$$E = \frac{\langle p^2 \rangle}{\rho_0 c_0^2} V \quad (2.3.1)$$

Assuming two-dimensional diffuse sound field in each corridor section, the power absorbed by the corridor surface is [51]

$$W_{abs} = E \frac{c_0}{d_{mfp}} \frac{A}{UdL} = \frac{Ec_0U\alpha}{\pi L_y L_z} \quad (2.3.2)$$

where $A=U\alpha dL$, a mean free path, $d_{mfp} = S\pi/U$ and the perimeter of the corridor section, $U = 2L_y + 2L_z$.

After travelling a distance d down a corridor where the end of the corridor occurs at $x=D$ (where the end surface has a reflection coefficient, R), the decrease in the sound pressure level (SPL) in decibels is

$$\Delta L = -10 \lg \left(10^{-\Delta L_{inf}/10} + R 10^{-\Delta L_{inf} \left(\frac{2D-d}{d} \right)^{10}} \right) \quad (2.3.3)$$

where ΔL_{inf} is the decrease in the SPL along the corridor (without end wall) at which the sound energy is reduced by the factor $\exp(-k\eta d)$

$$\Delta L_{inf} = \frac{10U\alpha d}{((\ln 10)\pi L_y L_z)} \quad (2.3.4)$$

2.4 Statistical Energy Analysis (SEA)

2.4.1 Classical SEA

The classical Statistical Energy Analysis (SEA) is used to predict sound and structure-borne sound transmission in built-up structure based on energy flow between different parts of the system of interest. SEA is treating a single space as a number of coupled volumes, called subsystems. Some enclosures have zones which have significantly different sound pressure level even though it is a single air volume when sound field is non-diffuse field.

Figure 2-3 illustrates general power flow consisting of six subsystems in accordance with conservation law of energy in SEA. Energy flows between subsystems represented by arrow and input power drives subsystem 1. Statistical energy in each subsystem transmits a portion of it to adjacent subsystems and dissipates a portion of it to out of system which never comes back to the system. The rate of energy flow is proportional to energy ratio between two subsystems.

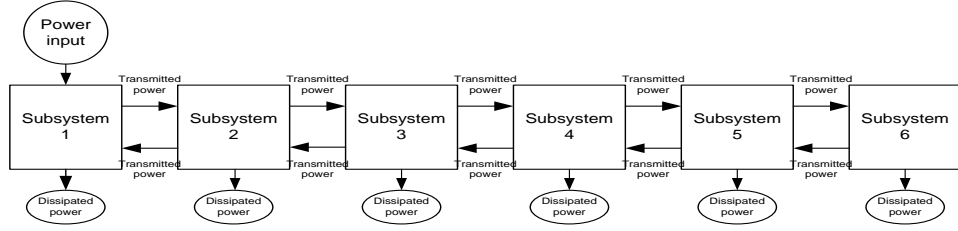


Figure 2-3. Schematic diagram of a six-subsystem SEA model showing only direct coupling.

2.4.1.1 General matrix

For SEA model comprised of N subsystems, the power balance equations are expressed with the generalized matrix solution as follows

$$\begin{bmatrix} \sum_{n=1}^N \eta_{1n} & -\eta_{21} & -\eta_{31} & \dots & -\eta_{N1} \\ -\eta_{12} & \sum_{n=1}^N \eta_{2n} & -\eta_{32} & & \\ -\eta_{13} & -\eta_{23} & \sum_{n=1}^N \eta_{3n} & & \\ \vdots & & & \ddots & \\ -\eta_{1N} & & & & \sum_{n=1}^N \eta_{Nn} \end{bmatrix} \begin{bmatrix} E_1 \\ E_2 \\ E_3 \\ \vdots \\ E_N \end{bmatrix} = \begin{bmatrix} \frac{W_{in}(1)}{\omega} \\ \frac{W_{in}(2)}{\omega} \\ \frac{W_{in}(3)}{\omega} \\ \vdots \\ \frac{W_{in}(N)}{\omega} \end{bmatrix} \quad (2.4.1)$$

where η_{ij} is the coupling loss factor (CLF) from subsystem i to j , and η_{ii} is the internal loss factor (ILF) for subsystem i . Eq. (2.4.1) can be expressed with simplified form

$$[\eta] \{E\} = \left\{ \frac{W_{in}}{\omega} \right\} \quad (2.4.2)$$

where $[\eta]$ is the square matrix of loss factors, $\{E\}$ is the column matrix for energy, and $\{W_{in}/\omega\}$ is the column matrix for power input terms.

In a three-dimensional diffuse field, the sound power incident upon a surface area, S , is given by

$$W = E \frac{c_0}{d_{mfp}} \frac{S}{S_T} \quad (2.4.3)$$

where the mean free path, d_{mfp} for three-dimensional space is

$$d_{\text{mfp}} = \frac{4V}{S_T} \quad (2.4.4)$$

where S_T is the total surface area.

The sound power in Eq. (2.4.3) can be expressed in terms of CLF, η_{ij} defined as the fraction of energy transmitted from subsystem i to subsystem j to another per radian cycle; hence

$$W_{ij} = \omega \eta_{ij} E_i \quad (2.4.5)$$

where ω is the angular frequency.

For two coupled subsystems, the consistency relationship is given by

$$\frac{\eta_{12}}{n_2} = \frac{\eta_{21}}{n_1} \quad (2.4.6)$$

The modal density, n for a two-dimensional space is

$$n_{2D} = \frac{2\pi fS}{c_0^2} + \frac{L_x + L_y}{c_0} \quad (2.4.7)$$

and for a three-dimensional space is

$$n_{3D} = \frac{4\pi f^2 V}{c_0^3} + \frac{\pi f S_T}{2c_0^2} + \frac{L_T}{8c} \quad (2.4.8)$$

where S is $L_y L_z$, S_T is $2(L_x L_y + L_y L_z + L_z L_x)$ and L_T is $4(L_x + L_y + L_z)$.

The CLF from one three-dimensional space to another space via a coupling area with known transmission coefficient can be calculated from Eq. (2.4.3), Eq. (2.4.4) and Eq. (2.4.5),

$$\eta_{ij} = \frac{c_0 S}{4\omega V_i} \tau_{NR} \quad (2.4.9)$$

where τ_{NR} is a non-resonant transmission coefficient.

The dissipated power due to internal losses is described by the ILF which describes the fraction of energy lost as heat in one radian cycle; hence

$$W_{ii} = \omega \eta_{ii} E_i \quad (2.4.10)$$

where η_{ii} is ILF of subsystem i and is defined as the fraction of energy lost from the subsystem as heat or as energy transmitted to other parts of the structure not included in the model.

From Eq. (2.3.2) and Eq. (2.4.10), the ILF can be calculated for a two-dimensional space using

$$\eta_{ii} = \frac{c_0 U \alpha}{\pi \omega L_y L_z} \quad (2.4.11)$$

and for a three-dimensional space, it can be calculated from Eq.(2.4.3), Eq. (2.4.4) and Eq. (2.4.10),

$$\eta_{ii} = \frac{c_0 S_T \bar{\alpha}}{4 \omega V_i} \quad (2.4.12)$$

where,

$$\bar{\alpha} = \frac{1}{S_T} \sum_i S_i \alpha_i \quad (2.4.13)$$

is average absorption coefficient.

2.4.1.2 Path analysis

With SEA, path analysis can be used to assess sound transmission from one subsystem to another subsystem. For a series of coupled subsystems as shown in Figure 2-3, the power balance for the first two subsystems can be written,

$$\omega \eta_{12} E_1 = \omega \eta_2 E_2 \quad (2.4.14)$$

From Eq. (2.4.14), the energy ratio between two subsystems, E_1/E_2 , can be expressed by energy transmission path, $1 \rightarrow 2$,

$$\frac{E_1}{E_2} = \frac{\eta_2}{\eta_{12}} \quad (2.4.15)$$

Therefore, for all subsystems with power injected into subsystem 1, energy ratio between subsystem 1 and subsystem N with energy flow along the subsystem chain, $1 \rightarrow 2 \rightarrow 3 \rightarrow \dots \rightarrow N$, is

$$\frac{E_1}{E_N} = \frac{\eta_2 \eta_3 \cdots \eta_N}{\eta_{12} \eta_{23} \cdots \eta_{(N-1)N}} \quad (2.4.16)$$

This energy ratio can be converted to sound pressure or velocity ratios.

2.4.2 Experimental SEA (ESEA)

Classical Statistical Energy Analysis (SEA) is a powerful predictive tool for analysing vibro-acoustical problems. However, it is not always possible to predict appropriate CLFs for complex coupling situations and/or complex subsystems. In order to overcome this problem, Experimental Statistical Energy Analysis (ESEA) can be used to determine CLFs.

2.4.2.1 General ESEA

The general ESEA (GESEA) is determined from the general SEA matrix and the formulation can be followed as [29]

$$\begin{bmatrix} \sum_{n=1}^N \eta_{1n} & -\eta_{21} & -\eta_{31} & \cdots & -\eta_{N1} \\ -\eta_{12} & \sum_{n=1}^N \eta_{2n} & -\eta_{32} & & \vdots \\ -\eta_{13} & -\eta_{23} & \sum_{n=1}^N \eta_{3n} & & \vdots \\ \vdots & & & \ddots & \\ -\eta_{1N} & & & & \sum_{n=1}^N \eta_{Nn} \end{bmatrix} \begin{bmatrix} E_{11} & E_{12} & E_{13} & \cdots & E_{1N} \\ E_{21} & E_{22} & E_{23} & & \vdots \\ E_{31} & E_{32} & E_{33} & & \vdots \\ \vdots & & & \ddots & \\ E_{N1} & & & & E_{NN} \end{bmatrix} = \begin{bmatrix} \frac{W_{in}(1)}{\omega} & 0 & \cdots & 0 \\ 0 & \frac{W_{in}(2)}{\omega} & & \vdots \\ \vdots & 0 & \frac{W_{in}(3)}{\omega} & \vdots \\ \vdots & & & \ddots \\ 0 & & & & \frac{W_{in}(N)}{\omega} \end{bmatrix} \quad (2.4.17)$$

where E_{ij} is the energy of subsystem i with power input into subsystem j .

ESEA requires power inject method (PIM) which excites one subsystem at a time and measure energy response of all the subsystems. PIM repeats excitation of a subsystem in turn until all energy responses are acquired for all subsystem excitation and this response matrix is used to determine unknown loss factors (LFs) without the use of modal density.

General ESEA (GESEA) has not only direct coupling loss factors between adjacent subsystems but also indirect coupling loss factors between non-adjacent subsystems that are not physically connected. This indicates that sound energy excited by a sound source can influence other subsystems even though subsystems are not directly coupled. Loss factors (LFs) are calculated by inverting energy matrix obtained from the power injection method (PIM). For large complex structure, the inversion of energy matrix may lead to ill-conditioned matrix which has negative CLFs values [63]. This inaccurate set of loss factors causes inappropriate SEA prediction. Hence, it requires modification to get accurate set of ESEA loss factors when there are physically implausible CLFs.

In this study, to improve ESEA outputs incorporated in an SEA model, a set of four rules are used:

- 1) If η_{ij} and η_{ji} are zero or positive then accept these values.
- 2) If η_{ij} is negative then use the consistency relationship to estimate it from η_{ji} .
- 3) If η_{ij} and η_{ji} are negative then set them both to zero.
- 4) If the TLF of a subsystem is lower than sum of its CLFs then the TLF is replaced with the sum of CLFs that have been modified according to rules (1), (2) and (3).

NB For some SEA systems, rule (2) may not be possible to implement if the modal density of each subsystem is unknown. However, with increasing frequency, the statistical modal density can be used as a reasonable approximation; hence the ratio of modal density between two subsystems becomes unity when their volumes are the same.

With GESEA, indirect CLFs are more likely to be prone to numerical errors than direct CLFs when two subsystems are strongly coupled with a large open boundary. Woodhouse [26] suggested that these incorrect CLFs can be modified within the error bands of the measurement since there will be errors in experimental measurements. Woodhouse corrected CLFs using fitting algorithms based on SEA matrix assumptions such as diagonal term should be always greater or at least equal to sum of elements in the same row (or column).

2.4.2.2 Alternative ESEA

Alternative ESEA (AESEA) has been suggested by Lalor [28] to avoid the problem of ill-conditioned matrices. This technique also incorporates power inject method (PIM) to obtain loss factors but the difference from GESEA is that only direct coupled subsystems are considered which is similar to general SEA approach. AESEA treats ILFs and CLFs separately in order to reduce the problems caused by large and badly conditioned energy matrix for large complex structure. The set of matrix for coupling loss factors η_{ri} (associating to the i^{th} subsystem) is

$$\begin{bmatrix} \eta_{li} \\ \vdots \\ \eta_{ri} \\ \vdots \\ \eta_{Ni} \end{bmatrix}_{r \neq i} = \frac{W_i}{\omega E_{ii}} \begin{bmatrix} \left(\frac{E_{11}}{E_{i1}} - \frac{E_{1i}}{E_{ii}} \right) & \dots & \left(\frac{E_{r1}}{E_{i1}} - \frac{E_{ri}}{E_{ii}} \right) & \dots & \left(\frac{E_{N1}}{E_{i1}} - \frac{E_{Ni}}{E_{ii}} \right) \\ \vdots & \ddots & \vdots & \ddots & \vdots \\ \vdots & \vdots & \left(\frac{E_{rr}}{E_{ir}} - \frac{E_{ri}}{E_{ii}} \right) & \vdots & \vdots \\ \vdots & \vdots & \vdots & \ddots & \vdots \\ \left(\frac{E_{1N}}{E_{iN}} - \frac{E_{1i}}{E_{ii}} \right) & \dots & \left(\frac{E_{rN}}{E_{iN}} - \frac{E_{ri}}{E_{ii}} \right) & \dots & \left(\frac{E_{NN}}{E_{iN}} - \frac{E_{Ni}}{E_{ii}} \right) \end{bmatrix}^{-1} \begin{bmatrix} 1 \\ \vdots \\ \vdots \\ \vdots \\ 1 \end{bmatrix} \quad (2.4.18)$$

The internal loss factors can be computed by substituting Eq. (2.4.18) into Eq. (2.4.2) which is given by

$$\eta_{ii} = \frac{W_i - \left\{ \sum_{j=1}^N E_{ij} \eta_{ij} \right\}_{j \neq i} + \left\{ \sum_{j=1}^N E_{ji} \eta_{ji} \right\}_{j \neq i}}{E_{ii}} \quad (2.4.19)$$

The internal loss factors can be directly calculated and which can be expressed in matrix form

$$\begin{bmatrix} \eta_{11} \\ \vdots \\ \eta_{NN} \end{bmatrix} = \frac{1}{\omega} \begin{bmatrix} E_{11} & \dots & E_{N1} \\ \vdots & \ddots & \vdots \\ E_{1N} & \dots & E_{NN} \end{bmatrix}^{-1} \begin{bmatrix} W_1 \\ \vdots \\ W_N \end{bmatrix} \quad (2.4.20)$$

These ILFs should be always positive values.

As mentioned above, this technique only considers the coupling between adjacent subsystems (physically connected subsystems) thus indirect coupling loss factors are assumed to be zero.

Assume a three-subsystem model such as

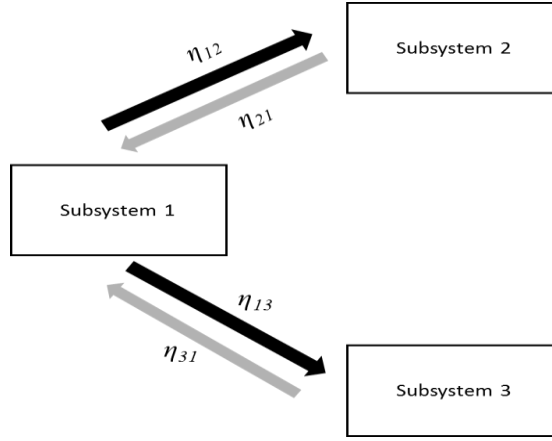


Figure 2-4. Schematic diagram of a three-subsystem SEA model showing only direct coupling.

where subsystem 1 is connected to 2 and 3 but subsystem 2 is disconnected to 3. Hence it indicates that the coupling loss factors η_{23} and η_{32} are treated as zero. The formulation in Eq. (2.4.18) can be expressed by rearranging the coupling loss factors

$$\begin{bmatrix} \eta_{12} \\ \eta_{21} \\ \eta_{13} \\ \eta_{31} \\ \dots \\ \eta_{23} \\ \eta_{32} \end{bmatrix} = \frac{1}{\omega} \begin{bmatrix} (\eta_{12}) & (\eta_{21}) & (\eta_{13}) & (\eta_{31}) & (\eta_{23}) & (\eta_{32}) \\ \left(\frac{E_{11} - E_{12}}{E_{21} - E_{22}} \right) & 0 & 0 & 0 & 0 & \left(\frac{E_{31} - E_{32}}{E_{21} - E_{22}} \right) \\ 0 & \left(\frac{E_{22} - E_{21}}{E_{12} - E_{11}} \right) & 0 & \left(\frac{E_{32} - E_{31}}{E_{12} - E_{11}} \right) & 0 & 0 \\ 0 & 0 & \left(\frac{E_{11} - E_{13}}{E_{31} - E_{33}} \right) & 0 & \left(\frac{E_{21} - E_{23}}{E_{31} - E_{33}} \right) & 0 \\ 0 & \left(\frac{E_{23} - E_{21}}{E_{13} - E_{11}} \right) & 0 & \left(\frac{E_{33} - E_{31}}{E_{13} - E_{11}} \right) & 0 & 0 \\ \dots & \dots & \dots & \dots & \dots & \dots \\ 0 & 0 & \left(\frac{E_{12} - E_{13}}{E_{32} - E_{33}} \right) & 0 & \left(\frac{E_{22} - E_{23}}{E_{32} - E_{33}} \right) & 0 \\ \left(\frac{E_{13} - E_{12}}{E_{23} - E_{22}} \right) & 0 & 0 & 0 & 0 & \left(\frac{E_{33} - E_{32}}{E_{23} - E_{22}} \right) \end{bmatrix}^{-1} \begin{bmatrix} \frac{W_2}{E_{22}} \\ \frac{W_1}{E_{11}} \\ \frac{W_3}{E_{33}} \\ \frac{W_1}{E_{11}} \\ \dots \\ \frac{W_3}{E_{33}} \\ \frac{W_2}{E_{22}} \end{bmatrix} \quad (2.4.21)$$

The formulation of above matrix can be simplified as the form

$$\begin{bmatrix} \eta_\alpha \\ \eta_\beta \end{bmatrix} = \frac{1}{\omega} \begin{bmatrix} E_{\alpha\alpha} & E_{\alpha\beta} \\ E_{\beta\alpha} & E_{\beta\beta} \end{bmatrix}^{-1} \begin{bmatrix} W_\alpha \\ W_\beta \end{bmatrix} \quad (2.4.22)$$

where η_β is zero because subsystems 2 and 3 are disconnected.

From Eq. (2.4.22) only the left upper side of sub-matrix in Eq. (2.4.21) is considered and can be rewritten by

$$[\eta_\alpha] = \begin{bmatrix} \eta_{12} \\ \eta_{21} \\ \eta_{13} \\ \eta_{31} \end{bmatrix} = \frac{1}{\omega} \left[\begin{array}{cccc} \left(\frac{E_{11}}{E_{21}} - \frac{E_{12}}{E_{22}} \right) & 0 & 0 & 0 \\ 0 & \left(\frac{E_{22}}{E_{12}} - \frac{E_{21}}{E_{11}} \right) & 0 & \left(\frac{E_{32}}{E_{12}} - \frac{E_{31}}{E_{11}} \right) \\ 0 & 0 & \left(\frac{E_{11}}{E_{31}} - \frac{E_{13}}{E_{33}} \right) & 0 \\ 0 & \left(\frac{E_{23}}{E_{13}} - \frac{E_{21}}{E_{11}} \right) & 0 & \left(\frac{E_{33}}{E_{13}} - \frac{E_{31}}{E_{11}} \right) \end{array} \right]^{-1} \begin{bmatrix} \frac{W_2}{E_{22}} \\ \frac{W_1}{E_{11}} \\ \frac{W_3}{E_{33}} \\ \frac{W_1}{E_{11}} \end{bmatrix} \quad (2.4.23)$$

The inversion of energy matrix $E_{\alpha\alpha}$ in Eq. (2.4.22) can be approximated since the energy of a directly driven subsystem must be always greater than that of a subsystem connected to it hence the inequality that needs to be satisfied is $E_{11}E_{22} \gg E_{12}E_{21}$ and $E_{11} \gg E_{32}$. It drives off-diagonal term of the energy matrix in Eq. (2.4.23) vanished thus the inversion of energy matrix can be approximated by

$$[E_{\alpha\alpha}]^{-1} \approx \begin{bmatrix} \frac{E_{21}}{E_{11}} & 0 & 0 & 0 \\ 0 & \frac{E_{12}}{E_{22}} & 0 & 0 \\ 0 & 0 & \frac{E_{31}}{E_{11}} & 0 \\ 0 & 0 & 0 & \frac{E_{13}}{E_{33}} \end{bmatrix} \quad (2.4.24)$$

Substituting Eq. (2.4.24) into Eq. (2.4.23) gives approximated coupling loss factors (CLFs)

$$\eta_{ij} \approx \frac{1}{\omega} \left(\frac{E_{ji}}{E_{ii}} \right) \left(\frac{W_i}{E_{jj}} \right) \quad (2.4.25)$$

In this study, both full matrix version of AESEA (Eq.(2.4.23)) and approximated version of AESEA (Eq.(2.4.25)) are used to determine direct CLFs. There will be difference between CLFs determined from both approaches when there is non-negligible indirect coupling between disconnected subsystems such as direct field.

2.4.3 Clustering analysis

SEA requires subdivision of a single system into coupled subsystems. This requires appropriate subdivision to give an accurate prediction model. In practice, partitioning is often performed on geometric subdivision for air volume or on different material parts for a structure. Optimal subdivision should give better SEA estimates.

Diaz-Cereceda et al [37] proposed modal based energy subdivision and showed success on a junction of three coupled plates as well as two rooms separated by a wall structure. The same approach for clustering subsystems is used in this study but with coupled volumes.

An enclosed volume can support three types of modes: axial, tangential and oblique. The subsystem is hierarchically formed from a cell which is a minimum unit with normalized modal energy contribution. The size of a cell is set to be equal to or greater than half the maximum wavelength considered so that it is physically reasonable in an SEA sense. The maximum wavelength is relevant to the lowest frequency of interest in frequency bands. Figure 2-5 describes hierarchical clustering process and each step follows determining normal energy. In order to calculate the normalized modal energy contribution to a certain cell, i , first the calculation of the averaged energy density is required, and a map of energy density e_{ij} is constructed for every mode j . For a rectangular room with rigid wall total energy for eigenmodes is given by [64]

$$E = \frac{1}{2} \iiint \left[\rho u^2 + \frac{1}{pc^2} p^2 \right] dx dy dz \quad (2.4.26)$$

where p is sound pressure for standing wave given by

$$\begin{aligned} p &= \psi_{n_x, n_y, n_z} e^{-i\omega t} \\ \psi_{n_x, n_y, n_z} &= \cos\left(\frac{\pi n_x x}{l_x}\right) \cos\left(\frac{\pi n_y y}{l_y}\right) \cos\left(\frac{\pi n_z z}{l_z}\right) \\ \omega &= \pi c_0 \sqrt{\left(\frac{n_x}{l_x}\right)^2 + \left(\frac{n_y}{l_y}\right)^2 + \left(\frac{n_z}{l_z}\right)^2} \end{aligned} \quad (2.4.27)$$

where ψ is the local mode shape (also called an eigenfunction) and ω is mode frequency (also called an eigenfrequency).

The particle motion gives rise to sound pressure and energy in Eq. (2.4.26) therefore sound particle velocity \mathbf{u} associated with sound pressure can be expressed by

$$\mathbf{u} = -\frac{1}{i\omega\rho} \text{grad}(p) \quad (2.4.28)$$

and in the x, y and z directions respectively, as

$$\begin{aligned} u_x &= \frac{1}{i\omega\rho} \frac{\partial p}{\partial x} = -\frac{1}{i\omega\rho} k_x \sin\left(\frac{n_x \pi x}{l_x}\right) \cos\left(\frac{n_y \pi y}{l_y}\right) \cos\left(\frac{n_z \pi z}{l_z}\right) \\ u_y &= \frac{1}{i\omega\rho} \frac{\partial p}{\partial y} = -\frac{1}{i\omega\rho} k_y \cos\left(\frac{n_x \pi x}{l_x}\right) \sin\left(\frac{n_y \pi y}{l_y}\right) \cos\left(\frac{n_z \pi z}{l_z}\right) \\ u_z &= \frac{1}{i\omega\rho} \frac{\partial p}{\partial z} = -\frac{1}{i\omega\rho} k_z \cos\left(\frac{n_x \pi x}{l_x}\right) \cos\left(\frac{n_y \pi y}{l_y}\right) \sin\left(\frac{n_z \pi z}{l_z}\right) \end{aligned} \quad (2.4.29)$$

where k_x , k_y and k_z are constants related to the wavenumber,

$$k_x = \frac{n_x \pi}{l_x} = \frac{\omega_x}{c_o} \quad k_y = \frac{n_y \pi}{l_y} = \frac{\omega_y}{c_o} \quad k_z = \frac{n_z \pi}{l_z} = \frac{\omega_z}{c_o} \quad (2.4.30)$$

The energy density at a certain element e_{ij} , can be calculated from Eq. (2.4.26). However the most meaningful variable is the normalised energy density \tilde{e}_{ij} , which is the difference between the energy itself e_{ij} at each cell and the averaged energy \bar{E}_j , of the system for each cell i and mode j , given by

$$\tilde{e}_{ij} = \frac{e_{ij} - \bar{E}_j}{S_j \sqrt{N}} \quad (2.4.31)$$

where

$$E_j = \frac{1}{N} \sum_{i=1}^N e_{ij} \quad (2.4.32)$$

is the mean energy density in the domain for mode j ,

$$S_j = \frac{1}{N} \sum_{i=1}^N (e_{ij} - \bar{E}_j)^2 \quad (2.4.33)$$

is the variance of e_{ij} for mode j and N is the number of cells.

Once the normalized energy maps are created, the distance between two cluster (begun with a cell) m and n is required to define whether two cells should be formed using the correlation distance between their energy vector \mathbf{x}_i , which is related to a cell i normalised energy density for mode j . The correlation distance is given by

$$d(\mathbf{x}_m, \mathbf{x}_n) = 1 - \frac{(\mathbf{x}_m - \bar{\mathbf{x}}_m)(\mathbf{x}_n - \bar{\mathbf{x}}_n)^T}{\sqrt{(\mathbf{x}_m - \bar{\mathbf{x}}_m)(\mathbf{x}_m - \bar{\mathbf{x}}_m)^T} \sqrt{(\mathbf{x}_n - \bar{\mathbf{x}}_n)(\mathbf{x}_n - \bar{\mathbf{x}}_n)^T}} \quad (2.4.34)$$

where

$$\mathbf{x}_m = \left(\frac{1}{N_m} \sum_j x_{mj} \right) \mathbf{1} \quad (2.4.35)$$

where $\mathbf{1}$ is a vector with all the components equal to one.

The correlation distance indicates the similarity between the energy vectors which only take their directions account into not the influence of their magnitudes because it is eliminated by a normalisation. The range of the correlation distance is between zero and two. When the values of correlation distance are close to zero and two it indicates that the direction of two vectors is very similar. On the other hand, when the value is one, the direction of the two vectors is very different.

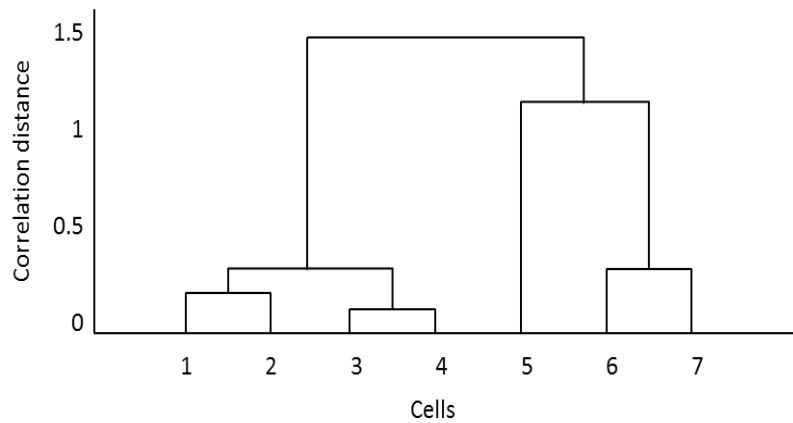


Figure 2-5. Hierarchical cell clustering process.

Once two cells are grouped as one, a new element is created and new correlation distances between the new elements are renewed. This procedure is repeatedly

carried out by updating the correlation distance for the hierarchical clustering until all adjacent clusters have a different direction of vectors.

2.5 Finite Element Method (FEM)

FEM is a numerical technique for solving complex elasticity by subdividing large continuous structure into very small element assemblies. The nodal responses of the elements are computed from equations of motion subject to a mass and stiffness matrix and the results are approximated by minimizing an associated error functions. The simple equations for FE are often linear partial differential equations (PDE) if they are linear, and vice versa. FE is very suitable for analysing problems over complicated structures at low frequency which is widely applied in engineering field as a computational tool for performing engineering analysis. It includes the use of mesh generation techniques for the divisions of a complex domain into small elements. In this study, ABAQUS program is used as a FE analysis tool.

The acoustic medium is modelled using AC3D8 eight-node linear acoustic brick elements for a cuboid system and using AC3D10 ten-node quadratic acoustic tetrahedron for a car cabin with an element size of 0.1m there are 34 elements per wavelength at 100 Hz. Lanczos eigensolver for real eigenvalues has been employed for modal analysis afterwards complex frequency analysis is carried out in order to get complex modal frequencies since the boundary conditions for the acoustic medium were specified in terms of specific acoustic impedances applied to rigid surfaces which is different from open area.

The validity of FEM with point source excitation has been verified though comparison with a Normal Mode Model (NMM) for an elongated room (30m x 1.5m x 2.5m, $c_0=343\text{m/s}$, $\rho=1.21\text{kg/m}^3$, bulk modulus $K_f=142355\text{N/m}^2$, point source $W=0.01\text{Watt}$). The power generated by a point source can be calculated from

$$W = 4\pi r^2 I = \frac{2\pi \hat{p}}{\rho c_0} \quad (2.5.1)$$

where peak pressure can be described using a peak volume velocity given by

$$\hat{Q} = \frac{4\pi \hat{p}}{\omega \rho} \quad (2.5.2)$$

FEM uses volume acceleration for acoustic analysis with a point source hence constant source power can be converted to the constant volume acceleration using Eq. (2.5.1) and Eq. (2.5.2). The point source is placed at the corner (0.25m, 0.25m, 0.25m) and the measurement position is in the diagonally opposite corner of the room. The sound pressure level from FEM and NMM are compared in Figure 2-6.

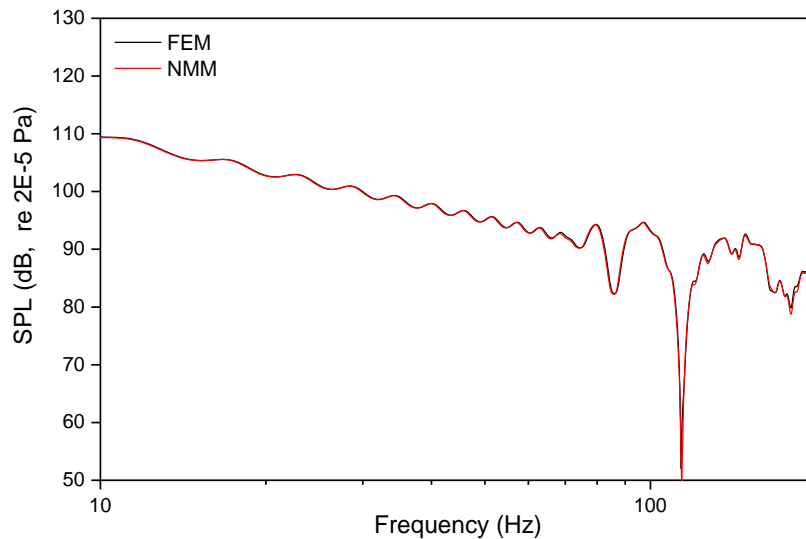


Figure 2-6. Comparison of FEM with NMM for sound pressure level at the corner position.

FEM shows very close agreement with NMM which indicates that the prediction with a point source using FEM can be reasonably used to determine the sound distribution in more complex volumes in Chapter 6.

FEM will be used for the modal analysis of open-ended volumes to gain insight into the mode shapes and modal responses in Chapter 4. It will also be used in Chapter 6 for the computation of the sound pressure level with a point source and radiating plate.

2.6 Experimental work

2.6.1 Empty corridor

Measurements have been undertaken on a real corridor linking Harrison Hughes building to the Active Learning Lab/Hele Shaw Lecture theatre at the University of Liverpool. The corridor (54.5 m x 2.1 m x 2.3 m) is illustrated in Figure 2-7. The surfaces are plasterboard on the walls and ceiling, and linoleum on the floor. On both sides of the walls there are windows/glazing.

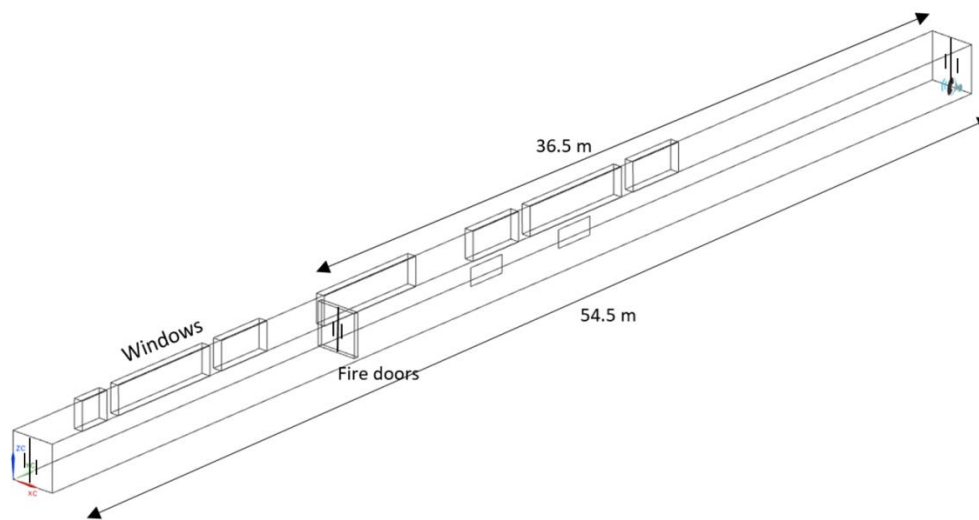


Figure 2-7. Schematic diagram of the corridor used for measurements.

As a sound source, the B&K sound power source type 4204 was used at the end of the corridor. An indication of the broadband noise output can be seen from the sound power in one-third octave bands in Table 2-1 [65]. Note that knowledge of the absolute sound power was not necessary as the measurements and predictions were compared using relative sound pressure levels.

TOB (Hz)	Sound power (dB re 10 ⁻¹² W)
100	74.3
125	75.8
160	76.8
200	77.8
250	77.2
315	76.6
400	76.4
500	76.9
630	78.4
800	81.5
1000	81.8
1250	82.4
1600	82.5
2000	81.3
2500	79.8
3150	77.2
4000	77.4
5000	78.2
6300	76.6
8000	75.7
10000	73.3

Table 2-1. B&K sound power source output.

A sound level meter NTi AUDIO XL2-TA was used to measure sound pressure levels in terms of $L_{eq,30s}$ in one-third octave frequency bands. A windscreen was used to minimise any effect from airflow near the source. Background noise was measured to ensure that the sound level was at least 10 dB above background.

Measurements were used to give a spatial average sound pressure level over the corridor cross-section in 1m steps down the corridor to give a total of 54 spatial average values. This spatial average was calculated from three different random microphone positions over the cross-section (but keeping the microphone a minimum distance of 0.5m from the boundary to avoid higher energy density near boundaries). Figure 2-8 shows the measurement setup.

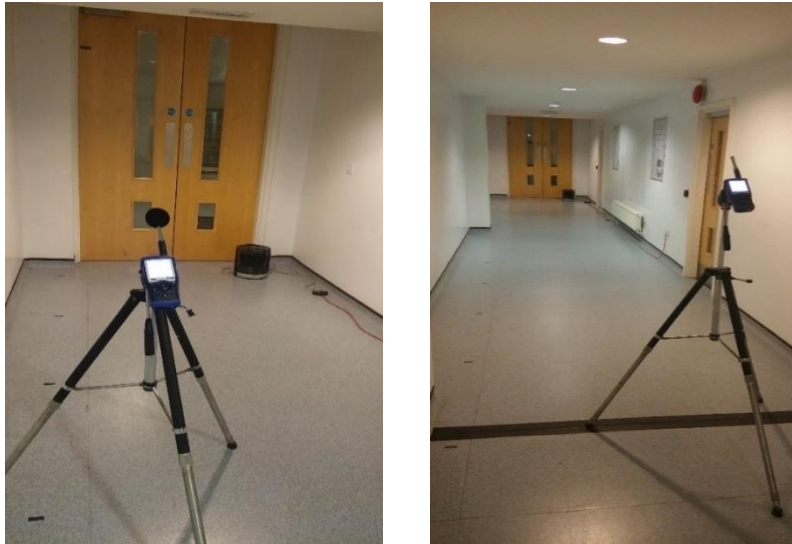


Figure 2-8. Measurement setup on a real corridor.

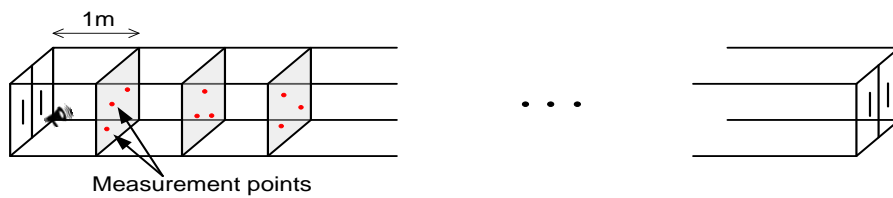


Figure 2-9. Measurement for the sound pressure along the empty corridor.

2.6.2 Corridor with staggered partitions

Measurements for another type of corridor were carried out by placing partitions along the empty corridor as illustrated in Figure 2-10. The size of the partition is 1.5m x 1.8m. Five partitions were used, located every six metres.

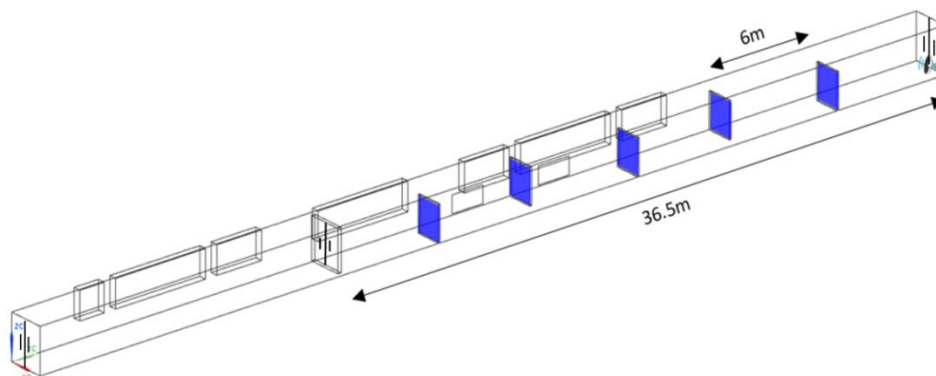


Figure 2-10. Schematic diagram of the corridor with partitions.

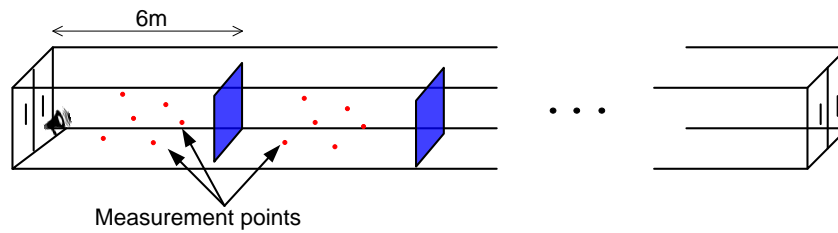


Figure 2-11. Measurements for the sound pressure at each subspace divided by partitions along the corridor.

In the six different volumes defined by the partitions, the positions for the measurements are randomly chosen with six different heights as indicated in Figure 2-11. To use ESEA measurements were taken with the source in each of the six different volumes.

2.6.3 Absorption coefficient of the partition

Measurement of the absorption coefficient of the partition (dimension 1.5m x 1.8m) was performed in a reverberation chamber (volume 122m³) which is used for measurements on a real corridor in Section 5.6. The measurement method was in accordance with BS EN ISO 354 (2003). A B&K type 2231 sound level meter was used to measure sound pressure and an omnidirectional sound power source was used for the measurements. Reverberation time was calculated using Dirac program. Measurements were carried out using two different positions for the omnidirectional sound power source.

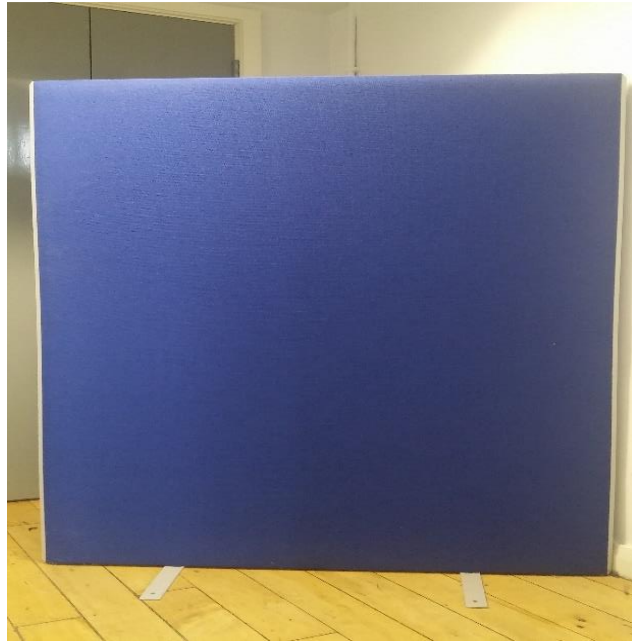


Figure 2-12. Partition used for the measurements.

The reverberation time T_1 of the empty chamber without partitions was measured using six different positions at least $\lambda/2$ apart (where λ is wavelength for the lowest frequency of interest), at least 1m from room surfaces and 2m from the sound source in one-third octave bands from 100-10,000 Hz. With the partitions, the same procedure of the measurement carried out to measure T_2 with microphone positions at least 1m away from the partition. The reverberation time T_2 was determined using two partitions as the change with and without one partition at high frequencies was less than 20% which can lead to incorrect estimation of the absorption coefficient.

The equivalent absorption area of the partition using reverberation times measured is given by

$$A = \frac{55.3V}{c_0} \left(\frac{1}{T_2} - \frac{1}{T_1} \right) \quad (2.6.1)$$

and absorption coefficient of the sample can be calculated by

$$\alpha_s = \frac{A}{S} \quad (2.6.2)$$

where S is total area of the two partitions (both sides).

The absorption coefficients for the partition are given in Table 2-2.



Figure 2-13. Measurement setup for the absorption coefficient of the partition used for the real corridor experiment in the reverberation chamber at two different position of the omnidirectional power source and with two partitions.

Frequency (Hz)	100	125	160	200	250	315	400	500	630	800	1000
Absorption coefficient, α_s	0.08	0.04	0.02	0.07	0.17	0.23	0.21	0.21	0.17	0.17	0.18

Frequency (Hz)	1250	1600	2000	2500	3150	4000	5000	6300	8000	10K
Absorption coefficient, α_s	0.2	0.24	0.28	0.33	0.39	0.46	0.53	0.68	0.82	0.73

Table 2-2. Measured absorption coefficient of the partition.

The measured absorption coefficients are assumed to be reasonable estimate that is applicable to the sound field in the corridor. This would be assessed in Chapter 5 through comparison of measurements and ray tracing.

Chapter 3 Characterization of sound field using spatial correlation

3.1 Introduction

Interpreting and quantifying spatial correlation coefficient is useful to determine sound fields for a given space. This chapter considers assessment of sound field inside different volume box-shaped rooms (30m^3 , 50m^3 and 120m^3) in comparison with the theory for a plane wave and three-dimensional diffuse field. Ray tracing model using Raynoise is used to produce idealised representations of sound field for analysis.

The general equation for the spatial correlation coefficient using instantaneous sound pressure at two different points i and j in a sound field is [2]

$$R(kd_{ij}) = \frac{\langle p_i p_j \rangle_t}{\sqrt{\langle p_i^2 \rangle_t \langle p_j^2 \rangle_t}} \quad (3.1.1)$$

where $p_i(t)$ and $p_j(t)$ are instantaneous sound pressure at time t at two points respectively, and angular bracket denotes time average. Thus

$$\langle p_i p_j \rangle_t = \frac{1}{T} \int_0^T p_i(t) p_j(t) dt \quad (3.1.2)$$

3.2 Spatial correlation for instantaneous sound pressure in a free-field and a diffuse field

The spatial correlation coefficient, R , between two different points in a space varies with wave number k and distance d between points.

In a free-field with a propagating plane wave, the sound pressures at two points, i and j , along the x-axis are $p_i(t) = \sin(\omega t + kx_i)$ and $p_j(t) = \sin(\omega t + kx_j)$ using Eq.(3.1.1),

$$\begin{aligned}
\langle p_i p_j \rangle &= \frac{1}{T} \int_0^T \sin(\omega t + kx_i) \sin(\omega t + kx_j) dt \\
&= \frac{1}{T} \int_0^T (\sin \omega t \cos kx_i + \cos \omega t \sin kx_i)(\sin \omega t \cos kx_j + \cos \omega t \sin kx_j) dt \\
&= \frac{1}{T} \int_0^T \sin^2 \omega t \cos kx_i \cos kx_j + \sin \omega t \cos \omega t \cos kx_i \sin kx_j + \cos \omega t \sin \omega t \sin kx_i \cos kx_j + \cos \omega t \sin kx_j \sin kx_i dt \\
&= \frac{1}{T} \int_0^T \frac{1}{2} (1 - \cos 2\omega t) \cos kx_i \cos kx_j + \frac{1}{2} (1 + \cos 2\omega t) \sin kx_i \sin kx_j dt \\
&= \frac{1}{2T} \int_0^T \cos kx_i \cos kx_j + \sin kx_i \sin kx_j dt \\
&= \frac{1}{2T} T (\cos(kx_i - kx_j)) \\
&= \frac{1}{2} (\cos(kx_i - kx_j))
\end{aligned} \tag{3.2.1}$$

Ignoring spatial dependence,

$$\begin{aligned}
\langle p_i^2 \rangle &= \langle p_j^2 \rangle = \frac{1}{T} \int_0^T \sin^2(\omega t) dt \\
&= \frac{1}{T} \int_0^T \frac{1}{2} (1 - \cos(2\omega t)) dt \\
&= \frac{1}{2T} \int_0^T (1 - \cos(2\omega t)) dt \\
&= \frac{1}{2}
\end{aligned} \tag{3.2.2}$$

Suppose that a plane wave of wavelength λ propagates past points i and j and the angle between the normal to the wave front and the line ij (see Figure 3-1). Hence, $R = \cos(kx_i - kx_j)$ where $(kx_i - kx_j) = kd_{ij} \cos \theta$ corresponds to a phase difference, such that

$$R(kd_{ij}) = \cos(kd_{ij} \cos \theta) \tag{3.2.3}$$

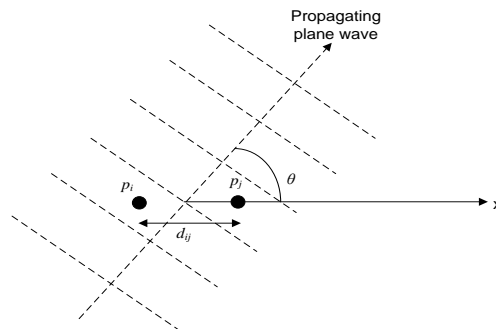


Figure 3-1. Plane wave propagating past points i and j at an angle θ .

The angle θ describes the direction of the incident sound wave. The value of R as a function of k and d for a random sound field in three-dimensional space has to be averaged with equal weighting corresponding to a diffuse field (see Figure 3-2) to all directions of the incident sound. This average of spatial correlation coefficient is given by [2]

$$R(kd_{ij}) = \frac{1}{4\pi} \int_0^{\pi} \int_0^{2\pi} \cos(kd_{ij} \cos \theta) \sin \theta d\phi d\theta = \frac{\sin kd_{ij}}{kd_{ij}} = \text{sinc}(kd_{ij}) \quad (3.2.4)$$

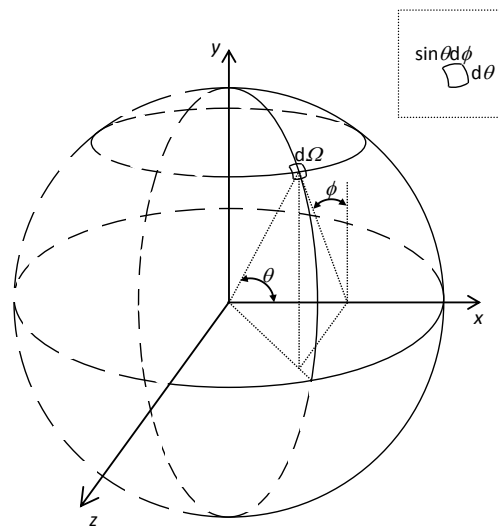


Figure 3-2. Sound wave incident from all possible angles in spherical coordinate system.

For incident sound propagating in only one plane there is a two-dimensional sound field for which [2]

$$R(kd_{ij}) = \frac{1}{2\pi} \int_0^{2\pi} \cos(kd_{ij} \cos \theta) d\theta = J_0(kd_{ij}) \quad (3.2.5)$$

where J_0 is the Bessel function of order zero.

Figure 3-3 shows the spatial correlation coefficient for 3D diffuse field and 2D diffuse field theory from Eq.(3.2.4) and Eq.(3.2.5). These two theories can be used as an indicator to identify a given sound field by comparing them with spatial correlation coefficients determined from measurements. For irregularly-shaped spaces such as large volume rooms with a relatively low ceiling height, 2D diffuse field theory might be suitable rather than 3D diffuse field theory.

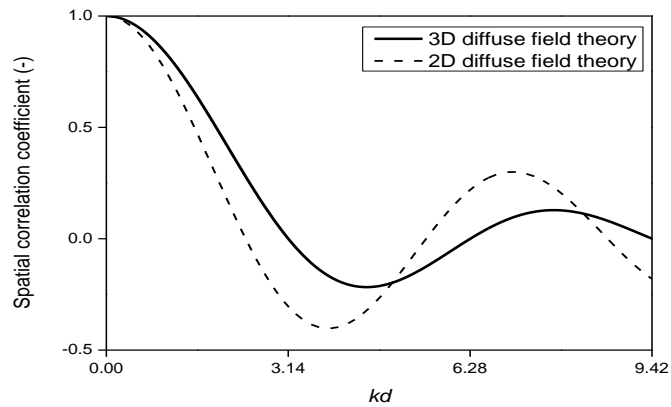


Figure 3-3. Spatial correlation as a function of kd in a three-dimensional diffuse field and a two-dimensional diffuse field.

3.3 Numerical experiments to determine R using ray tracing

A point source is modelled in the ray tracing model, LMS Raynoise, to determine sound pressure in different spaces. The source is assumed to be single frequency and coherent such that phase information is retained as the rays propagate. All boundaries are assigned a diffusion coefficient of unity so that all reflected sound power is in diffuse reflections.

Following the approach of Cook et al [2], an assessment of diffusivity is carried out by measuring the instantaneous sound pressure at two points i and j along mutually perpendicular directions. Ten randomly chosen measurement lines in both x - and z -axes are used with 0.1m spacing point to acquire sound pressure for ray tracing shown in Figure 3-4. Cook et al [2] used one fixed position, but in this thesis, three different approaches are considered that seem reasonable.

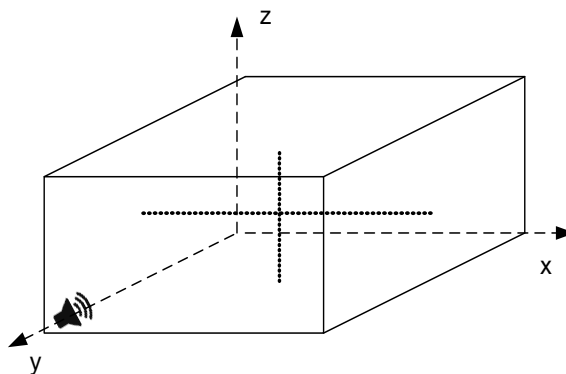


Figure 3-4. Schematic diagram of room used for ray tracing with measurement lines along x - and z -directions.

The spatial correlation is calculated using the following three approaches:

Option (1): Pairs of points formed by one fixed point at a position that is $\geq \lambda/2$ from the boundary that lies in a plane perpendicular to the measurement line, and all other points along the same line that are $\geq \lambda/2$ from the opposite boundary

Option (2): Pairs of points with a fixed spacing, d_{ij} , along each line

Option (3): All permutations of points with variable spacing, d_{ij} , along each line

With instantaneous sound pressure data acquired from ray tracing, the spatial correlation coefficient is determined using Eq.(3.1.1) for which the components in the numerator and denominator are

$$\begin{aligned} \langle p_i p_j \rangle_t &= \frac{1}{2} \text{Re}\{p_i p_j^*\} = \frac{1}{2} \text{Re}\left[(\text{Re}\{p_i\} + \text{Im}\{p_i\}j)(\text{Re}\{p_j\} + \text{Im}\{p_j\}j)\right] \\ &= \frac{1}{2} [\text{Re}\{p_i\}\text{Re}\{p_j\} + \text{Im}\{p_i\}\text{Im}\{p_j\}] \end{aligned} \quad (3.2.6)$$

$$\langle p_i^2 \rangle = \langle p_j^2 \rangle = \frac{1}{2} \text{Re}\{p_i p_i^*\} = \frac{1}{2} [\text{Re}\{p_i\}^2 + \text{Im}\{p_i\}^2] \quad (3.2.7)$$

where the asterisk indicates the complex conjugate.

This gives the spatial correlation coefficient as

$$R(kd_{ij}) = \frac{\text{Re}\{p_i\}\text{Re}\{p_j\} + \text{Im}\{p_i\}\text{Im}\{p_j\}}{\sqrt{[\text{Re}\{p_i\}^2 + \text{Im}\{p_i\}^2][\text{Re}\{p_j\}^2 + \text{Im}\{p_j\}^2]}} \quad (3.2.8)$$

The spatial correlation coefficient determined from ray tracing will be compared with plane wave theory (Eq.(3.2.3)) and three-dimensional diffuse field theory (Eq.(3.2.4)) in next chapters.

3.3.1 Spatial correlation for a propagating plane wave in a free-field

In this section, validation of the calculation of spatial correlation from ray tracing data using Eq.(3.2.8) is carried out through comparison with plane wave theory for a propagating plane wave. To simulate a free-field, an anechoic space is modelled with two different source positions as shown in Figure 3-5: (A) a point source aligned

with the measurement line along the x-axis and (B) a point source positioned at an angle to the measurement line. All measurement points are at least 1m away from the source. Spatial correlation coefficients are assessed against the Helmholtz number kd_{ij} .

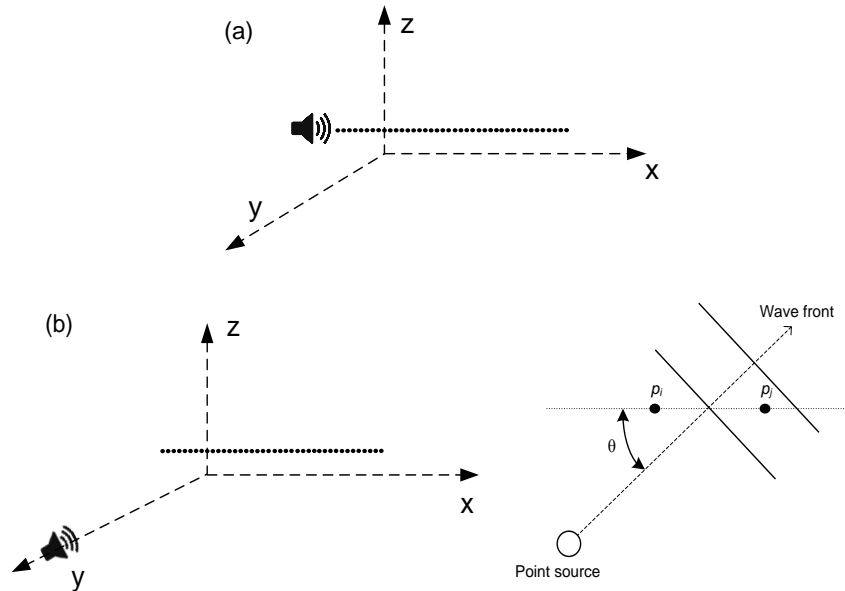


Figure 3-5. Two different source positions in an anechoic space. (a) A point source aligned with the measurement line along the x-axis and (b) a point source positioned at an angle to the measurement line.

For source position (A) the results are shown in Figure 3-6 (a) and (b) using options (2) and (3) respectively. The angle $\theta=0^\circ$; hence the spatial correlation coefficient is a function of kd_{ij} (rather than $kd_{ij}\cos\theta$). Option (2) has relatively few values compared to option (3); hence, the latter provides a better validation when all permutations of pairs are considered. This validates the calculation of spatial correlation from ray tracing data using Eq.(3.2.8).

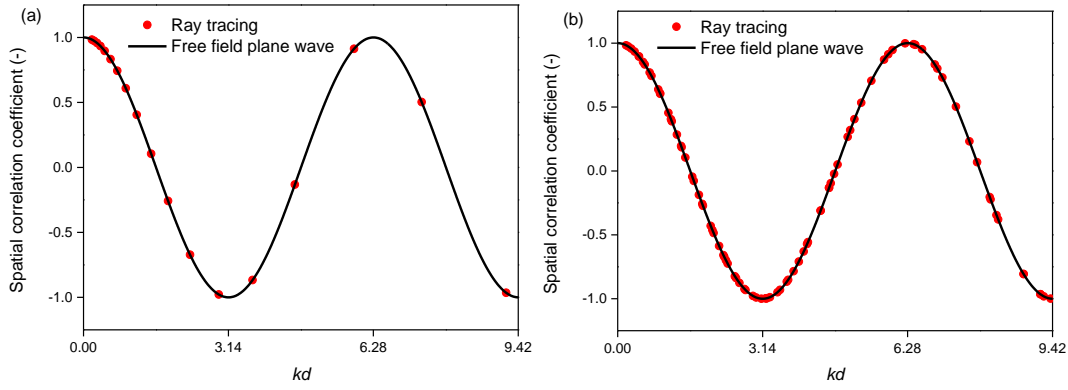


Figure 3-6. Spatial correlation for plane wave in a free field for source position (A) with (a) option (2) considering adjacent pairs of points along the line and with (b) option (3) considering all permutation pairs of points along the line.

For source position (B), the spatial correlation is $kd_{ij}\cos\theta$, where θ varies for each pair of points; hence averaging is necessary according to

$$R_{\text{average plane wave}}(kd) = \frac{\sum_{i=1}^N \bar{\mu}_i}{N} \quad (3.2.9)$$

where

$$\bar{\mu}_i = \frac{\sum_{j=1}^M kd_i \cos \theta_j}{M} \quad (3.2.10)$$

where M is the number of different incident angles and N is the number of different d values, $N=1$ for option (2) (fixed spacing of pairs) and $N \neq 1$ for option (3) (all permutations of pairs).

When comparing ray tracing data against this average plane wave it is necessary to consider whether the wave front that impinges upon each pair of points is a close approximation to a plane wave front rather than a spherical wave front. For source position (A) the plane wave assumption is always reasonable because the measurement line is always perpendicular to the spherical wave front. However, for source position (B) this is not the case. When the receiver is far from the point source ($kr \gg 1$) it is of interest to assess when the distance between two points is close enough for the plane wave approximation to a spherical wave to be reasonable. Figure 3-7 shows a spherical wave front and the assumed plane wave fronts.

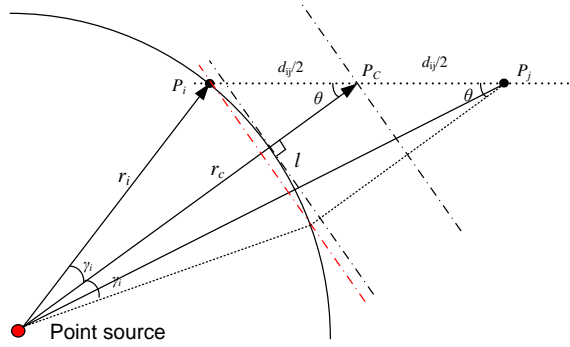


Figure 3-7. Approximation of spherical wave to plane wave. Dashed lines represent the plane wave and the solid arc represents the spherical wave front.

When the spherical wave front passes the point P1, P2 can be projected onto the plane wave front (red dash-dot line). An assessment of the plane wave approximation to a spherical wave can be described in terms of the ratio

$$ratio = \frac{d_{ij} \sin \theta}{l} \quad (3.2.11)$$

where

$$l = 2\gamma_i r_i \quad (3.2.12)$$

When the ratio is almost one, then it is reasonable to assume that the spherical wave can be approximated by a plane wave. Hence, the protocol tested in this section is only to include individual pairs of points from ray tracing in the average where both points satisfy a minimum value for the ratio. Comparison of plane wave theory with ray tracing is now made when the ratio is (a) >0 , (b) >0.9 , (c) >0.95 and (d) >0.99 .

For option (2) with source position (B), all four ratio requirements give the same result as shown in Figure 3-8. This shows exact agreement between ray tracing and plane wave theory at all kd values and also validates the calculation of spatial correlation from ray tracing data using Eq.(3.2.8).

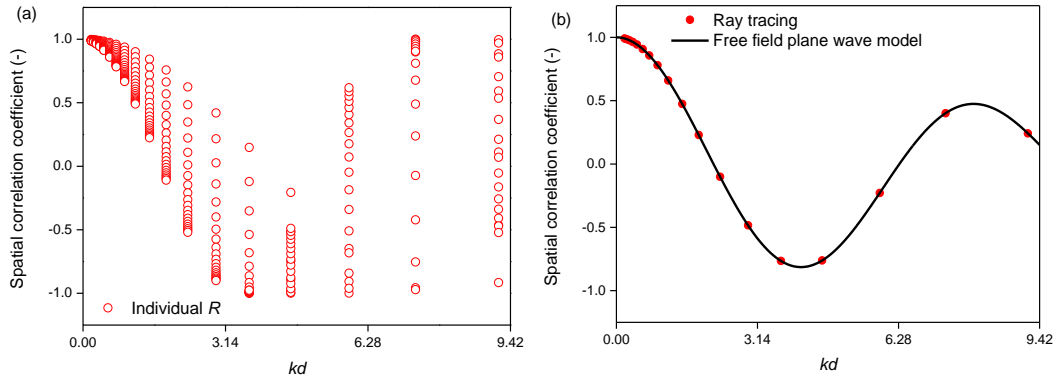


Figure 3-8. Spatial correlation for plane wave in a free field for source position (B) with option (2) considering adjacent pairs of points ($d=0.1\text{m}$) along the line (a) individual points and (b) average values using Eq. (3.2.9) and (3.2.10).

For option (3) with source position (B), Figure 3-9 shows R values from ray tracing and plane wave theory as a continuous function of kd with four different ratios (Eq. (3.2.9) and (3.2.12)). When calculating spatial correlation coefficients as a continuous function of kd , the plane wave approximation for R is $kd_{ij}\cos\theta$ for which the angle, θ , is calculated for each individual pair of points that satisfies the ratio requirement. However, to determine a continuous function the assumption is that all values of kd occur for these angles which will not always occur. For all four ratios, the results show that option (3) only gives close agreement for $kd < 2\pi$ and the largest differences occur for $2\pi < kd < 3\pi$, where there are either large d values or high frequencies. For ratios > 0 , > 0.9 and > 0.95 , the number of R values is nominally identical, however when ratio > 0.99 a large number of individual values are rejected and the spatial correlation coefficients indicate less agreement with the plane wave theory. To investigate if the aforementioned assumption is responsible for the large differences that occur with $2\pi < kd < 3\pi$, the next step is to compare ray tracing and plane wave theory based on the average of the individual pairs of points that have the same kd value.

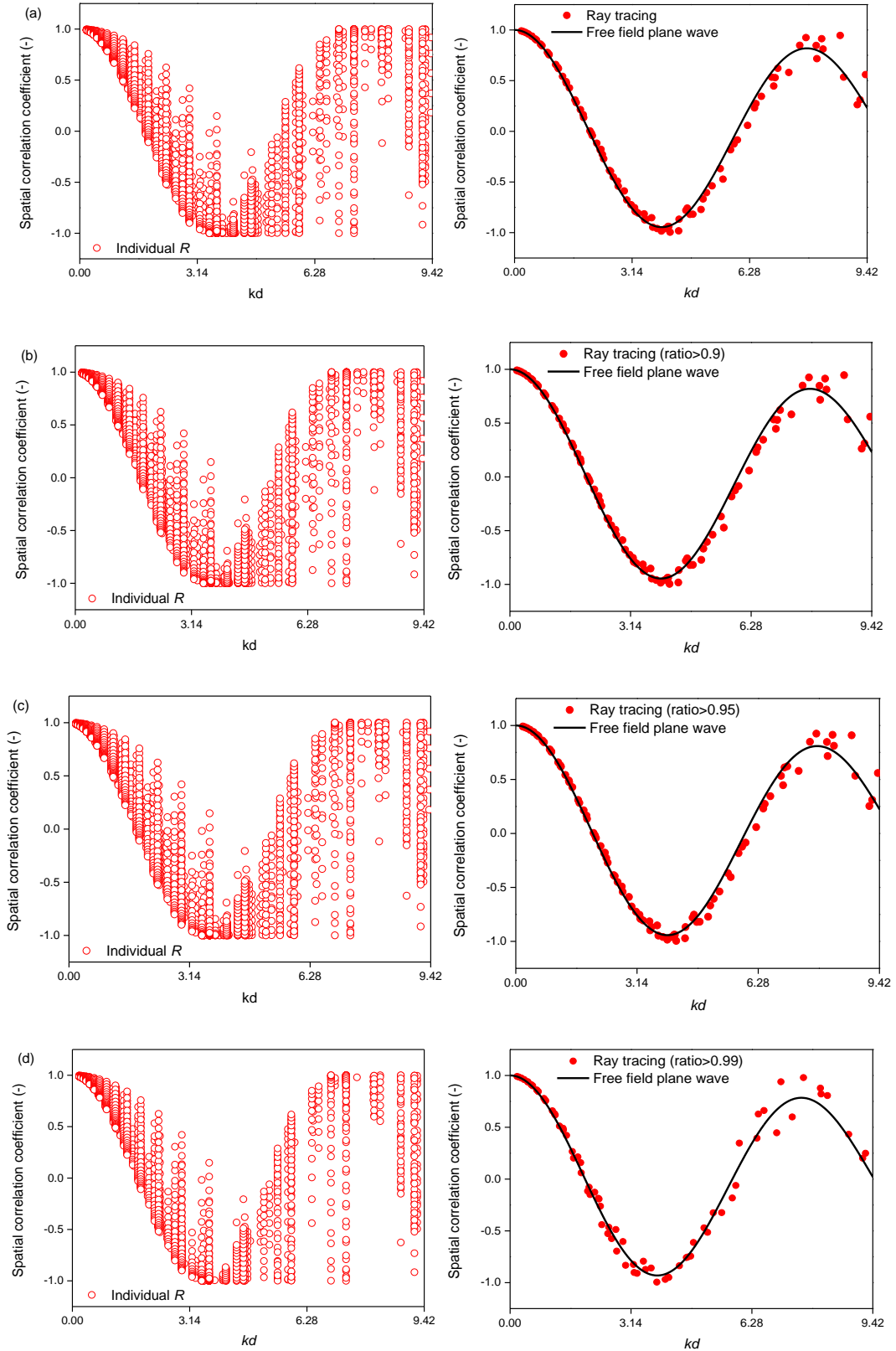


Figure 3-9. Spatial correlation for a point source in a free field for source position (B) with option (3) considering all permutations of points along the line for (left) individual points and (right) average values (Eq. (3.2.9) and (3.2.10)). Individual pairs of points are accepted on the following basis (a) >0 , (b) >0.9 , (c) >0.95 and (d) >0.99 .

Figure 3-10 shows these average R values for each kd value from ray tracing and plane wave theory using option (3). Graphs are shown for the four different ratios (Eq. (3.2.9) and (3.2.12)). In general, there is close agreement between ray tracing and plane wave theory for these individual kd values. Therefore it is likely that the errors seen in Figure 3-9 for $2\pi < kd < 3\pi$ occurred due to the averaging procedure (Eq. (3.2.9) and (3.2.10)) that is used to create the continuous kd curve. When the ratio is >0 , >0.9 , >0.95 the percentage errors are largest when R is approximately 0 ± 0.3 . However, with a stricter requirement based on a ratio of >0.99 the percentage differences are similar for all R (see Figure 3-10 (d)). This could lead to the conclusion that to assess the validity of using plane wave theory to determine the spatial correlation coefficient it would be better to use an inclusion requirement based on a ratio of >0.99 . However, comparison of Figure 3-9 (a) and (d) shows that this removes too many individual R values (in some cases there is only one pair of points that meet the criteria). In section 3.4 where ray tracing is used in a reverberant space excited by a point source, both plane wave theory and 3D diffuse field theory will be shown as a continuous function of kd to help identify whether the direct field primarily determines the spatial correlation coefficients determined from ray tracing. This section shows that it is a ratio requirement of >0 is reasonable and this will therefore be used in section 3.4.

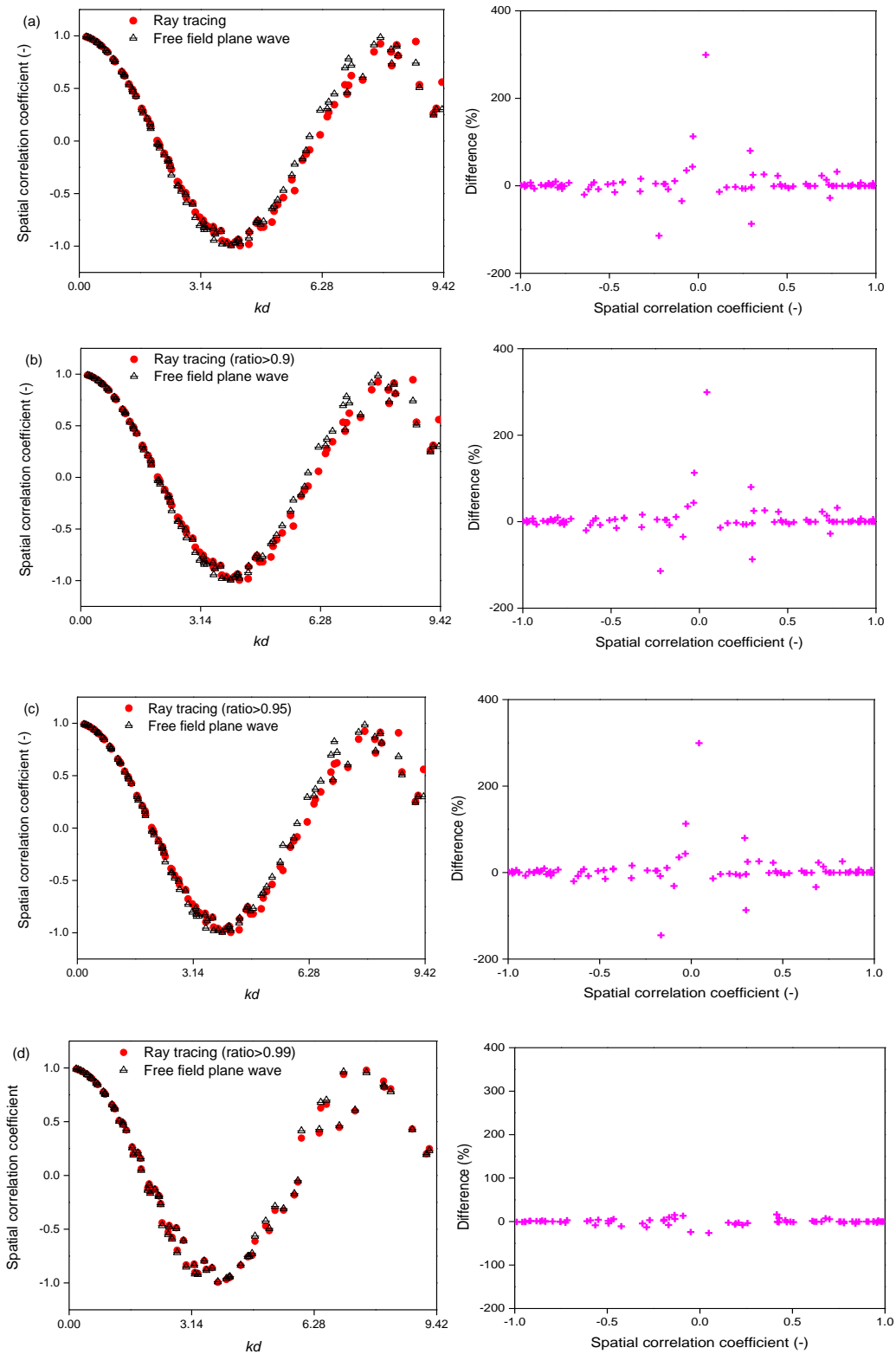


Figure 3-10. Spatial correlation for a point source in a free field for source position (B) with option (3) considering all permutations of points along the line for (left) average R values for each kd value from ray tracing and plane wave theory and (right) percentage difference between ray tracing and plane wave theory. Individual pairs of points are accepted on the following basis (a) >0 , (b) >0.9 , (c) >0.95 and (d) >0.99 .

3.3.2 Spatial correlation in a reverberant field - distribution of individual R values

In this section, individual R values in one-third octave bands are calculated using ray tracing using measurement lines along the x- and z-axes in a 50m^3 reverberation room (5m x 4m x 2.5m). All surfaces have an absorption coefficient of 0.02 and a diffusion coefficient of 1.0 so that the room is highly reverberant with an estimated Sabine reverberation time of 4.7s. In the previous section on the free-field it was only necessary to consider a single measurement line, however in a reverberant field it is necessary to consider multiple lines because the diffuse field assumptions of equal probability of waves arriving from all directions is only likely to be approximately valid when averaging along several lines within the room volume. For this reason, ten measurement lines were chosen along the x- and z-axes respectively. All measurement points are at least $>\lambda/2$ from the boundary to avoid regions near reflecting boundaries where the energy density is higher than in the central zone of the room [66]. This means that one-third octave band centre frequencies below 160Hz are not considered; hence the frequency range calculated with Raynoise is one-third octave band centre frequencies from 160Hz to 5000Hz. Note that the sound source used in ray tracing is a single frequency, whereas most measurements [2,13,15] would use broadband noise or a warble tone; however, due to spatial averaging with multiple measurement lines the use of a single frequency is not expected to be problematic.

Figure 3-11 and Figure 3-12 show individual spatial correlation coefficients for each adjacent pair of points (corresponding to option (2) in Section 3.3). For each pair of points the distance, d_{ij} is 0.1m in the x- and z-directions. Each column of values in the graph represents a single frequency because the distance between the points in each pair is fixed. It is notable that there are a range of R values at each kd value and that these lie in the range ± 1 for $kd > \pi/2$. For this reason, the result from any individual pair of points cannot be meaningfully compared with the 3D diffuse field theory. For this reason, the next section considers spatial averaging.

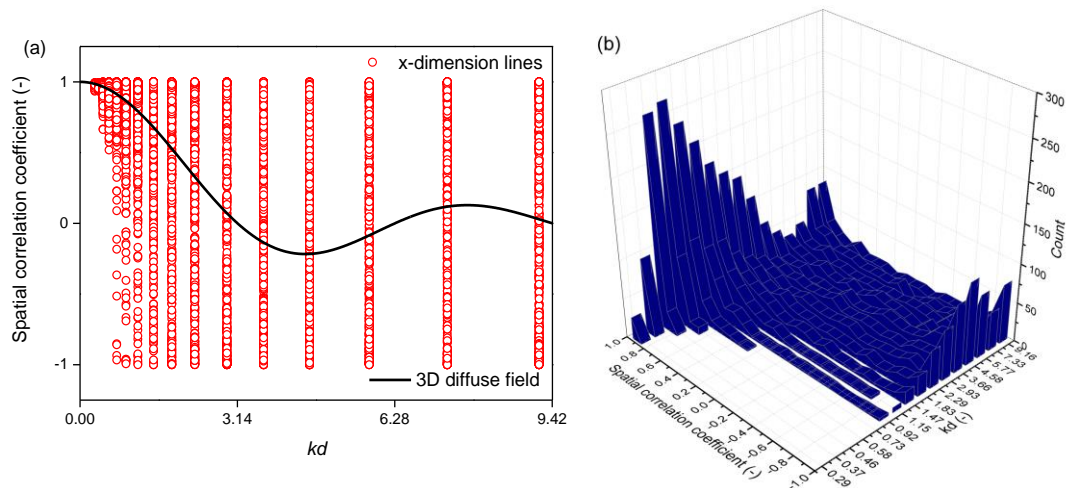


Figure 3-11. Individual spatial correlation coefficients for each pair of points calculated from adjacent pairs of points that are at least $\lambda/2$ away from the boundary, and that lie along each measurement line up to a distance that is $\lambda/2$ away from the opposite boundary in 50m^3 room. (a) Ten measurement lines along the x-direction for comparison with three-dimensional diffuse field theory, (b) Distribution of individual coefficients from x-direction lines.

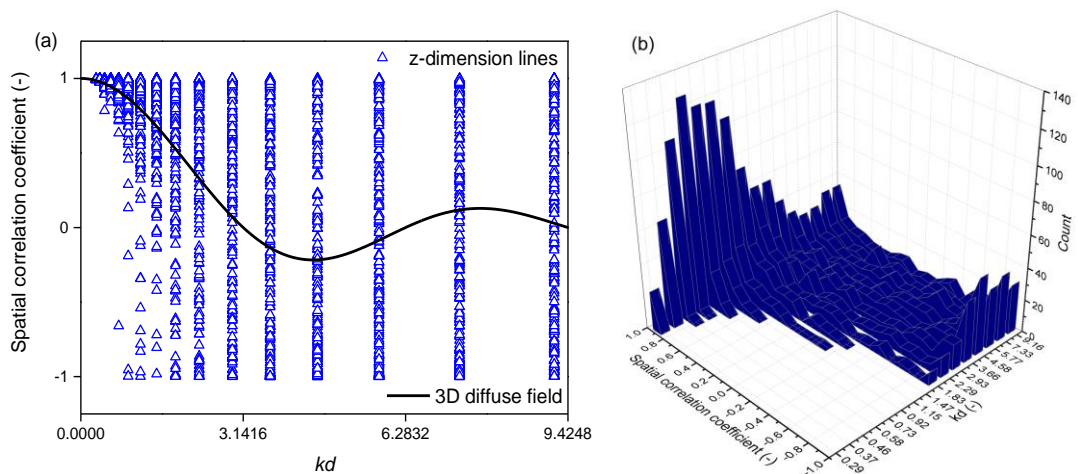


Figure 3-12. Individual spatial correlation coefficients for each pair of points calculated from adjacent pairs of points that are at least $\lambda/2$ away from the boundary, and that lie along each measurement line up to a distance that is $\lambda/2$ away from the opposite boundary. (a) Ten measurement lines along the z-direction for comparison with three-dimensional diffuse field theory, (b) Distribution of individual coefficients from z-direction lines.

3.4 Average spatial correlation in different reverberation rooms

In this section, average R values for instantaneous sound pressure from three different reverberation rooms (with different absorption coefficients but always with a diffusion coefficient of 1.0) are compared with 3D diffuse field theory and average values using plane wave theory to model the direct field from the point source (Eq. (3.2.9) and (3.2.10)). The results are plotted in terms of the spatial correlation coefficient against kd where individual points represent R at a single frequency.

As before, all measurement points are at least $>\lambda/2$ from the boundary to avoid regions near reflecting boundaries where the energy density is higher than in the central zone of the room.

Three different room volumes are considered: 30m^3 (4m x 3m x 2.5m), 50m^3 (5m x 4m x 2.5m) and 120m^3 (6m x 5m x 4m).

In each room, the same absorption coefficient was applied to all surfaces. For the 30m^3 room, two absorption coefficients, $\alpha=0.01$ and $\alpha=0.1$, were used which gave Sabine reverberation times of 8.1s and 0.8s. For the 50m^3 room, two absorption coefficients, $\alpha=0.02$ and $\alpha=0.3$, were used which gave Sabine reverberation times of 4.7s and 0.3s. For the 120m^3 room, only an absorption coefficient of $\alpha=0.3$ was used to give a Sabine reverberation time of 0.4s.

For all rooms and absorption coefficients considered, the reverberation distance [38] is $<1\text{m}$ and all the points on the measurement lines are $>1\text{m}$ from the point source. For this reason, it is not expected that the measurement points will lie in a region that is significantly affected by the direct field.

For the 30m^3 , 50m^3 and 120m^3 rooms, the lowest frequency used in the ray tracing was 200Hz, 160Hz and 100Hz respectively and the highest frequency was always 5000Hz.

3.4.1 One fixed point with variable points (Option (1) used by Cook et al)

Option (1) is used at single frequencies as shown on Figure 3-13 to Figure 3-17.

For the 30m³ room with $\alpha=0.01$: For both x- and z-directions, the average R from ray tracing follows the plane wave theory from 250 to 400Hz and tends to follow the 3D diffuse field theory from 500 to 2500Hz except for 1600Hz in the z-direction.

For the 30m³ room with $\alpha=0.1$: For both x- and z-directions, the average R from ray tracing follows the plane wave theory from 250 to 400Hz when $kd < 2\pi$ and does not follow the 3D diffuse field theory at any frequency.

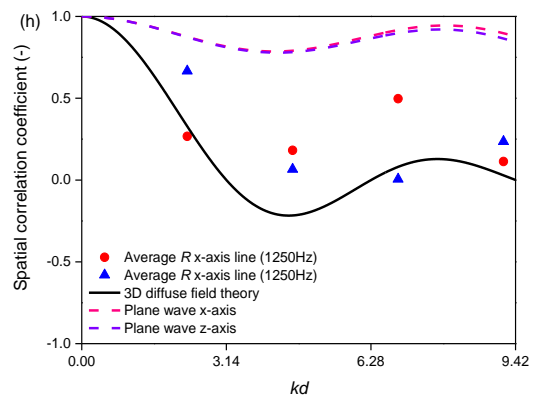
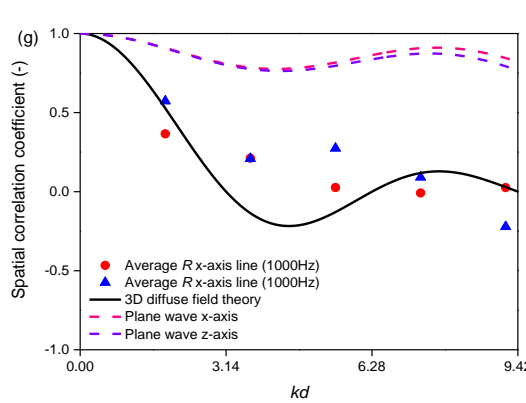
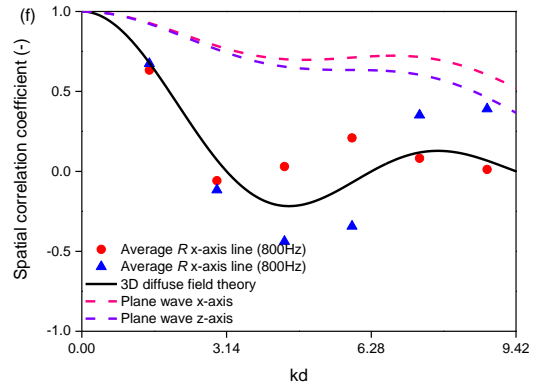
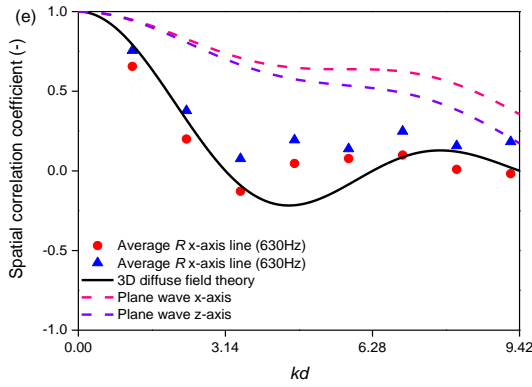
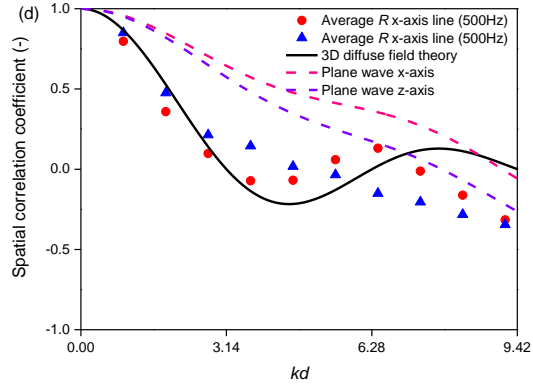
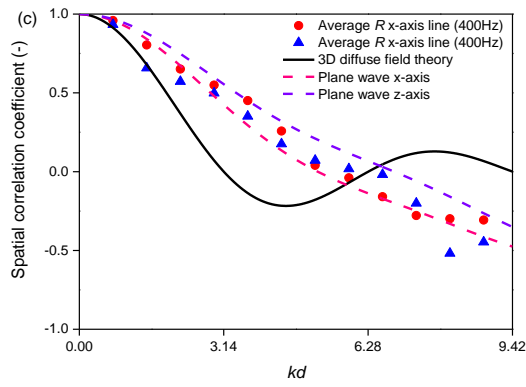
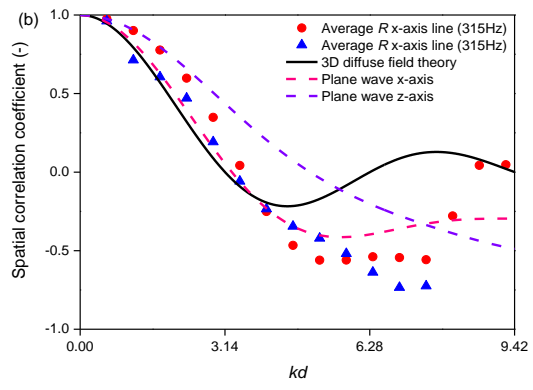
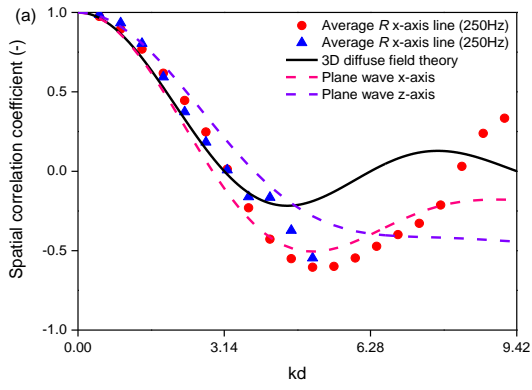
For the 50m³ room with $\alpha=0.02$: For the x-directions, the average R from ray tracing follows the plane wave theory from 250 to 315Hz when $kd < 2\pi$. For the x-direction, the average R from ray tracing tends to follow the 3D diffuse field theory from 630 to 2500Hz. For the z-direction, the average R from ray tracing tends to follow the 3D diffuse field theory from 1250 to 2500Hz.

For the 50m³ room with $\alpha=0.3$: For both x- and z-directions, the average R from ray tracing tends to follow the plane wave theory from 250 to 2500Hz and does not follow the 3D diffuse field theory at any frequency.

For the 120m³ room with $\alpha=0.3$: For both x- and z-directions, the average R from ray tracing tends to follow the plane wave theory from 250 to 2500Hz and does not follow the 3D diffuse field theory at any frequency.

The general conclusion is that the use of option (1) at single frequencies leads to conclusions that seem inappropriate, and there is inconsistency in the conclusions drawn from the x- and z-directions. This is likely to be because the fixed point is at a distance of $\lambda/2$ from the boundary, and this would limit the number of measurement pairs that can be considered in the z-direction compared to the x-direction.

Referring to the original work by Cook et al [2] who used this approach, it is noted that the fixed position did not vary with frequency but no detail was given on what distance the fixed position was from the wall.



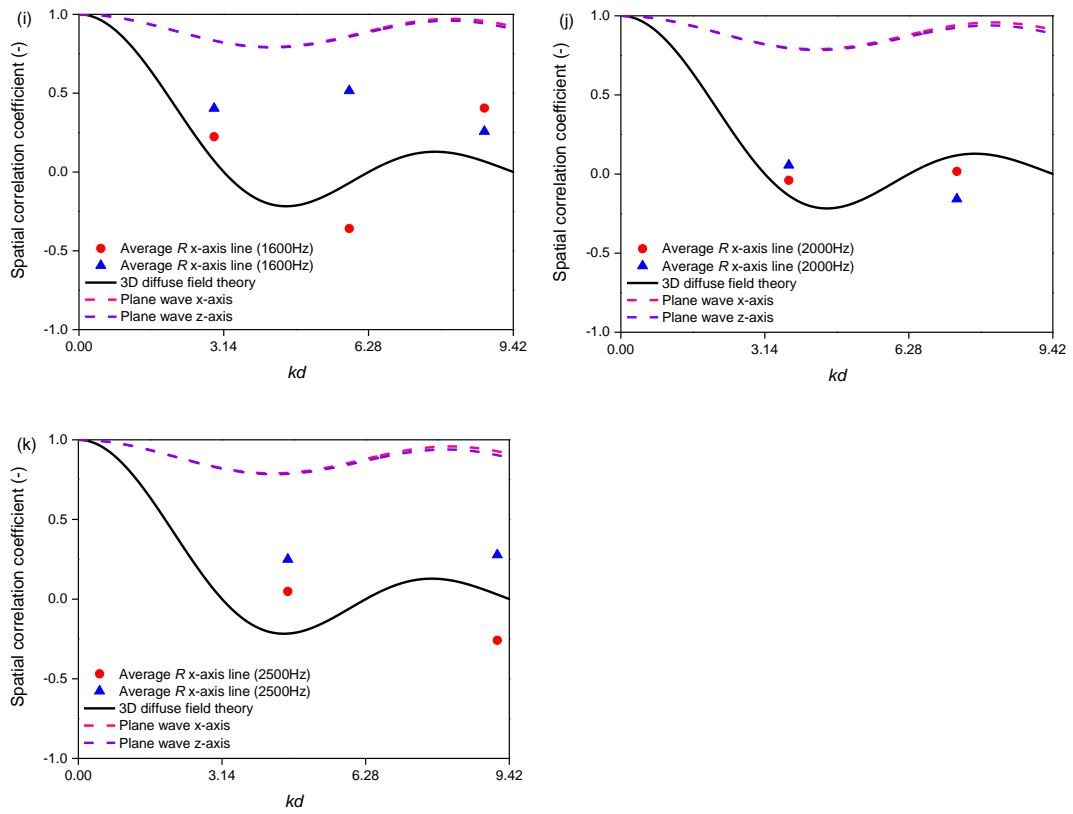
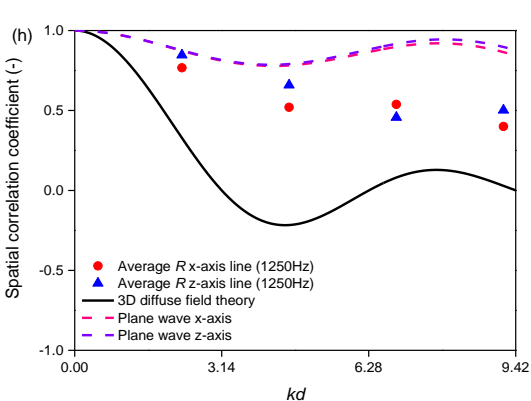
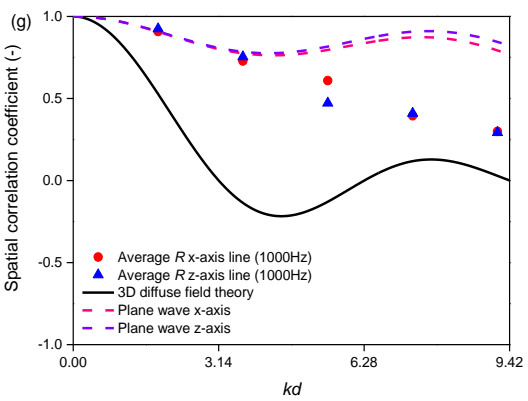
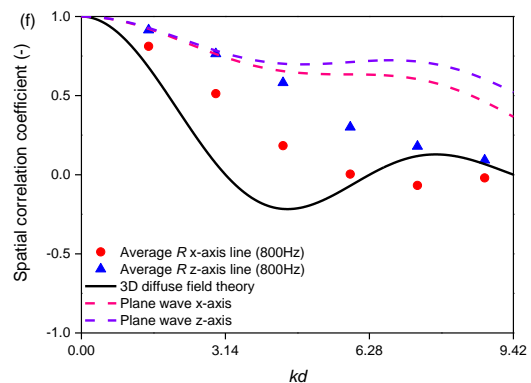
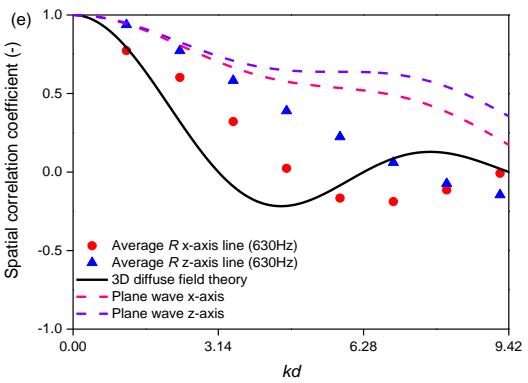
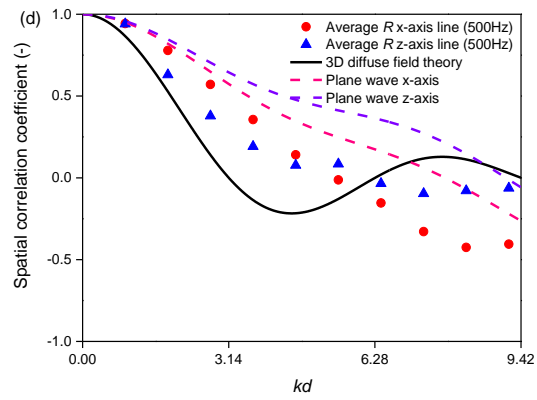
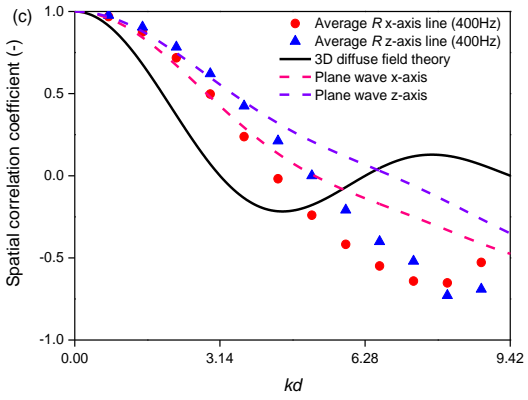
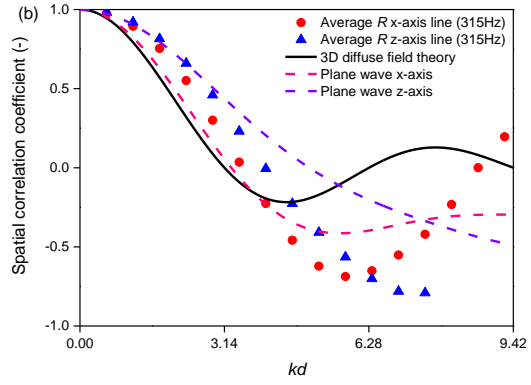
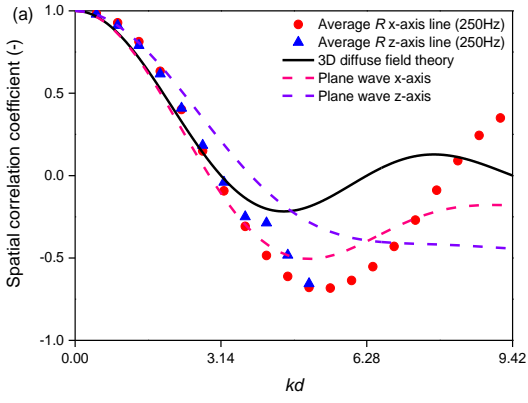


Figure 3-13. Average spatial correlation in 30m^3 room ($\alpha=0.01$) along x- and z-axis ten measurement lines using option (1) compared with plane wave and diffuse field theory in one-third octave frequency.



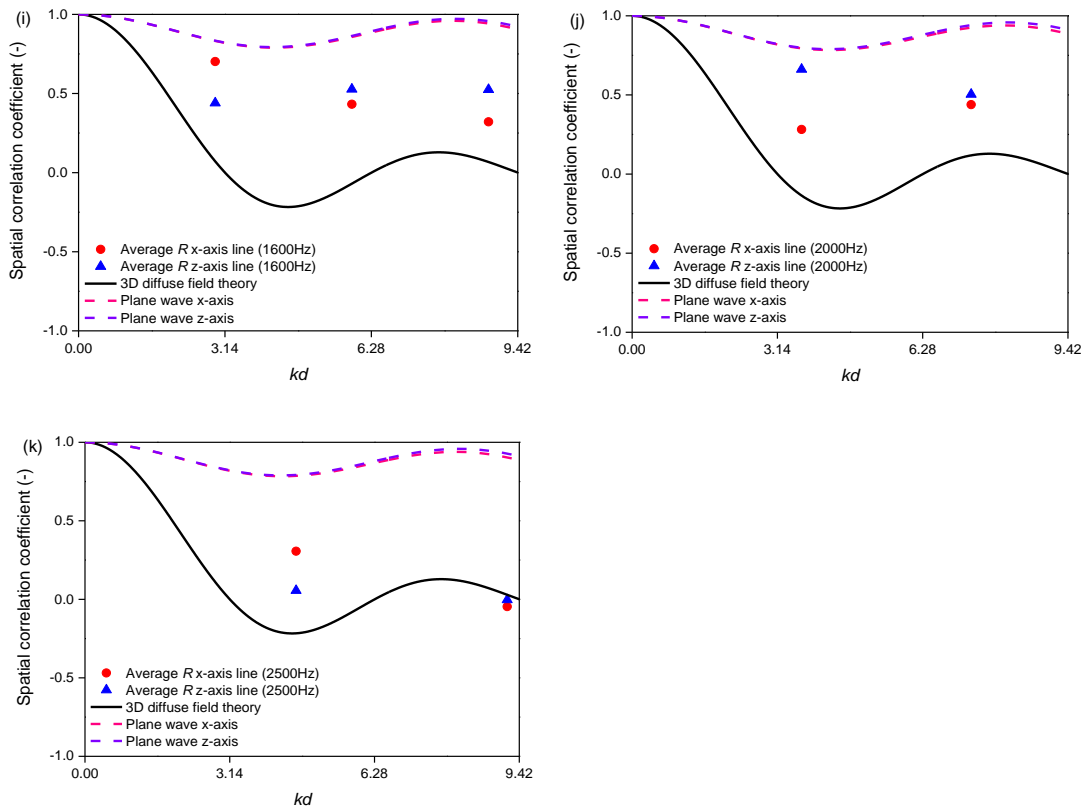
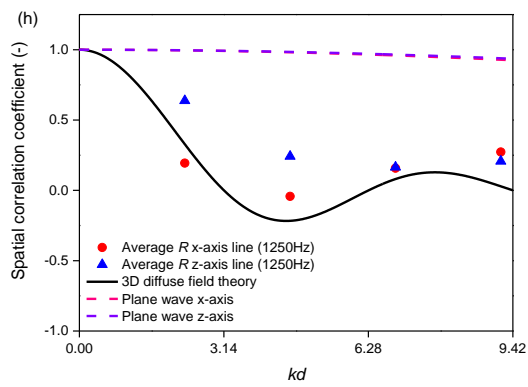
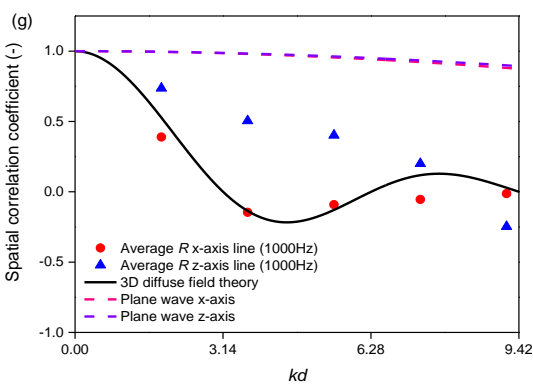
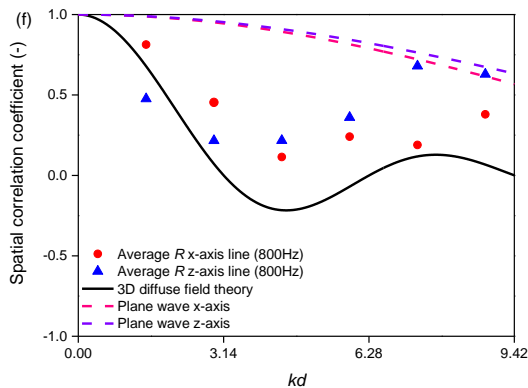
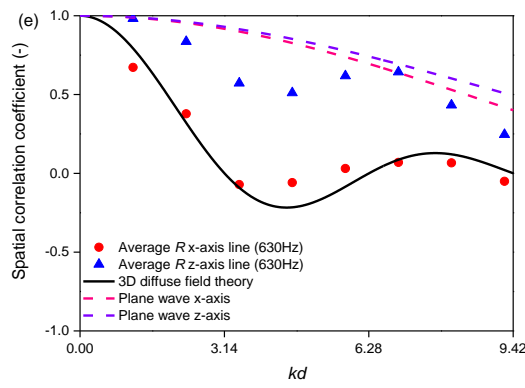
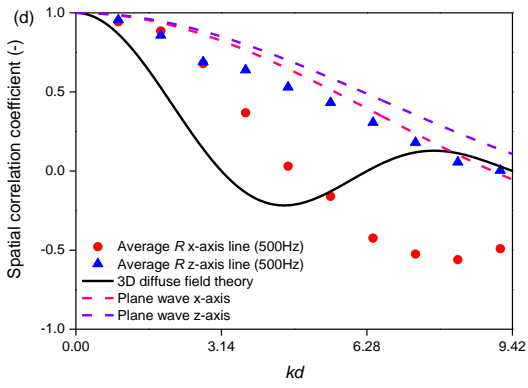
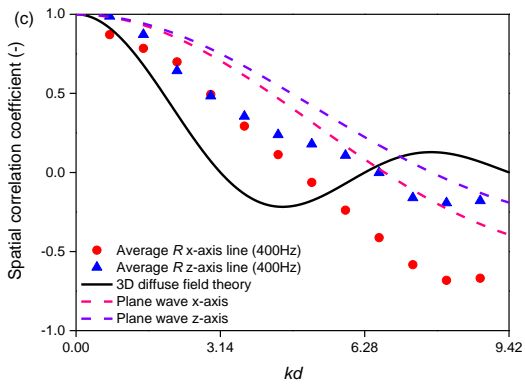
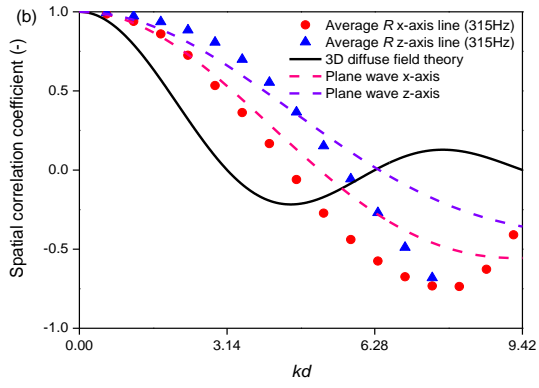
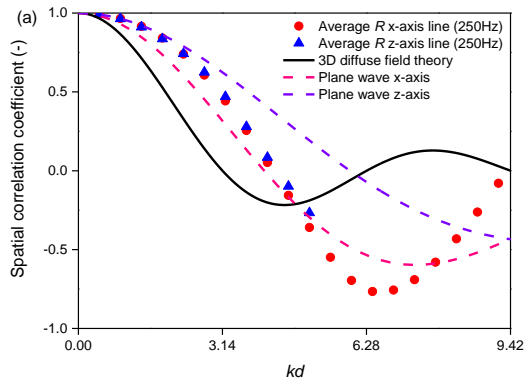


Figure 3-14. Average spatial correlation in 30m^3 room ($\alpha=0.1$) along x- and z-axis ten measurement lines using option (1) compared with plane wave and diffuse field theory in one-third octave frequency.



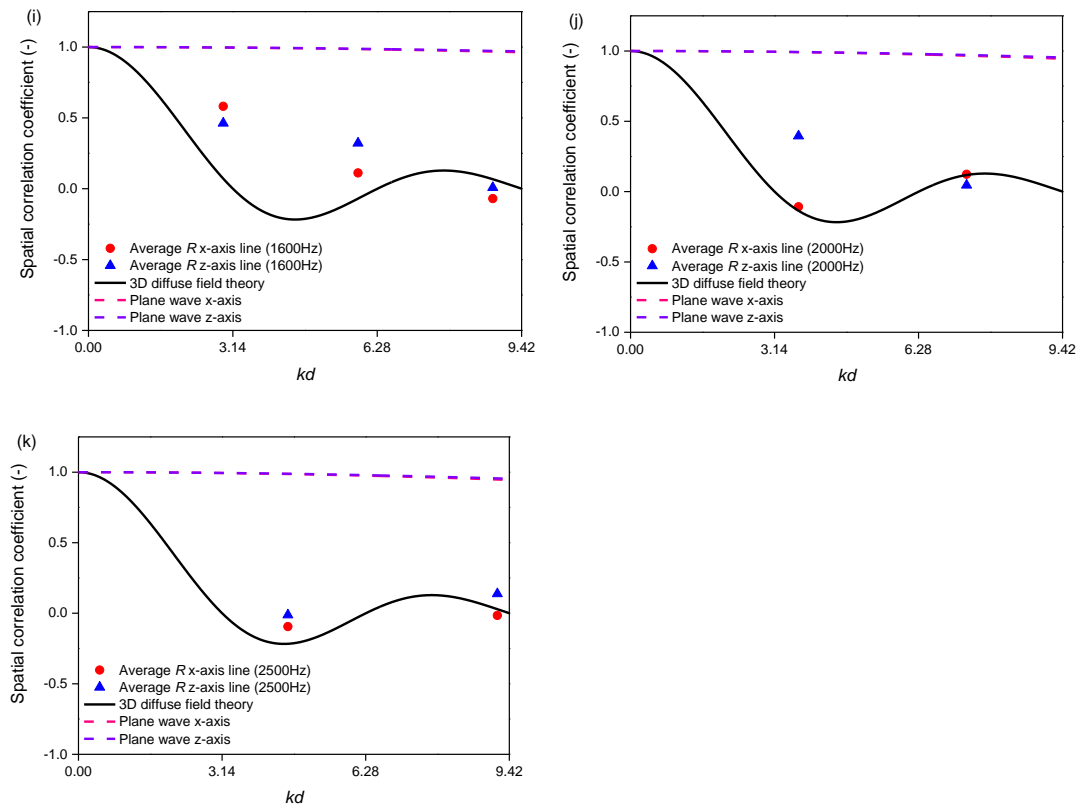
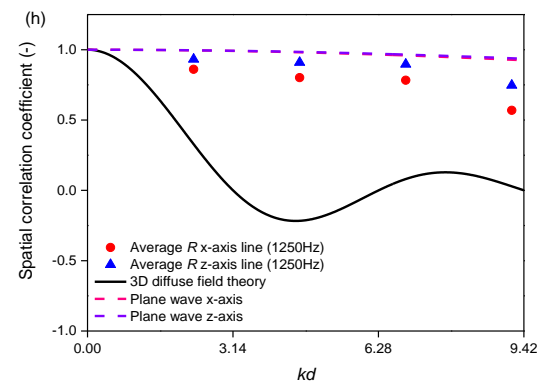
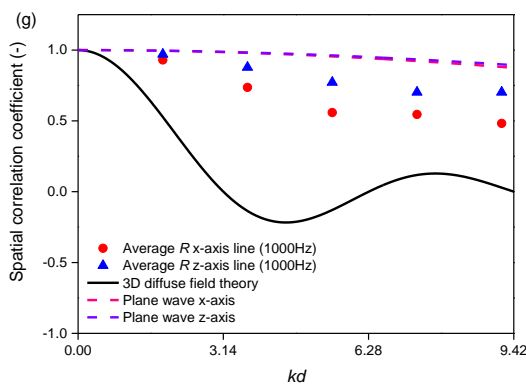
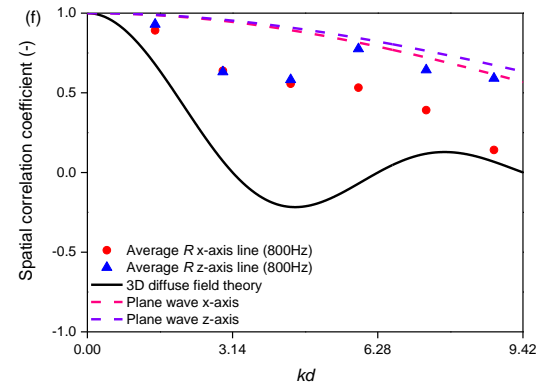
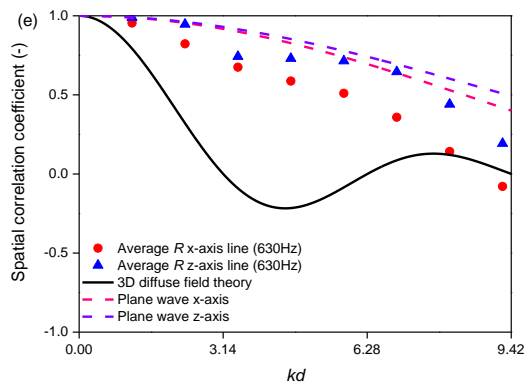
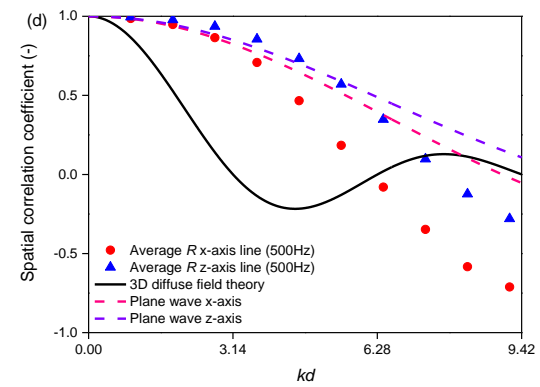
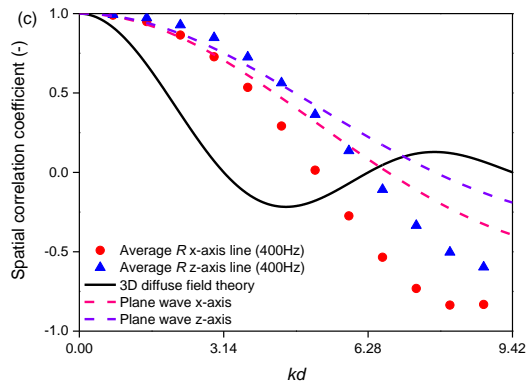
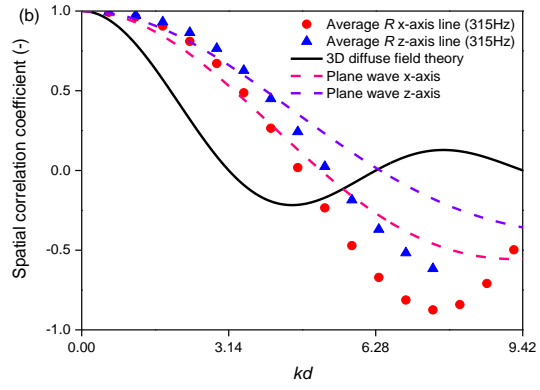
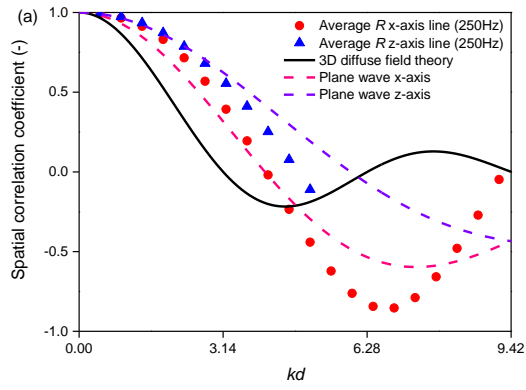


Figure 3-15. Average spatial correlation in 50m^3 room ($\alpha=0.02$) along x- and z-axis ten measurement lines using option (1) compared with plane wave and diffuse field theory in one-third octave frequency.



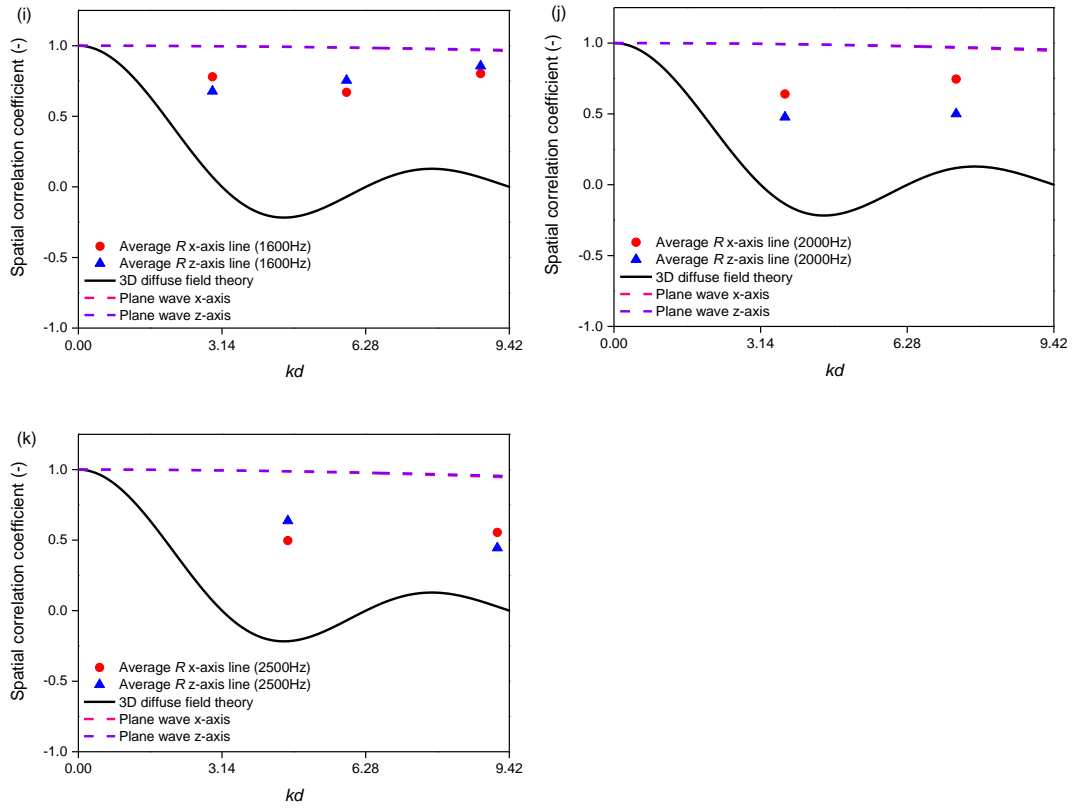
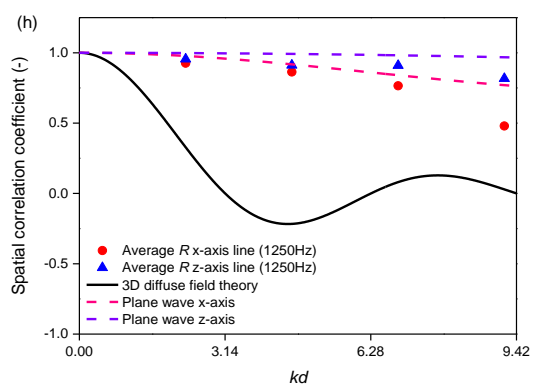
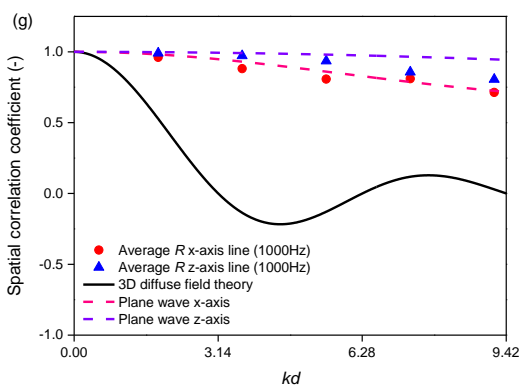
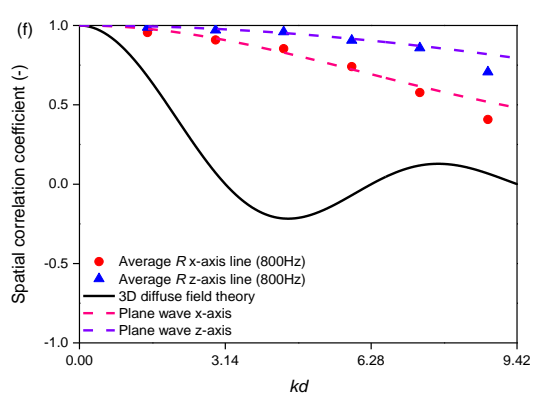
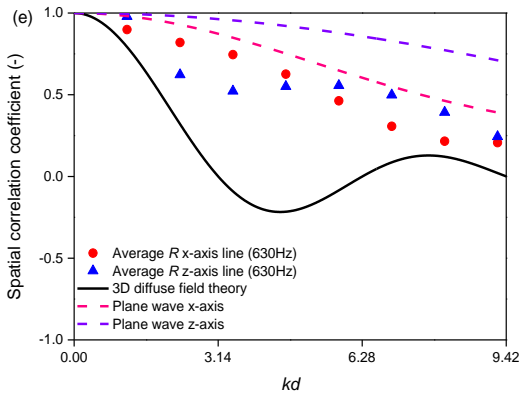
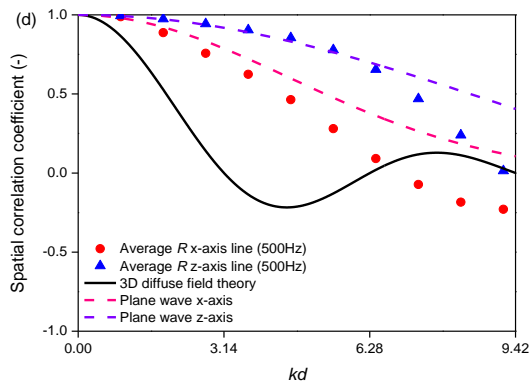
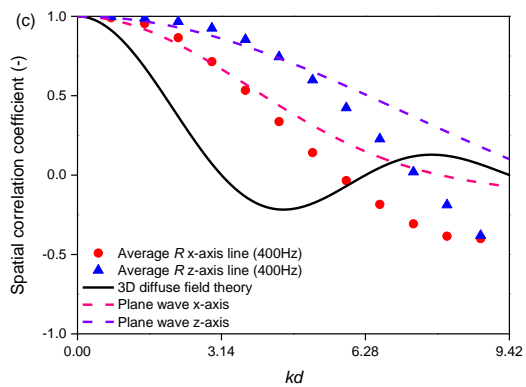
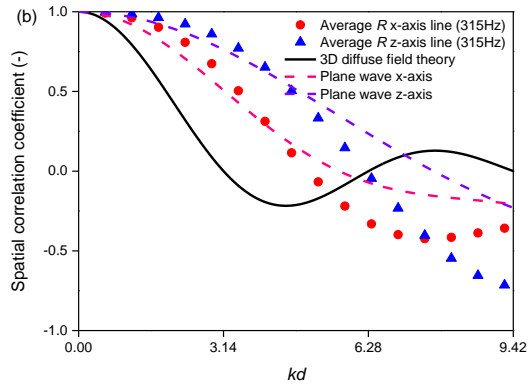
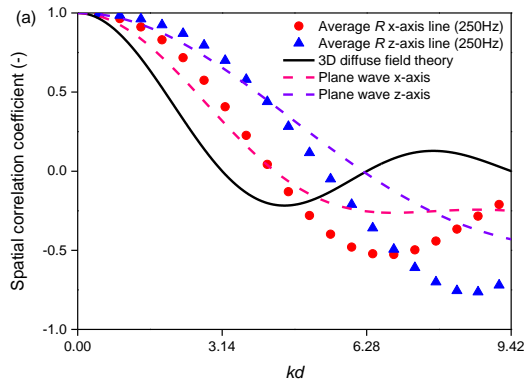


Figure 3-16. Average spatial correlation in 50m^3 room ($\alpha=0.3$) along x- and z-axis ten measurement lines using option (1) compared with plane wave and diffuse field theory in one-third octave frequency.



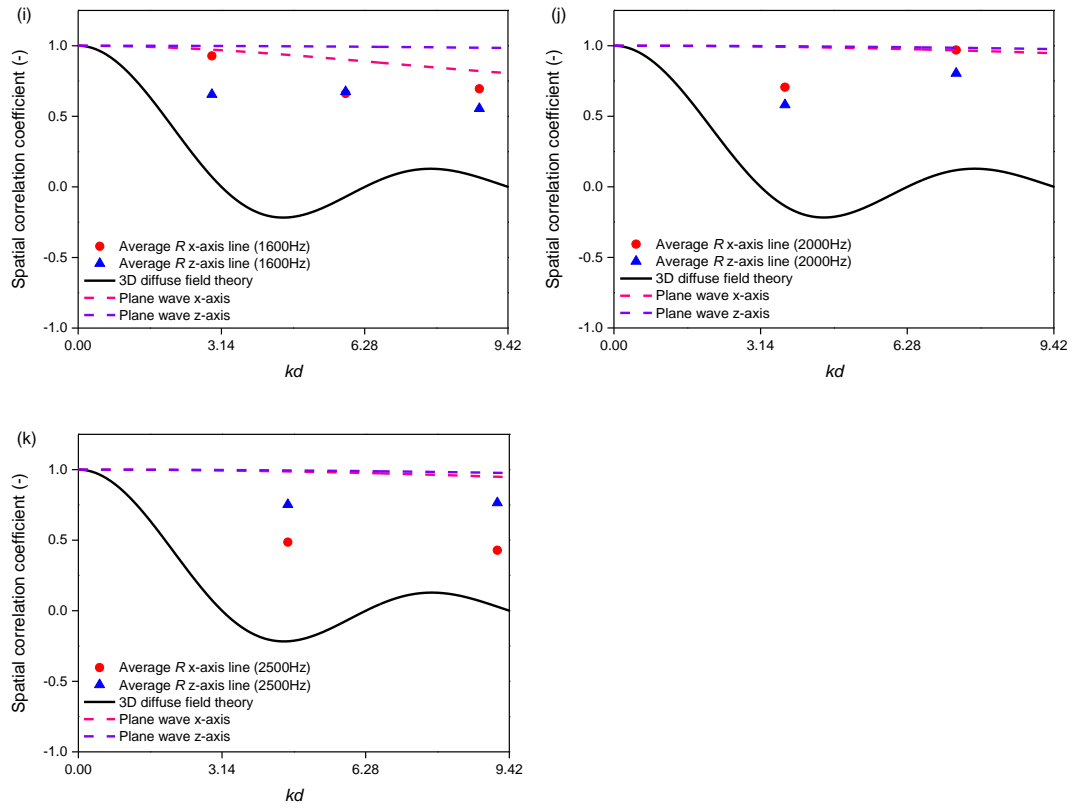


Figure 3-17. Average spatial correlation in 120m^3 room ($\alpha=0.3$) along x- and z-axis ten measurement lines using option (1) compared with plane wave and diffuse field theory in one-third octave frequency.

3.4.2 Pair of points with fixed spacing (Option (2))

Figure 3-18 to Figure 3-22 show average spatial correlations calculated using option (2) fixed spacing of pairs (see Section 3.3) along measurement lines in the x- and z-directions with spacings of 0.1m, 0.2m, 0.4m, 0.6m and 0.8m.

For the 30m³ room with $\alpha=0.01$: When $d=0.1\text{m}$ and $d=0.2\text{m}$, the average R from ray tracing follows 3D diffuse field theory for $0 < kd < 3\pi$. When $d=0.4\text{m}$, the average R from ray tracing follows the plane wave theory for $0 < kd < \pi$ but for $\pi < kd < 2\pi$, there are indications that R is getting closer to the 3D diffuse field theory rather than the plane wave theory. When $d > 0.4\text{m}$, the average R from ray tracing follows the plane wave theory for $0 < kd < 2\pi$ but for $2\pi < kd < 3\pi$, there are indications that R is getting closer to the 3D diffuse field theory rather than the plane wave theory. For all d , the average R from ray tracing is close to zero as indicated by both the 3D diffuse field theory and the plane wave theory for $kd > 3\pi$.

For the 30m³ room with $\alpha=0.1$: When $d=0.1\text{m}$, the average R from ray tracing follows 3D diffuse field theory for $0 < kd < 3\pi$. When $d=0.2\text{m}$, the average R from ray tracing follows the plane wave theory for $0 < kd < \pi$ but for $\pi < kd < 2\pi$, there are indications that R is getting closer to the 3D diffuse field theory rather than the plane wave theory. When $d > 0.2\text{m}$, the average R from ray tracing follows the plane wave theory for $0 < kd < 2\pi$ but for $2\pi < kd < 3\pi$, there are indications that R is getting closer to the 3D diffuse field theory rather than the plane wave theory. For all d , the average R from ray tracing is close to zero as indicated by both the 3D diffuse field theory and the plane wave theory for $kd > 3\pi$.

For the 50m³ room with $\alpha=0.02$: When $d=0.1\text{m}$ and $d=0.2\text{m}$, the average R from ray tracing follows 3D diffuse field theory for $0 < kd < 2\pi$. When $d=0.4\text{m}$, the average R from ray tracing follows the plane wave theory for $0 < kd < \pi$ but for $\pi < kd < 2\pi$, there are indications that R is getting closer to the 3D diffuse field theory rather than the plane wave theory. When $d > 0.4\text{m}$, the average R from ray tracing follows the plane wave theory for $0 < kd < 3\pi$ but for $3\pi < kd < 4\pi$, there are indications that R is getting closer to the 3D diffuse field theory rather than the plane wave theory. For all d , the average R from ray tracing is close to zero as indicated by both the 3D diffuse field theory and the plane wave theory for $kd > 4\pi$.

For the 50m³ room with $\alpha=0.3$: When $d=0.1\text{m}$, the average R from ray tracing follows the plane wave theory for $0 < kd < \pi$ but for $\pi < kd < 3\pi$, there are indications that R is getting closer to 3D diffuse field theory. When $d > 0.1\text{m}$, the average R from ray tracing follows the plane wave theory for $0 < kd < 3\pi$ but for $3\pi < kd < 4\pi$, there are indications that R is getting closer to the 3D diffuse field theory rather than the plane wave theory. For all d , the average R from ray tracing is close to zero as indicated by both the 3D diffuse field theory and the plane wave theory for $kd > 4\pi$.

For the 120m³ room with $\alpha=0.3$: When $d=0.1\text{m}$, the average R from ray tracing follows the plane wave theory for $0 < kd < \pi$ but for $\pi < kd < 3\pi$, there are indications that R is getting closer to 3D diffuse field theory. When $d > 0.1\text{m}$, the average R from ray tracing follows the plane wave theory for $0 < kd < 3\pi$ but for $3\pi < kd < 4\pi$, there are indications that R is getting closer to the 3D diffuse field theory rather than the plane wave theory. For all d , the average R from ray tracing is close to zero as indicated by both the 3D diffuse field theory and the plane wave theory for $kd > 4\pi$.

The general conclusion from using option (2) is that the smallest spacing tends to follow 3D diffuse field theory and the largest spacing tends to follow the plane wave theory for $0 < kd < 2\pi$. At high frequencies in lightly damped spaces it would be expected that the general trend would be for the average R from ray tracing to follow 3D diffuse field theory. However, with increasing frequency the average R from ray tracing, 3D diffuse field theory and plane wave theory all tend to zero so it is not possible to identify this trend.

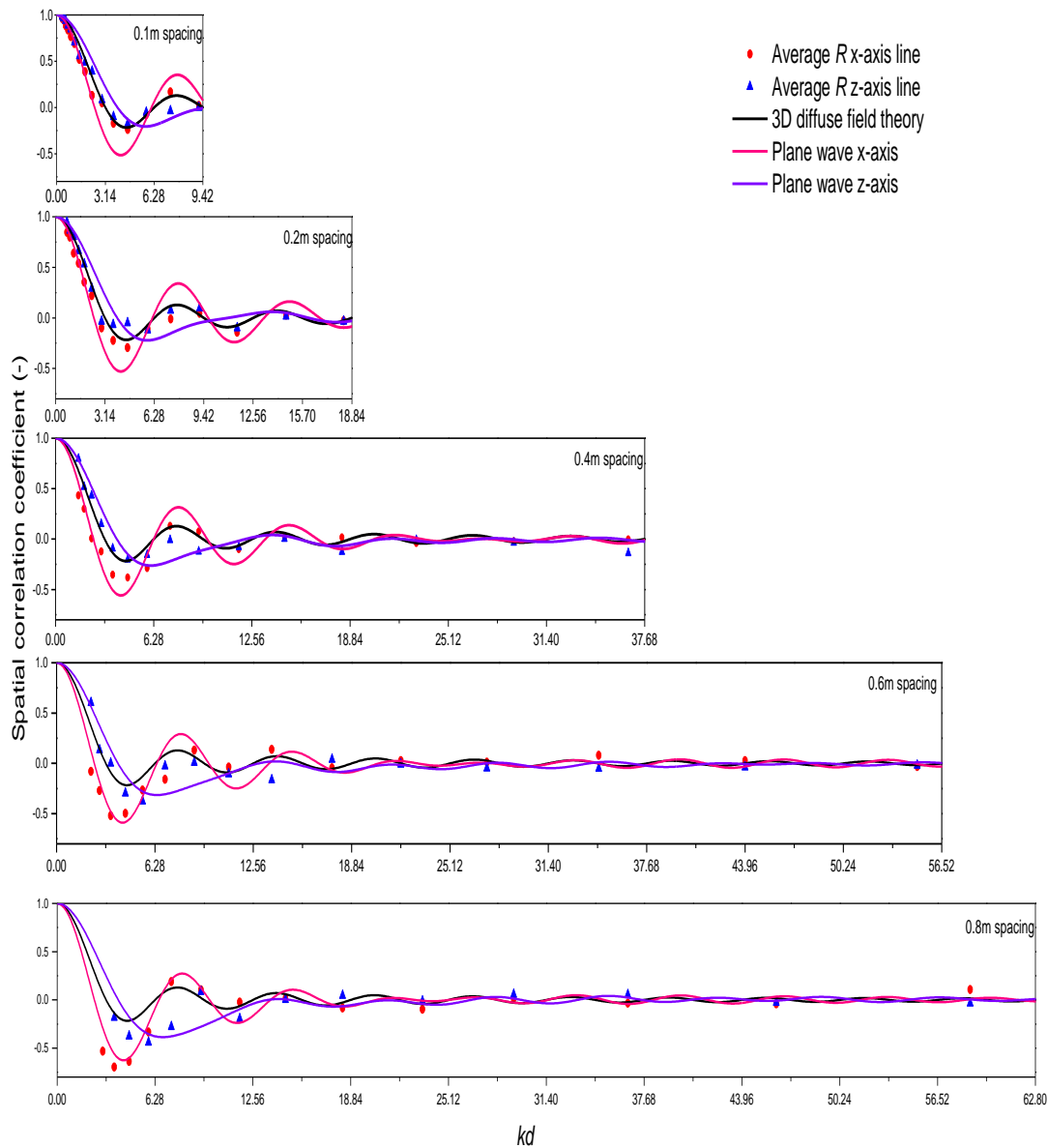


Figure 3-18. Average spatial correlation in 30m^3 room ($\alpha=0.01$) along x- and z-axis ten measurement lines with option (2) pairs of points with a fixed spacing, average plane wave and diffuse field theory. All measurement points are at least $\lambda/2$ away from the boundary, and that lie along each measurement line up to a distance that is $\lambda/2$ away from the opposite boundary. Fixed spacing with 0.1m, 0.2m, 0.4m, 0.6m and 0.8m.

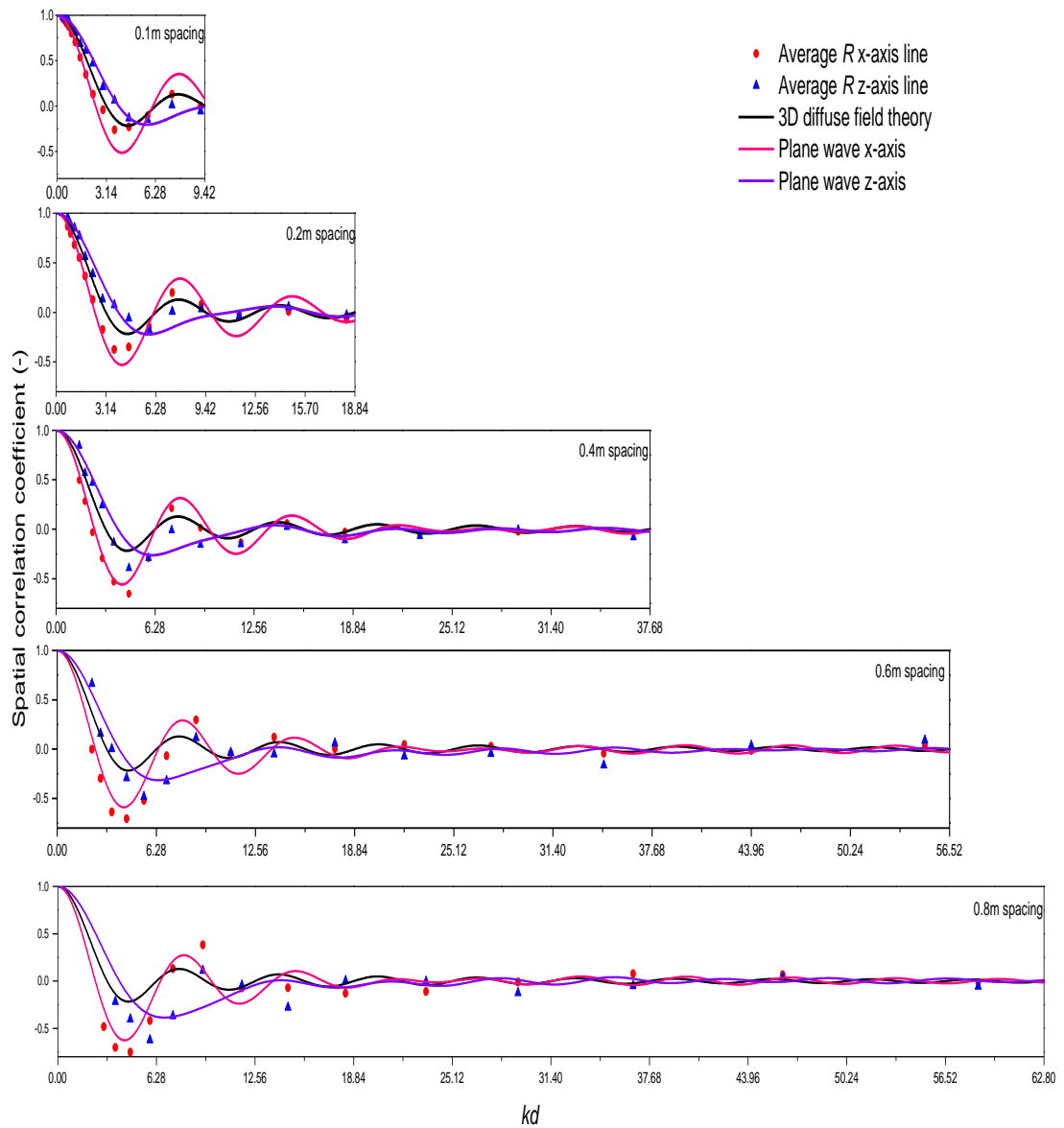


Figure 3-19. Average spatial correlation in 30m^3 room ($\alpha=0.1$) along x- and z-axis ten measurement lines with option (2) pairs of points with a fixed spacing, average plane wave and diffuse field theory. All measurement points are at least $\lambda/2$ away from the boundary, and that lie along each measurement line up to a distance that is $\lambda/2$ away from the opposite boundary. Fixed spacing with 0.1m, 0.2m, 0.4m, 0.6m and 0.8m.

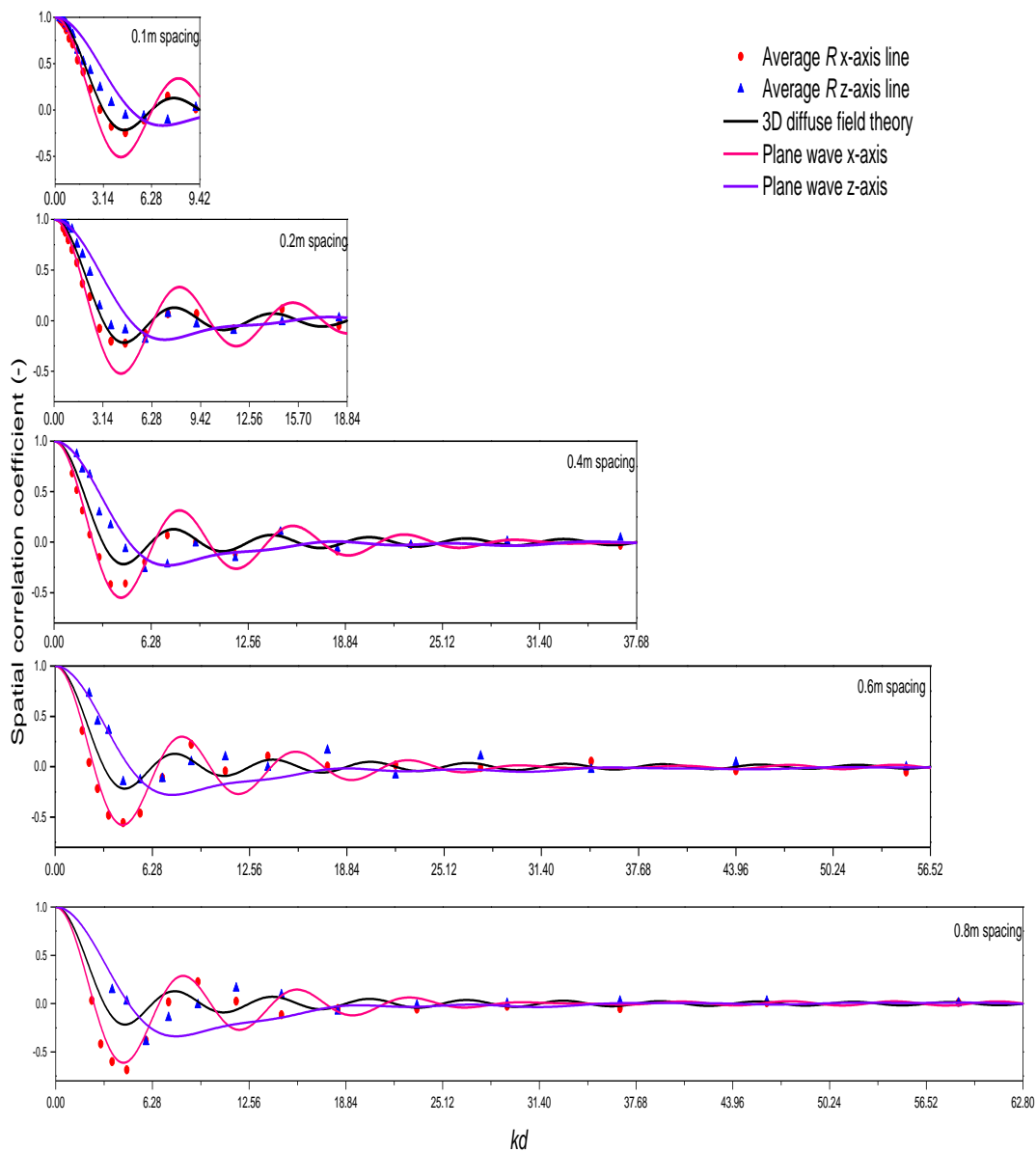


Figure 3-20. Average spatial correlation in 50m^3 room ($\alpha=0.02$) along x- and z-axis ten measurement lines with option (2) pairs of points with a fixed spacing, average plane wave and diffuse field theory. All measurement points are at least $\lambda/2$ away from the boundary, and that lie along each measurement line up to a distance that is $\lambda/2$ away from the opposite boundary. Fixed spacing with 0.1m, 0.2m, 0.4m, 0.6m and 0.8m.

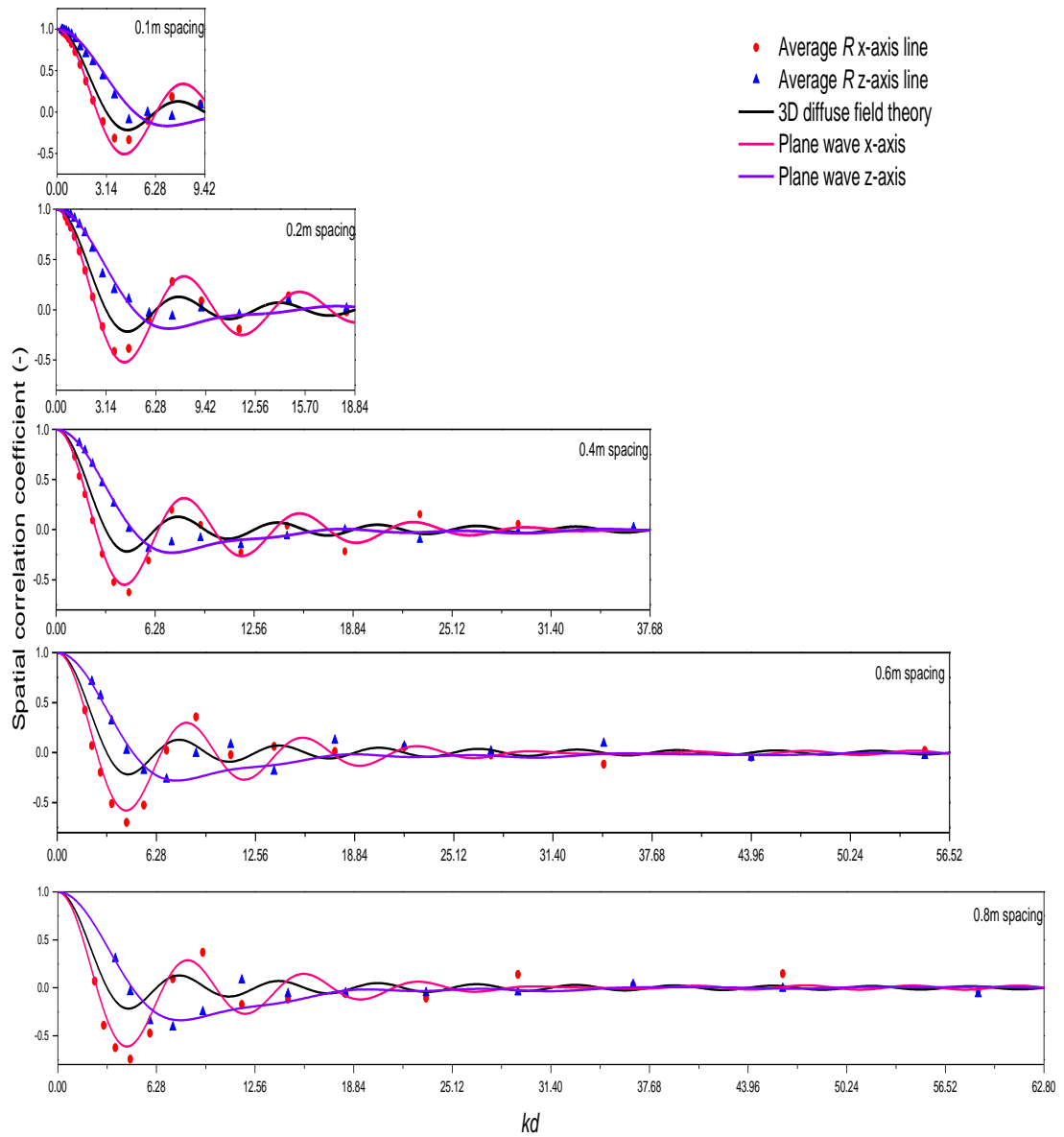


Figure 3-21. Average spatial correlation in 50m^3 room ($\alpha=0.3$) along x- and z-axis ten measurement lines with option (2) pairs of points with a fixed spacing, average plane wave and diffuse field theory. All measurement points are at least $\lambda/2$ away from the boundary, and that lie along each measurement line up to a distance that is $\lambda/2$ away from the opposite boundary. Fixed spacing with 0.1m, 0.2m, 0.4m, 0.6m and 0.8m.

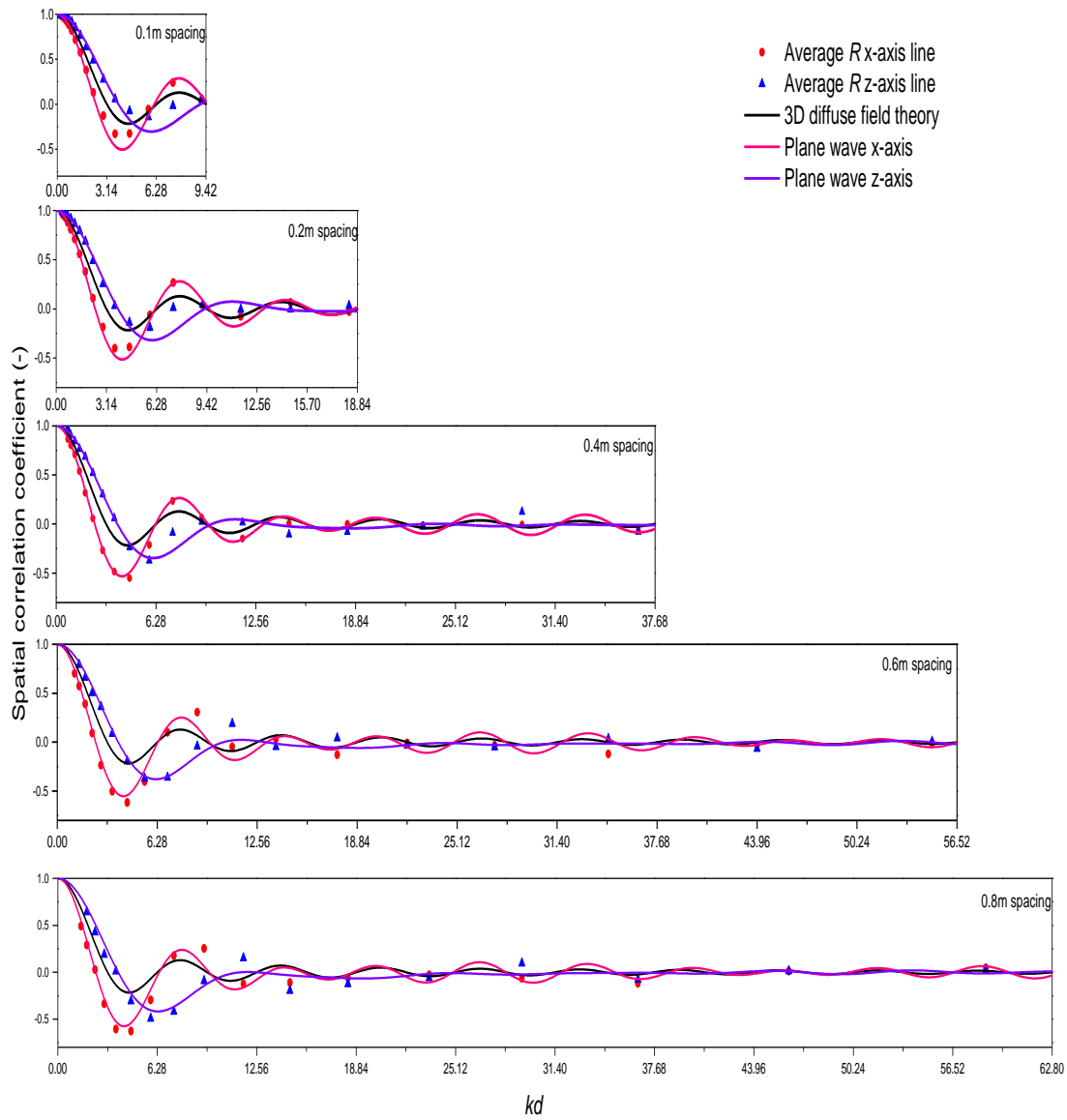


Figure 3-22. Average spatial correlation in 120m^3 room ($\alpha=0.3$) along x- and z-axis ten measurement lines with option (2) pairs of points with a fixed spacing, average plane wave and diffuse field theory. All measurement points are at least $\lambda/2$ away from the boundary, and that lie along each measurement line up to a distance that is $\lambda/2$ away from the opposite boundary. Fixed spacing with 0.1m, 0.2m, 0.4m, 0.6m and 0.8m.

3.4.3 Pair of points with variable spacings (Option (3))

Figure 3-23 to Figure 3-27 show average spatial correlations calculated using option (3) for all permutation of pairs along measurement lines in the x- and z-directions.

For the 30m³ room with $\alpha=0.01$: In the x-direction, average R values follow the plane wave theory for $kd < 2\pi$, then for $2\pi < kd < 5\pi$ they still tend to follow the plane wave theory rather than the 3D diffuse field theory but there is increased scatter. In the z-direction, average R values follow the 3D diffuse field theory for $kd < \pi$, then for $\pi < kd < 4\pi$ there is increased scatter. For both x- and z-directions when $kd > 5\pi$, the average R from ray tracing clusters around the zero line as indicated by both the 3D diffuse field theory and the plane wave theory but there is significantly increased scatter compared with option (2).

For the 30m³ room with $\alpha=0.1$: In the x-direction, average R values follow the plane wave theory for $kd < 4\pi$, then for $4\pi < kd < 5\pi$ there is increased scatter. In the z-direction, average R values are close to both the 3D diffuse field theory and plane wave theory for $kd < \pi$, then for $\pi < kd < 5\pi$ there is increased scatter. For both x- and z-directions when $kd > 5\pi$, the average R from ray tracing clusters around the zero line as indicated by both the 3D diffuse field theory and the plane wave theory but there is significantly increased scatter compared with option (2).

For the 50m³ room with $\alpha=0.02$: In the x-direction, average R values follow the plane wave theory for $kd < 2\pi$, then for $2\pi < kd < 5\pi$ they still tend to follow the plane wave theory rather than the 3D diffuse field theory but there is increased scatter. In the z-direction, average R values are close to both the 3D diffuse field theory and plane wave theory for $kd < 2\pi$, then for $2\pi < kd < 7\pi$ there is increased scatter. For both x- and z-directions when $kd > 7\pi$, the average R from ray tracing clusters around the zero line as indicated by both the 3D diffuse field theory and the plane wave theory but there is significantly increased scatter compared with option (2).

For the 50m³ room with $\alpha=0.3$: In the x-direction, average R values follow the plane wave theory for $kd < 4\pi$ then for $4\pi < kd < 9\pi$ there is increased scatter. In the z-direction, average R values follow the plane wave theory for $kd < 2\pi$, then for $2\pi < kd < 5\pi$ there is increased scatter. For both x- and z-directions when $kd > 9\pi$, the average R from ray tracing clusters around the zero line as indicated by both the 3D

diffuse field theory and the plane wave theory but there is significantly increased scatter compared with option (2).

For the 120m³ room with $\alpha=0.3$: In the x-direction, average R values follow the plane wave theory for $kd < 3\pi$, then for $3\pi < kd < 8\pi$ there is increased scatter. In the z-direction, average R values are close to both the 3D diffuse field theory and plane wave theory for $kd < \pi$, then for $\pi < kd < 4\pi$ it follows the plane wave theory but with increased scatter. For both x- and z-directions when $kd > 8\pi$, the average R from ray tracing clusters around the zero line as indicated by both the 3D diffuse field theory and the plane wave theory but there is significantly increased scatter compared with option (2).

The fact that the ray tracing data tends to cluster around the plane wave theory (even for relatively large, lightly damped rooms such as the 50m³ room with $\alpha=0.02$) suggests that option (3) is not a robust way to assess the sound field. In contrast to option (2), option (3) shows increased scatter which is attributed to the fact that kd represents many different combinations of frequency and distance d . For this reason, option (3) is now considered again but using single frequencies as shown on Figure 3-28 to Figure 3-32.

For the 30m³ room with $\alpha=0.01$: For both x- and z-directions, the average R from ray tracing follows the plane wave theory from 250 to 500Hz and follows the 3D diffuse field theory from 630 to 2500Hz.

For the 30m³ room with $\alpha=0.1$: For both the x- and z-directions, the average R from ray tracing follows the plane wave theory from 250 to 1250Hz and follows the 3D diffuse field theory from 1600 to 2500Hz.

For the 50m³ room with $\alpha=0.02$: For both x- and z-directions, the average R from ray tracing follows the plane wave theory from 250 to 630Hz and follows the 3D diffuse field theory from 800 to 2500Hz.

For the 50m³ room with $\alpha=0.3$: For both x- and z-directions, the average R from ray tracing follows the plane wave theory from 250 to 2000Hz and follows the 3D diffuse field theory at 2500Hz.

For the 120m³ room with $\alpha=0.3$: For both x- and z-directions, the average R from ray tracing follows the plane wave theory from 250 to 2500Hz.

The general conclusion is that the use of option (3) at single frequencies leads to conclusions that seem intuitively reasonable, i.e. the direct field tends to dominate at low-frequencies (even though the measurement points are outside the reverberation distance) and the sound field becomes approximately diffuse at high frequencies. One possibility would be to use the Schroeder frequency [67] to see if this corresponds to the crossover from a plane wave field to a diffuse field. For the 30m³ room with $\alpha=0.01$ and $\alpha=0.1$ the Schroeder frequency is 1042Hz and 329Hz respectively. For the 50m³ room with $\alpha=0.02$ and $\alpha=0.3$ the Schroeder frequency is 614Hz and 158Hz respectively. For the 120m³ room with $\alpha=0.3$ the Schroeder frequency is 120Hz. Referring to the crossover frequencies identified above it is clear that the Schroeder frequency is not a useful indicator of the frequency above which the spatial correlation coefficient corresponds to 3D diffuse field theory.

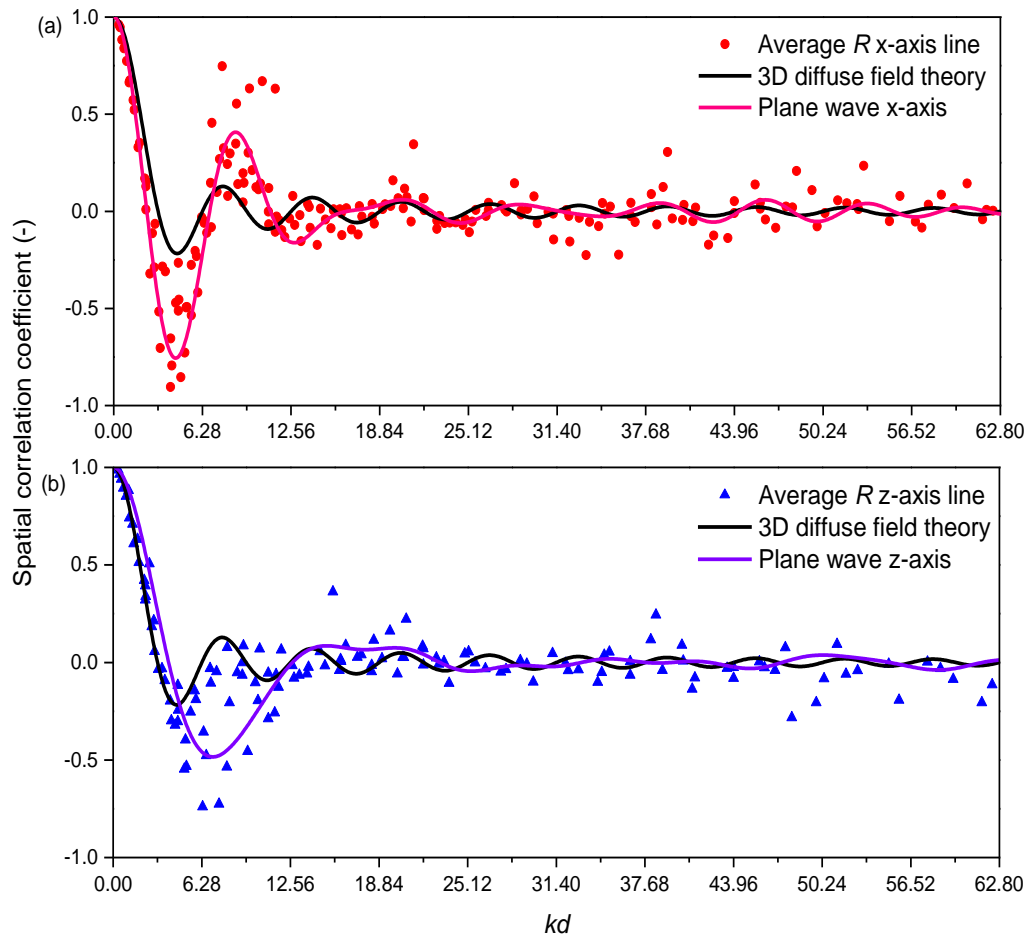


Figure 3-23. Average spatial correlation in 30m^3 room ($\alpha=0.01$) along x- and z-axis ten measurement lines with option (3) all permutations of pairs, plane wave and diffuse field theory.

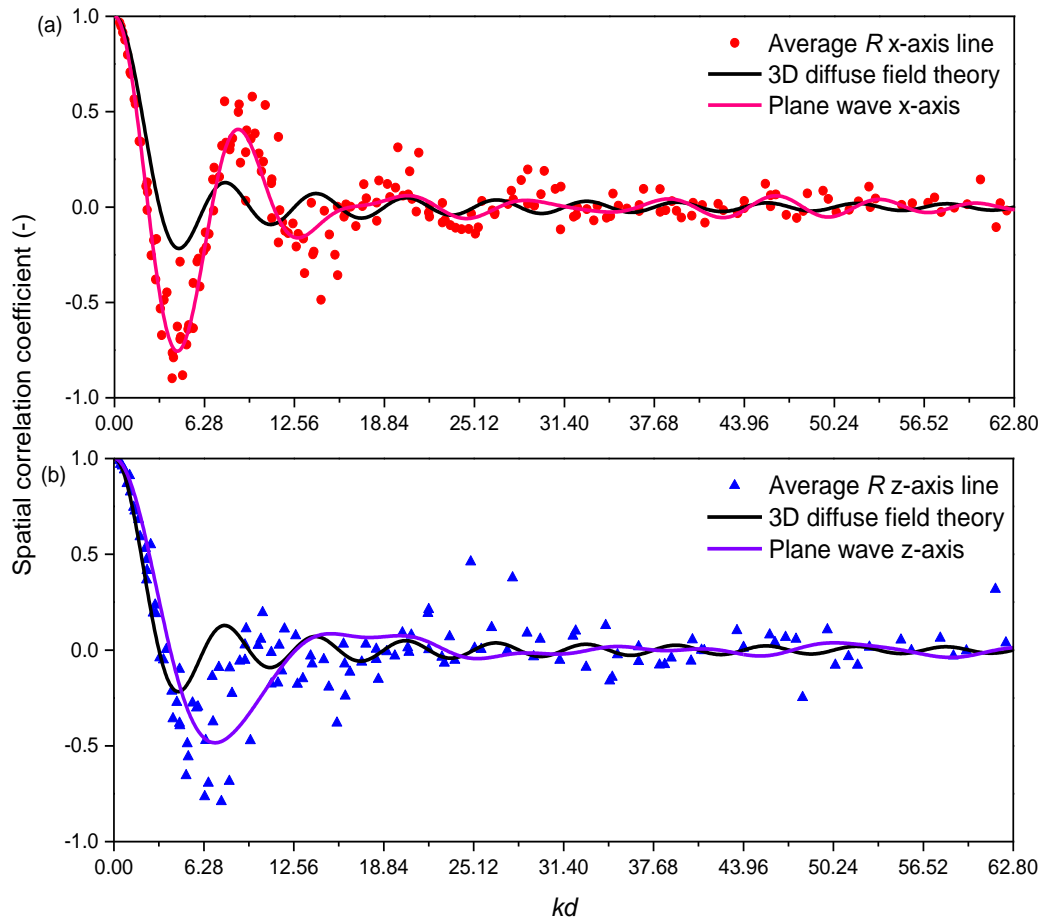


Figure 3-24. Average spatial correlation in 30m^3 room ($\alpha=0.1$) along x- and z-axis ten measurement lines with option (3) all permutations of pairs, plane wave and diffuse field theory.

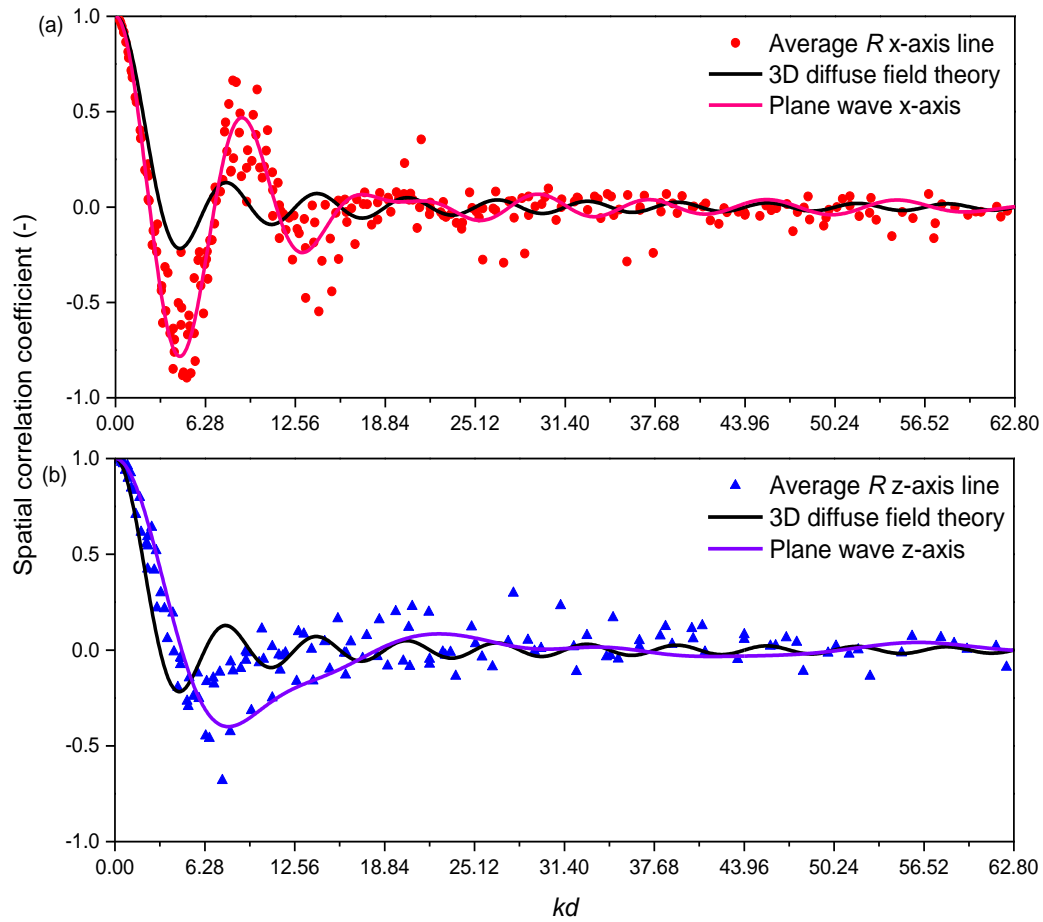


Figure 3-25. Average spatial correlation in 50m^3 room ($\alpha=0.02$) along x- and z-axis ten measurement lines with option (3) all permutations of pairs, plane wave and diffuse field theory.

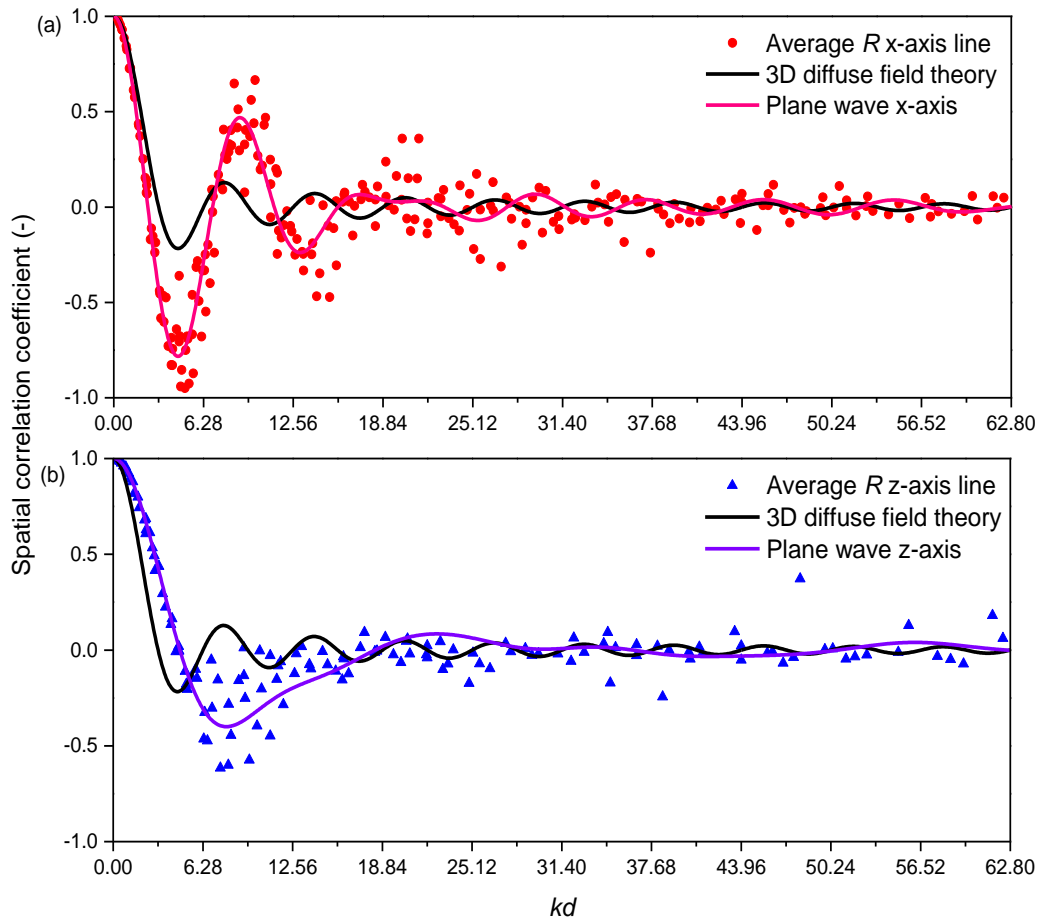


Figure 3-26. Average spatial correlation in 50m^3 room ($\alpha=0.3$) along x- and z-axis ten measurement lines with option (3) all permutations of pairs, plane wave and diffuse field theory.

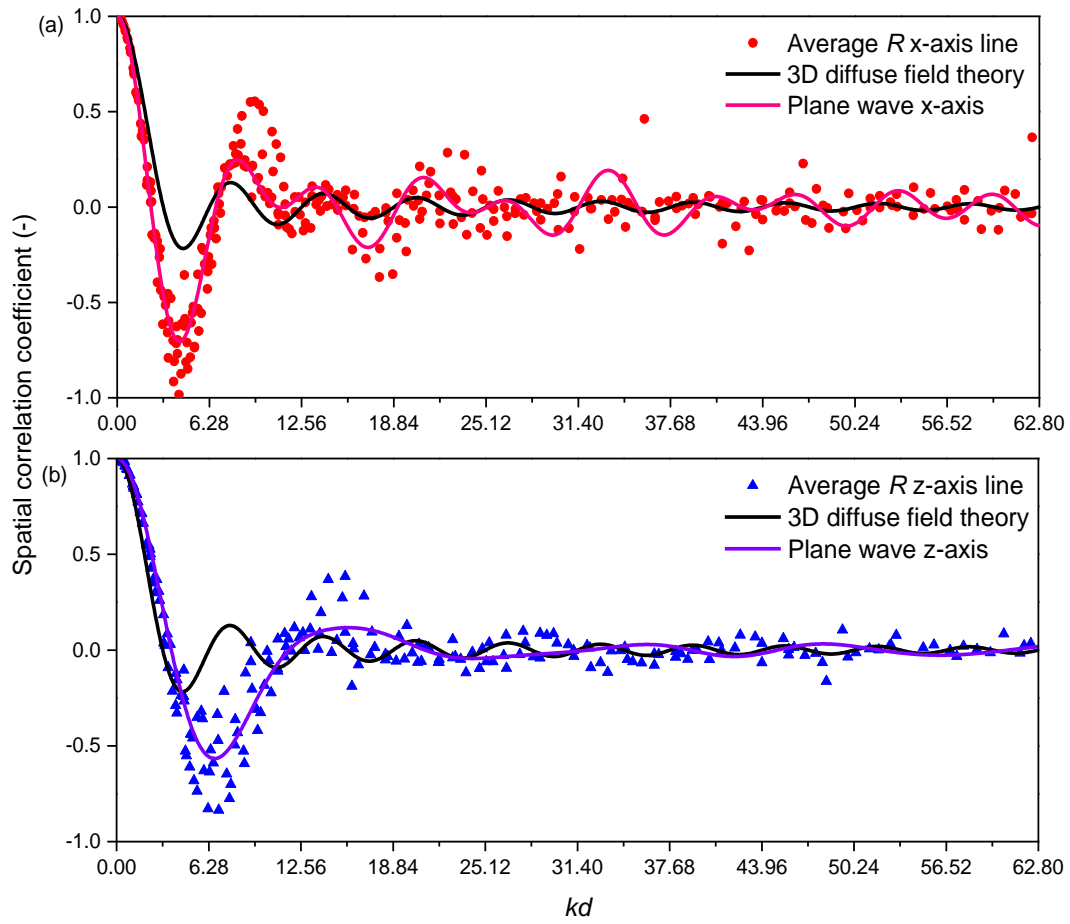
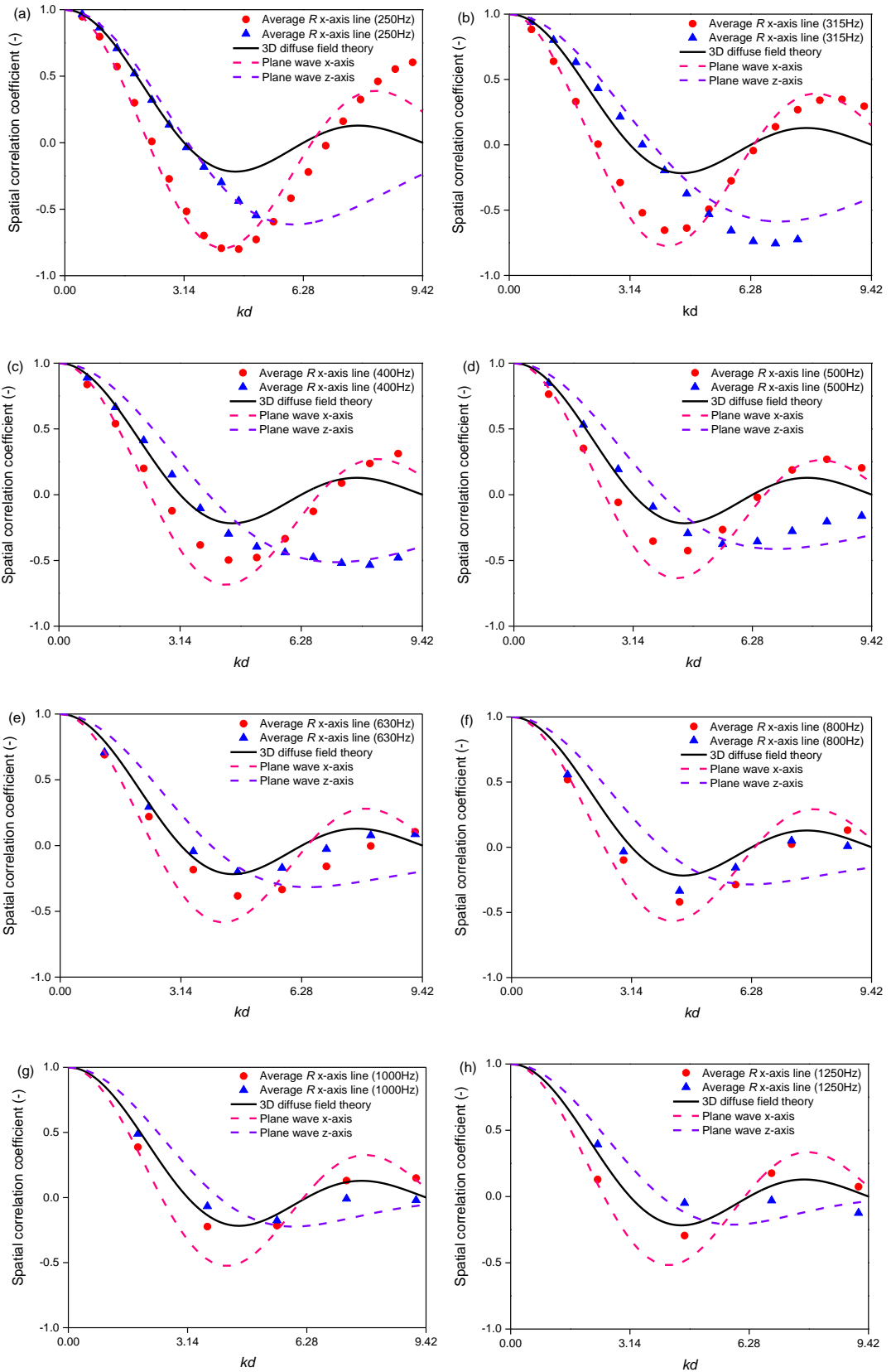


Figure 3-27. Average spatial correlation in 120m^3 room ($\alpha=0.3$) along x- and z-axis ten measurement lines with option (3) all permutations of pairs, plane wave and diffuse field theory.



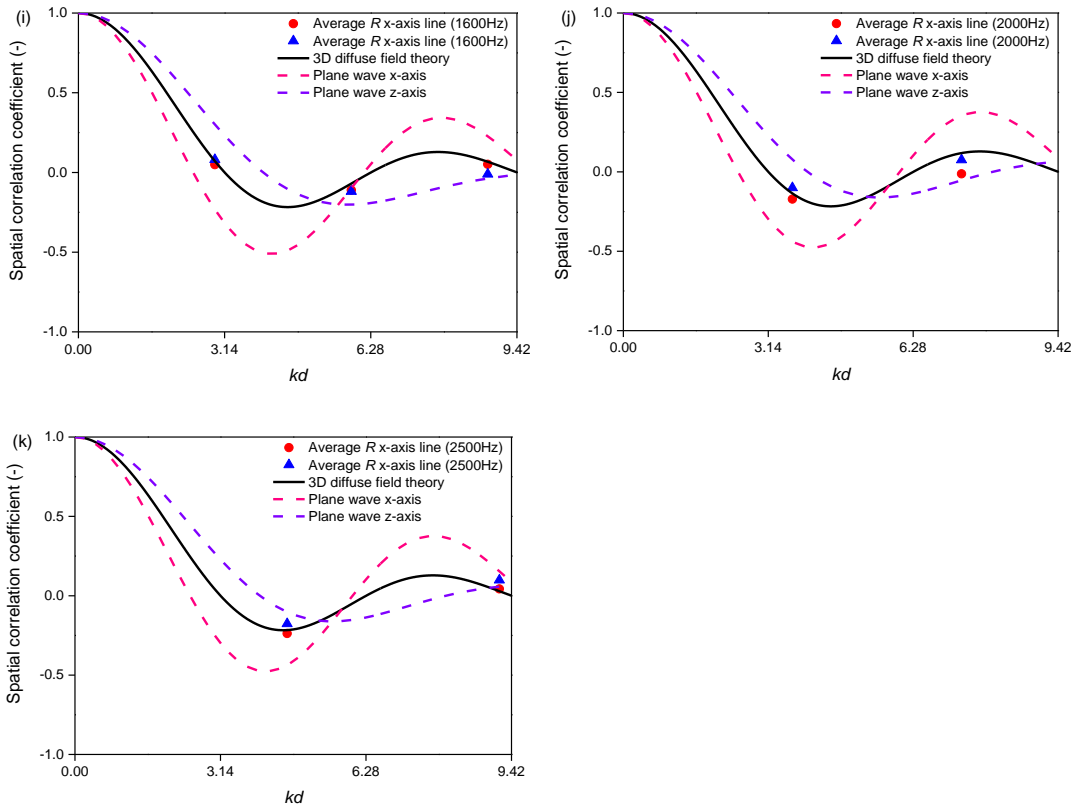
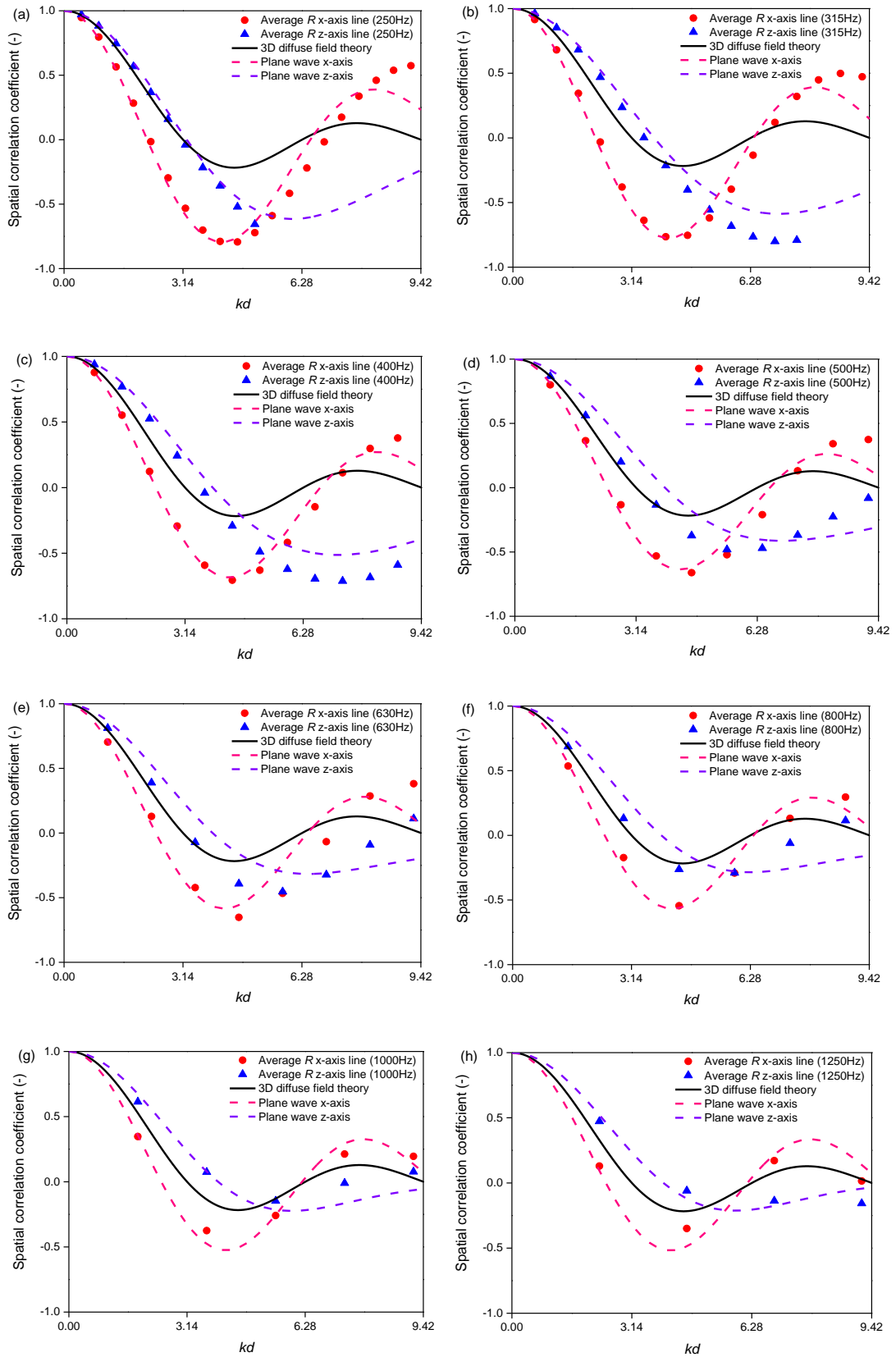


Figure 3-28. Average spatial correlation in 30m^3 room ($\alpha=0.01$) along x- and z-axis ten measurement lines with option (3) all permutations of pairs, plane wave and diffuse field theory in terms of frequency.



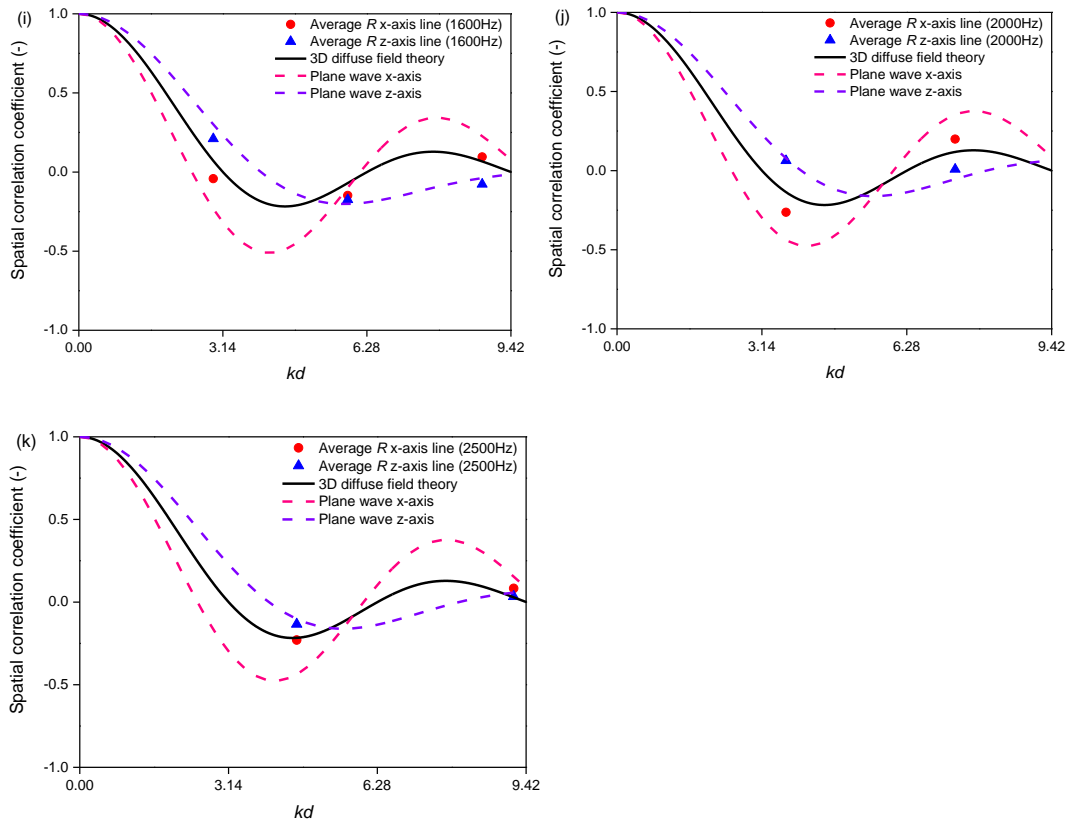
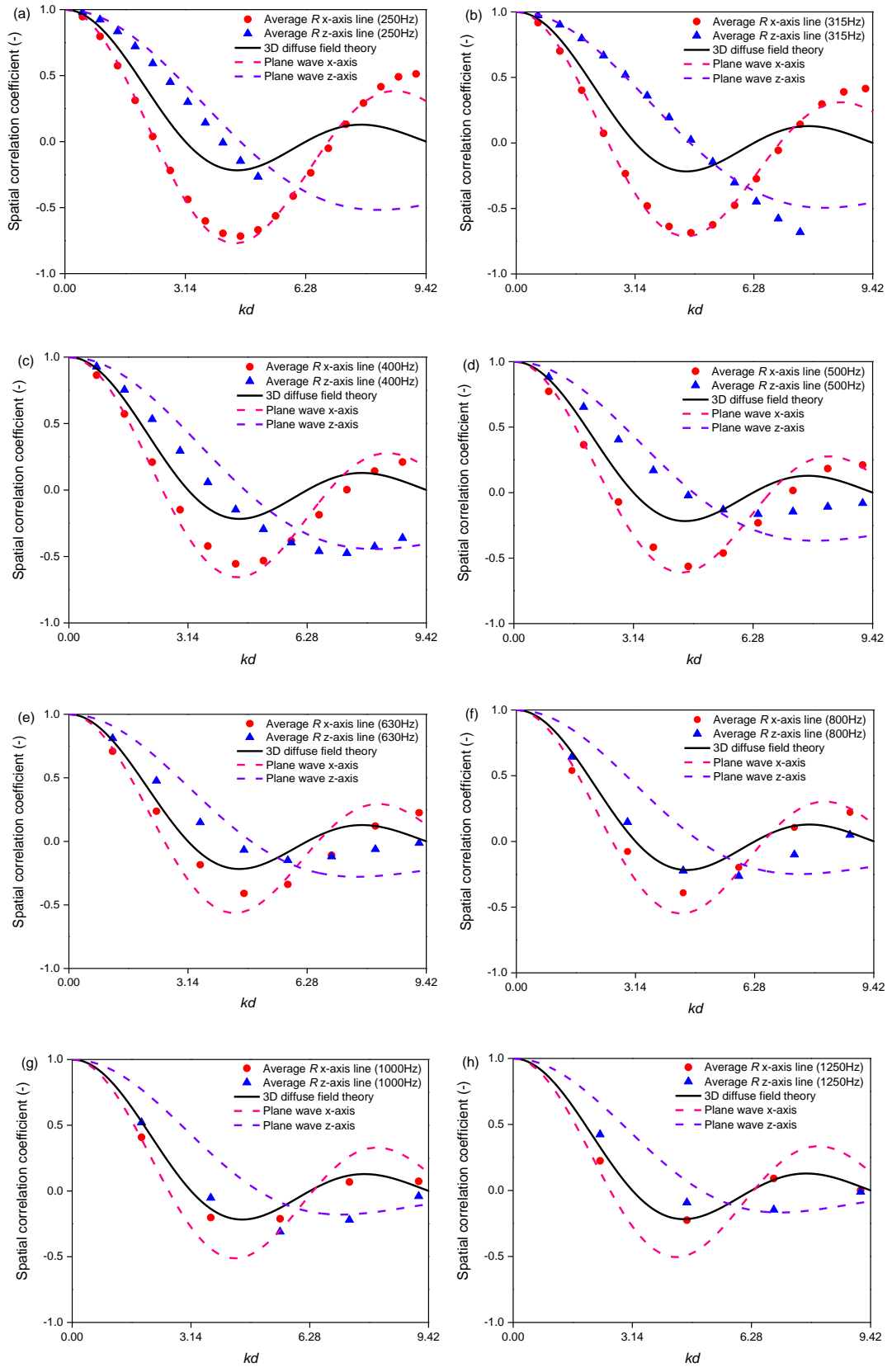


Figure 3-29. Average spatial correlation in 30m^3 room ($\alpha=0.1$) along x- and z-axis ten measurement lines with option (3) all permutations of pairs, plane wave and diffuse field theory in terms of frequency.



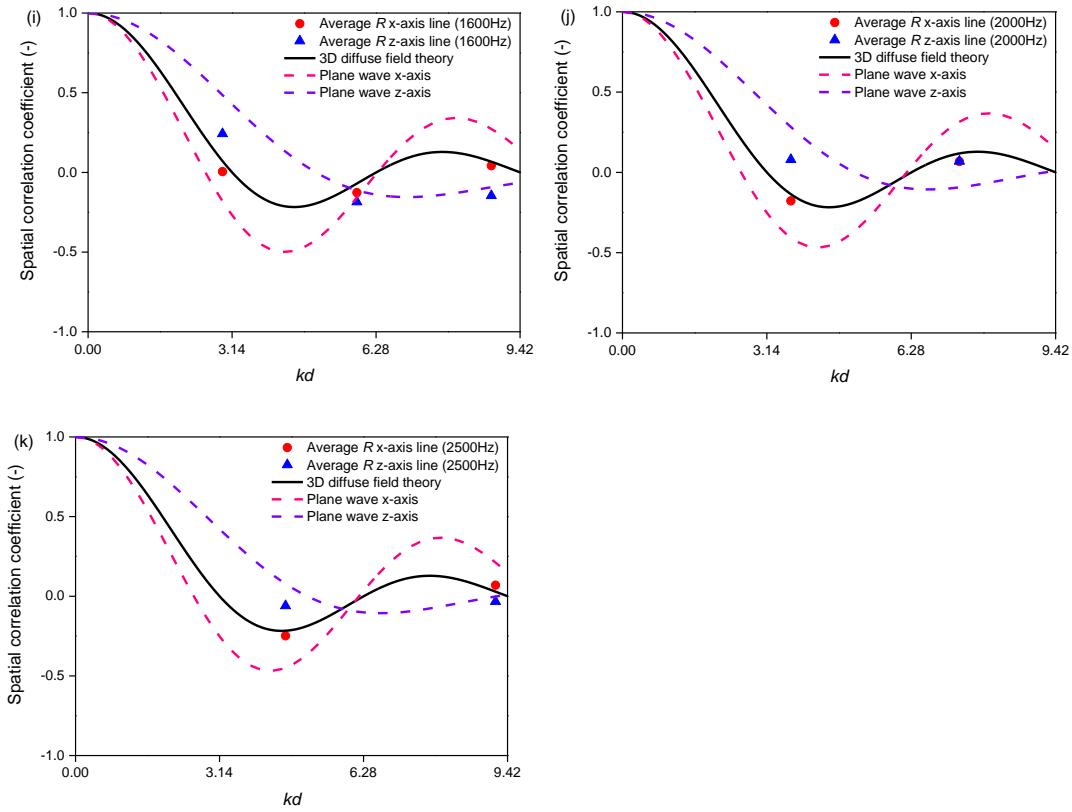
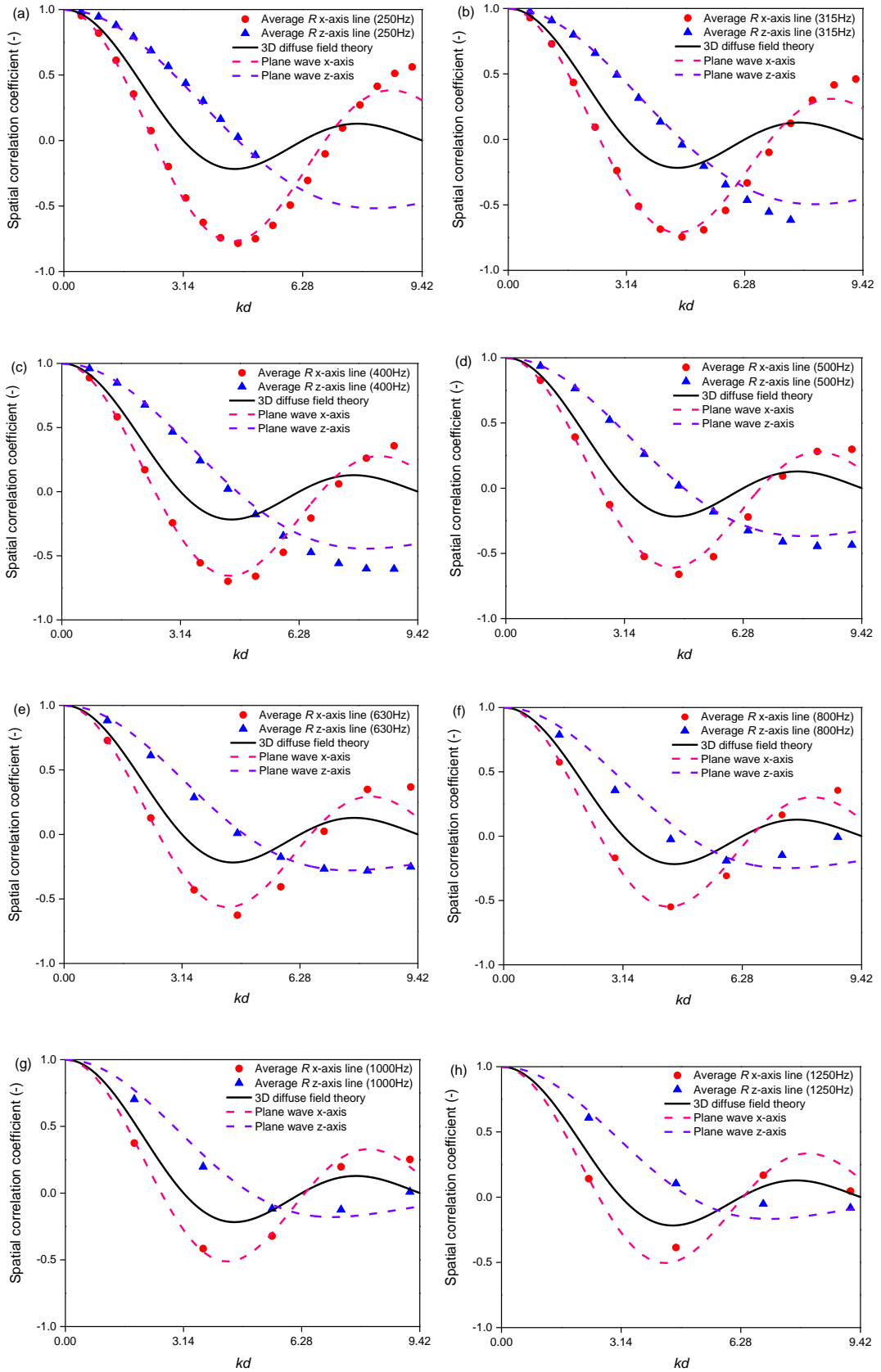


Figure 3-30. Average spatial correlation in 50m^3 room ($\alpha=0.02$) along x- and z-axis ten measurement lines with option (3) all permutations of pairs, plane wave and diffuse field theory in terms of frequency.



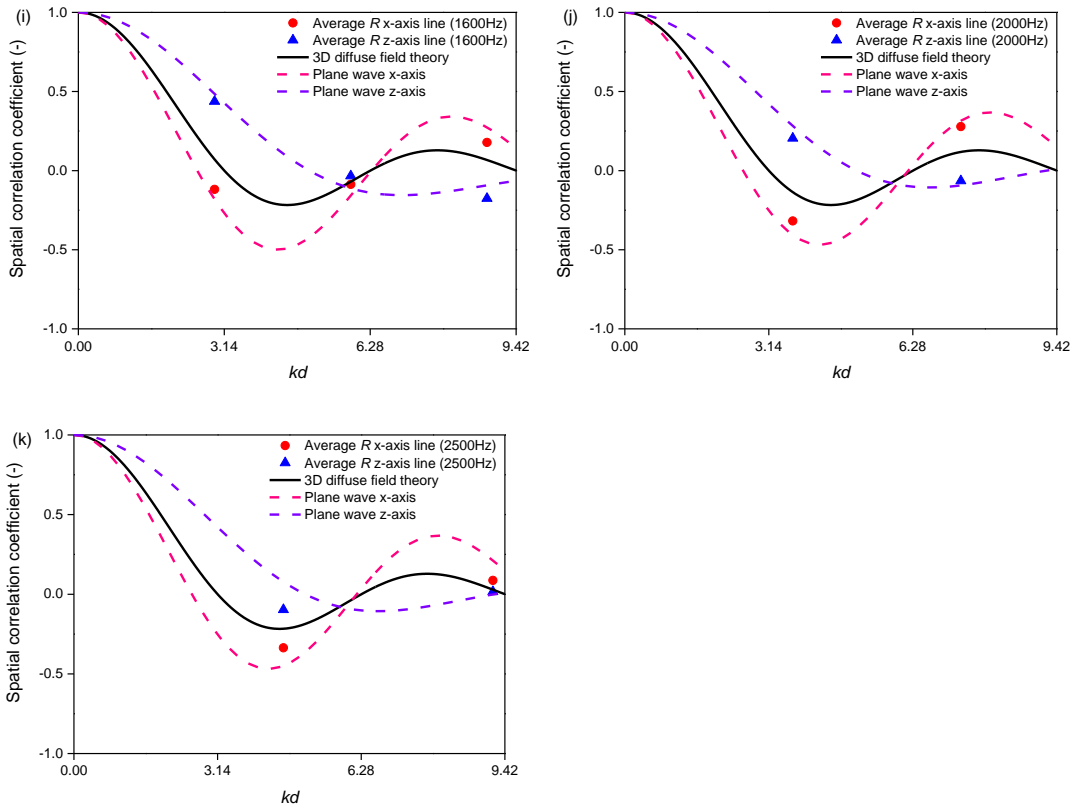
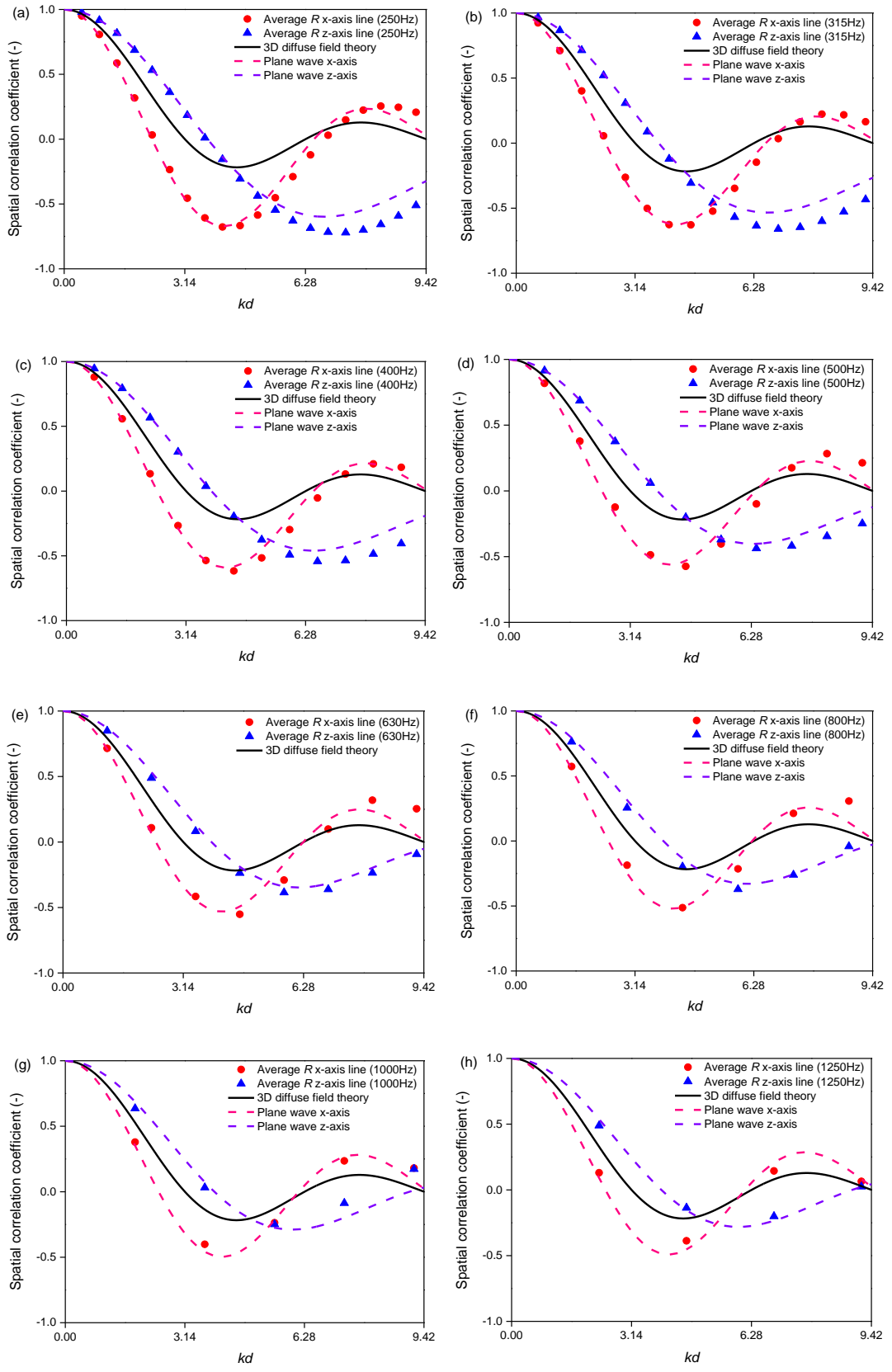


Figure 3-31. Average spatial correlation in 50m^3 room ($\alpha=0.3$) along x- and z-axis ten measurement lines with option (3) all permutations of pairs, plane wave and diffuse field theory in terms of frequency.



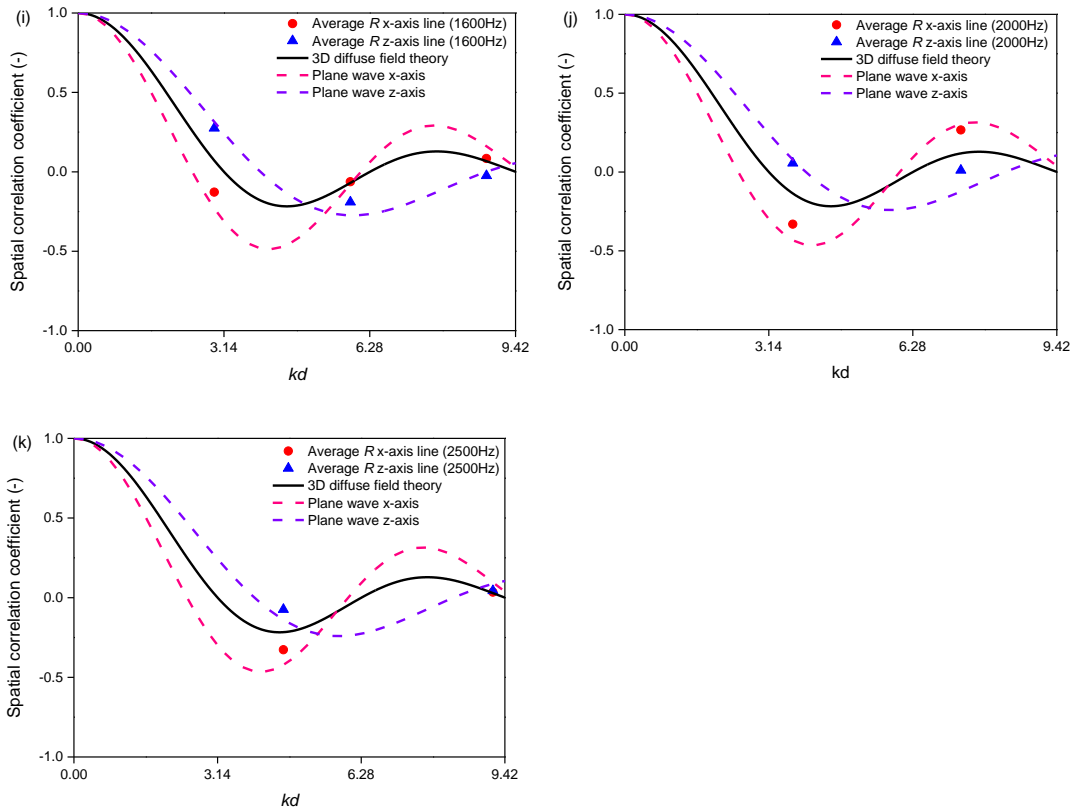


Figure 3-32. Average spatial correlation in 120m^3 room ($\alpha=0.3$) along x- and z-axis ten measurement lines with option (3) all permutations of pairs, plane wave and diffuse field theory in one-third octave frequency.

3.5 Conclusions

In this chapter, three different methods have been assessed for the measurement of spatial correlation coefficients. However, these gave conflicting indications as to whether the sound field can be considered diffuse. It was notable that although the measurement points were outside the reverberation distance, there were frequencies that followed the plane wave theory based on the direct field from the point source.

The general conclusion is that option (1) (pairs of points formed by one fixed point at a position that is $\geq \lambda/2$ from the boundary that lies in a plane perpendicular to the measurement line, and all other points along the same line that are $\geq \lambda/2$ from the opposite boundary) can lead to conclusions that seem inappropriate however the use of option (2) (pairs of points with a fixed spacing, d_{ij} , along each line) and option (3) (all permutations of points with variable spacing, d_{ij} , along each line) is reasonable. This might suggest that the option (1) is incorrect or that the reverberation distance is not appropriate when assessing phase differences between two points because it is based only on levels.

In conclusion it is difficult to definitively identify when a sound field in a box-shaped space can be considered as diffuse using ray tracing data, even though some authors have shown it is feasible using measurements [2,12,13]. Therefore, if it is not possible for a relatively simple volume such as a box it will not be feasible to attempt this for complex spaces, such as long corridors or small car cabins. For this reason, the sound fields in the complex spaces in the remainder of this thesis are not assessed using the spatial correlation coefficient.

Chapter 4 Measurements and prediction of sound transmission along an elongated cuboid

4.1 Introduction

In elongated spaces, such as corridors where one dimension is much greater than the other two and the other two are still large compared to the acoustic wavelength, the sound field can be significantly different to a diffuse field [38,68,69,70]. This chapter concerns the prediction and experimental validation of sound transmission along an empty cuboid containing a point sound source.

The numerical experiments in this chapter use ray tracing to provide predictions of the sound field, which are compared with other prediction models. The empty cuboid considered for the numerical modelling has dimensions of 30 m x 1.5 m x 2.5 m using the coordinate system indicated in Figure 4-1.

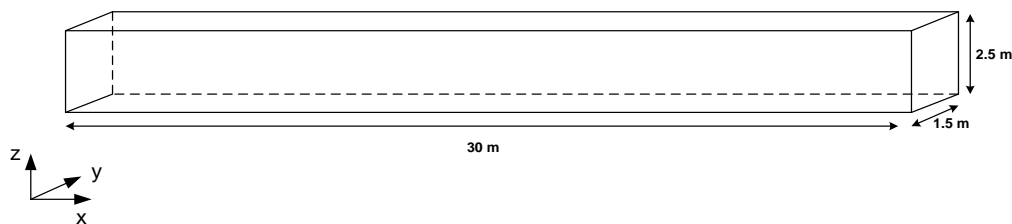


Figure 4-1. Empty cuboid system used for numerical modelling.

The chapter initially compares the ray tracing results against a model for the direct sound field and models for a propagating 2D sound field based on work by Redmore and Flockton [49]. Different SEA models are assessed with coupling loss factors that are either predicted or determined by using ESEA on the ray tracing output. The last section in the chapter is a case study based on measurements on an empty corridor which is used to validate the prediction models.

4.2 Direct field

The direct field describes sound rays which travel directly from the source to any receiver point in a straight line. For a point source which generates a sound power W , the energy density of the direct field w_d , at a distance d , from the source is [51]

$$w_d = \frac{W}{4\pi c_0 d^2} \quad (3.3.1)$$

It has been verified that the direct field calculated using ODEON with an absorption coefficient of $\alpha=1$ on all corridor surfaces gives the same results as Eq.(3.3.1); hence for the sake of convenience, ODEON is used for all the direct field calculations on the rectangular grid of positions in the corridor.

In order to assess the importance of the direct field compared to the reverberant field ray tracing models were created in ODEON using absorption coefficients of (a) $\alpha=0.1$, (b) $\alpha=0.3$ or (c) $\alpha=0.6$ on all surfaces. Each model used either specular or diffuse reflections for all surfaces. Sound was generated from a point source at one end of the corridor at a position (0.25m,0.25m,0.25m). Sound pressure levels were predicted on a rectangular grid with 0.25m spacing using all positions that were ≥ 0.25 m away from the point source and up to 0.5m away from the all boundaries.

The decrease in sound pressure level along the corridor is shown in Figure 4-2. As expected, the predicted decrease due to the direct field is closest to the ray tracing result that uses the highest absorption coefficient ($\alpha=0.6$). Especially, after 5m it is ray tracing using diffuse rather than specular reflections that is closest to the direct field with $\alpha=0.6$. The general trend is that the direct field tends to be more dominant with diffuse rather than specular reflections because specular reflections ensure that the reflected rays propagate down the corridor whereas diffuse reflections can lead to some reflected energy returning back towards the source. The reflection of sound from the opposite end of the corridor to the source, causes the ray tracing curves to decrease slightly between 25m and 30m due to the end wall reflection as shown by Redmore [71], particularly when $\alpha=0.1$ and $\alpha=0.3$. This is clearer for specular than diffuse reflections.

Although the direct field can dominate over the reflected field when the surfaces have diffuse reflections and high absorption coefficients it is clear that predicting the

reflected field will be important in real corridors which will often have several surfaces with $\alpha < 0.6$ over the frequency range from 50Hz to 5kHz.

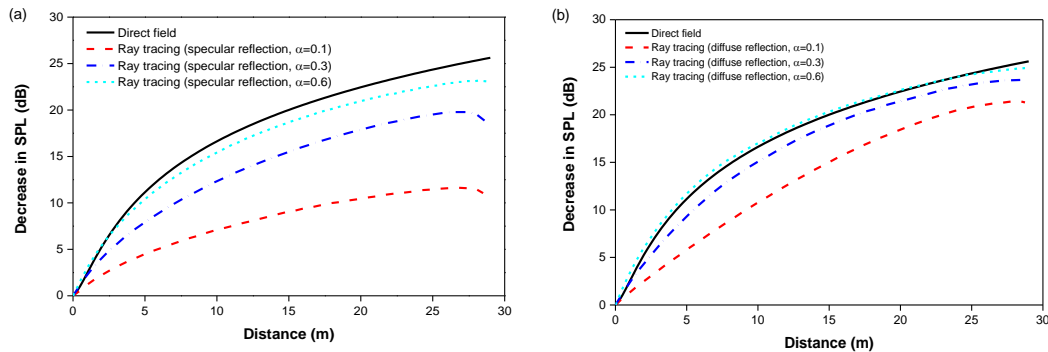


Figure 4-2. Empty cuboid model: Comparison of direct field with ray tracing models (different absorption coefficients) using (a) specular reflections and (b) diffuse reflections.

4.3 Propagating 2D diffuse field

4.3.1 Decrease in sound pressure level along a corridor

In this section, sound propagation is considered using the propagating 2D diffuse field model described in Section 2.3 that treats the sound field as two-dimensional ‘slices’ to calculate the decrease in SPL along the corridor using Eq. (2.3.3). This considers propagation along the corridor in the forward direction with a correction for the end reflection at the end of the corridor.

Figure 4-3 compares this propagating 2D model with ray tracing using three different absorption coefficients. Figure 4-3 (a) shows that for $\alpha = 0.1$ the propagating 2D model is closer to ray tracing assuming specular reflection than diffuse reflection. This is because specular reflections place emphasis on forward propagation (i.e. rays travelling away from the source down the length of the corridor). In contrast, diffuse reflections place equal emphasis on forward propagation and backwards propagation (i.e. sound rays returning up the corridor towards the source). The trend that the decrease in SPL with specular reflections is less than that with diffuse reflections is corresponding to the result observed in the paper by Kang [72]. Comparing Figure 4-3 (a) with Figure 4-3 (b) and (c) that have higher absorption coefficients indicates that the differences between ray tracing assuming specular and diffuse reflections are largest with the lowest absorption coefficient (Figure 4-3 (a)). The reason for this is

that the direct field becomes increasingly dominant as the absorption coefficient increases. However, the model does not account for the direct field because it purely assumes a propagating 2D reverberant field. As the surfaces of the corridor become more absorptive, inclusion of the direct field is likely to improve accuracy of the analytical prediction in the decrease in SPL along the corridor. This is considered in the next section.

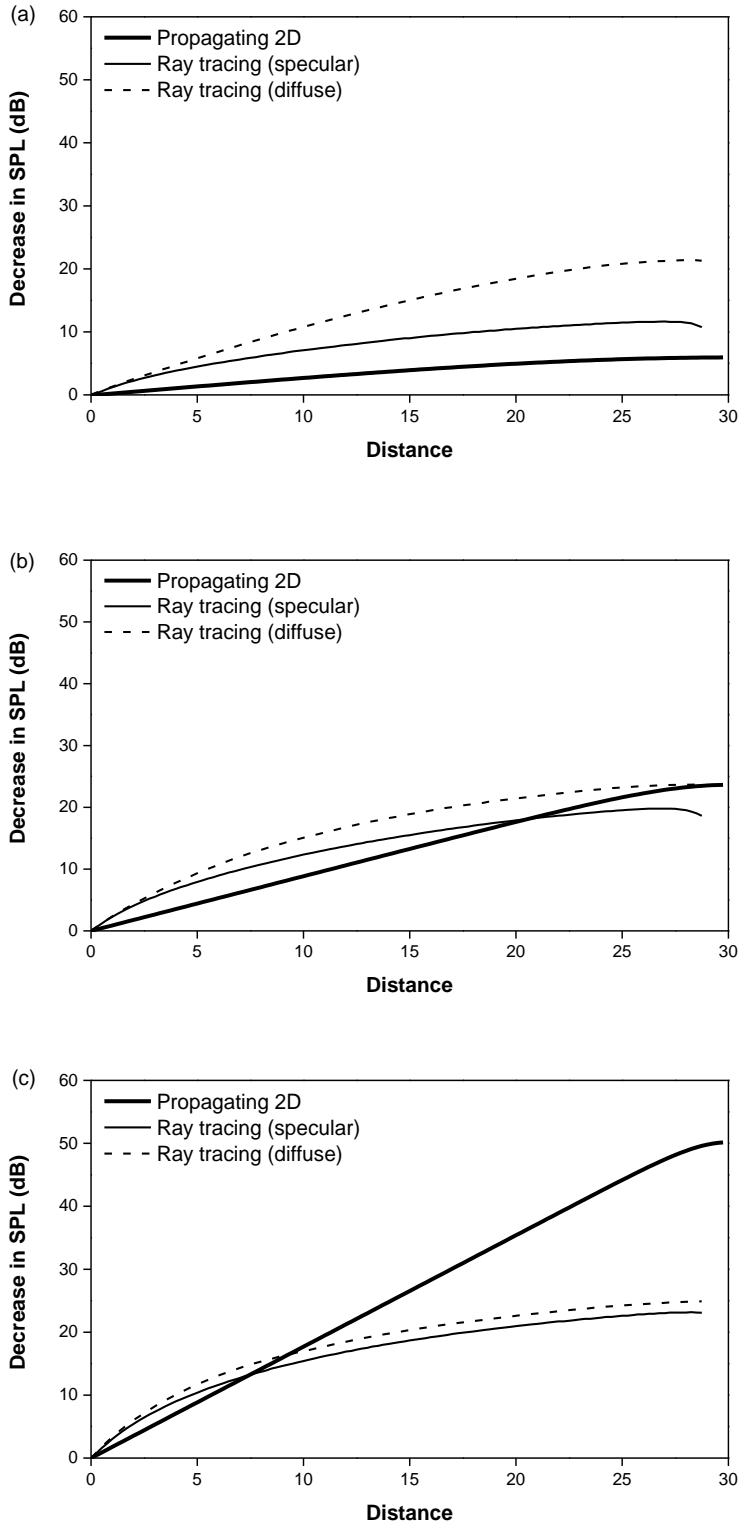


Figure 4-3. Empty cuboid model: Comparison of the propagating 2D diffuse field model with ray tracing models in terms of the decrease in sound pressure level for (a) $\alpha=0.1$, (b) $\alpha=0.3$ and (c) $\alpha=0.6$.

4.3.2 Incorporating the direct field in the propagating 2D diffuse field model

Based on the above finding that the direct field can sometimes be important, this section combines the propagating 2D model with the direct field. The predicted decrease in SPL is compared with the ray tracing results for $\alpha=0.1$, $\alpha=0.3$ and $\alpha=0.6$ in Figure 4-4. Note that the direct field is less important for $\alpha=0.1$ and $\alpha=0.3$.

Figure 4-4 (a) and (b) show that the propagating 2D model with direct field is closer to the ray tracing compared to the propagating 2D model by itself. This suggests that the direct field is not important for low absorption coefficients. On the other hand, Figure 4-4 (c) shows that for $\alpha=0.6$ the propagating 2D model with direct field is in closer agreement with the ray tracing model than the propagating 2D model by itself, particularly beyond a distance of 10 m. This shows that when a corridor has surfaces with relatively high absorption coefficients the propagating 2D model can be improved through inclusion of the direct field. Kang [46] assessed the propagating 2D model with direct field and showed it predicted a larger decrease in SPL with increasing distance than that estimated from the image source method for a 120m long enclosure (representing an underground station). However, buildings which are primarily considered in this thesis are required to have fire doors along the corridor to obey the relevant regulations for the safety so that in practice most corridors are no longer than 40m between fire doors [45]. For this reason, a 30m long corridor is considered for the investigation of sound transmission along the corridor which is assessed by the propagating 2D model and ray tracing, and two approaches show reasonable agreements (<3dB) even at high absorption coefficient which is similar to the results shown by Kang [46].

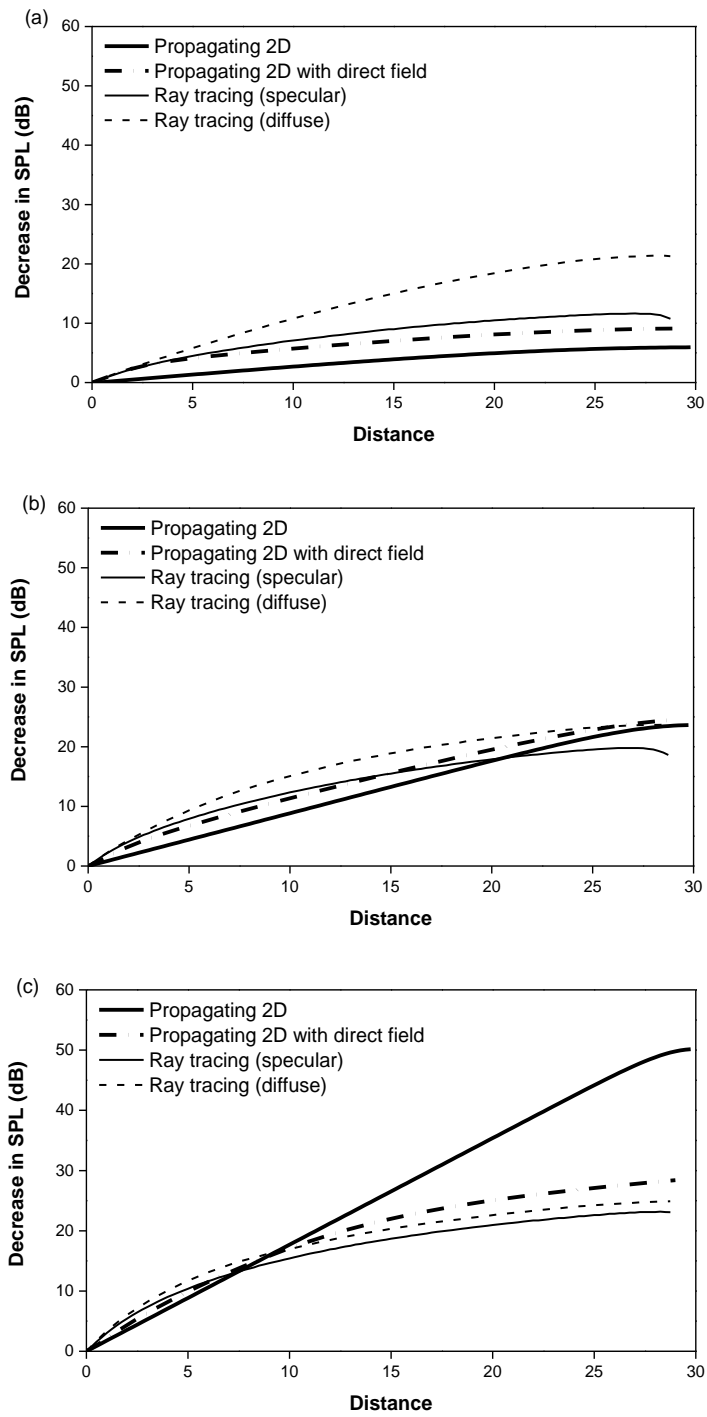


Figure 4-4. Empty cuboid model: Comparison of the propagating 2D diffuse field model incorporating the direct field with the ray tracing model for (a) $\alpha=0.1$, (b) $\alpha=0.3$ and (c) $\alpha=0.6$

4.3.3 Comparison of measurements and propagating 2D diffuse field model

Measurements on a real corridor were carried out in the Harrison Hughes building at the University of Liverpool. A sketch of this corridor is shown in Figure 2-7 in Section 2.6.1.

Sound pressure level measurements were taken at three different positions in the cross-section of the corridor at 1m intervals and averaged to give one-third octave band results as shown in Figure 2-9. Between 63Hz and 315Hz, Figure 4-5 shows that the decrease in SPL does not linearly decrease but shows significant fluctuations whereas at higher frequencies the decrease in SPL is approximately linear. This indicates modal behaviour at low frequencies that may not be suited to statistical prediction models based on diffuse field assumptions. However, the trends of the decrease in SPL at high frequencies are close to the propagating 2D model and the gradient of the decrease in SPL with distance increases with increasing frequency.

At a distance of 36m from the source, the cross-sectional dimensions of the corridor change due to the frame of a fire door. This causes a discontinuity in the curve for the decrease in SPL as indicated in Figure 4-5.

Two different approaches are considered to investigate the average absorption coefficient, $\bar{\alpha}$ of the real corridor. The first is an empirical approach which involves curve fitting the measurements to the propagating 2D model. This is performed by computing the Mean Square Error (MSE) between the measurements and the model, and then by using the minimum MSEs to find the optimum average absorption coefficients, $\bar{\alpha}$ in each one-third octave band. For curve fitting, only measurement data from the source position up to 36.5m are used to avoid the point where there is a change in cross-section of the corridor at the fire door. The curve fitting is implemented in two different ways; one considers the direct field near the source (i.e. nearfield) (see Figure 4-6) and the other only considers the direct field beyond a distance of 5m (see Figure 4-7). In both cases, measurements can be closely fitted to the propagating 2D models. However, when fitting from 0m (see Figure 4-6) there are some discrepancies between 0m and 15m for 400Hz and 800Hz, which could be due to the direct field which was shown to be influential in Section 4.3.2. For this reason the results from the 5m starting point are used to give the optimum average

absorption coefficients listed in Table 4-1. (NB. The estimated absorption coefficients are also within 0.02 of the values when using the 0m starting point.)

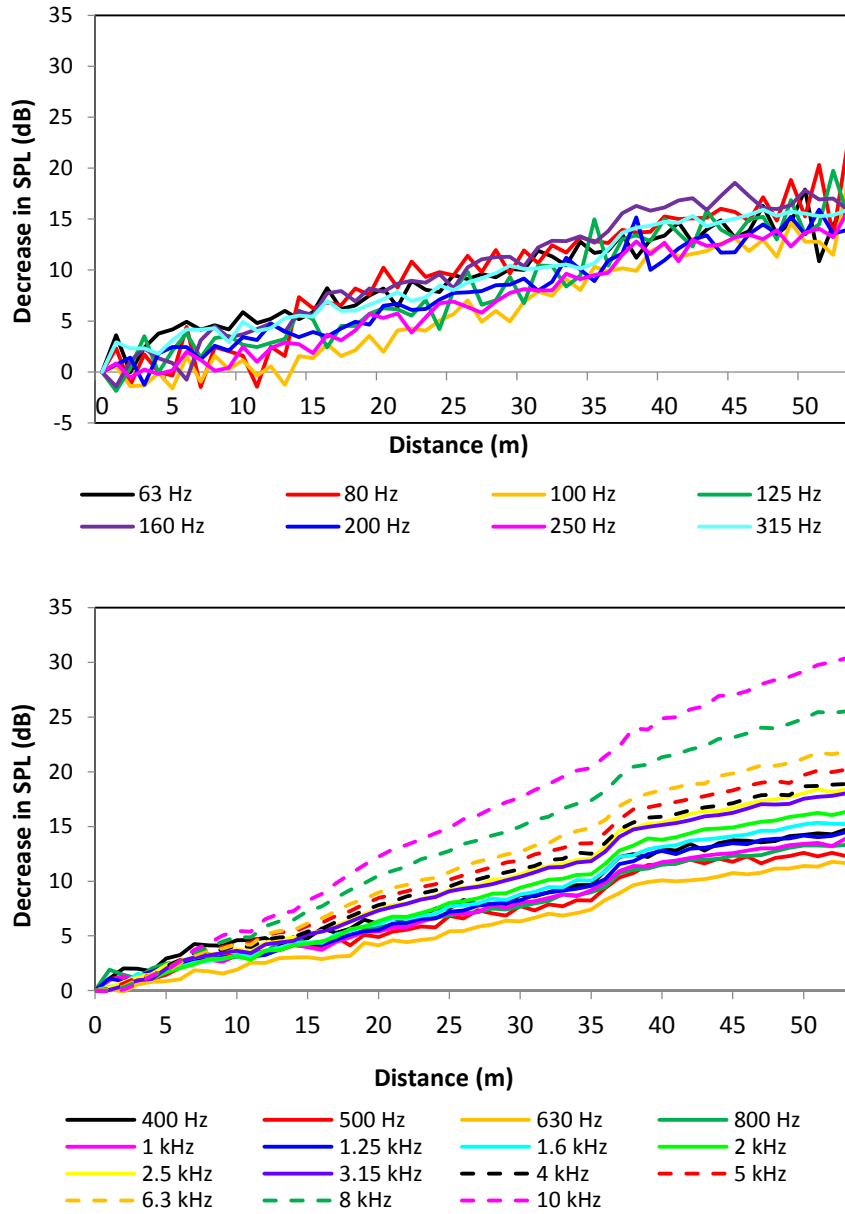


Figure 4-5. Real corridor: Measured decrease in sound pressure level.

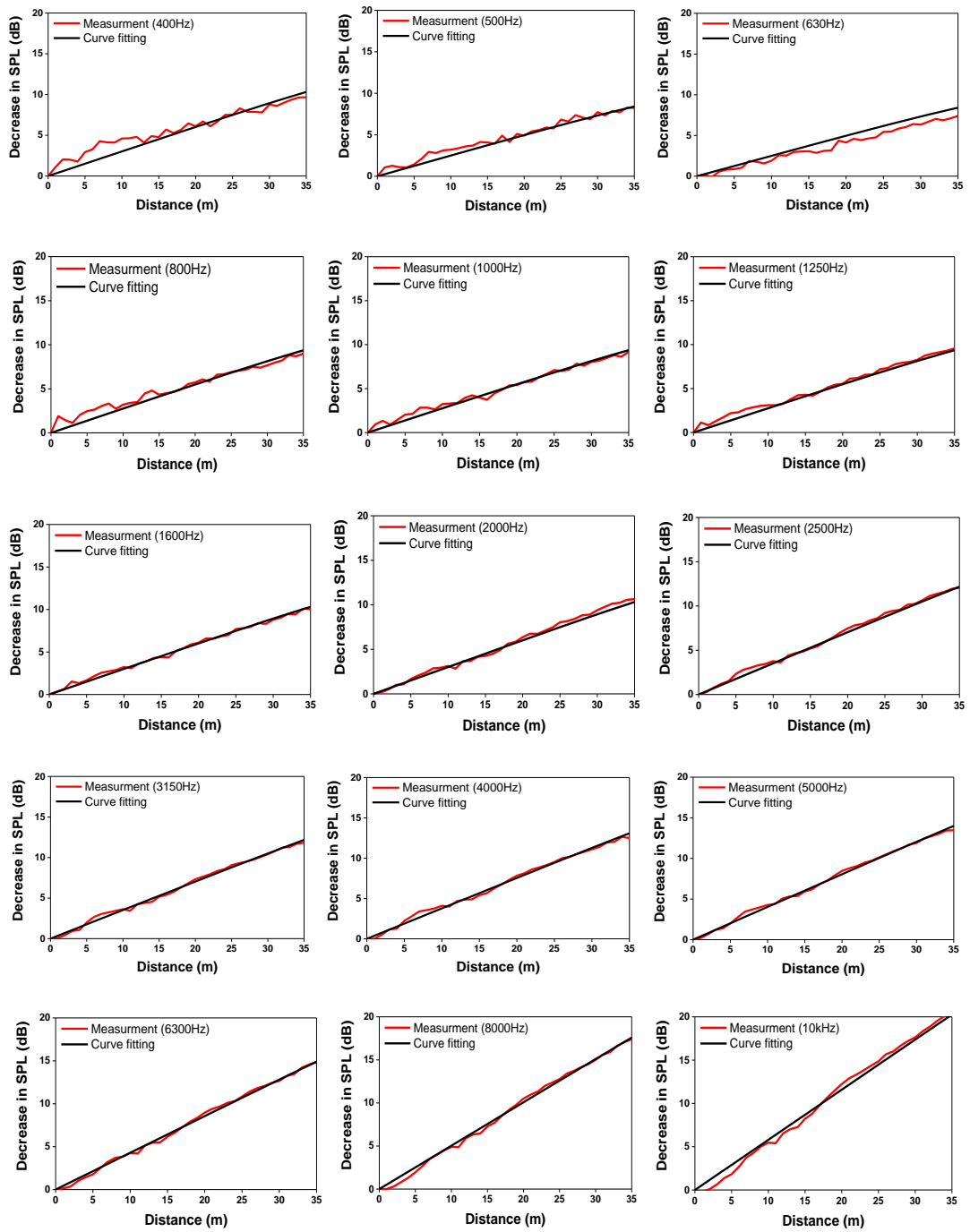


Figure 4-6. Real corridor: Curve fitting of measurements including points near the source with the propagating 2D diffuse field models (red line represents measurements and black line represents propagating 2D models).

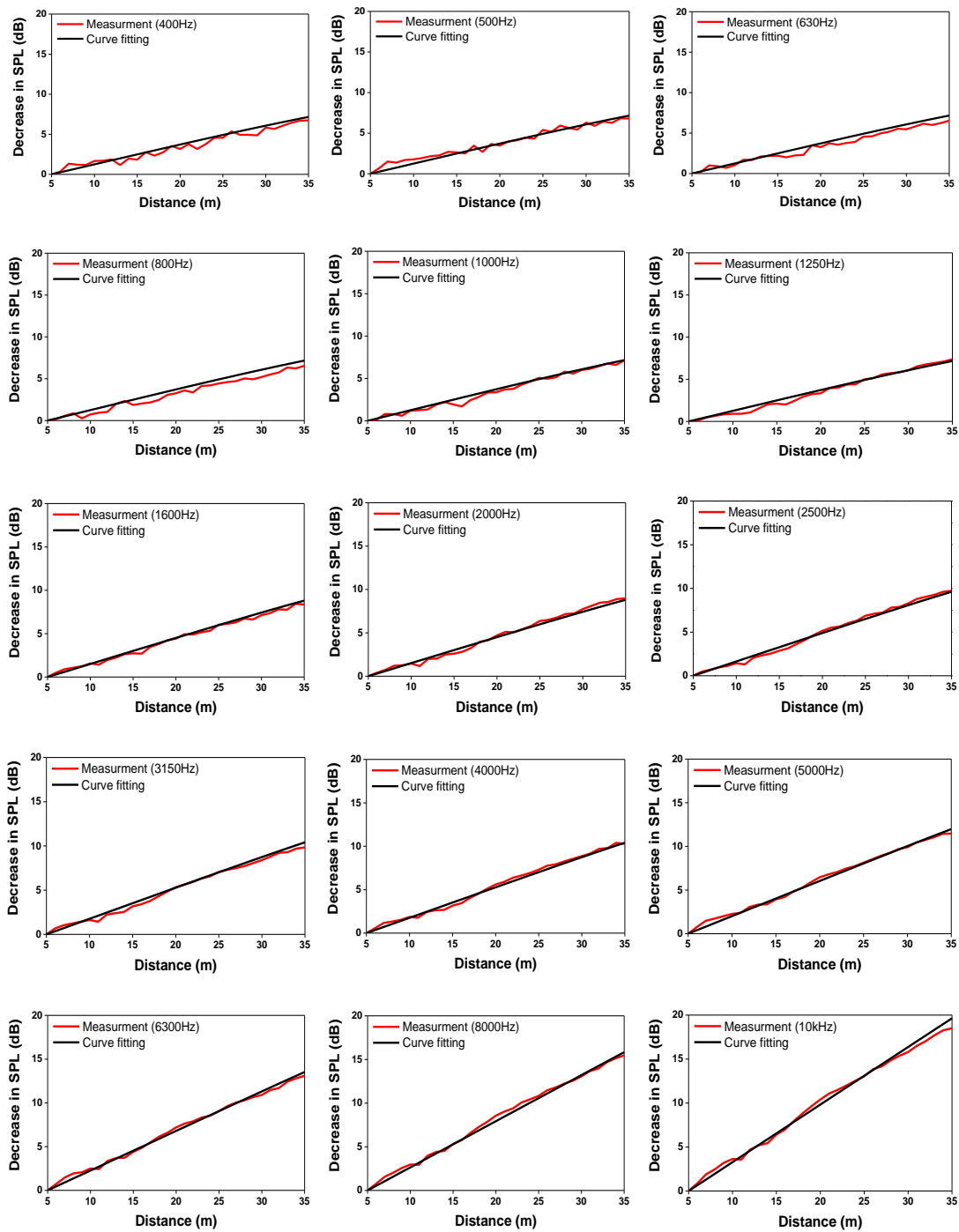


Figure 4-7. Real corridor: Curve fitting of measurements excluding points near the source with the propagating 2D diffuse field models (red line represents measurements and black line represents propagating 2D models).

Frequency (Hz)	400	500	630	800	1k	1.25k	1.6k	2k	2.5k	3.15k	4k	5k	6.3k	8k	10k
Absorption coefficient (-)	0.12	0.1	0.1	0.11	0.11	0.11	0.12	0.12	0.14	0.14	0.15	0.16	0.17	0.2	0.23

Table 4-1. Real corridor: Absorption coefficients determined from curve fitting in one-third octave bands.

The second approach is a more standard approach based on laboratory measurements of which absorption coefficients are taken from the ODEON material database. The ODEON material database has octave band rather than one-third octave band data. These absorption coefficients are given in Table 4-2 for the walls, ceiling, floor and windows and are used to estimate an average absorption coefficient, $\bar{\alpha}$ using Eq. (2.4.13). The absorption coefficients for the doors at the ends of the corridor were not known; hence, the average absorption coefficient for the corridor cross-section was also used for the doors. Air absorption was calculated in accordance with ISO 9613 (RH of 70% and temperature of 20°C) and is given in Table 4-3. ISO 9613 gives one-third octave bands; therefore, the average absorption coefficients are converted to octave bands by arithmetically averaging them.

Frequency (Hz)	63	125	250	500	1k	2k	4k	8k
Linoleum on concrete (floor)	0.02	0.02	0.02	0.03	0.04	0.04	0.05	0.05
13mm plaster board on 25mm stud no mineral wool (wall and ceiling)	0.16	0.16	0.15	0.07	0.08	0.05	0.06	0.06
Windows with double glazing (2-3mm)	0.1	0.1	0.07	0.05	0.03	0.02	0.02	0.05

Table 4-2. Real corridor: Absorption coefficients from ODEON material database in octave bands.

Frequency (Hz)	63	125	250	500	1k	2k	4k	8k
Air absorption area (m ²)	0.02	0.09	0.28	0.68	1.22	2.26	5.87	19.80

Table 4-3. Air absorption in terms of absorption area - calculated according to ISO 9613 (70% RH, 20°C).

The estimated average absorption coefficients from these two approaches are plotted in Figure 4-8 for the following situations based on the ODEON database:

- 1) Without windows
- 2) With windows
- 3) With windows and with air absorption

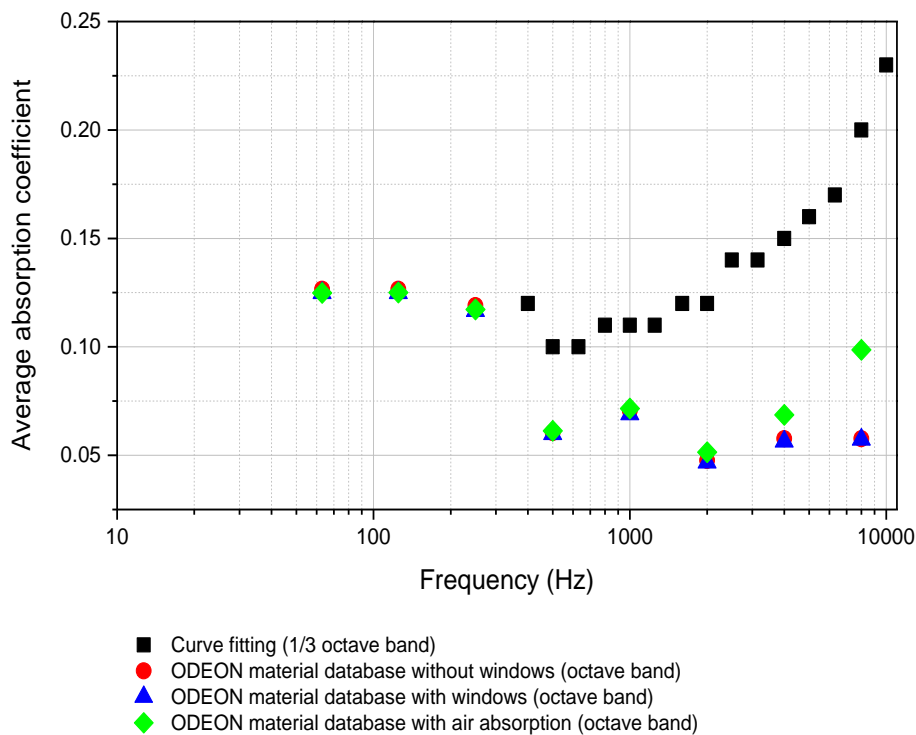


Figure 4-8. Real corridor: Estimated averaged absorption coefficients from curve fitting and the ODEON material database.

The results show a large difference between the two approaches. Including or excluding windows along the corridor did not significantly change the estimate based on ODEON data. With increasing frequency, the discrepancy between curve fitting and the estimate from the database becomes larger. One possibility is that air absorption needs to be considered. However, air absorption only becomes significant at and above 4kHz as indicated in Figure 4-8. The inclusion of air absorption is not sufficient to significantly reduce the discrepancy between the two approaches. Another reason for the significant increase in the absorption coefficient at high frequency is that the measurement of the random incidence absorption coefficient of a material is sensitive to temperature and relative humidity above 2kHz even when the same specimen is used for the measurement -see Tachibana [73]. From Cox and D'Antonio [74] it is noted that there can be significant uncertainty in the measured absorption coefficient from Round Robin tests.

An average absorption coefficient for the surfaces of the corridor has been estimated using two different approaches: curve fitting or using standard material database. Above 400Hz there are large discrepancies between the two approaches hence both values will be assessed using an ODEON model of the corridor in Section 4.6.

4.4 SEA model

In the previous sections, prediction models have been assessed that primarily consider forward propagation from one end of a corridor to the other in terms of the direct field and a 2D propagating field. In this section, an SEA model is considered which requires consideration of the corridor as a series of coupled reverberant volumes.

4.4.1 Consideration of open-ended spaces as SEA subsystems

When a single volume is subdivided into subsystems, the assumption in SEA is that they are weakly coupled and that the subsystem response can be considered in terms of the local modes of each subsystem. This section considers the latter requirement. In most SEA models in buildings the rooms are closed cuboids. Taking the empty cuboid as an example, consider subdividing the volume into four equal volume

subsystems as shown in Figure 4-9. Note that subsystems 1 and 2 have a different number of ‘open’ coupling areas/boundaries; subsystem 1 has five closed boundaries and one open end, whereas subsystem 2 has four closed boundaries and two open ends. Therefore an assessment of open-ended cuboid volumes is required to consider whether the SEA approach is appropriate. This section considers the change in the modes of cuboid volumes with different boundary conditions.

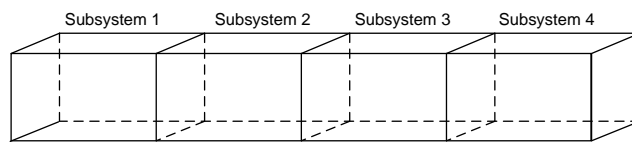


Figure 4-9. Example SEA model of an empty cuboid composed of four subsystems.

4.4.1.1 Modal response of open-ended space subsystems using FEM

The variation of the modal responses in terms of boundary conditions is investigated with Finite Element Methods (FEM). Five models of cuboid spaces are considered as shown in Figure 4-10. These are a cuboid with closed ends, a cuboid with one open end, a cuboid with two open ends, a cuboid with one partly-open end and a cuboid with two partly-open ends. Note that the partly open-ends are relevant to a corridor with staggered partitions in Chapter 5 but it is useful to compare all the different boundary conditions together in this section.

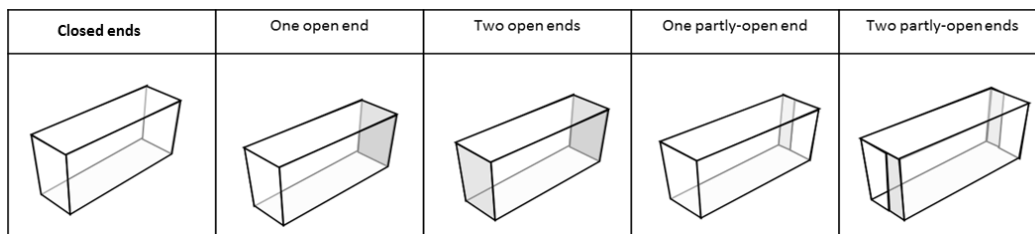
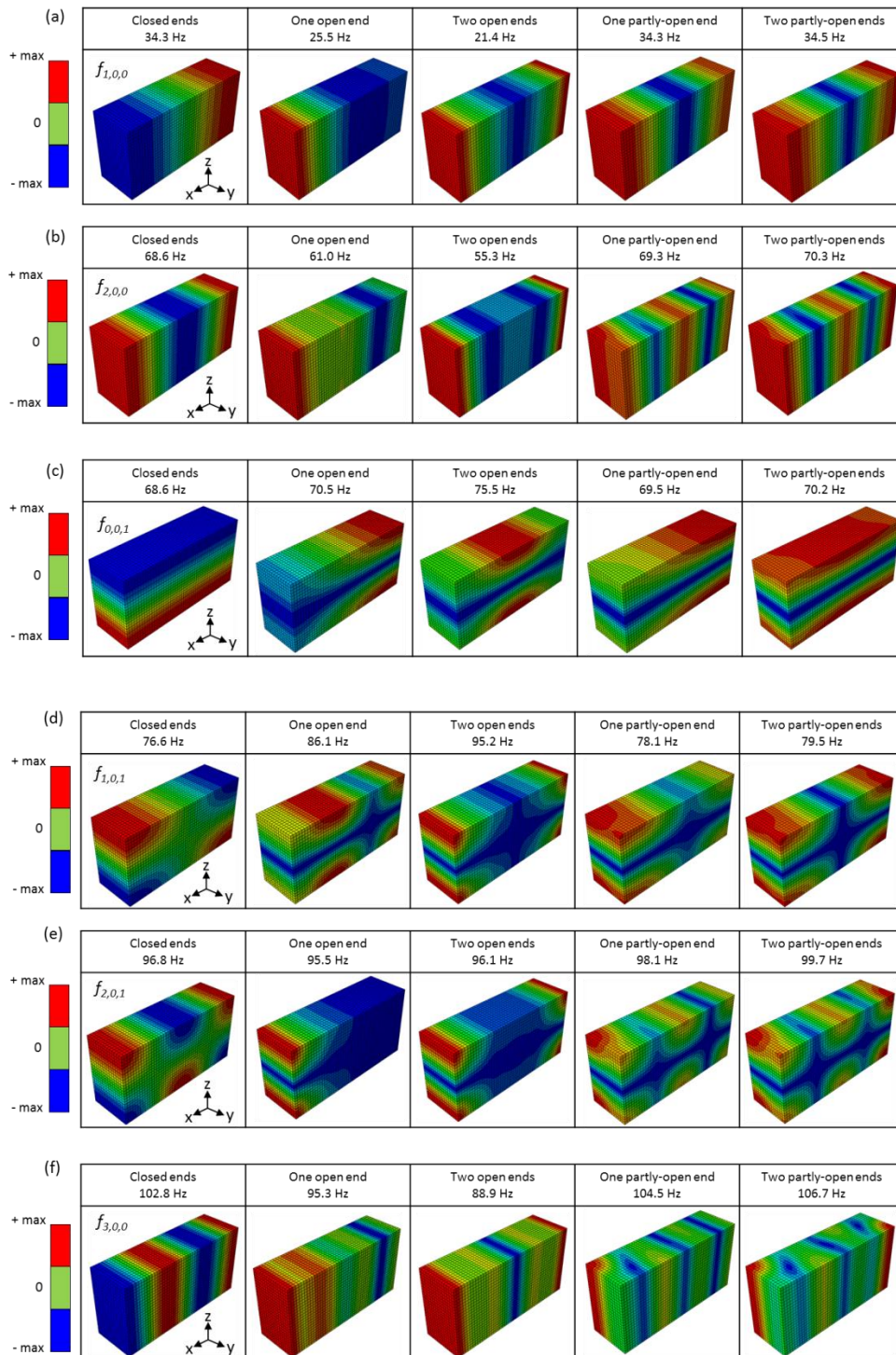


Figure 4-10. FEM models for modal responses of cuboids with closed, open or partly open ends (grey colour indicates an open area).

Modal responses are shown in Figure 4-11 and are grouped in rows corresponding to mode shapes with similar features (e.g. wave motion predominantly along one axis or plane). The lowest frequency mode for the closed cuboid is the axial mode, $f_{1,0,0}$, however, with one or two open ends the eigenfrequency is significantly lower. For a cuboid with one or two partly-open ends the eigenfrequency is similar to a closed cuboid. These general trends are followed when the wave motion is an axial mode with wave motion perpendicular to the open area (e.g. (a), (b) and (f) in Figure 4-11), whereas with wave motion perpendicular to end surfaces of the cuboid (e.g. Figure 4-11 (c)) this no longer occurs. For other modes, a specific rule is not found to describe characteristics based on the direction of wave motion and boundary conditions.

Although there is evidence that the different boundary conditions can significantly change the mode shape, it is concluded that when dealing with frequency bands that contain a sufficiently large number of modes, then subsystem response could be described statistically based on modal densities for local modes.



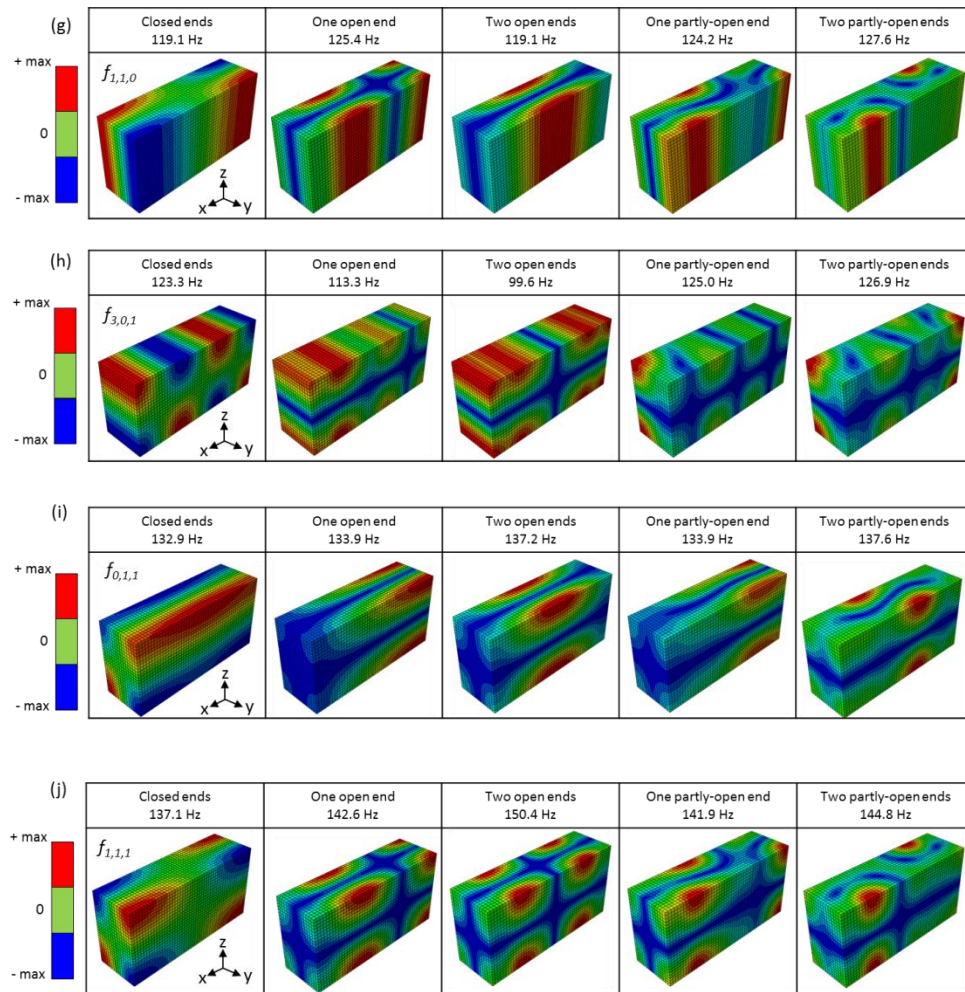


Figure 4-11. Modal responses for the five FEM models.

Consideration of the modal density is now required for the SEA model. The modal density is calculated by dividing the number of modes by the frequency bandwidth (e.g. one-third octave band) which is given by

$$n(f) = \frac{N}{B} \quad (3.5.1)$$

where N is the mode count and B is the bandwidth which is computed by

$$B = f_n^{high} - f_n^{low} \quad (3.5.2)$$

where f_n^{high} and f_n^{low} represent higher and lower band limits for the n^{th} one-third octave band which are defined by $f_n^{high} = 2^{1/6} f_n$ and $f_n^{low} = f_n / 2^{1/6}$ respectively.

The results in Figure 4-12 indicate that below 80 Hz there are either zero modes or one mode in a one-third octave band. However, at and above 80Hz there is at least one mode every band regardless of the boundary conditions. Above 125Hz the statistical estimates of modal density for a closed cuboid using Eq. (2.4.8) provide a reasonable estimate for the cuboid with different boundary conditions.

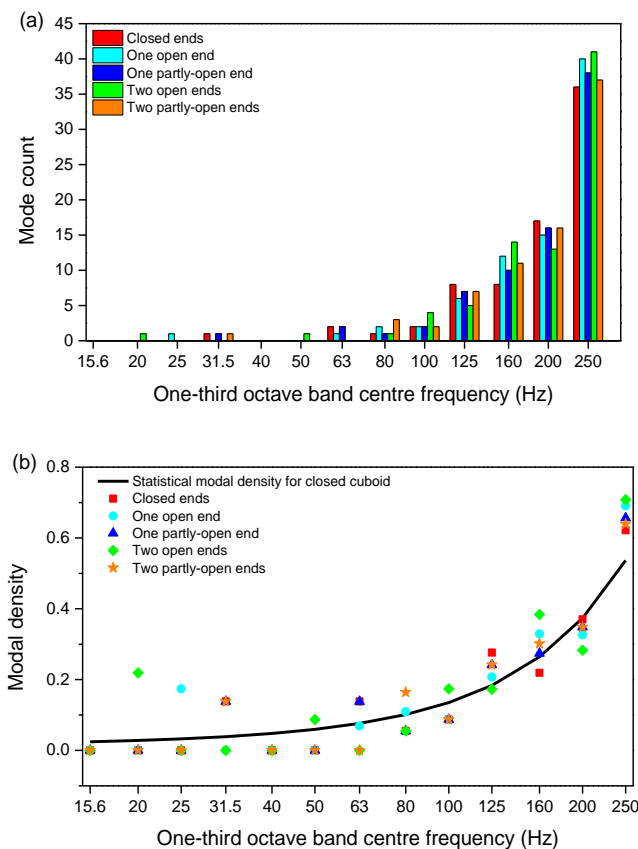


Figure 4-12. (a) Mode count and (b) Modal density of different boundary conditions in terms of one-third octave band centre frequency.

4.4.1.2 Clustering approach to define open-ended subsystems

The previous section indicates that modal density estimates based on a closed cuboid are reasonable for the various open-ended cuboids that form a corridor. In this section the definition of subsystems through the use of clustering analysis (Section 2.4) is introduced based on local modes. SEA subsystems are defined as a group of similar energy modes suggested by Lyon [8]. Modal analysis of the corridor requires consideration of three types of modes: axial, tangential and oblique modes.

The cell size used for clustering is a length of 1.5 m, 2.5 m and 5 m along the x-direction (i.e. the y- and z-direction dimensions are fixed by the corridor cross-section) for each one-third octave frequency band. The frequencies for which a half-wavelength is longer than the cell size are neglected (indicated by yellow shading in Figure 4-13) since the length of cells should be equal to or greater than a half-wavelength to ensure a modal response. Figure 4-13 shows the SEA subsystems that are defined by the clustering approach (referring to Section 2.4). The result depends on the choice of modes and the cell size. For many modes, however, the most frequent clustering outcome is a single system for which SEA is not relevant. Therefore, subdivision using equal lengths simple way of defining subsystems will be considered as a practical when it is necessary to predict a decrease in level along the corridor.

(a) Axial mode

Frequency (Hz)	Cell size (m)		
	1.25	2.5	5
63			30
80		30	30
100		30	30
125		30	30
160	30	30	30
200	30	30	d e g
250	30	30	30
315	30	30	30
400	30	30	g g
500	30	30	
630	30	30	g g
800	30	30	30
1000	30	g g	30
1250	30	30	30
1600	30	30	30

(b) Tangential mode

Frequency (Hz)	Cell size (m)		
	1.25	2.5	5
63			h d
80		30	30
100		30	30
125		30	30
160	a a a a a a a a a a a b a a a a a a a a a a	30	30
200	a a a a a a a a a a a b a a a a a a a a a a	30	e e e
250	30	30	30
315	30	30	30
400	30	30	30
500	30	30	30
630	30	30	30
800	30	30	30
1000	30	30	30
1250	30	30	30
1600	30	30	30

(c) Oblique mode

Frequency (Hz)	Cell size (m)		
	1.25	2.5	5
63			No modes
80		No modes	No modes
100		No modes	No modes
125		b b d b d f	30
160	c b b b b b b b b b b c	30	g g
200	a b a a a a a a a a b a a a a a a a a b a	30	30
250	a a a a a a a a a a a a b a a a a a a a a a a a	30	30
315	30	30	30
400	30	30	30
500	30	30	30
630	30	30	30
800	30	30	30
1000	30	30	30
1250	30	30	30
1600	30	30	30

Figure 4-13. Subsystem lengths defined using the clustering approach using 1.25m, 2.5m and 5m cell sizes for axial, tangential and oblique modes (a=1.25m, b=2.5m, c=3.75m, d=5m, e=10m, f=12.5m, g=15m and h=25m).

4.4.2 SEA

An SEA model is now used to investigate sound transmission along the empty cuboid. Such an elongated space using SEA has been studied in industrial field [75,76]. The empty cuboid in Figure 4-14 is initially subdivided into six coupled subsystems with equal volume. This is a practical modelling choice for simplicity, rather than the approach based on clustering. In the source subsystem the sound pressure level is calculated assuming a diffuse sound field using

$$SPL = SWL + 10 \lg \frac{4}{A} \quad (3.5.3)$$

where SWL is sound power level (re 10^{-12} W) in dB and A is the absorption area of the subsystem.

The empty cuboid SEA model is represented in Figure 4-14 with parameters and geometry given in Table 4-4. The corridor boundaries are considered to be rigid with an absorption coefficient $\alpha=0.3$ on all boundaries. A point source is positioned at the end of the corridor in subsystem 1 at the coordinate (0.25m, 0.25m,0.25m).

ODEON is used to calculate average sound pressure levels in each subsystem. A regular grid is used to specify points at which calculations of the sound pressure level are required. The grid spacing is 0.25 m in the x- and y- directions but 0.5 m in the z- direction. All reflected rays in the model are considered to be uncorrelated for both specular and diffuse reflections; this is suitable for the assumptions made in the SEA model.

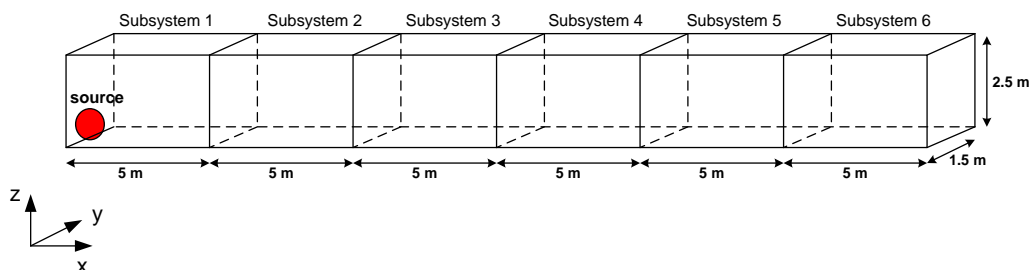


Figure 4-14. Empty source position and the numbering corridor model indicating the subsystem.

Power input (W)	0.01 W
Air density, ρ_0 (kg/m ³)	1.21
Speed of sound, c_0 (m/s)	343
Absorption coefficient, α	0.1, 0.3, 0.6

Table 4-4. Input parameters for the corridor models.

The decrease in sound pressure level from the ray tracing output is calculated from the difference between the energy of subsystem 1 and the other subsystems by spatial averaging of all grid points in each subsystem. It is calculated as a function of the distance along the corridor from subsystem 1 to 6. Two different SEA models are considered with ILFs and CLFs defined in Table 4-5.

Table 4 5The loss factors in SEA model A1 and A2 are calculated using Eq. (2.4.9), Eq. (2.4.11) and Eq. (2.4.12). The ILF of the subsystems at the ends of the corridor (subsystems 1 and 6) are considered as two-dimensional volumes in SEA model A1 and two- and three-dimensional volumes in SEA model A2.

Empty cuboid				
Subsystem	Classical SEA Model No. A1 2D ILF. All CLFs are defined as 3D		Classical SEA Model No. A2 2D and 3D ILF. All CLFs are defined as 3D	
	ILF/Modal density	CLF calculated for use with consistency relationship	ILF/Modal density	CLF calculated for use with consistency relationship
1	2D	1→2	3D	1→2
2	2D	2→3	2D	2→3
3	2D	3→4	2D	3→4
4	2D	4→5	2D	4→5
5	2D	5→6	2D	-
6	2D	-	3D	6→5

Table 4-5. Empty cuboid model: Assignment of coupling and internal loss factors for two different SEA models.

The decrease in SPL for both reflections with respect to three different absorption coefficients are shown in Figure 4-15. The general trend is that SEA model A2 shows less agreement with ray tracing than A1, especially for subsystem 5. This suggests that treating all subsystem ILFs as 2D rather than 3D is more appropriate. A comparison of the diffuse field SPL in the source subsystem from Eq. (3.5.3) with the two SEA models is shown in Table 4-6. This shows that the predicted SPL in the source subsystem with SEA model A1 is in closer agreement with the diffuse field SPL than SEA model A2, i.e. when the subsystem is treated as 2D. With low absorption coefficient ($\alpha=0.1$), the results shown that the ray tracing with specular reflection is in good agreement with the propagating 2D model in Figure 4-15 (a) but not with SEA model A1, and vice versa with diffuse reflection in Figure 4-15 (b). This indicates that with low absorption and specular reflections, SEA overestimates the decrease in SPL along the corridor. The SEA prediction shows better agreement with ray tracing using diffuse rather than specular reflections as the former satisfies SEA assumptions on a diffuse sound field.

With $\alpha=0.3$, Figure 4-15 (c) and (d), the ray tracing and the propagating 2D models are in close agreement with each other for specular and diffuse reflections. This suggests that the relatively simple propagating 2D is still reasonable compared to SEA. The fact that classical SEA gives different results depending on the choice of ILFs indicates that this parameter is critical. As discussed in the previous section for the corridor with high absorption coefficient, the direct sound from the point source is necessary to increase the accuracy of the prediction model. Figure 4-15 (e) and (f) for $\alpha=0.6$ also show disagreement between ray tracing and SEA. With diffuse reflections, inclusion of the direct field is likely to be more important.

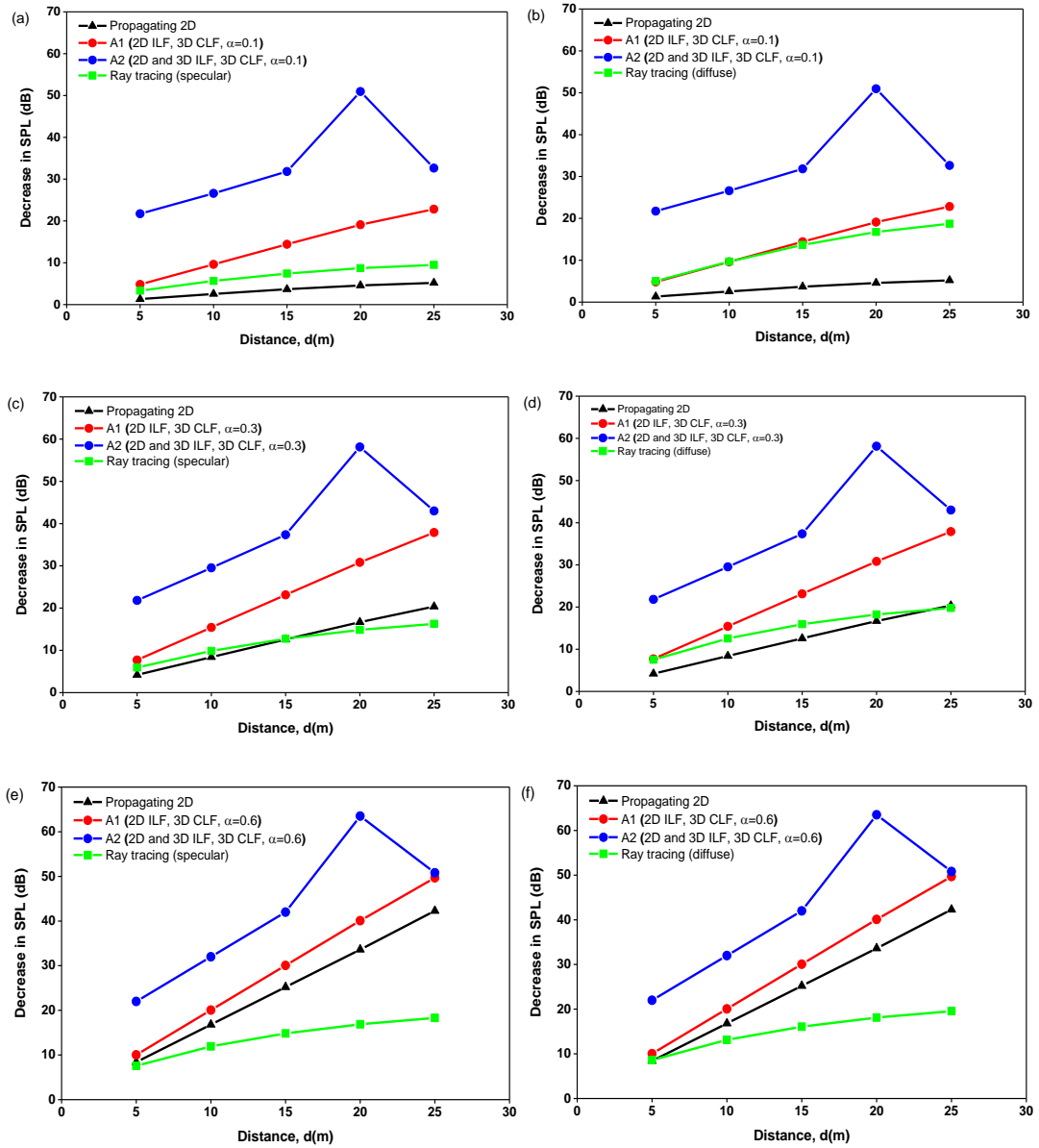


Figure 4-15. Empty cuboid model: Decrease in sound pressure level for empty cuboid SEA models with specular reflections and diffuse reflections with different absorption coefficients for the boundaries. (a,b) $\alpha=0.1$, (c,d) $\alpha=0.3$, (e,f) $\alpha=0.6$.

Difference between SEA and diffuse field (dB)	SEA Model No. A1	SEA Model No. A2
Subsystem 1 ($\alpha=0.1$)	0.5	2.8
Subsystem 1 ($\alpha=0.3$)	-0.2	1.3
Subsystem 1 ($\alpha=0.6$)	-0.3	0.8

Table 4-6. Empty cuboid model: Difference between SEA and diffuse field SPL in the source subsystem.

To predict the decrease in SPL regardless of the absorptivity of surfaces it is concluded that all subsystems should be treated as two- rather than three-dimensional. This finding is supported by the finding that the predicted SPL in the source subsystem with SEA model A1 is in closer agreement with the diffuse field SPL than SEA model A2. The overestimated decrease in SPL along the corridor with SEA indicates that the SPL in other subsystems is not accurately predicted due to incorrect coupling loss factors. Therefore SEA could potentially be improved by considering other methods to determine the loss factors.

4.4.3 Forced SEA

For an elongated cuboid space such as a corridor, energy losses occur over distance despite there being no physical boundary between them. This indicates potential difficulties in assigning internal and coupling loss factors in an SEA model. Craik [77] has shown that one possibility for a corridor is to force the SEA model to follow the propagating 2D model of Redmore and Flockton (see Section 4.3).

Craik's approach suggests that the corridor system can be subdivided into arbitrary subsystems. For example, assume three adjacent subsystems i , j , and k , (e.g. subsystems 2, 3 and 4 in Figure 4-14) for which the power balance for subsystem j can be written as

$$E_i \eta_{ij} + E_k \eta_{kj} = E_j (\eta_{jj} + \eta_{ji} + \eta_{jk}) \quad (3.5.4)$$

With subdivision of the corridor into subsystems of equal length, d , then all the coupling loss factors between subsystems will be equal and the energy ratio between adjacent subsystems is such that $E_i/E_j = E_j/E_k$. Therefore, Eq. (3.5.4) can now be written in terms of η_{ii} as the internal loss factor which applies to each subsystem and η_{ij} as the coupling loss factor between all adjacent subsystems this is given by

$$\frac{\eta_{ii}}{\eta_{ij}} = \frac{E_i}{E_j} + \frac{E_j}{E_i} - 2 \quad (3.5.5)$$

If the attenuation between adjacent subsystems is not too large, Eq. (3.5.5) can be approximated to

$$\frac{\eta_{ii}}{\eta_{ij}} \approx \left(\ln \frac{E_i}{E_j} \right)^2 \quad (3.5.6)$$

Figure 4-16 describes an approximate ratio that can be substituted for the ratio between internal loss factor and coupling loss factor when the attenuation between adjacent subsystems is less than 5 dB for which the errors between the exact loss factor ratio and the approximate ratio are less than 0.5dB.

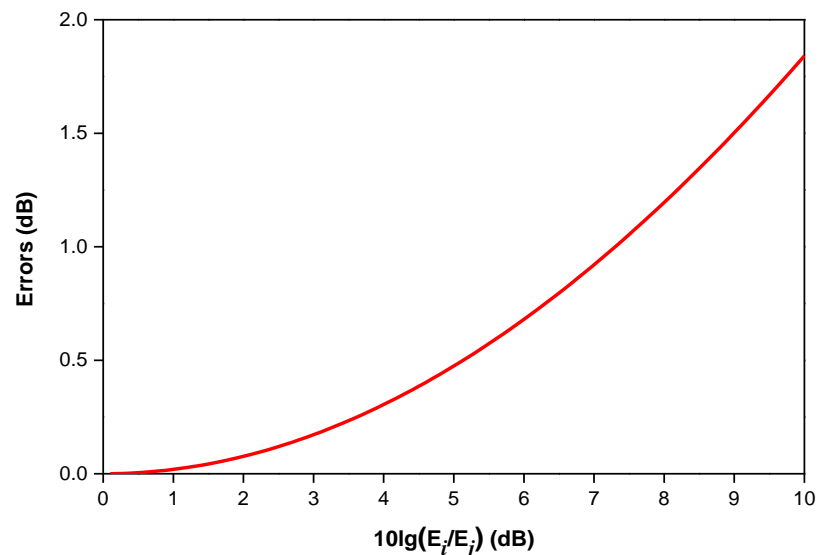


Figure 4-16. Forced SEA model: Errors between exact and approximate energy ratio in terms of the energy decrease between adjacent subsystems.

After travelling a distance, d , the sound energy decrease in decibels, Δ , between any two subsystems along the corridor is $d\Delta = 10\lg(E_i/E_j)$ giving

$$\frac{\eta_{ii}}{\eta_{ij}} = \left(\frac{\ln 10}{10} d\Delta \right)^2 \quad (3.5.7)$$

where Δ is attenuation/m given by [49]

$$\Delta = \frac{10}{\ln 10} \frac{\pi}{8} \frac{U\alpha}{L_y L_z} \quad (3.5.7)$$

For the internal loss factor there are two options:

- 1) Use an internal loss factor corresponding to a 2D sound field (Eq. (2.4.11))
- 2) Use an internal loss factor corresponding to a 3D sound field (Eq. (2.4.12))

This results in two options to calculate a coupling loss factor that is a function of the internal loss factor as described by

- 1) A coupling loss factor calculated assuming an internal loss factor for a 2D sound field from Eq. (2.4.11) and Eq. (3.5.7)

$$\eta_{ij} = \frac{100c_0 U \alpha}{(\ln 10)^2 \Delta^2 d^2 \pi \omega L_y L_z} \quad (3.5.8)$$

where α is the absorption coefficient for the surfaces that form each 2D subsystem (i.e. side walls, floor and ceiling).

- 2) A coupling loss factor calculated assuming an internal loss factor for a three-dimensional sound field from Eq. (2.4.12) and Eq. (3.5.7)

$$\eta_{ij} = \frac{100c_0 S_T \bar{\alpha}}{(\ln 10)^2 \Delta^2 d^2 4\omega V_i} \quad (3.5.9)$$

where $\bar{\alpha}$ is the average absorption coefficient (NB. For an end subsystem, this is the average of the end all, side walls, floor and ceiling).

The forced SEA models are considered with ILFs in terms of 2D and 3D spaces to calculate CLFs between subsystems shown in Table 4-7. The CLFs for forced SEA are calculated with Eq. (3.5.8) and Eq. (3.5.9). Two options were considered for the ILF of a 3D subsystem, one assuming that there was an acoustically transparent wall

between subsystems with $\alpha=1.0$, and another ignoring the absorption of this acoustically transparent wall.

As in the previous section, three absorption coefficients ($\alpha=0.1, 0.3$ and 0.6) are used to assess the forced SEA model in Figure 4-17. Figure 4-17 (a) and (c) show that the forced SEA models B1 and B3 are in close agreement with the propagating 2D model whereas SEA model B2 overestimates the decrease in SPL. When the boundaries have low absorption, the forced SEA model is closer to ray tracing with specular reflections than with diffuse reflection. The assumption for the relationship between the ILF and CLF (Eq.(3.5.7)) applies when the energy ratio between subsystems is close to the decrease predicted by Eq. (2.3.4). The inclusion of the transparent wall in the subsystem ILF in SEA model B2 leads to an underestimate of the coupling. In contrast, with high absorption in Figure 4-17 (c), three of the forced SEA models show close agreement with the propagating 2D since sufficient absorption of the energy by the boundaries leads to the energy decrease between subsystems. However, it is not necessary or appropriate to use the forced SEA model because sound propagation is dominated by the direct field as shown back on Figure 4-2.

Subsystem	Forced SEA Model No. B1 2D ILF	Forced SEA Model No. B2 3D ILF including acoustically transparent walls with absorption coefficient $\alpha=1.0$ between subsystems	Forced SEA Model No. B3 3D ILF excluding acoustically transparent walls
	ILF/Modal density		
1	2D	3D	3D
2	2D	3D	3D
3	2D	3D	3D
4	2D	3D	3D
5	2D	3D	3D
6	2D	3D	3D

Table 4-7. Empty cuboid model: Coupling and internal loss factors for two different forced SEA models.

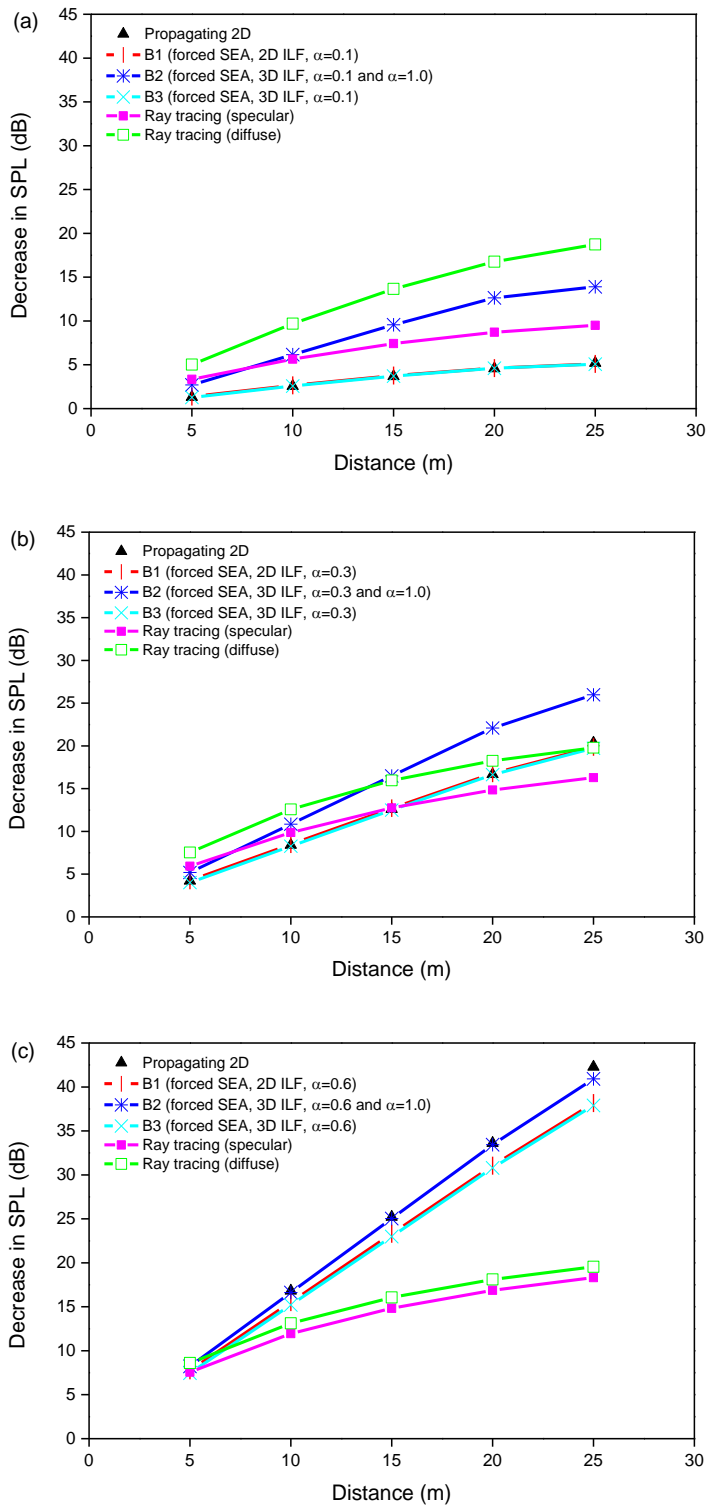


Figure 4-17. Empty cuboid model: Decrease in sound pressure level for forced SEA model with absorption coefficient for the boundaries of (a) 0.1, (b) 0.3 and (c) 0.6.

4.4.4 SEA with direct field and forward propagation

From Section 4.3.2, there is evidence that the direct field influences the accuracy of the prediction model when the space has highly absorptive boundaries (specular or diffuse reflections). In this section, three types of forward propagation from the point source to receiver points are considered. The direct field (referred to as a Type 1 sound field) is considered alongside Types 2 and 3 involving reflections from corridor surfaces as indicated in Figure 4-18.

For Types 1, 2 or 3, ray tracing is used to calculate the sound field at each point by changing the absorption of different boundaries to be anechoic (i.e. $\alpha=1$) as indicated in Figure 4-18. Type 1 describes the rays that propagate directly from the point source to the receiver (i.e. the direct field), Type 2 describes rays which only reflect from boundaries in subsystem 1 before reaching the receiver and Type 3 describes rays which are reflected at least once outside subsystem 1 before reaching the receiver. The sound pressure level measured for Types 1, 2 and 3 are averaged in each subsystem and energetically added to the predicted sound pressure level from SEA.

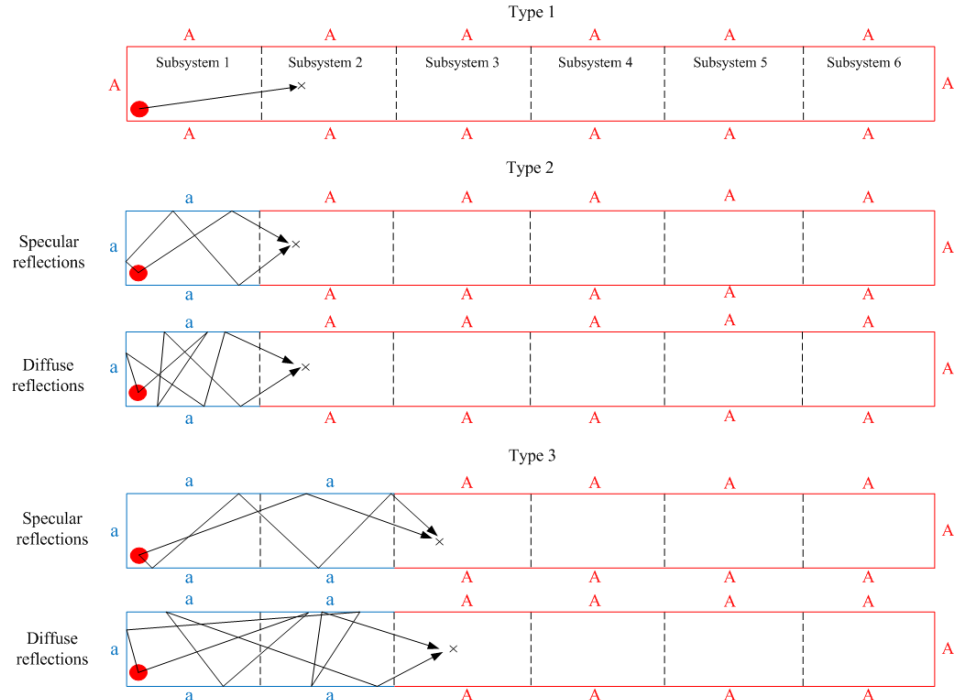


Figure 4-18. Three different types of forward propagation in a corridor: (Key: ‘a’ indicates boundaries with the actual absorption coefficient, ‘A’ indicates anechoic boundaries where $\alpha=1$, ‘x’ indicates a grid point in the receiving subsystem).

It was noted in Section 4.4.2 that SEA using 2D ILFs was appropriate; hence this approach is now carried out with the inclusion of Types 1, 2 and/or 3. The results are shown in Figure 4-19 for which addition of the direct field and forward propagation into SEA significantly improves the estimate. For specular and diffuse reflections, Figure 4-19 (a) and (b) show that incorporating the direct field (Type 1) into SEA only gives a small improvement in the agreement with ray tracing. For specular and diffuse reflections Figure 4-19 (e) and (f) then shows that including all type of forward propagation into SEA gives close agreement with ray tracing assuming specular reflections (a maximum of 3 dB difference), but that there is closer agreement with diffuse reflections. For diffuse reflections, Figure 4-19 (c) and (d) show that SEA with direct and forward propagation Type1 and Type 2 improves the estimate similarly to the combination of Type1, Type2 and Type3, whereas the inclusion of Type 3 is necessary to achieve close agreement when there are specular reflections. This is because specular reflection primarily propagates sound waves away from the source down the corridor, but the rays can come back towards the source with diffuse reflections. This mechanism leads to different improvement of SEA. In Section 4.3.2, it was shown that inclusion of the direct field (Type 1) can be important but the above results suggest that there are more factors that can be considered to improve the accuracy of SEA. It is seen here that SEA models incorporating the three types of forward propagation show reasonable agreement with ray tracing for both specular and diffuse reflections.

Predictive SEA assumes weakly coupled subsystems and (apart from non-resonant transmission of airborne sound across a plate separating two rooms) these models tend not to involve indirect coupling. However, as the three types of forward propagation have been shown to be important it is now appropriate to consider how the direct field and forward propagations could be incorporated in an SEA model as a form of indirect coupling. One possibility is to use Experimental SEA (ESEA) with ray tracing output to determine direct and indirect coupling loss factors as well as total loss factors. This is considered in the next section.

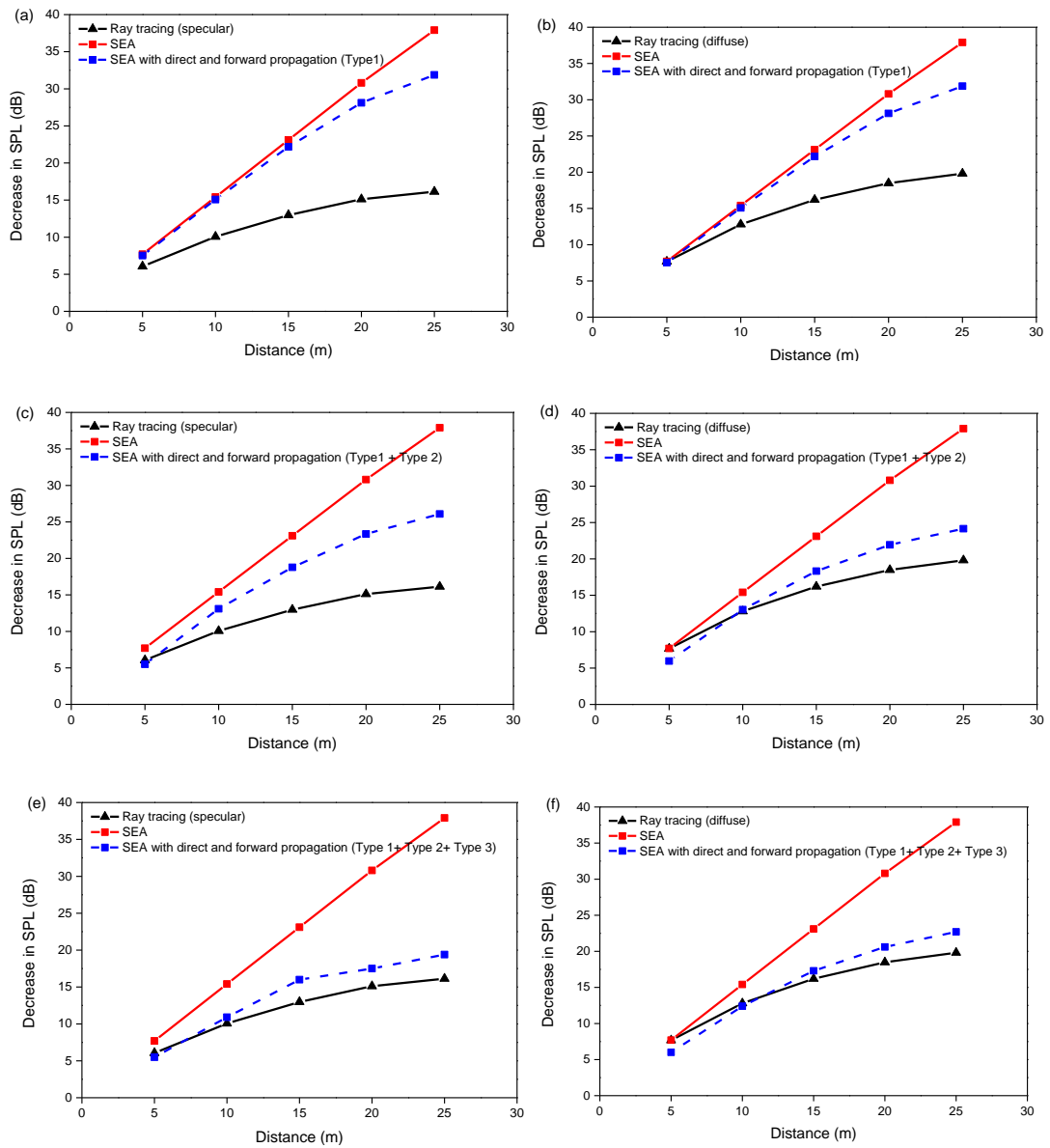


Figure 4-19. Empty cuboid model (all corridor boundaries have $\alpha=0.3$): Comparison of SEA, SEA with direct field and forward propagation and ray tracing with specular reflections and diffuse. (a,b): Type1, (c,d): Type1+Type2, (e,f): Type1+Type2+Type3.

4.5 SEA using ESEA

An alternative approach to SEA is to use ESEA (in the forms of GESEA and AESEA) to determine loss factors which can then be incorporated into an SEA model. Before using ESEA, verification of this approach has been carried out to confirm the accuracy of GESEA for an artificial set of SEA loss factors (although these could be considered indicative of what might be expected for a corridor). Firstly, three artificial loss factor matrices $[\eta]$ were created for solution with classical SEA to give subsystem energies – see Eq.(3.6.1), Eq.(3.6.2) and Eq.(3.6.3). For ease of understanding, loss factors are shown in decibels although the actual matrix calculations used linear values. $[\eta]_A$ is fully filled with direct and indirect CLFs, $[\eta]_B$ is composed of direct and indirect CLFs with regard to the subsystem 1, and $[\eta]_C$ is composed of only direct CLFs.

$$[\eta]_A = \begin{bmatrix} 110 & 100 & 90 & 87 & 84 & 81 \\ 100 & 110 & 100 & 90 & 87 & 84 \\ 90 & 100 & 110 & 100 & 90 & 87 \\ 87 & 90 & 100 & 110 & 100 & 90 \\ 84 & 87 & 90 & 100 & 110 & 100 \\ 81 & 84 & 87 & 90 & 100 & 110 \end{bmatrix} \quad (3.6.1)$$

$$[\eta]_B = \begin{bmatrix} 110 & 100 & 90 & 87 & 84 & 81 \\ 100 & 110 & 100 & 0 & 0 & 0 \\ 90 & 100 & 110 & 100 & 0 & 0 \\ 87 & 0 & 100 & 110 & 100 & 0 \\ 84 & 0 & 0 & 100 & 110 & 100 \\ 81 & 0 & 0 & 0 & 100 & 110 \end{bmatrix} \quad (3.6.2)$$

$$[\eta]_c = \begin{bmatrix} 110 & 100 & 0 & 0 & 0 & 0 \\ 100 & 110 & 100 & 0 & 0 & 0 \\ 0 & 100 & 110 & 100 & 0 & 0 \\ 0 & 0 & 100 & 110 & 100 & 0 \\ 0 & 0 & 0 & 100 & 110 & 100 \\ 0 & 0 & 0 & 0 & 100 & 110 \end{bmatrix} \quad (3.6.3)$$

These are artificial loss factor matrices for predictive SEA that are composed of different direct and indirect CLFs where the values are shown in dB re 10^{-12} . The entries for the energy matrix $[E]$ to be used in ESEA are calculated from the artificial

loss factor matrix using classical SEA. The validity of the loss factor matrices obtained from the calculated energy balance matrix are then assessed by calculating the errors in dB between estimated and original loss factors. Errors for the coupling loss factors were very low, typically 0.01dB. This indicates that ESEA predicts highly reliable coupling loss factors if the energy balance matrix is correctly estimated.

In the next stage, the energy balance matrix has been obtained using the ray tracing models with specular and diffuse reflection by relocating the point source into every subsystem in turn to carry out PIM in the empty cuboid for the ray tracing, the source positions in each subsystem are shown in Figure 4-20.

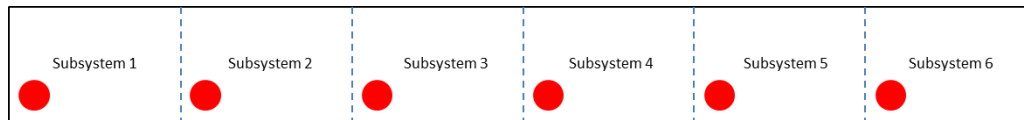


Figure 4-20. Empty cuboid model: Point source locations for the power injection method (PIM)

The direct coupling loss factors of η_{12} and η_{23} obtained from GESEA and AESEA are compared with that of predictive SEA in Figure 4-21. Note that full matrix and approximate AESEA give the same result so no distinction is made here. This shows that the coupling loss factors with specular reflections tend to be higher than one with diffuse reflections. Nevertheless, estimated coupling loss factors are both within 3dB of the predicted coupling loss factors.

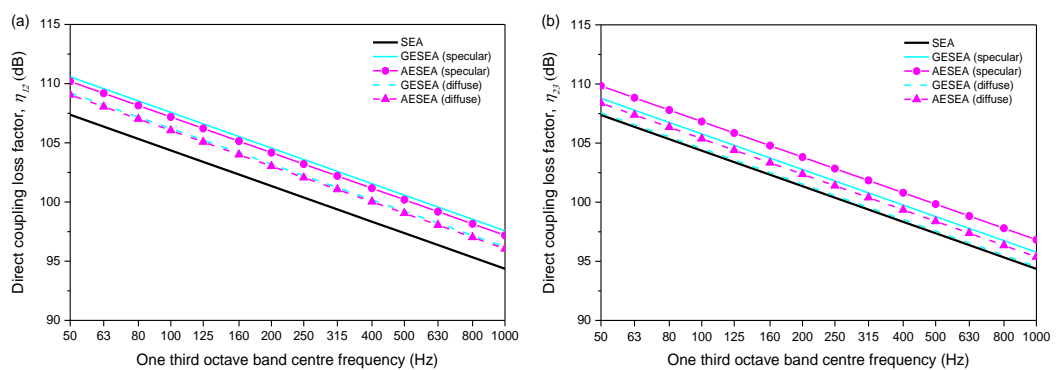


Figure 4-21. Comparison of direct coupling loss factors of (a) η_{12} and (b) η_{23} estimated from ESEA with predictive SEA.

The results of the SEA models incorporating CLFs from ESEA from ray tracing are shown in Figure 4-22. The SEA models using GESEA CLFs show close agreement with ray tracing assuming specular or diffuse reflections. Invalid CLFs with negative values determined from GESEA are modified by the rules defined in Section 2.4.2 before being incorporated in the SEA model (see Appendix A). For subsystems 3, 4, 5 and 6, SEA incorporating CLFs determined from full matrix AESEA shows closer agreement with predictive SEA than SEA incorporating CLFs determined from approximate AESEA for the ray tracing model assuming specular reflections. This indicates that there is indirect coupling between non-adjacent subsystems. The difference between CLFs determined from full matrix AESEA and approximate AESEA is <3dB. With diffuse reflections, SEA using AESEA CLFs (full matrix or the approximate version) underestimates the sound transmission compared to the ray tracing results. In general, the results indicate that predictive SEA is not able to accurately predict sound transmission between subsystems unless the indirect CLFs between physically disconnected subsystems are included.

As a result, the consideration of indirect CLFs determined from GESEA is necessary to predict appropriate energy flow between subsystems when propagation via Types 1, 2 and 3 (as defined in Section 4.4.4) are dominant.

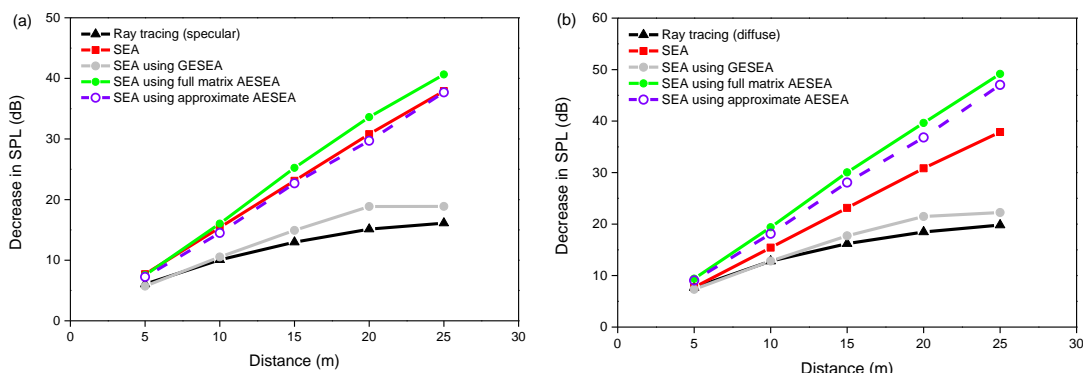


Figure 4-22. Empty cuboid model: Comparison of SEA using ESEA with ray tracing (a) with specular reflections and (b) with diffuse reflections ($\alpha=0.3$).

4.6 Case study: Experimental work on an empty corridor

An assessment of the ODEON model is now carried out to investigate which absorption coefficients determined from the two different approaches in Section

4.3.3 should be considered for the real corridor. Measurements were carried out in one-third octave bands but the ray tracing was carried out using octave band centre frequencies. Therefore, the measured sound pressure levels were converted to octave bands for comparison with ray tracing.

Figure 4-23 compares the decrease in SPL from measurements with ray tracing. The ray tracing model uses the absorption coefficients estimated by curve fitting with the propagating 2D model (see Table 4-1 in Section 4.3.3). It is seen that ray tracing with specular or diffuse reflections that use this average absorption coefficient do not show close agreement with the measurements. The curve fitting approach tends to overestimate the absorption coefficient. A reason for this can be found in Section 4.3.2, which considered the comparison between the propagating 2D model and ray tracing. When the absorption coefficient was 0.1, then ray tracing with diffuse reflections tended to overestimate the decrease in the sound pressure level although with specular reflection it was much closer to the propagating 2D model. This also occurs in Figure 4-23 where specular reflections generally show closer agreement with increasing frequency than diffuse reflections but the agreement increases when the absorption coefficient increases with increasing frequency (see Figure 4-8). Ray tracing with diffuse reflection does not provide a reasonable estimate across the frequency range.

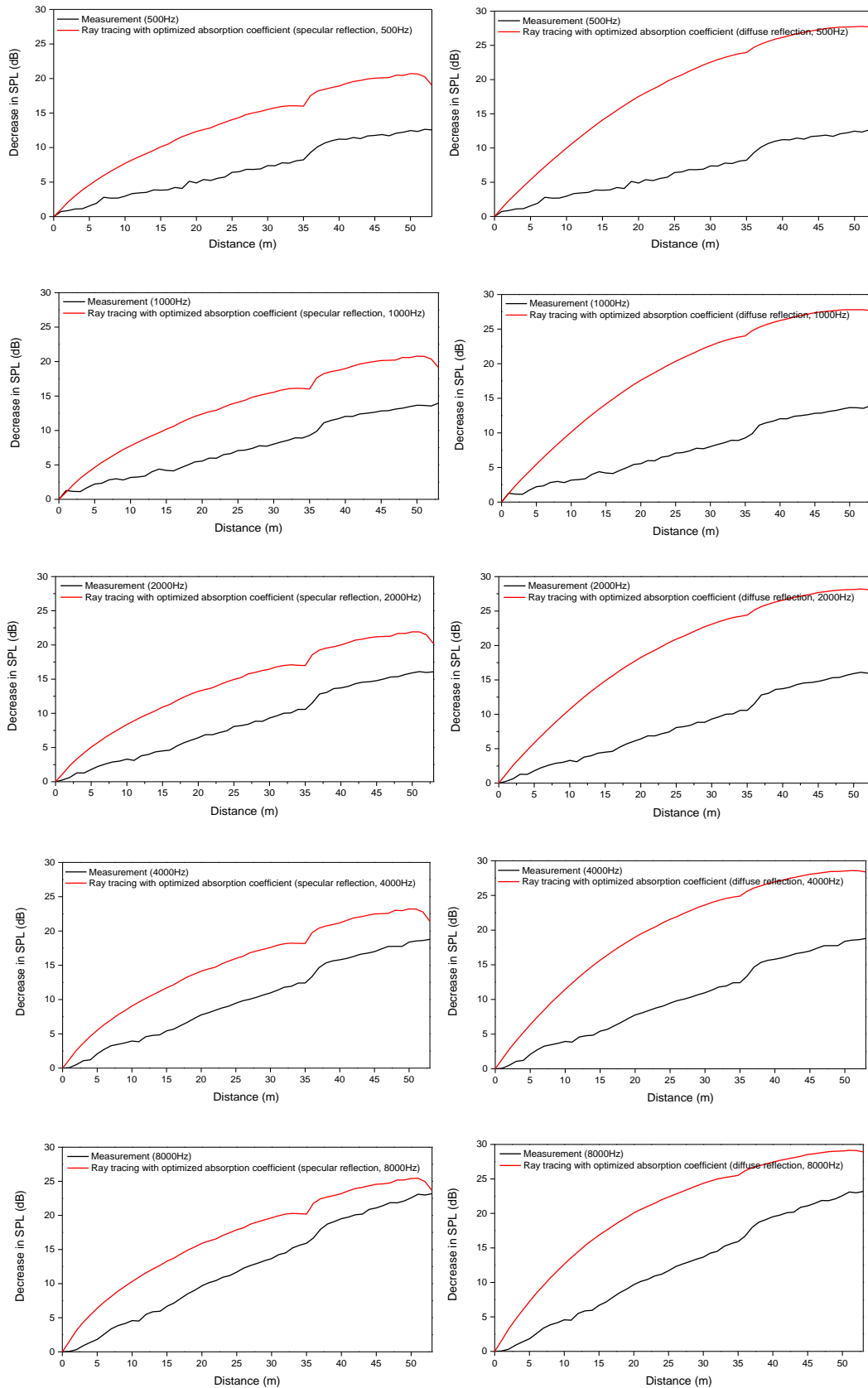


Figure 4-23. Real corridor: Comparison of measurements with ray tracing using average absorption coefficients estimated by curve fitting with the propagating 2D model.

Due to the lack of agreement discussed above when using absorption coefficients estimated from curve fitting, the measurements are now compared with ray tracing using absorption coefficients from the ODEON database in Figure 4-24. This shows that ray tracing assuming specular reflections is in reasonable agreement with measurements up to 4000 Hz. In this frequency range the average absorption coefficients are between 0.04 and 0.13, which are significantly lower than estimated by curve fitting. At 8000 Hz, the ray tracing assuming specular reflections underestimates the decrease in the sound pressure level with increasing distance whereas with diffuse reflections it shows good agreement with the measurements. This indicates that the sound field approximates a diffuse field with increasing frequency. The prediction model with specular reflections shows good agreement with measurement. However, the cross-section of the corridor is non-uniform due to window reveals, columns and the frame of the fire door, which is included as an extra surface area to predict the average absorption coefficient. In addition, the ‘standard materials’ in the ODEON database do not necessarily represent the actual materials used in this study. Despite these issues, these data provide a reasonable estimate of the decrease in SPL which is better than the estimate based on curve fitting.

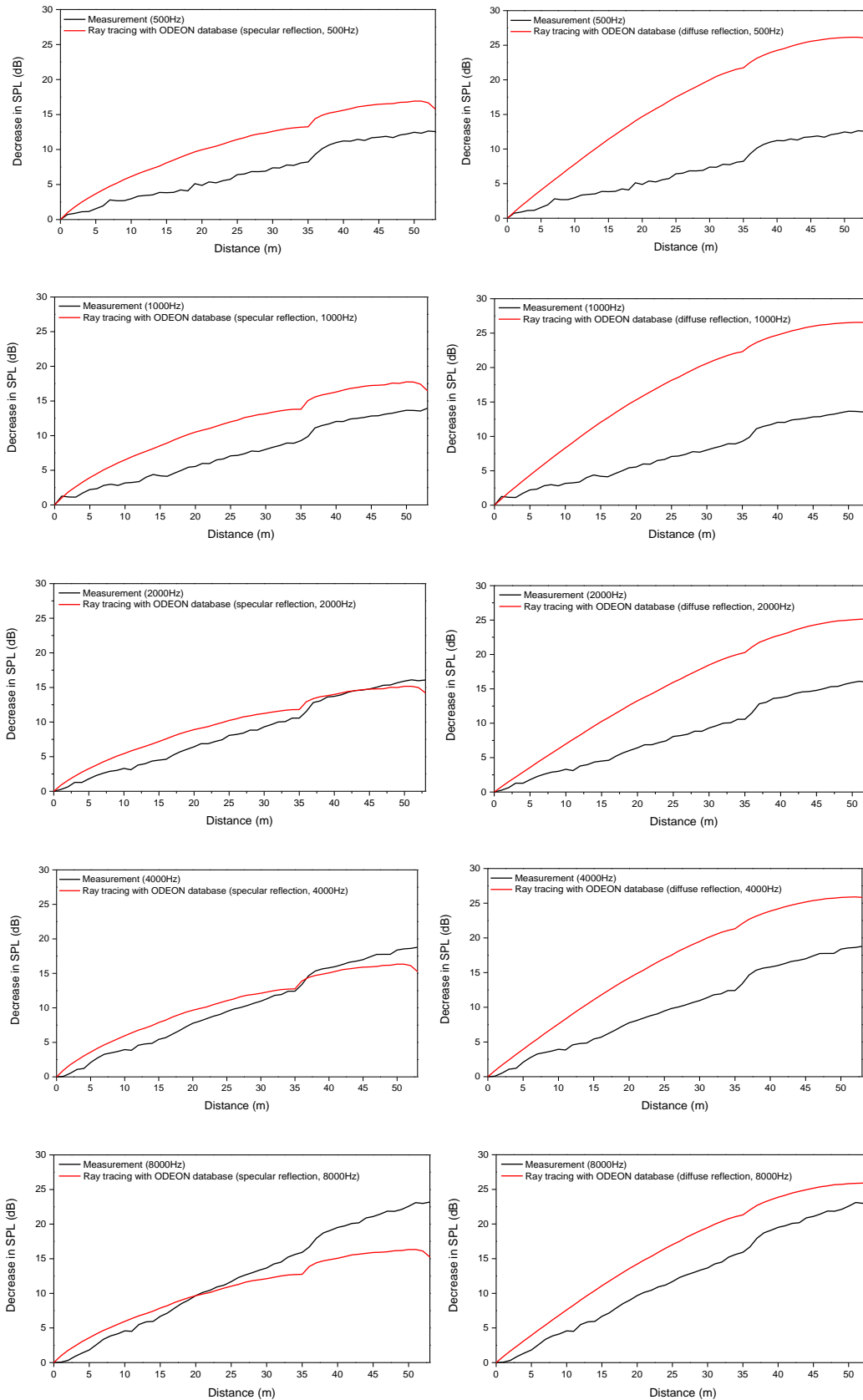


Figure 4-24. Real corridor: Comparison of measurements with the ray tracing using average absorption coefficients of standard material (from ODEON database) in the decrease in SPL along the corridor.

Predictive SEA is now used to model the corridor composed of six subsystems of 6m length. The comparator is ray tracing assuming specular reflection which is justified by the agreement in Figure 4-24. The ray tracing model of the corridor is from the end of the corridor up to the fire door which is at the 36m point (due to the change in corridor cross-section at the fire door which was discussed in Section 4.3.2). Average absorption coefficients calculated from standard materials were assigned to all corridor surfaces except for the window glazing. The reason for this is that the absorption coefficient of the glass is significantly different from the other materials at high frequency; hence the absorption coefficient for windows was applied to the glazed area. ESEA models based on GESEA and AESEA were implemented by applying PIM in ray tracing to obtain the energies required to determine indirect and direct CLFs.

Figure 4-25 shows the predicted decrease in SPL along the corridor in SEA models and ray tracing assuming specular reflections using absorption coefficients from the ODEON material database without windows in octave bands (see Section 4.3.3). Four octave bands are shown covering the frequency range from 500 to 4000Hz. Predictive SEA, SEA using CLFs estimated from full matrix AESEA or approximate AESEA are similar and do not show agreement with ray tracing. In contrast, ray tracing is in close agreement with SEA using GESEA CLFs and measurements on the real corridor. This indicates that indirect coupling loss factors are required to simulate forward propagation from the source to receiver subsystems. The absorption coefficients used for the ray tracing do not exceed 0.1 at and above 500Hz; hence the direct field is unlikely to be significant. The sound field predicted by ray tracing assuming specular reflections differs from diffuse reflections when $\alpha \approx 0.1$ at low- and mid-frequencies as seen previously in Figure 4-15 (a). However, in the real corridor the reflections are likely to become closer to diffuse reflections at frequencies at and above 8000Hz as indicated in Figure 4-24. Similarly, Figure 4-26 shows that ray tracing with diffuse reflections is in close agreement with measurements on the real corridor as well as with classical SEA. This indicates that with diffuse reflections and a low absorption coefficient, $\alpha \leq 0.1$ then classical SEA can reasonably predict sound transmission whereas SEA with CLFs estimated from AESEA with diffuse reflections tends to overestimate the decrease in SPL.

The agreement between ray tracing and SEA using CLFs estimated from GESEA indicates that indirect coupling loss factors need to be included in SEA.

In conclusion, it is not feasible to estimate absorption coefficients using curve fitting based on the propagating 2D model as this tends to overestimate the values. The ray tracing assuming specular reflections using the absorption coefficient from ODEON material database gives closest agreement with the measurements although ray tracing assuming diffuse reflections shows better agreement at 8000Hz. Predictive SEA is not appropriate to predict the decrease in SPL along the corridor when sound field is determined by specular reflections, however, SEA can be improved by incorporating CLFs from GESEA which includes indirect coupling loss factors. This suggests that the parameters leading to additional energy transmission between subsystems can be compensated by considering indirect coupling loss factors from GESEA. At present, it is not possible to predict these indirect coupling loss factors.

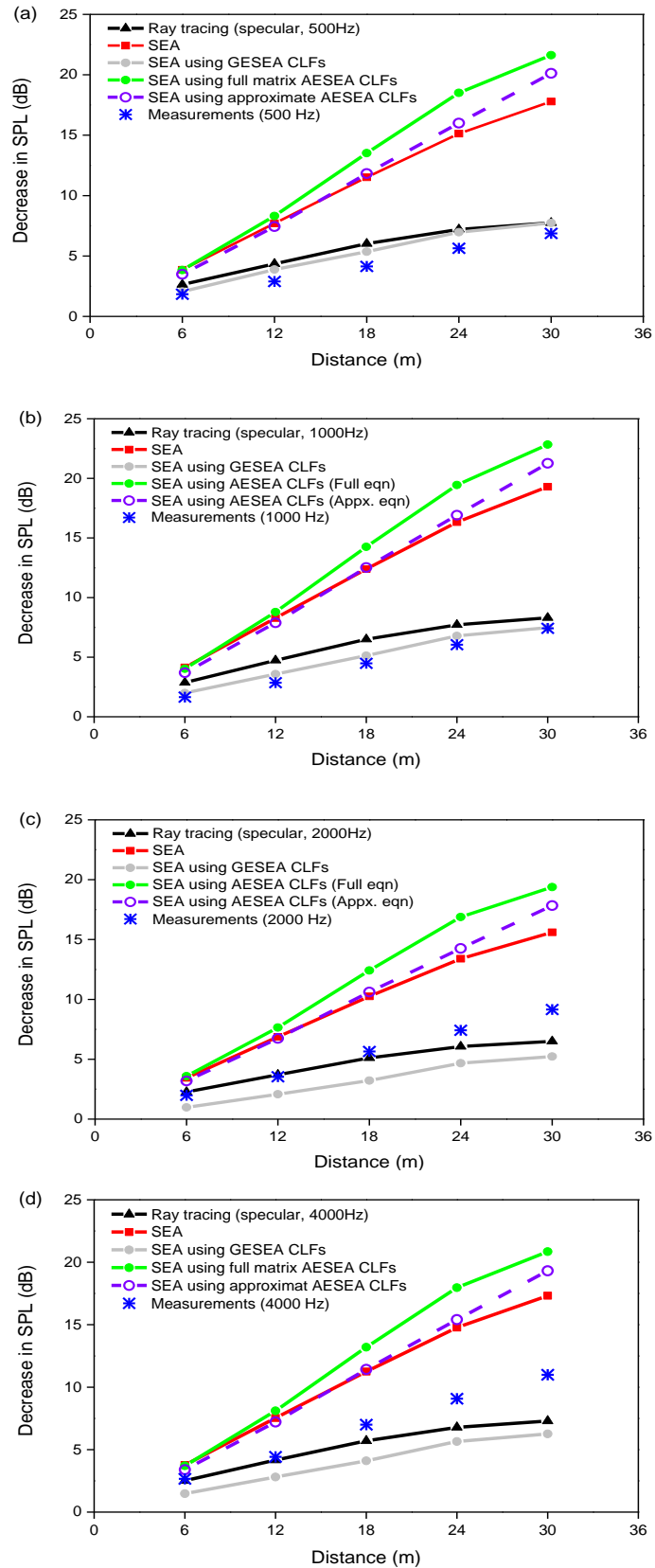


Figure 4-25. Real corridor: Comparison of measurements, SEA models, and ray tracing with specular reflection using absorption coefficients for the boundaries from the ODEON material database without windows (in octave bands from 500 to 4000Hz).

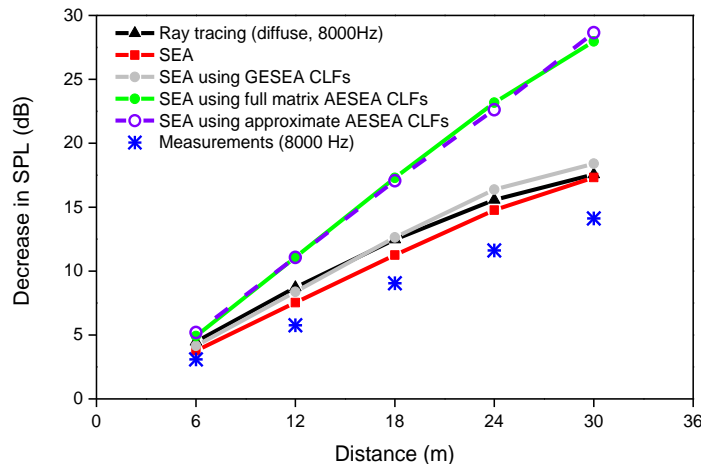


Figure 4-26. Real corridor: Comparison of measurements, SEA models, and ray tracing with diffuse reflections using absorption coefficients for the boundaries from the ODEON material database without windows for the 8000Hz octave band.

4.7 Conclusions

In this chapter, the prediction of sound propagation along an elongated cuboid, representing a long empty cuboid, has been considered using ray tracing, direct and diffuse field models, SEA and ESEA.

A propagating 2D model has been considered which assumes a two-dimensional diffuse sound field propagating along the corridor when the source is at one end. This model overestimates sound transmission for low levels of surface absorption where the direct field is insignificant, and underestimates sound transmission for high levels of surface absorption where the direct field is significant. However, there is an intermediate level of absorption for the surfaces that will give reasonable agreement with this model. By incorporating the direct field in this propagating 2D model it is possible to increase the agreement with ray tracing except for low level of surface absorption when there are diffuse reflections. However, this approach is not particularly useful when sound transmission needs to be predicted in larger SEA models which combine the corridor and the rooms behind door that face into the corridor. For this reason, SEA models were considered in this chapter.

SEA requires subdivision of the corridor into cuboid subsystems with one or two opening at each end. FEM models have been used to calculate the eigenfrequencies of these subsystems which indicates that above the first few modes, the mode counts could be determined from statistical estimates. Two possibilities to define these

subsystems have been considered: (1) a practical subdivision into equal length subsystems and (2) a clustering approach based on normal mode analysis which resulted in a single system for SEA unable to be applied. The latter depends on the mode type under consideration (axial, tangential, oblique).

In the comparison of ray tracing with predictive SEA models based on a transmission coefficient of unity between adjacent subsystems it was found there was closer agreement when the subsystems were assumed to support two-dimensional rather than three-dimensional sound fields. In addition, the agreement was closest when diffuse rather than specular reflections were assumed in the ray tracing and this finding primarily applied when the corridor surfaces had an absorption coefficient of 0.1 rather than higher values. However, the assumption of a transmission coefficient of unity on the interface between adjacent subsystems resulted in an overestimate of the decrease in SPL. Following the approach of Craik, an SEA model was ‘forced’ to follow the propagating 2D model but this suffers from the same limitation that the direct field can be important. Ray tracing models were therefore used to consider the sound energy from the direct field alongside two types of forward propagation in each subsystem. Type 1 describes the rays that propagate directly from the point source to the receiver (i.e. the direct field), Type 2 describes rays which only reflect from boundaries in subsystem 1 before reaching the receiver and Type 3 describes rays that are reflected at least once outside subsystem 1 before reaching the receiver. The sound pressure level measured for Type 1, 2 and 3 are averaged in each subsystem and energetically added to the SPL from predictive SEA. Although it gave reasonable agreement with ray tracing, ESEA was considered to encompass the issues of (a) overestimating the coupling loss factors and (b) needing to incorporate the direct field and two types of forward propagation. ESEA gave better estimates of the coupling loss factors and was used to assess whether indirect coupling loss factors could represent the direct field and two types of forward propagation. SEA predictions that incorporated coupling loss factors determined from the general form of ESEA (GESEA) which accounts for indirect coupling gave improved agreement with ray tracing assuming specular or diffuse reflections.

For measurements on a real corridor, two approaches have been used to estimate the average absorption coefficient (1) using standard data based on laboratory measurements from ODEON and (2) curve fitting to the measured decrease in SPL

using the propagating 2D model. The latter was significantly higher than the former above 315Hz. The former was found to give reasonable agreement between measurement and ray tracing assuming specular reflections up to the 4000Hz octave band, and diffuse reflections in the 8000Hz octave band.

The next chapter will build on the findings from this chapter to consider elongated cuboid space with staggered partitions at regular intervals. In this way, the validity of the SEA approach will be assessed when there is no direct line of sight down the corridor.

Chapter 5 Measurements and prediction of sound transmission along an elongated cuboid with staggered barriers

5.1 Introduction

In this chapter, an elongated cuboid with staggered barriers at regular intervals will be used to assess prediction using SEA when there is a partial barrier between subsystems. The reason for assessing this is that the barriers prevent the direct field rays from a point source travelling between non-adjacent subsystems. It is recognised that this is not a common situation for corridors in buildings, but it begins to make a closer link to aircraft cabins and train carriages where the seats form a kind of barrier.

The main dimensions are the same as with the empty cuboid, but it incorporates staggered barriers with 0.5m wide gap between the subsystems as shown in Figure 5-1. Due to the barriers, the direct field (Type 1 defined in Section 4.4.4) is no longer a significant factor in sound propagation along the cuboid on this model but the other two types of forward propagation (Types 2 and 3 defined in Section 4.4.4) can still occur.

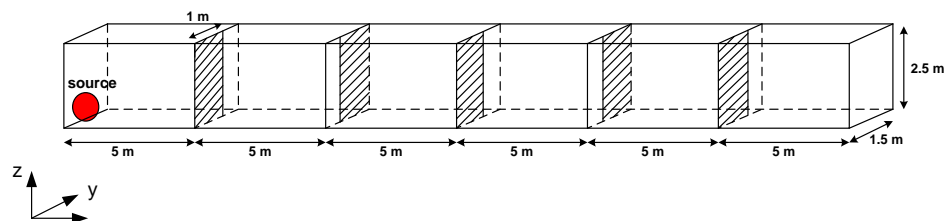


Figure 5-1. A cuboid model with staggered barriers.

5.2 Ray tracing with and without diffraction around a barrier

When the sound rays hit the vertical edge of a barrier, diffraction can occur; hence the first step is to assess the importance of diffraction when assuming specular and diffuse reflections. The implementation of diffraction in ODEON is described in Section 2.2.2.

The ray tracing assessment of diffraction uses an absorption coefficient of $\alpha=0.3$ for all surfaces with all other parameters the same as that of the empty cuboid. The resulting decrease in SPL along the cuboid with and without diffraction around a barrier are shown in Figure 5-2. There is a change up to 0.4dB in the decrease in SPL between subsystem 2 up to subsystems 3 and 4. In general, the inclusion of diffraction gives a negligible change ($\ll 1$ dB) in the decrease in SPL.

As the effect of diffraction is negligible, it will not be included in the ray tracing models in the remainder of this chapter.

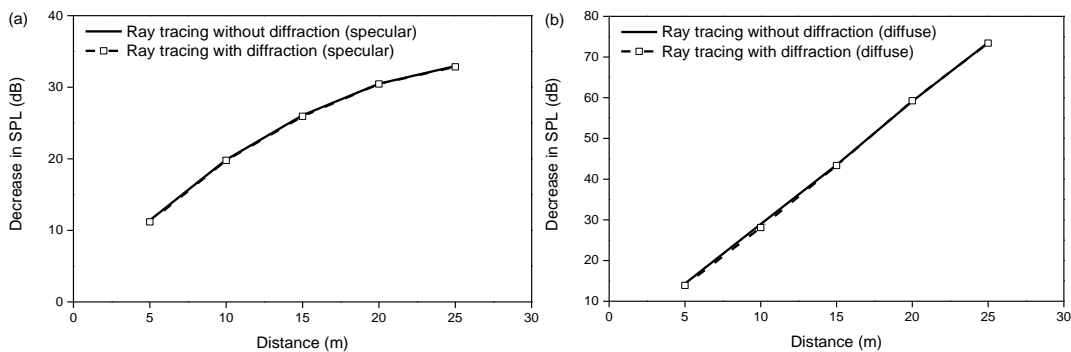


Figure 5-2. Cuboid model with staggered barriers: Comparison of ray tracing with or without diffraction around a barrier using (a) specular reflections and (b) diffuse reflections.

5.3 SEA model

For the cuboid with staggered barriers, subsystems are assigned on the basis that the barriers demarcate the volumes as indicated in Figure 5-1. In Section 4.4.1 FEM analysis was used to compare the mode shapes of these subsystems against a closed cuboid, a one open end cuboid and a two open ends cuboid. It was concluded that when dealing with frequency bands that contain a sufficiently large number of modes, then the response of subsystems could be described statistically based purely on modal densities for local modes.

For the cuboid with staggered barriers, the barriers almost enclose each subsystem. Hence the internal and coupling loss factors used for predictive SEA are calculated using Eq.(2.4.9) and Eq.(2.4.12) from Section 2.4.1 which assume three-dimensional

sound fields in each subsystem. This is in contrast to the empty cuboid for which it was shown that it was appropriate to consider two-dimensional sound fields.

The comparison of ray tracing and predictive SEA is shown in Figure 5-3. Predictive SEA overestimates the decrease in SPL along the cuboid compared to ray tracing assuming specular reflections (a similar trend to the empty cuboid) but it underestimates for diffuse reflections. This indicates that coupling loss factors are underestimated or overestimated for specular and diffuse reflections respectively. To improve the accuracy of the coupling loss factors, modifying CLFs by the use of ESEA with PIM is considered, as this was successful with the empty cuboid.

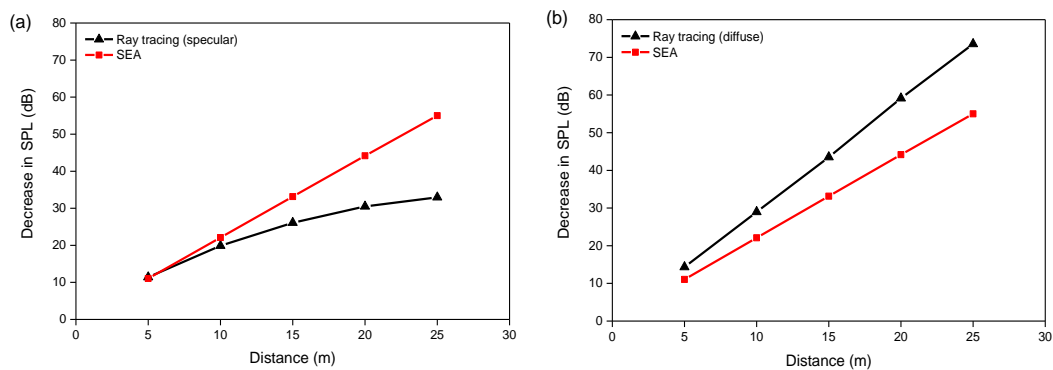


Figure 5-3. Cuboid model with staggered barriers (cuboid boundaries have $\alpha=0.3$): Comparison of SEA and the ray tracing (a) with specular reflections and (b) with diffuse reflections.

5.4 SEA using ESEA

For the empty cuboid the source position for the PIM was the same in each subsystem (refer back to Figure 4-22). However, for this cuboid with staggered barriers it is necessary to identify optimal or suitable source positions for the PIM in case they can significantly affect the accuracy of coupling loss factors.

Possible permutations of source positions (excluding those in openings) are shown in Figure 5-4. These are determined by considering two different propagation directions; 1) biased towards forward propagation (blue) and 2) biased towards backward propagation (green). The main source positions in subsystem 1 are represented using three different colours: red (source 1), orange and purple (source 2 and 3).



Figure 5-4. Point source locations for PIM.

It is now necessary to identify suitable source positions in each subsystem to carry out the PIM. Due to ‘lines of sight’ through the open area between subsystems it was hypothesised that choosing different source positions in each subsystem might lead to errors in the estimated coupling loss factors. The first stage is an assessment of the source position in subsystem 1.

Table 5-1 shows the difference between the direct coupling loss factor determined from GESEA (e.g. η_{12}) from ray tracing assuming specular reflections and that predicted based upon an open area (Eq.(2.4.9)). Note that these values do not vary when the source position in the other subsystems is changed. Only ray tracing assuming specular reflections is considered because it was shown in Figure 5-3 that this gives closer agreement with predicted SEA than ray tracing assuming diffuse reflections. The existence of an opening means that the assumption of a diffuse field in each subsystem is unlikely to be appropriate. The results show that different source positions lead to differences in the coupling loss factor up to 1.9dB. The use of red source (Source 1) is closest to the predicted coupling loss factor and therefore the remainder of this section will use the red source position in the source subsystem and evaluate the effect of different source permutations in the other subsystems.

	Source in subsystem 1	Difference between the GESEA CLFs and the predicted CLF $10\lg(\eta_{\text{GESEA}} / \eta_{\text{Predicted}})$ (dB)
Specular reflection		η_{12}
Source 1	●	0.6
Source 2	●	1.1
Source 3	●	-1.9

Table 5-1. Cuboid model with staggered barriers: Difference between the direct coupling loss factor, η_{12} determined from GESEA and from predicted SEA in dB with different main sources.

For the other subsystems, four permutations of source position are now considered to perform PIM described as cases A, B, C and D. It is a reasonable assumption that the direct coupling loss factor between adjacent subsystems should be similar, even though the sound field in subsystems 1 and 6 are likely to be different to the other because they only have one opening rather than two. For this reason, the direct coupling loss factors and the standard deviation of the direct coupling loss factors estimated from GESEA and AESEA are shown in Table 5-2. This shows that the direct coupling loss factors determined from GESEA give the same values as AESEA. It is noteworthy that case A has the lowest standard deviation for the direct coupling loss factors, and therefore this is likely to be optimal.

a) Specular reflections

		Subsystem			Difference between the ESEA CLFs and the predicted CLF $10\lg(\eta_{\text{ESEA}} / \eta_{\text{Predicted}})$ (dB)					σ (dB)
		1	2-5	6	η_{12}	η_{23}	η_{34}	η_{45}	η_{56}	
Case A	Biased towards forward propagation – Version 1	●	●	●	0.6	1.5	1.1	1.5	1.1	0.37
Case B	Biased towards backward propagation – Version 1	●	●	●	0.6	-2.1	-2.1	-2.1	-2.2	1.23
Case C	Biased towards forward propagation – Version 2	●	●	●	0.6	1.5	1.1	1.5	1.2	0.37
Case D	Biased towards backward propagation – Version 2	●	●	●	0.6	-2.1	-2.1	-2.1	-2.2	1.23
	AESEA	1	2-5	6	η_{12}	η_{23}	η_{34}	η_{45}	η_{56}	σ (dB)
Case A	Biased towards forward propagation – Version 1	●	●	●	0.6	1.5	1.1	1.5	1.1	0.36
Case B	Biased towards backward propagation – Version 1	●	●	●	0.6	-2.0	-2.1	-2.1	-2.2	1.22
Case C	Biased towards forward propagation – Version 2	●	●	●	0.6	1.5	1.1	1.5	1.2	0.36
Case D	Biased towards backward propagation – Version 2	●	●	●	0.6	-2.0	-2.1	-2.1	-2.2	1.23

b) Diffuse reflections

		Subsystem			Difference between the ESEA CLFs and the predicted CLF $10\lg(\eta_{\text{ESEA}} / \eta_{\text{Predicted}})$ (dB)					
	GESEA	1	2-5	6	η_{12}	η_{23}	η_{34}	η_{45}	η_{56}	σ (dB)
Case A	Biased towards forward propagation – Version 1	●	●	●	-1.1	0.2	-0.3	0.2	-0.4	0.52
Case B	Biased towards backward propagation – Version 1	●	●	●	-1.1	3.4	3.4	3.5	3.3	1.99
Case C	Biased towards forward propagation – Version 2	●	●	●	-1.1	0.2	-0.3	0.2	-0.5	0.52
Case D	Biased towards backward propagation – Version 2	●	●	●	-1.1	3.4	3.4	3.4	3.2	1.99
	AESEA	1	2-5	6	η_{12}	η_{23}	η_{34}	η_{45}	η_{56}	σ (dB)
Case A	Biased towards forward propagation – Version 1	●	●	●	-1.1	0.1	-0.3	0.1	-0.4	0.51
Case B	Biased towards backward propagation – Version 1	●	●	●	-1.1	3.4	3.3	3.4	3.2	1.98
Case C	Biased towards forward propagation – Version 2	●	●	●	-1.1	0.1	-0.3	0.1	-0.5	0.51
Case D	Biased towards backward propagation – Version 2	●	●	●	-1.1	3.4	3.3	3.4	3.2	1.98

Table 5-2. Cuboid model with staggered barriers: Difference between the direct CLFs determined from ESEA and from predicted SEA in dB (a) specular reflections and (b) diffuse reflections for different source permutations with source 1 (red) and standard deviation (σ) in dB.

The next step is to compare ray tracing and SEA using ESEA CLFs for the four cases in terms of the decrease in SPL along the cuboid with staggered barriers. This is shown in Figure 5-5.

Ray tracing assuming specular reflections shows closest agreement ($<0.3\text{dB}$) with SEA using GESEA CLFs for all cases. Both SEA using AESEA CLFs and SEA do not include indirect coupling and both tend to overestimate the decrease in SPL. This indicates that consideration of indirect coupling in GESEA is essential to predict sound transmission along the cuboid with specular reflections. Note that the most influential indirect couplings are η_{1j} where j represents the j^{th} receiving subsystem (when $j \neq 1$ and $j \neq 2$).

Ray tracing assuming diffuse reflections shows close agreement ($<9\text{dB}$) with SEA using GESEA CLFs and SEA using AESEA CLFs for cases A and C; this indicates that indirect coupling is not important with diffuse reflections which is the opposite of what was observed with specular reflections. This provides more evidence that identifying optimal source permutations from the lowest standard deviations is appropriate because cases A and C were previously identified as having the lowest standard deviations in Table 5-2. From this point on, case A will be used in the remainder of the numerical experiments because cases A and C are similar and there seems to be less logic in choosing case C where the source position in subsystems 1 and 6 is the mirror image of each other.

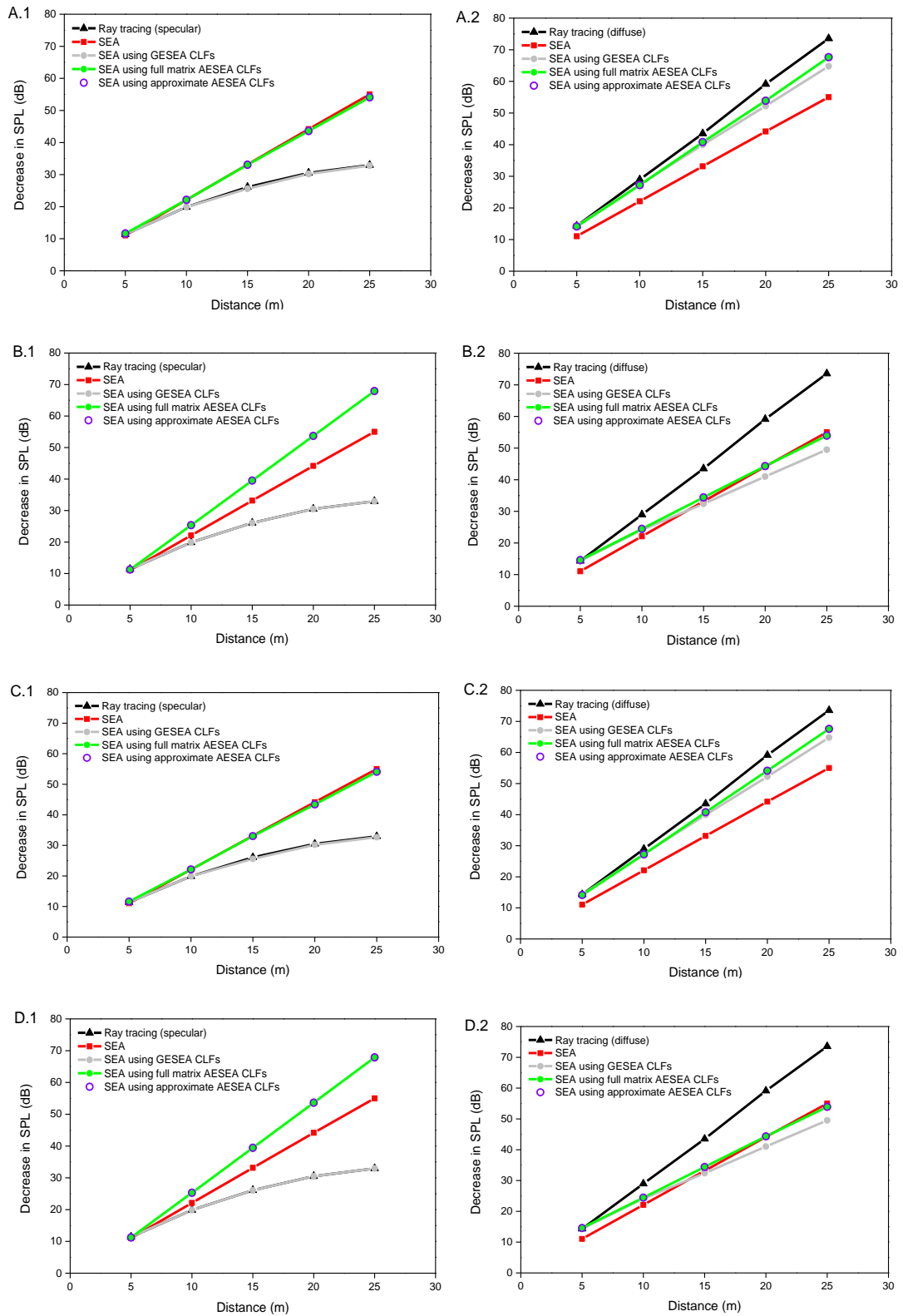


Figure 5-5. Cuboid model with staggered barriers (cuboid boundaries have $\alpha=0.3$): Comparison of SEA using ESEA with ray tracing (1) with specular reflections and (2) with diffuse reflections with respect to different source permutations for cases A, B, C and D.

An SEA model is not usually tied to a specific source position and therefore other source positions in subsystem 1 are now considered along with the average of three possible source positions to see whether reasonable predictions can be gained for a non-specific source position. In a similar way to Table 5-2, Table 5-3 shows a comparison of three different cases (E, F and G) in terms of the direct coupling loss factors. The results indicate that the yellow source gives a lower standard deviation than the red source or the combination of red, yellow and purple sources. However, the combination of red, yellow and purple sources gives a GESEA η_{12} that is closest to the predicted η_{12} . This demonstrates that there might be potential in using the average of the three source positions to give a model that applies to more than one specific source positions.

























		Subsystem			Difference between the GESEA CLFs and the predicted CLF $10\lg(\eta_{\text{ESEA}} / \eta_{\text{Predicted}})$ (dB)					σ (dB)
		1	2-5	6	η_{12}	η_{23}	η_{34}	η_{45}	η_{56}	
	Specular reflections									
Case A	Biased towards forward propagation – Source 1				0.6	1.5	1.1	1.5	1.1	0.37
Case E	Biased towards forward propagation – Source 2				-1.1	1.5	1.1	1.5	1.1	0.20
Case F	Biased towards forward propagation – Source 3				1.9	1.5	1.1	1.5	1.1	1.47
Case G	Biased towards forward propagation – Average sources 1,2 and 3				-0.1	1.5	1.1	1.5	1.1	0.65
	Diffuse reflections									
Case A	Biased towards forward propagation – Source 1				-1.1	0.2	-0.3	0.2	-0.4	0.52
Case E	Biased towards forward propagation – Source 2				-0.3	0.2	-0.3	0.2	-0.4	0.26
Case F	Biased towards forward propagation – Source 3				3.3	0.2	-0.3	0.2	-0.4	1.53
Case G	Biased towards forward propagation – Average sources 1,2 and 3				0.6	0.2	-0.3	0.2	-0.4	0.41

Table 5-3. Cuboid model with staggered barriers: Direct CLFs between adjacent subsystems determined using GESEA for different sources and standard deviation (σ) in dB.

Figure 5-6 shows the difference in the decrease in SPL between ray tracing (using the red source (source 1) and assuming specular reflections) and SEA using GESEA CLFs with different sources. The main conclusion is that the difference is approximately 0dB when the actual source position is used for ESEA. Although the analysis in the previous paragraph indicated that the combination of red, yellow and purple sources might be beneficial, it is seen here that the difference increases with increasing distance (>10dB in subsystem 6) from the source subsystem and the values are too large to be feasible for practical implementation of ESEA. Hence identification of the optimal source distribution using the lowest standard deviation is only valid when the source position in the source subsystem is the same as the actual source. However, when the actual source position is unknown then the combination of source positions is an alternative option.

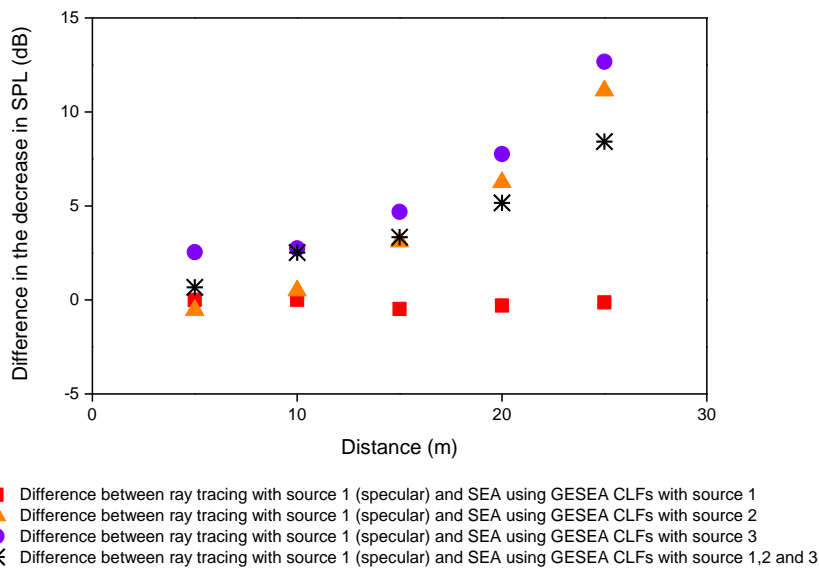


Figure 5-6. Cuboid model with staggered barriers: Difference in decrease in SPL between ray tracing using the red source (specular reflections) and SEA using GESEA CLFSs with difference sources.

In conclusion, it is shown that using ESEA to give CLFs for inclusion in an SEA model increases the accuracy of predictions. It was seen that the inclusion of indirect coupling from GESEA was necessary to give close agreement with ray tracing assuming specular reflections but not with diffuse reflections. The indirect coupling loss factors that significantly improve the agreement are η_{ij} where i indicates the

source subsystem and j indicates the j^{th} receiving subsystem (when $j \neq i$ and $j \neq (i \pm 1)$). The optimal source distribution in the other subsystems can be identified from the lowest standard deviation of the direct coupling loss factors.

The rules for source distributions to implement PIM for ESEA are:

- 1) The source position used in the source subsystem in the actual situation should be the same as the position used in that subsystem for the PIM.
- 2) Source positions should preferably be (a) in a corner away from the opening and (b) in the direct line-of-sight of apertures for forward propagation rather than backwards propagation.
- 3) When there are coupled subsystems that are adjacent to each other which should logically have the same coupling loss factor (e.g. 2 to 3, 3 to 4) then the optimal source positions are those with the lowest standard deviation.

When the actual source position is unknown, the average of a few possible source positions in the source subsystem is a reasonable option to implement ESEA; however, the errors tend to increase in receiving subsystems far from the source.

5.5 SEA/ESEA model with sources located in other subsystems

The point source supplying energy to the space can be located in a variety of positions. For example, it can be positioned in the middle of cuboid or multiple sources can also generate sound simultaneously. In order to evaluate the validity of SEA and ESEA in different situations, this section considers two cases: 1) a point source in subsystem 2 and 2) a single point source in each subsystem.

5.5.1 Point source in subsystem 2

The results in the previous section indicated that when using SEA with predicted CLFs the errors increase rapidly after the receiving subsystem that is immediately adjacent to the source subsystem.

For the point source in subsystem 2, Figure 5-7 shows the decrease in SPL predicted using SEA and ray tracing. With specular reflections, SEA using GESEA or ASEA CLFs with case A shows close agreement with SEA and ray tracing. This indicates

that indirect coupling is not as important as when the source was in subsystem 1 because direct coupling primarily determines sound transmission along the cuboid when the source and receiving subsystems are closer. However, with diffuse reflections, SEA using GESEA or ASEA CLFs with case A show close agreement with ray tracing but not predictive SEA. For predictive SEA the CLFs tend to be overestimated when there are diffuse reflections.

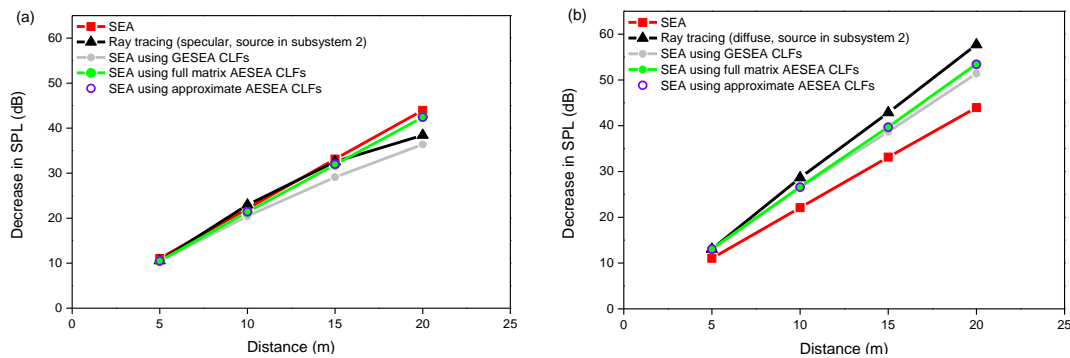


Figure 5-7. Cuboid model with staggered barriers: Comparison of SEA using ESEA with ray tracing using the source in subsystem 2 (a) with specular reflections and (b) with diffuse reflections (cuboid boundaries have $\alpha=0.3$). Case A source distribution is used for SEA model.

In conclusion, SEA and SEA using ESEA CLFs give a reasonable estimate of noise assessment with specular reflections when a source closer to the middle of cuboid rather than at the end. This is because the effect of indirect coupling is less critical when the distance between the source and receiving subsystems is reduced. However, SEA underestimates the decrease in SPL when there are diffuse reflections, which indicates that the predicted CLF is likely to be overestimated. For this reason, it is preferable to implement ESEA for a single source when it is unknown whether there are specular or diffuse reflections.

5.5.2 Multiple sources

In reality, there could be sources in all subsystems so it is of interest to assess the errors in such a case. This section considers six sources with a point source in each subsystem that generate sound simultaneously. An output power of 1W, 0.2W, 0.5W,

0.8W, 0.1W and 0.3W is injected in subsystems 1 to 6 respectively. Figure 5-8 compares the sound pressure levels in each subsystem from ray tracing with (a) predictive SEA, (b) SEA using GESEA CLFs and (c) SEA using AESEA CLFs. The results show that predictive SEA is similar to ray tracing assuming specular and diffuse reflections (up to 3dB difference) and SEA using CLFs determined from AESEA and GESEA estimate the same SPL. Therefore, SEA is suitable with a source in each subsystem (regardless of whether there are specular or diffuse reflections) because indirect coupling does not play a significant role.

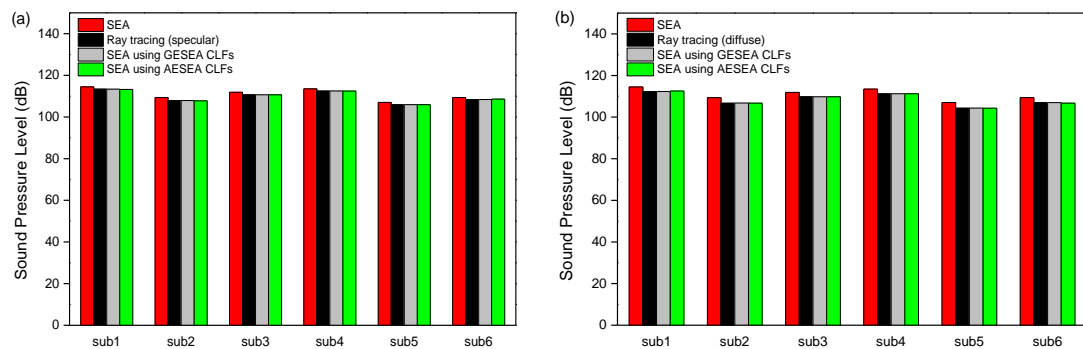


Figure 5-8. Cuboid model with staggered barriers (cuboid boundaries have $\alpha=0.3$): Comparison of SPL in each subsystem estimated from SEA, SEA using ESEA and ray tracing (a) with specular reflections and (b) with diffuse reflections using multiple sources.

5.6 Case study: Corridor with staggered partitions

Measurements on the same corridor as Section 4.6 in the Harrison Hughes building at the University of Liverpool (see Figure 2-10) were made using movable office partitions. Note that these are called ‘partitions’ rather than ‘barriers’ because they are not full height. These partitions were fabric covered board with dimensions 1.5m x 1.8m (see photo in Figure 2-12 in Section 2.6.2).

The corridor is modelled using six subsystems (up to the fire door) in SEA. Sound pressure level measurements were taken at six random positions in each subsystem and averaged in one-third octave bands (see Figure 2-11 in Section 2.6.2). Figure 5-9 shows the standard deviation of measured sound pressure levels at six positions every subsystem. At frequencies below 160Hz where there are relatively few modes, the standard deviation shows large fluctuations whereas at high frequencies where

there are many modes the curve becomes smooth with values less than 2dB. The large standard deviations occur at low frequencies below the fundamental frequency of the first oblique mode, 114.2Hz in Table 5-4.

The highest standard deviation at low frequencies is ≈ 6 dB. Note that the expected maximum value for a pure tone in a diffuse field is 5.6dB [78]. This indicates that might only be one mode dominating the response in some of these low-frequency bands.

In this section, the analysis will mainly focus on frequency bands at and above 160Hz where the spatial variation is relatively low.

Direct CLFs from AESEA are now compared with the predicted CLF assuming an open area. TLFs from AESEA are also compared with the predicted TLF using absorption coefficients from ODEON material database (as used for empty corridor in Section 4.3.3) for surfaces of the corridor and estimated absorption coefficient by measurement in Section 2.6.3 for barriers. The absorption coefficient for the partition was measured in one-third octave bands and converted to octave bands for consistency with the approach in ODEON material database.

Figure 5-10 shows the TLF, direct CLF and their ratio estimated from SEA and AESEA. Figure 5-10 (a) shows the TLFs in octave band centre frequency. SEA tends to give a lower estimate than AESEA and this occurs with the direct CLFs in Figure 5-10 (b) as well. These absolute values do not give insight into energy flow from one subsystem to the other but this can be assessed using their ratio as indicated in Figure 5-10 (c). This ratio corresponds to the energy ratio between the source and adjacent receiving subsystem as indicated in Section 2.4.1.2 when energy flows in the forward direction away from the source and all subsystems are in a linear chain. At low frequencies below 2000Hz, SEA tends to transmit less energy compared to AESEA. With increasing frequency, the energy ratio estimated from SEA and AESEA become closer.

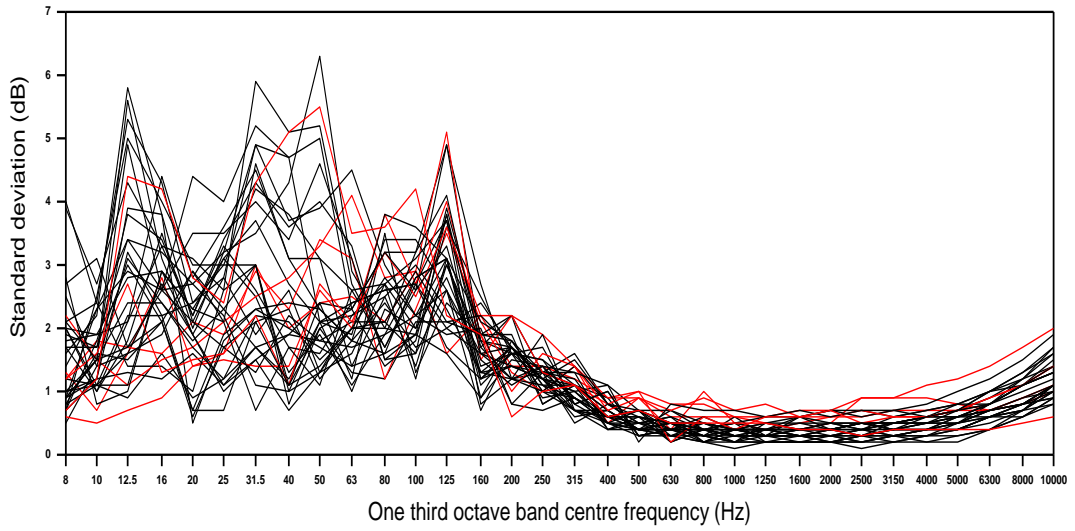


Figure 5-9. Real corridor with staggered partitions: Standard deviation of measured SPL on the real corridor with partitions in one-third octave band (red line: source subsystem, black line: receiving subsystems).

Room Modes		Hz
Axial mode	$f(1,0,0)$	28.6
	$f(0,0,1)$	74.6
	$f(0,1,0)$	163.3
Tangential mode	$f(1,0,1)$	79.8
	$f(1,1,0)$	86.5
	$f(0,1,1)$	110.6
Oblique mode	$f(1,1,1)$	114.2

Table 5-4. Fundamental modes and frequencies for a closed cuboid space (6m x 2.1m x 2.3m).

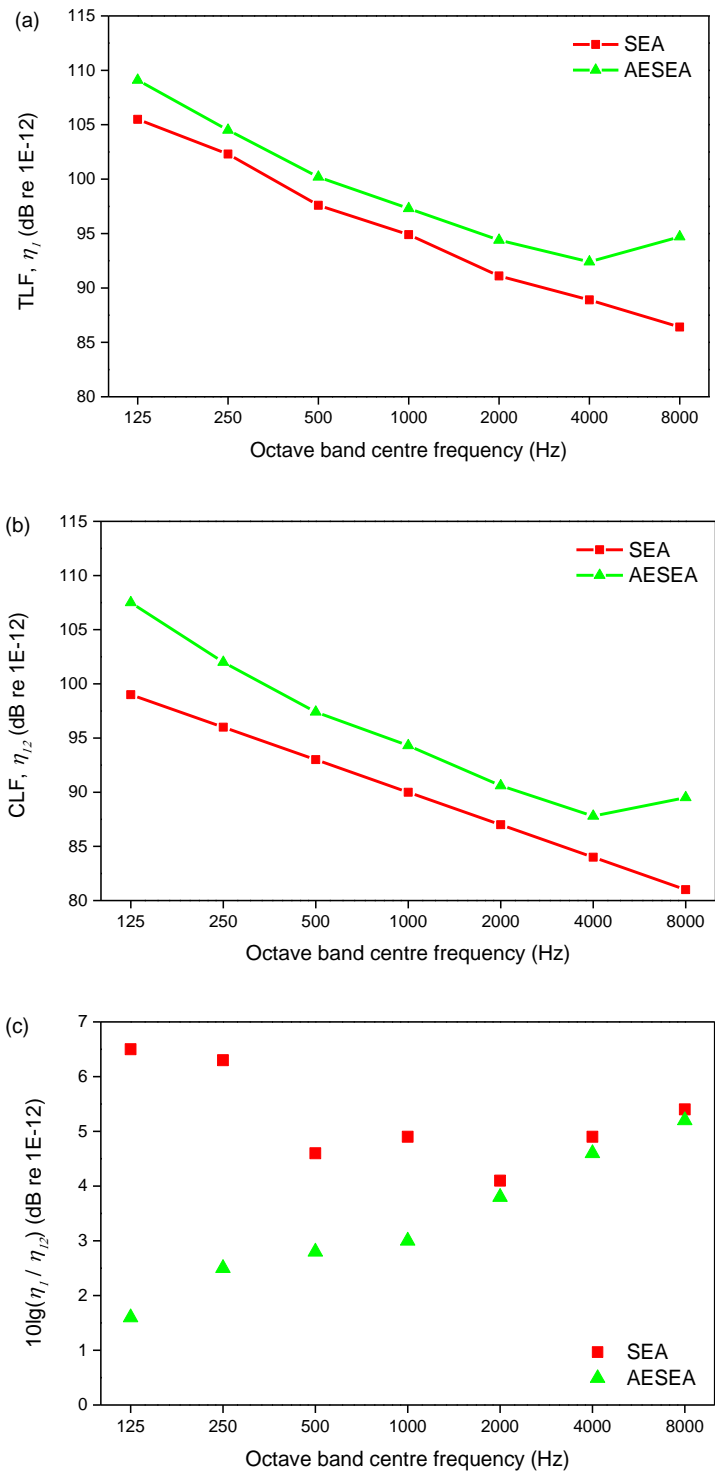


Figure 5-10. Real corridor with staggered partitions: Comparison of (a) total loss factors (TLFs), (b) coupling loss factors (CLFs) and (c) energy ratio $10\lg(\eta_1/\eta_{12})$ estimated from SEA using ODEON material database with barrier and AESEA based on experimental measurements. NB AESEA results using the full matrix and approximation are nominally identical.

The propagating 2D diffuse field model is considered here to assess sound transmission along the corridor; however, it needs to be modified to apply to different geometric corridor system. The model was previously described in Section 4.3.2 but energy losses are taken into account at the barrier as illustrated in Figure 5-11.

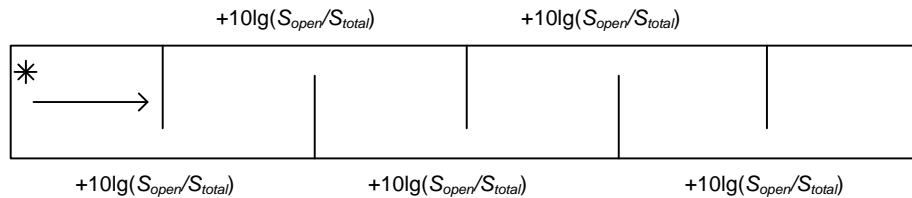
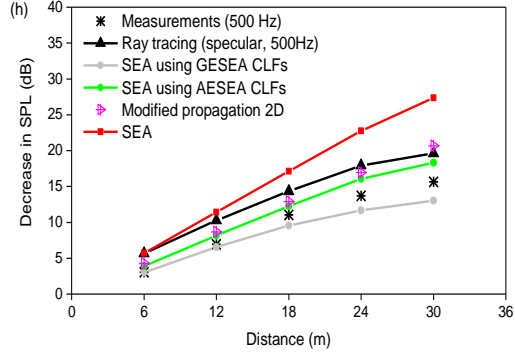
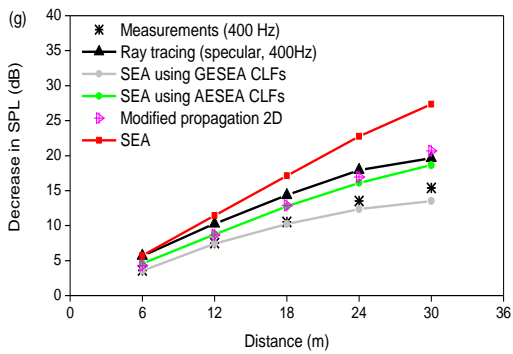
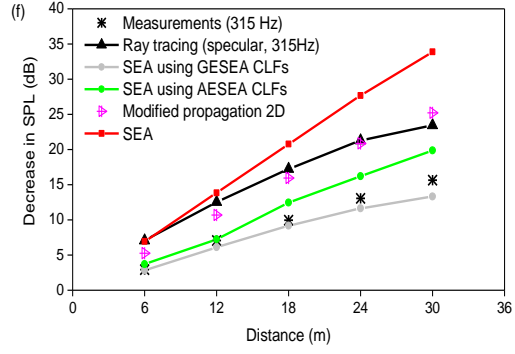
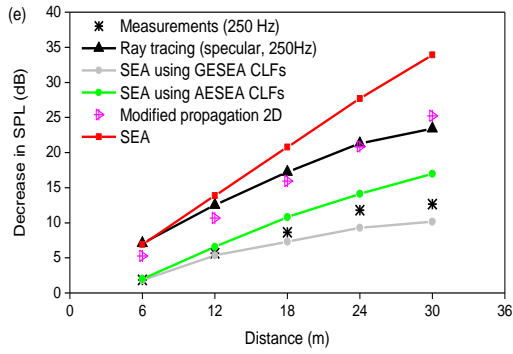
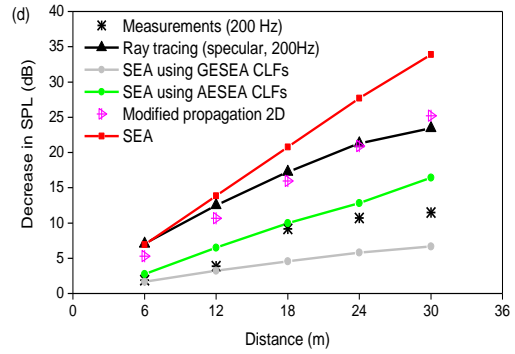
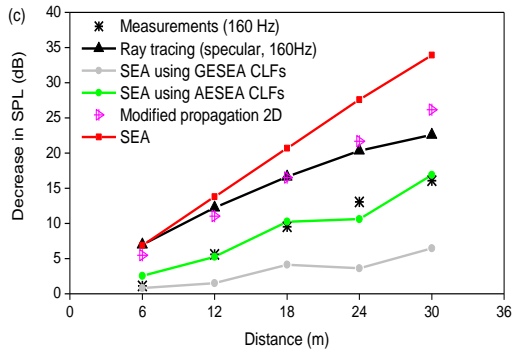
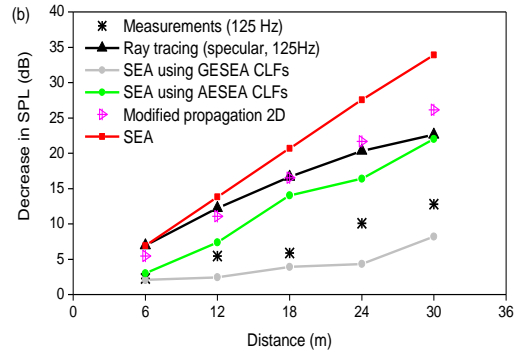
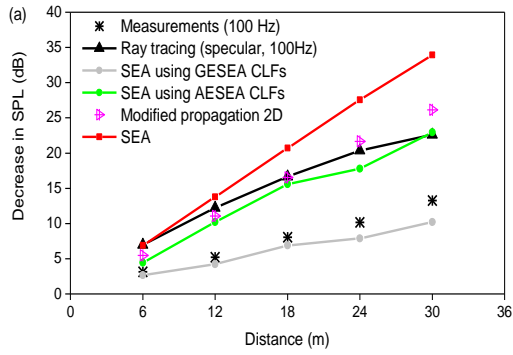
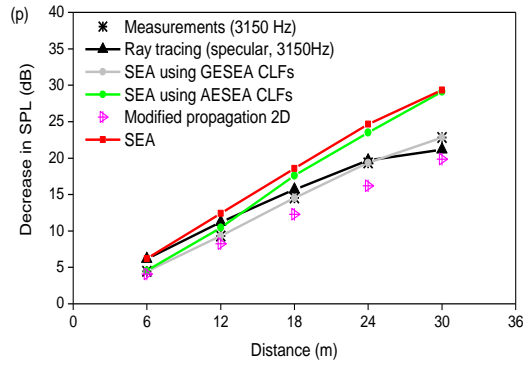
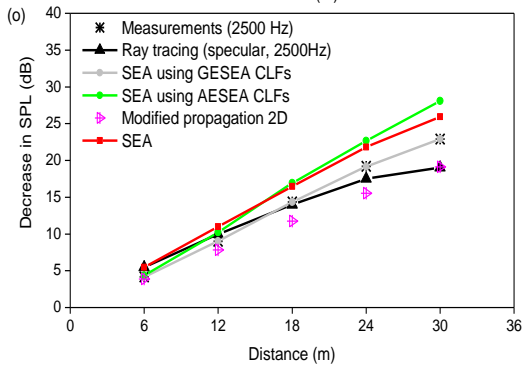
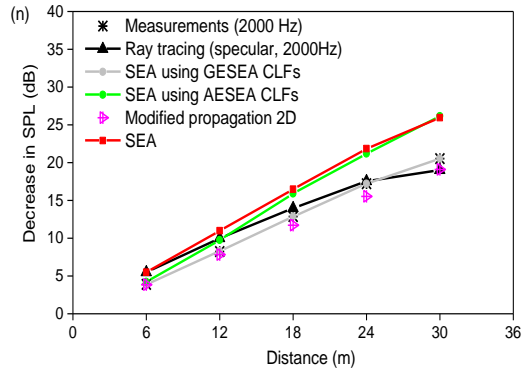
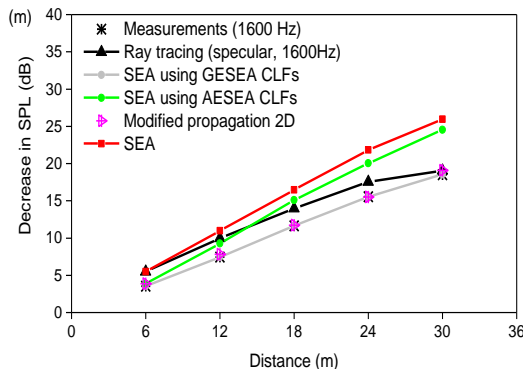
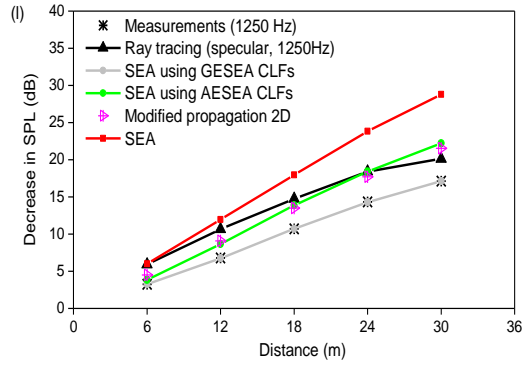
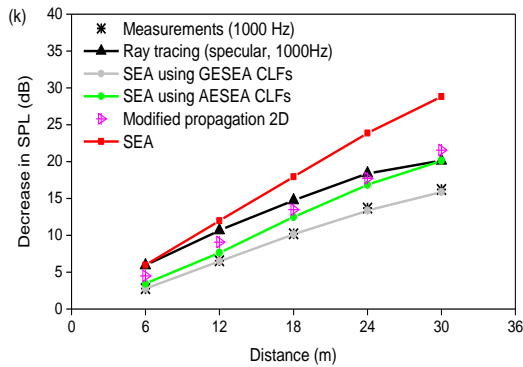
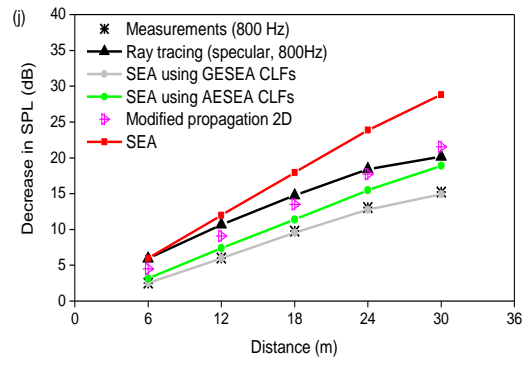
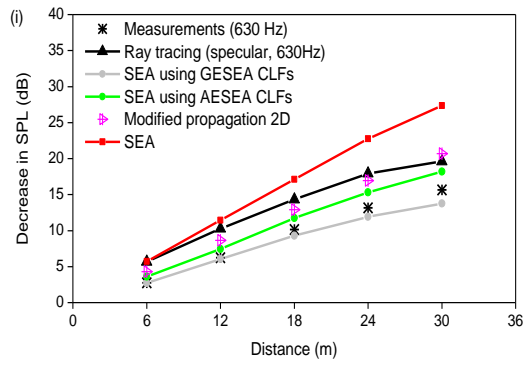


Figure 5-11. Modified propagation 2D diffuse field model (S_{open} : open area, S_{total} : cross-section of corridor).

Measurements are compared with ray tracing, SEA using CLFs estimated from ESEA, SEA and modified propagation 2D model in one-third octave bands, which are shown in Figure 5-12. At low frequencies between 100Hz and 200Hz, measurements show a nonlinear decrease in SPL along the corridor and there is no consistent agreement with any model which might be attributed to the large standard deviations seen in Figure 5-9. At 160Hz SEA using AESEA CLFs does not give data since ILFs determined from AESEA have negative values. However, measurements are in reasonable agreement with SEA using CLFs determined from ESEA above 200Hz and with ray tracing assuming specular reflections above 315Hz since ray tracing is implemented in octave band frequencies instead. In general, SEA with GESEA CLFs gives closer agreement than SEA with AESEA CLFs. The agreement between measurements and ray tracing indicates that measured absorption coefficients for partitions (see Section 2.6.3) are reasonable although sound field is unknown.

Above 2000Hz there is agreement between SEA and measurements which corresponds to the frequency at which the energy ratio also corresponds to the ratio of coupling to total loss factor with AESEA (see Figure 5-10). This indicates that SEA can reasonably predict sound transmission at high frequencies. The modified propagation 2D model only shows close agreement with measurements between 400Hz and 5000Hz.





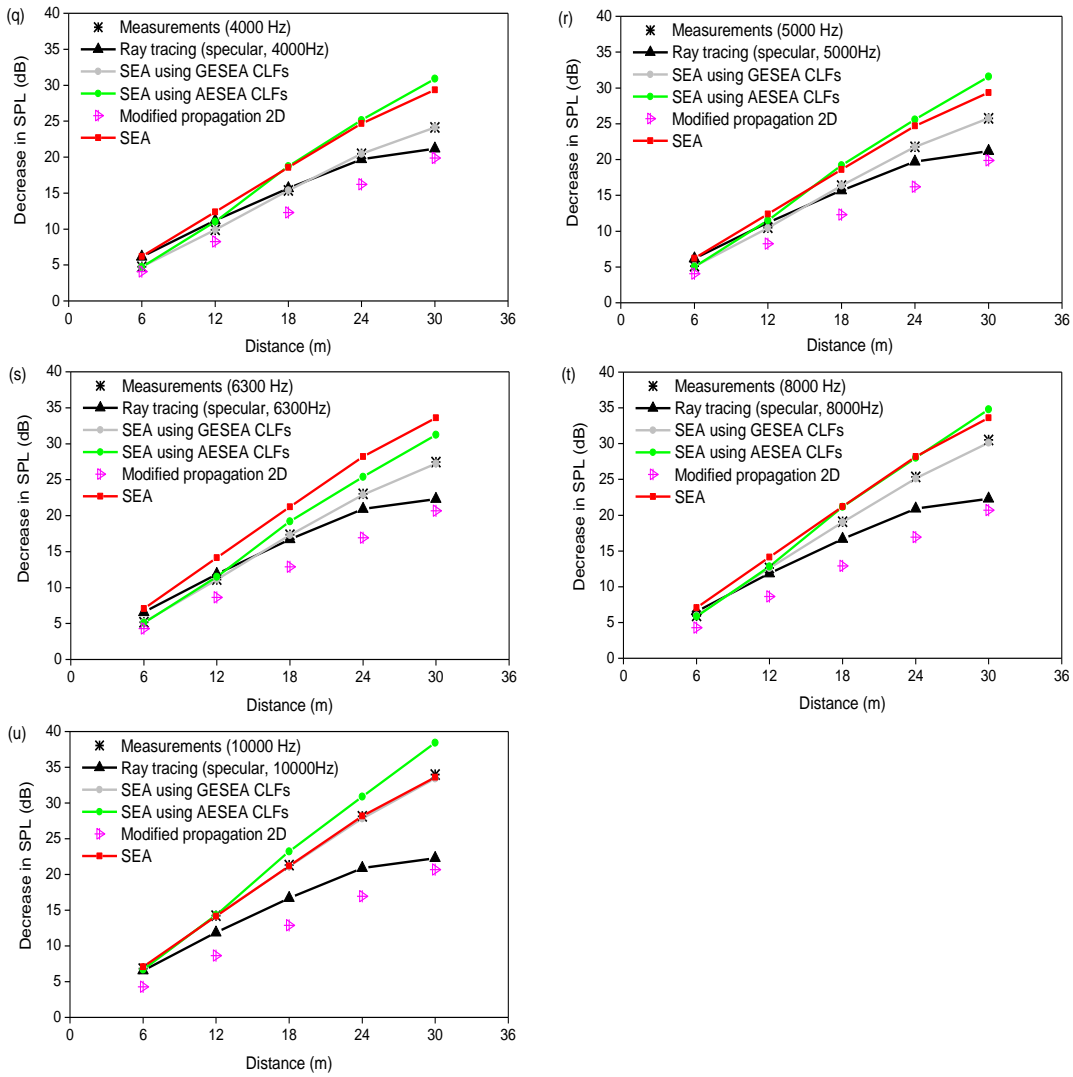


Figure 5-12. Real corridor with staggered partitions: Comparison of measurements with SEA using GESEA CLFs and SEA using AESEA CLFs in the decrease in SPL along the corridor.

In conclusion, it is feasible to predict sound transmission along the corridor with staggered barriers using SEA using GESEA CLFs. SEA using AESEA CLFs also gives reasonable estimates with consideration of only direct CLFs but it is recommended to account for indirect CLFs to increase the accuracy.

5.7 Conclusions

In this chapter, a cuboid with staggered barriers has been considered for the prediction of sound propagation using ray tracing, SEA and ESEA.

Predictive SEA gave overestimated decrease in SPL along the cuboid compared to ray tracing assuming specular reflections whereas it was underestimated with diffuse reflections.

SEA incorporating CLFs determined from ESEA has used to give improved agreement with ray tracing assuming specular or diffuse reflections. ESEA used for partly-open coupled subsystems requires consideration of source distributions for PIM to obtain appropriate energy balance matrix used to estimate CLFs. Ray tracing were therefore used to calculate sound energy from two versions of source permutations in each subsystem. Version 1 uses the source positioned with biased towards forward propagation, Version 2 uses the source positioned with biased towards backward propagation. Note that the main source position should be the exactly same as the source subsystem in SEA and possible source positions should be symmetrically distributed. SEA using GESEA CLFs showed closer agreement with ray tracing assuming specular reflections than using CLFs determined from AESEA but SEA incorporating CLFs determined from the both forms of ESEA gave good agreement with ray tracing assuming diffuse reflections when using a source biased towards forward propagation rather than biased towards backward propagation. In addition, the agreement was found when the standard deviation of direct CLFs is lowest which is convincing since all subsystems are equal therefore direct CLFs between adjacent subsystems should be similar. A general model working for any source has been considered by average in three positions but this gave imprecise estimate compared to using the same source in the source subsystem.

Predictive SEA and SEA using any form of ESEA CLFs with a source in subsystem 2 gave close SPL in each subsystem to ray tracing assuming specular reflections.

This was evident that direct CLFs are dominant when the distance between the source and receiving subsystem is increasing. For the view of practice, a source in each subsystem was operated simultaneously and it is found that SEA using ESEA CLFs and predictive SEA were suitable to assess sound transmission along a cuboid regardless of specular or diffuse reflections.

Measurements on a real corridor using barriers in one-third octave band were compared with SEA, SEA using ESEA CLFs and modified propagation 2D. Modified propagation 2D considered additional energy loss at every barrier position by subtracting the ratio of total cross-section area to coupled open area. SEA using GESEA CLFs gave close agreement with the measurements rather than using AESEA CLFs above 250Hz. It was found to give large standard deviation in sound pressure levels measured at low frequencies below following fundamental frequency of the first oblique mode, 114Hz. A two-dimensional diffuse sound propagating was evident in agreement with the measurements from 400Hz to 5000Hz on one-third octave band. Predictive SEA gave close agreement with the measurements when energy ratio between two subsystems using estimate of TLFs and CLFs is appropriately predicted in comparison of that from AESEA.

In the next chapter, the validity and applicability of SEA approach will be assessed by taking a car cabin when the space is compact and formed in complex coupled system.

Chapter 6 Prediction of sound transmission in a compact cavity

6.1 Introduction

In the previous chapters, sound transmission has been assessed in elongated spaces using SEA models of which subsystems are serially coupled in chain. However, there are also problems predicting sound transmission in small, compact acoustic cavities. As an example of compact space in this chapter, a car cabin is considered in this chapter. The driver and passengers can be exposed to different sound levels; hence there are reasons to subdivide the cabin space into more than one subsystem for the purpose of using SEA.

In this chapter the ESEA approach developed in Chapters 4 and 5 to make SEA models using GESEA CLFs and AESEA CLFs for the car cabin. The first part of the chapter concerns numerical experiments using ray tracing on a rectangular cuboid, which represents an idealisation of a car cabin. This idealisation is useful to (a) simplify the open area which connect the front to the rear of the cabin because in a real car cabin there are several open areas (e.g. gaps on either side of the front seats and around the headrest), and (b) simplify the demarcation between different types of absorption in the lower and upper parts of the car. The second part of the chapter considers the actual sound field inside a car cabin, which is predicted using FEM below the 1000Hz octave band, and ray tracing at and above the 1000Hz octave band.

6.2 Numerical experiments with rectangular cuboid space representing an idealised car cabin

Before assessing a car cabin, which is geometrically complex, a simple cuboid space with a volume similar to a car cabin (4.05m^3) is modelled as indicated in Figure 6-1. This cuboid space has a partial-height barrier in the centre with high surface absorption ($\alpha=0.9$) that corresponds to the front car seats. This corresponds to fabric seats (above 200Hz) for which the absorption has been experimentally determined in the literature [79,80,81]. The lower surfaces of the cuboid are also modelled with an absorption coefficient of $\alpha=0.9$. The upper surfaces are modelled using a low

absorption coefficient $\alpha=0.03$ which corresponds to glass (ODEON material database).

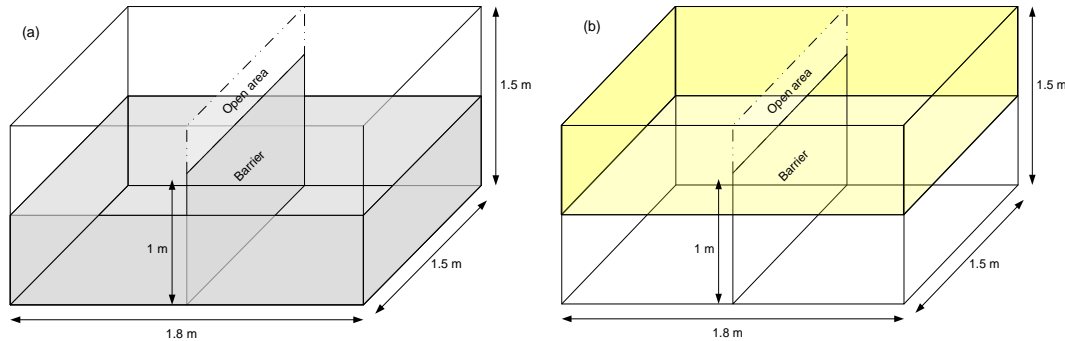


Figure 6-1. Idealised car cabin: (a) high absorption coefficients (grey: $\alpha=0.9$) and (b) low absorption coefficients (yellow: $\alpha=0.03$).

Figure 6-2 shows the modal density of the cuboid space calculated with FEM for comparison with the statistical modal density for an equivalent single volume. FEM gives slightly higher mode counts because of the partial barrier which subsystem-divides the volume and is not accounted for in the statistical estimate. For the 63Hz and 125 Hz bands the mode shapes are shown in Table 6-1. In the 63Hz band, there is only one mode; hence SEA is not suitable but it is of interest to assess what happens with ESEA because an experimenter might not be aware that there was only one mode. In the 125Hz band, it is reasonable to consider SEA modelling with seven modes.

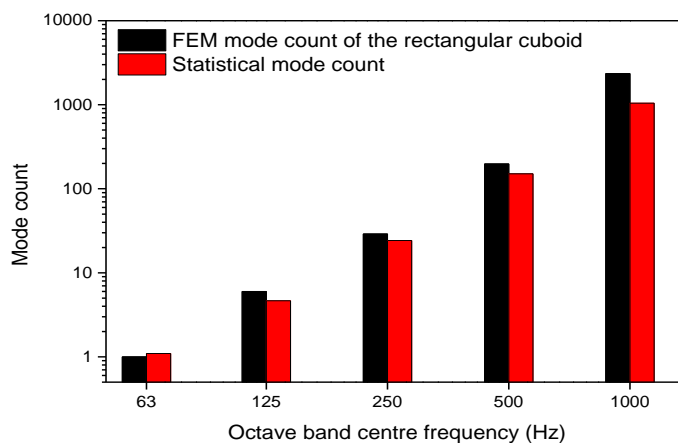


Figure 6-2. Idealised car cabin: Modal density of the rectangular cuboid in octave bands.

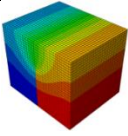
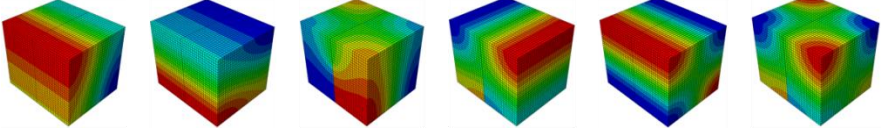
Octave band (Hz)	Modes
63	
125	

Table 6-1. Idealised car cabin: FEM mode shapes in 63Hz and 125Hz octave bands.

6.2.1 Division into two subsystems

The cuboid space is first considered as two coupled subsystems divided by the barrier as illustrated in Figure 6-3. This subdivision is intended to be representative of the front and rear seat spaces in a car cabin.

For octave bands from 63 to 1000 Hz, FEM is used to determine the response in the subsystems. At higher frequencies, the response in the subsystems is determined from ray tracing assuming diffuse reflections and using a point source positioned at a distance 0.2m away from the three boundaries forming a corner. The average sound pressure level in each subsystem is calculated from a grid of points (0.1m spacing in the x-, y- and z-directions) which are $\geq 0.2\text{m}$ away from boundaries. The response is determined with the point source in each of the two subsystems to provide data for ESEA.

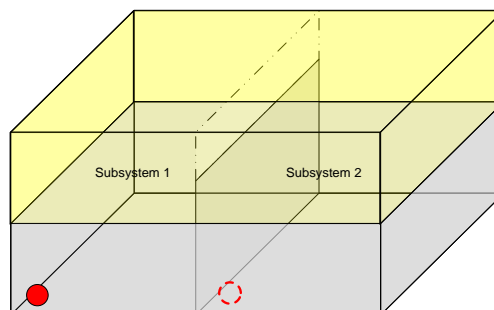


Figure 6-3. Idealised car cabin: SEA model composed of two subsystems (solid circle: main source position, open circle: additional source position used for PIM).

Figure 6-4 shows the SPL in each subsystem from FEM and SEA using ESEA CLFs. Both SEA using GESEA CLFs and SEA using AESEA CLFs are in closest agreement with FEM in all octave bands between 63Hz and 1000Hz. However, in the 63Hz octave band, the cuboid space (when treated as a single volume) only has one mode; hence, SEA and any form of ESEA are invalid as they both predict energy transmission between coupled modes. The fact that the response can be predicted to an accuracy within 0.5dB even when the proposed SEA/ESEA model is invalid, demonstrates that with ESEA it is possible to get the ‘right answer for the wrong reasons’. Therefore, to avoid incorrect subdivisions in practice, it is always necessary to have an estimate of the mode count of the complete volume before subdividing it into more than one subsystem. In the 125Hz band and above there are at least six modes in the single volume and it is reasonable to attempt an SEA/ESEA model.

Figure 6-5 shows the SPL in each subsystem from ray tracing and SEA using ESEA CLFs. SEA using GESEA CLFs and AESEA CLFs are in close agreement with ray tracing which indicates that this subdivision into front and rear spaces is reasonable. The differences in SPL between the two subsystems is 11dB which is sufficiently large to suggest that (a) they are not strongly coupled and (b) that treating a single space as a single space with an average SPL is unlikely to be appropriate when modelling spaces such as car cabins.

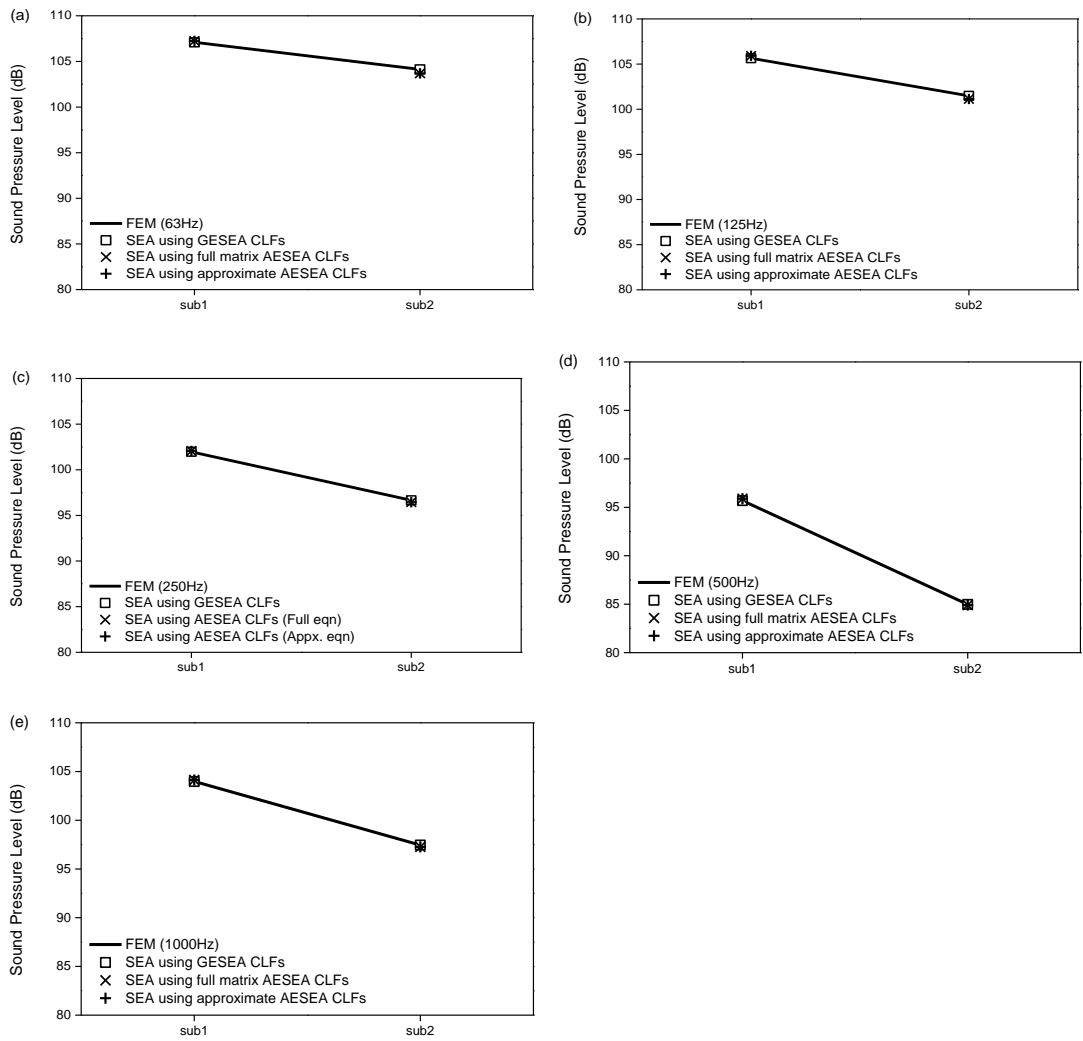


Figure 6-4. Idealised car cabin: Comparisons of SPL in each subsystem from SEA using ESEA with FEM from 63 to 1kHz octave bands. Source: Subsystem 1.

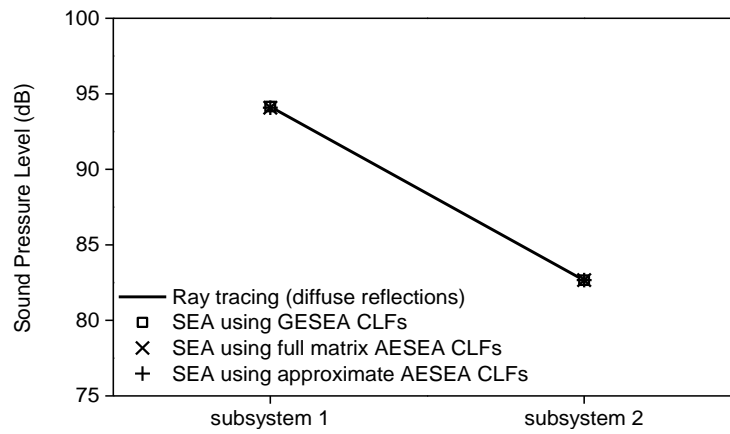


Figure 6-5. Idealised car cabin: Comparison of SPL in each subsystem estimated from SEA using ESEA with ray tracing assuming diffuse reflections. Source: Subsystem 1.

6.2.2 Division into four subsystems

In this section, the cuboid space is subdivided into four subsystems taking two different approaches; 1) using horizontal subdivision of the upper and lower half of the space and 2) using vertical subdivision of left and right half of the space as illustrated in Figure 6-6.

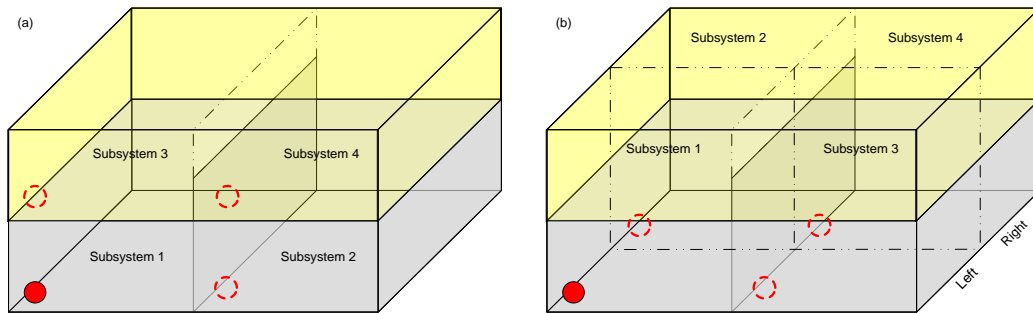


Figure 6-6. Idealised car cabin: SEA model composed of four subsystems (a) horizontal subdivision and (b) vertical subdivision (solid circle: main source position, open circle: additional source positions used for PIM).

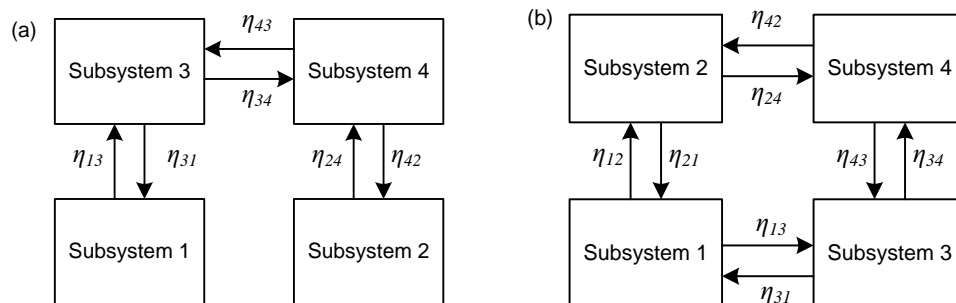


Figure 6-7. Idealised car cabin: Four subsystem SEA model showing only direct coupling between subsystems (a) horizontal subdivision and (b) vertical subdivision.

Two types of four subsystem SEA models are also implemented in FEM at low frequencies and by ray tracing at high frequencies to determine the energy responses in the subsystem. The number of positive and negative CLFs and ILFs are given in Appendices.

At 63Hz, horizontal subdivision is problematic because the complete cuboid volume only has one mode and the TLFs determined from GESEA and ILFs from AESEA

are negative; hence no data is shown in Figure 6-8 (a). Vertical subdivision has similar issues although the ILFs from AESEA are positive and SEA using CLFs from approximate AESEA shows reasonable agreement with FEM in Figure 6-8(f). Hence, as with the two-subsystem model, approximate AESEA gives an estimate even though the use of SEA/ESEA is strictly invalid.

At 125Hz, horizontal subdivision is problematic because direct CLFs determined from full matrix AESEA and ILFs from AESEA are negative; hence no AESEA data is shown in Figure 6-8 (b) and SEA using GESEA CLFs differs from FEM by up to 12dB. In contrast, with vertical subdivision, SEA using approximate AESEA CLFs shows close agreement with FEM.

For 250Hz, 500Hz and 1kHz, there is close agreement (within 1.8dB) between FEM, SEA using GESEA CLFs and SEA using AESEA CLFs for vertical subdivision. This indicates that indirect coupling is not required in order to gain good agreement. However, with horizontal subdivision at 250Hz and 1000Hz, some of the ILFs determined from AESEA using Eq.(2.4.20) have negative values; hence no AESEA data is shown in Figure 6-8 (c) and (e) and agreement between FEM and SEA using GESEA CLFs is only reasonable for subsystems 1, 3 and 4. This problem with negative ILFs with AESEA does not occur at 500Hz and there is close agreement between FEM and SEA using GESEA CLFs. The fact that GESEA gives results at 250Hz, 500Hz and 1000Hz when AESEA does not give results for 250Hz and 1000Hz, indicates that indirect coupling might be required for an accurate SEA model. However, the fact that there is strong indirect coupling between subsystems 1 and 2 casts doubt on whether this indirect coupling is correctly quantified.

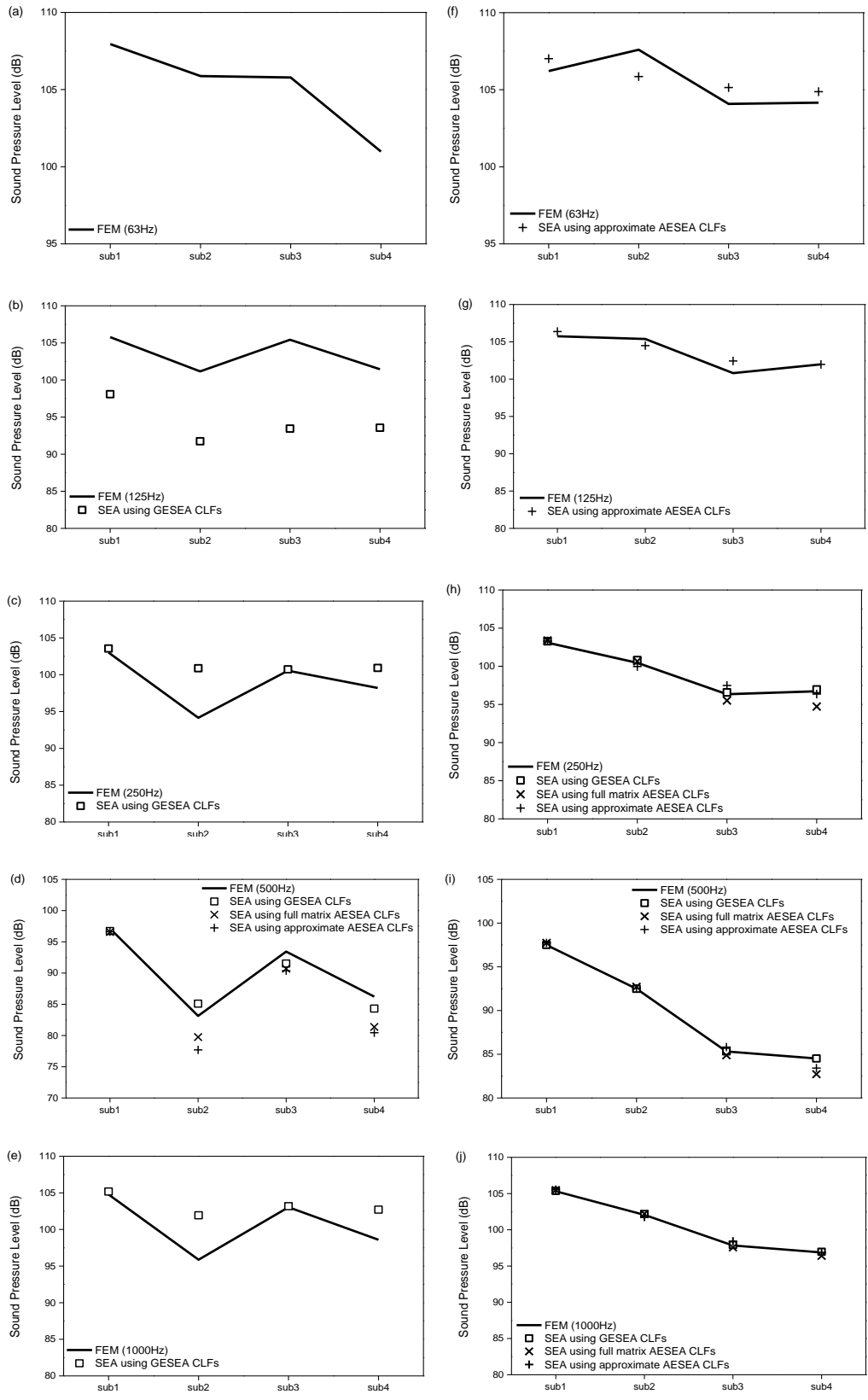


Figure 6-8. Idealised car cabin: Comparisons of SPL in each subsystem from SEA using ESEA with FEM from 63 to 1kHz octave bands for four subsystem SEA models ((a),(b),(c),(d) and (e) are with horizontal subdivision and (f),(g),(h),(i) and (j) are with vertical subdivision). Source: Subsystem 1.

Figure 6-9 (a) shows that with horizontal subdivision the direct CLFs determined from full matrix AESEA and ILFs from AESEA are negative; hence no data is shown. However, Figure 6-9 (b) shows close agreement (within 1.1dB) between ray tracing, SEA using GESEA CLFs and SEA using AESEA CLFs for vertical subdivision.

These results suggest that subdividing into front and rear spaces is reasonable because the difference between the SPL in front and rear subsystems is sufficiently large. However, the differences in SPL between upper and lower subsystems (subsystem 1 and 3 in Figure 6-9 (a)) with horizontal subdivision and between left and right subsystems (subsystems 1 and 2 in Figure 6-9 (b)) with vertical subdivision are <1.7dB; hence these could potentially be treated as a single subsystem even though the absorptive surfaces are significantly different in upper and lower spaces. It is noteworthy that vertical subdivision gives more accurate estimate. The vertical subsystems have surfaces with significantly different absorption coefficients which is not an ideal condition to approximate a diffuse field. It is possible that the existence of a large open boundary between subsystems means that the requirement for uniformly distributed absorption is less critical.

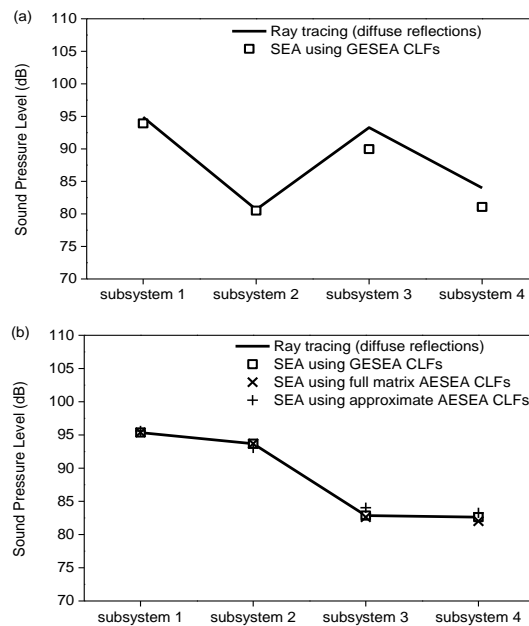


Figure 6-9. Idealised car cabin: Comparison of SPL in each subsystem estimated from SEA using ESEA with ray tracing assuming diffuse reflections (a) horizontal subdivision and (b) vertical subdivision. Source: Subsystem 1.

6.2.3 Division into eight subsystems

In this section, the cuboid space is considered as eight subsystems that is combination of horizontal and vertical subdivisions in the previous section, as illustrated in Figure 6-10.

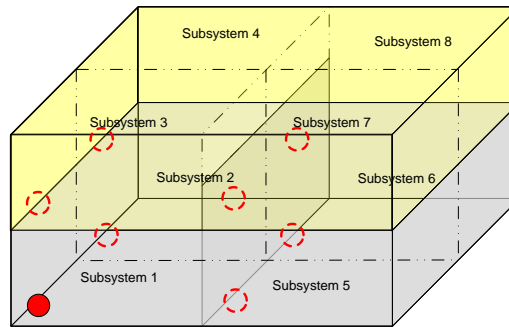


Figure 6-10. Idealised car cabin: SEA model composed of eight subsystems (solid circle: main source position, open circle: additional source positions used for PIM).

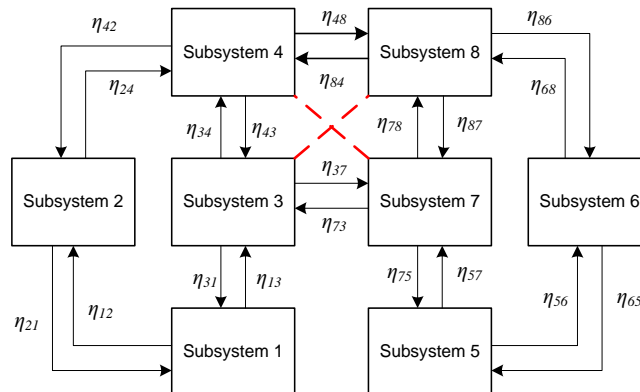


Figure 6-11. Idealised car cabin: Eight subsystem SEA model showing only direct coupling between subsystems. Dashed red lines indicated that two subsystems are not directly coupled by an open area because they are diagonally adjacent but coupling is expected to occur.

Figure 6-12 shows the SPL in each subsystem implemented by FEM and SEA using ESEA CLFs. At 63Hz the TLFs determined from GESEA and ILFs from AESEA are negative; hence no data is shown. At 125Hz there is a similar issue with AESEA; hence no data is shown but SEA using GESEA CLFs does not have negative values.

At and above 250Hz, SEA using AESEA CLFs gives no data because of negative ILFs. However, SEA using GESEA CLFs shows reasonable agreement with FEM except for subsystems 5 and 6 (where there are differences of more than 5dB for 250Hz and 1000Hz). This problem with the prediction for the lower back seat volume also occurred with the four-subsystem model with horizontal subdivision (i.e. subsystem 2 corresponding to subsystems 5 and 6 in the eight-subsystem model) and will now be investigated by looking at the strength of the indirect coupling.

Table 6-3 shows indirect CLFs determined from GESEA and full matrix AESEA. At 500Hz, the direct CLF from a chosen source subsystem is at least 8dB higher than the indirect CLFs from that same source subsystem whereas at 250Hz and 1000Hz it is only 0.6dB higher. As Figure 6-12 shows SEA using GESEA CLFs overestimating the SPL in subsystems 5 and 6, it is likely that the indirect CLFs are overestimated at 250Hz and 1000Hz compared to at 500Hz.

Table 6-4 (a) and (b) show results from SEA path analysis (Eq.(2.4.16)) for the direct and indirect paths between source subsystem 1 and receiving subsystem 5 and between source subsystem 1 and receiving subsystem 6. The lowest energy level difference corresponds to the strongest path. Between subsystems 1 and 5 for 250Hz and 1kHz, it is seen that path $1 \rightarrow 5$ is stronger than $1 \rightarrow 3 \rightarrow 7 \rightarrow 5$ and $1 \rightarrow 2 \rightarrow 4 \rightarrow 7 \rightarrow 5$, and therefore the cause of the overestimate in the SPL is the indirect CLF η_{15} . However, when the SPL is correctly predicted at 500Hz between subsystems 1 and 5, path $1 \rightarrow 5$ is of similar strength to $1 \rightarrow 3 \rightarrow 7 \rightarrow 5$.

Between subsystems 1 and 6 for 250Hz, the strongest path is $1 \rightarrow 5 \rightarrow 6$ but path $1 \rightarrow 3 \rightarrow 8 \rightarrow 6$ is also strong, and both are stronger than $1 \rightarrow 6$ and $1 \rightarrow 2 \rightarrow 4 \rightarrow 8 \rightarrow 6$; therefore the overestimate in the SPL is partly caused by the indirect CLF η_{15} and partly by η_{38} . For 1kHz there are three similarly strong paths, $1 \rightarrow 6$, $1 \rightarrow 5 \rightarrow 6$ and $1 \rightarrow 3 \rightarrow 8 \rightarrow 6$ and the overestimate in the SPL can be attributed to the indirect CLFs η_{15} , η_{16} and η_{38} . In contrast, at 500Hz the paths in Table 6-4 are of similar strength and the estimated SPL is close to FEM (see Figure 6-12 (d)).

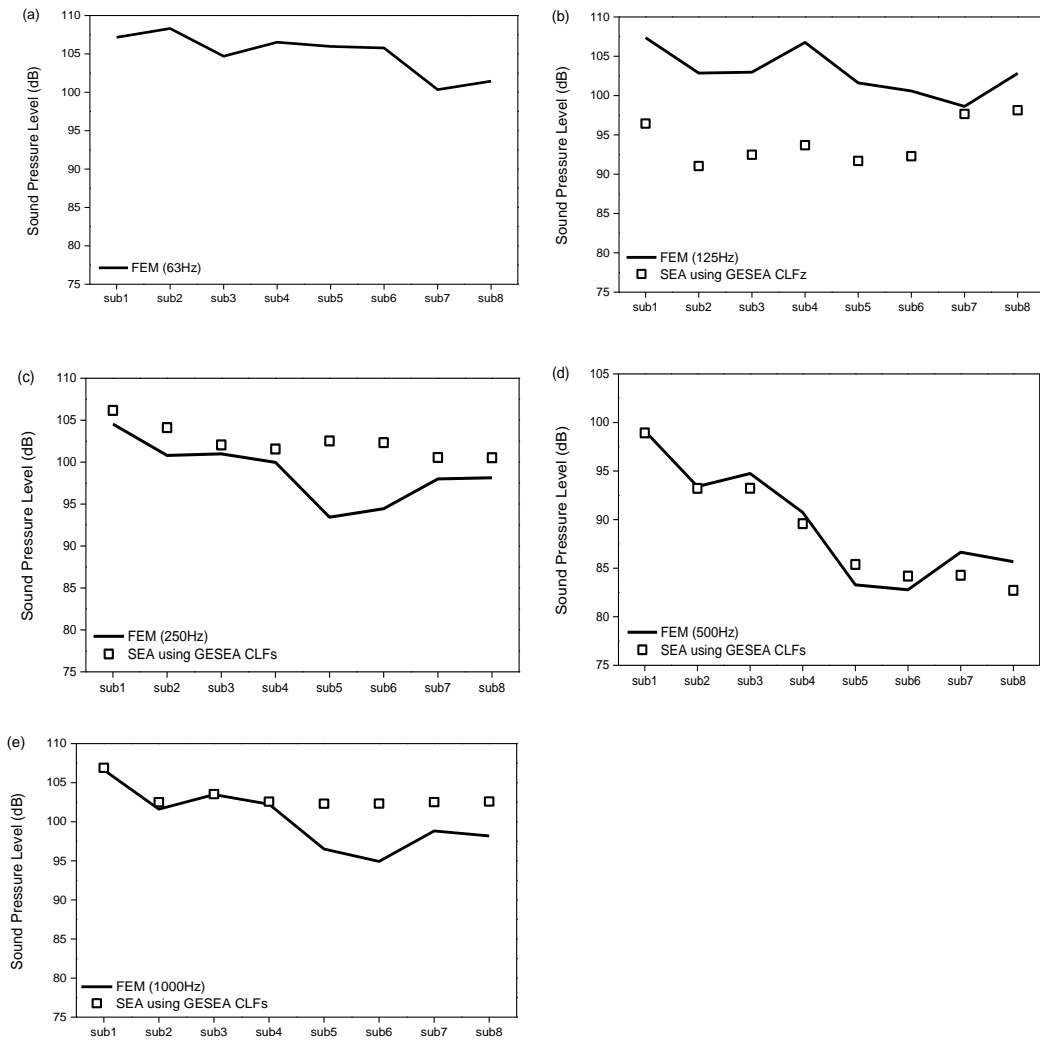


Figure 6-12. Idealised car cabin: Comparisons of SPL in each subsystem from SEA using ESEA with FEM from 63 to 1000Hz octave bands. Source: Subsystem 1.

250Hz dB (re-12)	η_{12}	η_{13}	η_{24}	η_{34}	η_{37}	η_{48}	η_{56}	η_{57}	η_{68}	η_{78}
GESEA	108.7	107.7	107.7	108.8	107.6	107.6	108.0	111.0	111.0	110.7
AESEA	107.6	107.9	107.9	109.0	109.2	109.0	106.5	112.2	111.3	111.8

500Hz dB (re-12)	η_{12}	η_{13}	η_{24}	η_{34}	η_{37}	η_{48}	η_{56}	η_{57}	η_{68}	η_{78}
GESEA	108.7	108.1	108.1	106.5	104.6	104.6	109.1	107.5	107.5	107.7
AESEA	108.4	108.0	108.0	106.0	104.6	104.5	108.4	107.7	107.4	107.6

1kHz dB (re-12)	η_{12}	η_{13}	η_{24}	η_{34}	η_{37}	η_{48}	η_{56}	η_{57}	η_{68}	η_{78}
GESEA	97.7	99.0	98.9	100.9	95.2	95.0	98.3	100.8	100.8	102.2
AESEA	97.8	98.9	98.9	101.1	97.7	97.8	97.8	100.7	100.5	102.4

Table 6-2. Idealised car cabin: Direct CLFs determined from GESEA and full matrix AESEA at 250Hz, 500 Hz and 1kHz octave bands. NB AESEA results using the full matrix and approximation are nominally identical.

250Hz dB (re-12)	η_{15}	η_{16}	η_{25}	η_{26}	η_{38}	η_{47}
GESEA	102.7	87.8	87.8	102.7	107.0	107.0

500Hz dB (re-12)	η_{15}	η_{16}	η_{25}	η_{26}	η_{38}	η_{47}
GESEA	95.4	89.0	89.0	95.4	96.8	96.8

1kHz dB (re-12)	η_{15}	η_{16}	η_{25}	η_{26}	η_{38}	η_{47}
GESEA	90.5	90.3	90.2	90.5	98.5	98.4

Table 6-3. Idealised car cabin: Indirect CLFs determined from GESEA which are as strong as direct CLFs at 250Hz, 500Hz and 1000Hz octave bands.

(a) Transmission path from subsystem 1 to 5

Frequency (Hz)	Energy level difference (dB)		
	Shortest path involving only direct CLFs 1→3→7→5	Shortest path involving only indirect CLFs 1→5	Path involving direct and indirect CLFs (diagonal transmission between subsystems 4 and 7) 1→2→4→7→5
250	18.8	11.4	24.4
500	18.7	19.6	33.4
1000	20.1	13.7	24.1

(b) Transmission path from subsystem 1 to 6

Frequency (Hz)	Energy level difference (dB)			
	Shortest path involving only direct CLFs 1→2→4→8→6	Shortest path involving only indirect CLFs 1→6	Shortest path involving direct and indirect CLFs 1→5→6	Path involving direct and indirect CLFs (diagonal transmission between subsystems 3 and 8) 1→3→8→6
250	23.8	29.2	17.4	19.4
500	25.5	26.5	25.5	26.5
1000	27.5	15.7	19.6	16.8

Table 6-4. Idealised car cabin: Path analysis (a) between subsystem 1 and 5 and (b) between subsystem 1 and 6 for 250Hz, 500Hz and 1000Hz.

Figure 6-13 shows the SPL determined from ray tracing and SEA using ESEA CLFs. SEA using GESEA CLFs gives closer agreement with ray tracing but SEA using AESEA CLFs is not shown due to negative ILFs.

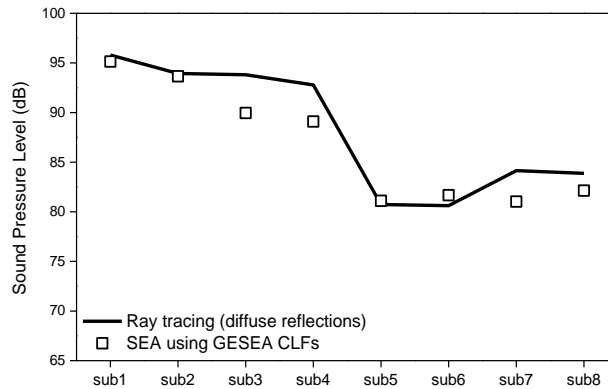


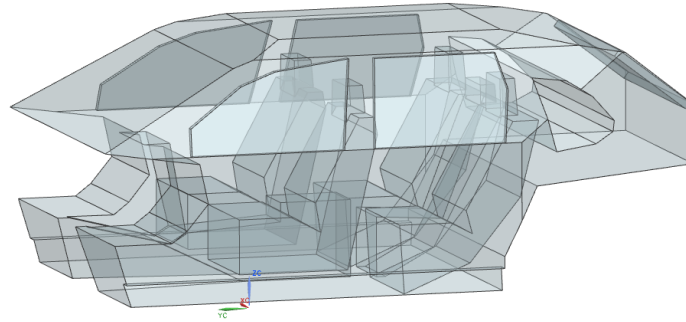
Figure 6-13. Idealised car cabin: Comparison of SPL in each subsystem estimated from SEA using ESEA with ray tracing assuming diffuse reflections. Source: Subsystem 1.

A useful finding was that when there was only one mode, it was sometimes possible to give an estimate (i.e. with the two subsystem model and vertical four subsystem model using CLFs determined from approximate AESEA), even though the use of SEA/ESEA is invalid. Hence, it is necessary to be cautious when using ESEA at low frequencies when the mode count in the octave bands of interest is unknown. The main finding was that in the bands from 250Hz to 1000Hz, the general trend from the four-subsystem model with horizontal subdivision and eight-subsystem model is that SEA using GESEA CLFs gives reasonable agreement with FEM than SEA using AESEA CLFs because AESEA determined negative ILFs for some frequencies. It implies that indirect coupling might be required for an accurate SEA model. For four-subsystem model with vertical subdivision, SEA using GESEA and AESEA CLFs give closest agreement with FEM regardless of frequency band.

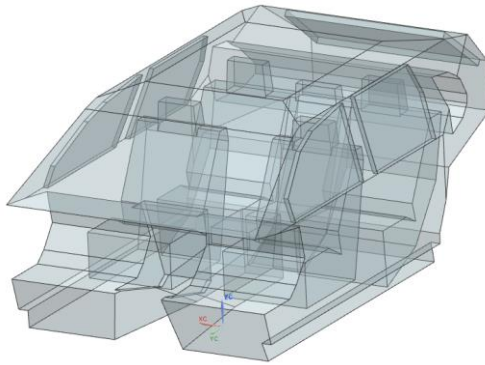
6.3 Numerical experiments based on real car cabin geometry

In the previous section, it was verified that ESEA can also reasonably estimate sound transmission when compact space is modelled as a number of coupled spaces. Now SEA considers a car cabin to assess the validity of ESEA for a complex space.

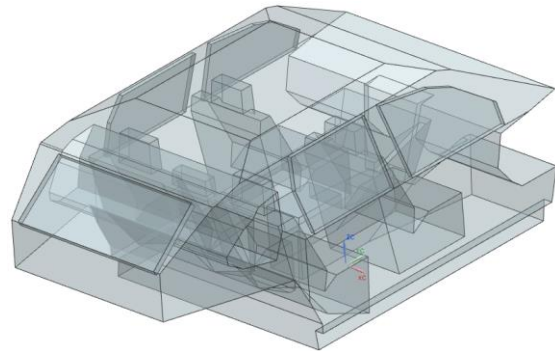
For the car cabin, the cabin geometry corresponds to the interior of a Porsche Cayenne (2009). The CAD file was downloaded from 3D CAD BROWSER [82] but required some simplification by removing some small protrusions. The resulting model is shown in Figure 6-14.



(a) Side view of the car cabin



(b) Front view



(c) Rear view

Figure 6-14. Car cabin model (a) side view of the car cabin, (b) front view of the car cabin and (c) rear view of the car cabin.

6.3.1 Car cabin model

Sound injected inside the cabin can be from a variety of sources [54,83]. These different sound injections can lead to various SPL zones hence further subdivision is required to consider.

The car cabin model in Figure 6-14 can be subdivided into three spaces: front seat volume, rear seat volume and boot volume.

This is adopted in a sense of practical subdivision based on the structural SEA subsystems to which energy is dominantly transmitted and affected. Possible practical reasons to create further subdivisions for the upper/lower parts and left/right sides at the front and rear seat volume are given by Musser [54]:

- 1) Radiated sound from the windscreen could be considered to radiate only into the upper volume in the front of the car

- 2) Radiated sound from the left/right side windows could be considered just to radiate into the upper volume above the seats on the left/right sides
- 3) Tyre-borne vibration causes floor vibration which radiates into the lower volumes
- 4) Glazed roof radiates principally into the upper volumes in the front and rear seating area

Note that the boot is usually an isolated enclosure so it is logical to treat it as a separate subsystem.

For the above reasons, SEA models are considered with the following numbers of subsystems: 1) three subsystems (front seat, rear seat and boot), 2) five subsystems with horizontal subdivision (front upper, front lower, rear upper, rear lower and boot), 3) five subsystems with vertical subdivision (front left, front right, rear left, rear right and boot) and 4) nine subsystems (front left upper, front left lower, front right upper, front right lower, rear left upper, rear left lower, rear right upper, rear right lower and boot).

6.3.2 SEA using ESEA with single point source

Prior to using SEA the mode count of the car cabin in octave bands is calculated with FEM and compared with a statistical estimate for an arbitrary volume by using the first term of Eq. (2.4.8). The comparison is shown in Figure 6-15. In the 250Hz band there are at least 10 modes and by the 1000Hz band there are approximately 1000 modes. Hence if the car cabin is treated as a single subsystem, an SEA model would be feasible at and above 125Hz; however in the next section it will be shown that the difference in SPL between the front and back of the car is sufficiently large that considering a single subsystem is not appropriate. The mode count from FEM is slightly greater than the statistical estimate but at 1000Hz the percentage difference is 34% which indicates that statistical estimates of mode counts in such a complex space are potentially useful.

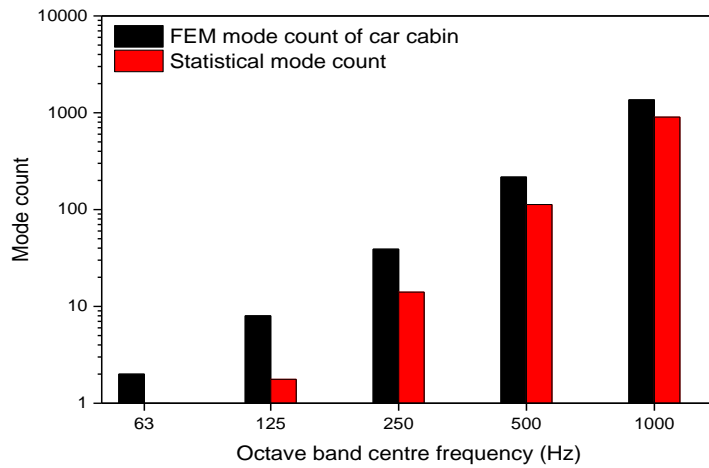


Figure 6-15. Car cabin: Mode count in octave bands.

Figure 6-16 shows possible subdivisions of the car cabin (3.96m³) into SEA subsystems with source positions used to implement PIM for ESEA where each point source is positioned at least 0.2m away from boundaries. Source positions for PIM are near the windscreen ((1),(2) - left/right), driver/passenger leg space ((3),(4),(5),(6) - front left/right, rear left/right), mouth ((7),(8) - left/right) and boot ((9) - centre).

Ray tracing assumes three absorption coefficients for seats, windows and other parts which are $\alpha=0.9$, $\alpha=0.03$ (from ODEON material database in Table 6-5) and $\alpha=0.5$ respectively. FEM modelling used ABAQUS used the same absorption coefficients as the ray tracing except for the windows. This is because glass absorption can significantly vary below 1000Hz depending on frequency hence different values are applied to the analysis in each octave band.

Frequency (Hz)	63	125	250	500	1000	2000	4000	8000
Single pane of glass	0.18	0.18	0.06	0.04	0.03	0.02	0.02	0.02

Table 6-5. Absorption coefficient from ODEON material database for window glass in octave bands.

Using ODEON the spatial average SPL in each subsystem is calculated at grid points with 0.1 spacing in x-, y- and z-direction, which are at least 0.2m away from boundaries.

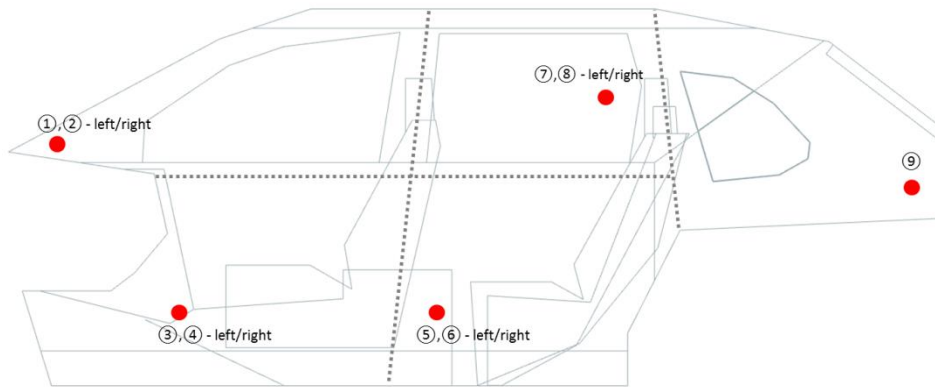


Figure 6-16. Car cabin: Subdivisions for SEA subsystems and source positions for PIM.

6.3.2.1 Three subsystems

The car cabin is initially modelled as three coupled subsystems representing the front seat, rear seat and the boot. The SPL in each subsystem is calculated from ray tracing using a point source near the windscreen in the front seat volume.

Figure 6-17 shows the SPL normalised to the source subsystem in the three subsystems. The difference in SPL between the front and rear seat subsystems is $\approx 6\text{dB}$. This level difference is sufficiently large to indicate that for the purpose of noise control and sound quality assessment it might not be useful to treat the front and rear seat volumes together as a single volume.

The combination of source positions 1, 8 and 9 in Figure 6-16 is used to implement ESEA. Figure 6-18 shows the open area between subsystems and Table 6-7 describes the open areas and volumes of each subsystem.

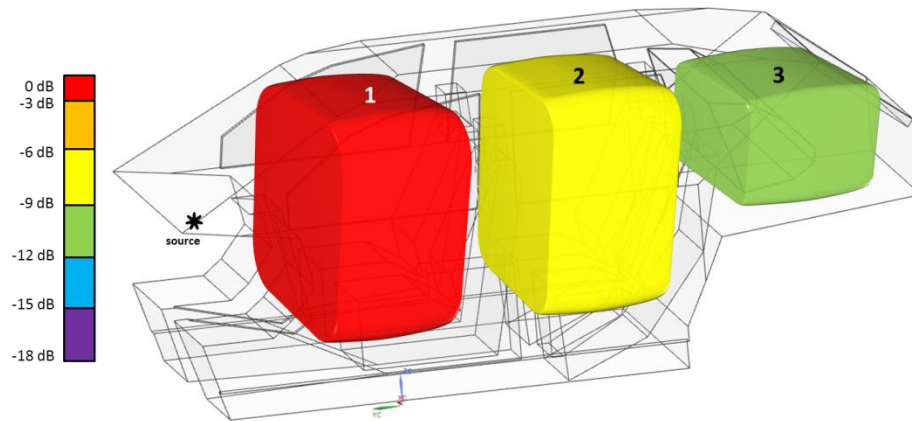


Figure 6-17. Car cabin: Three subsystem model: Ray tracing results in terms of the sound pressure level in each subsystem relative to the source subsystem. Point source in front left subsystem.

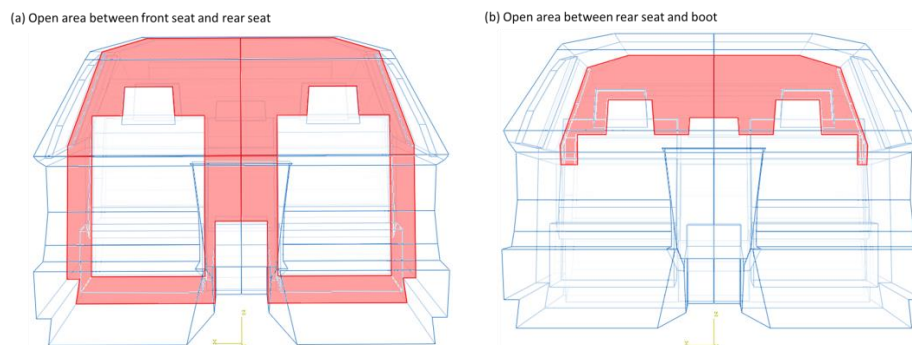


Figure 6-18. Car cabin: Open area (shaded red) between adjacent subsystems (a) front seat to rear seat and (b) rear seat to boot.

Subsystem	SPL in each subsystem relative to the source subsystem (dB)
1	0
2	8.2
3	1.7

Table 6-6. Car cabin: SPL in each subsystem relative to the source subsystem.

Subsystem		Volume (m ³)	Subsystems coupled by open area		Open area (m ²)
1	Front seat	1.71	1 to 2	Front to Rear	1.07
2	Rear seat	1.45	2 to 3	Rear to Boot	0.82
3	Boot	0.8			

Table 6-7. Car cabin: Three subsystem model: subsystem volumes and open area between adjacent subsystems.

6.3.2.2 Five subsystems with horizontal subdivision

In this section, the car cabin is modelled as five coupled subsystems that are front upper, front lower, rear upper, rear lower and the boot respectively. The SPL in each subsystem normalised to the source subsystem is shown in Figure 6-19. Differences between the source subsystem and the four receiving subsystems range from 6dB to 12dB. As with the three-subsystem model, these differences are sufficiently large to be of interest in an assessment for noise control and sound quality.

The combination of source positions 1, 3, 7, 5 and 9 in Figure 6-16 is used to implement ESEA. Figure 6-20 shows the open area between subsystems and Table 6-9 gives the open areas and volumes of each subsystem.

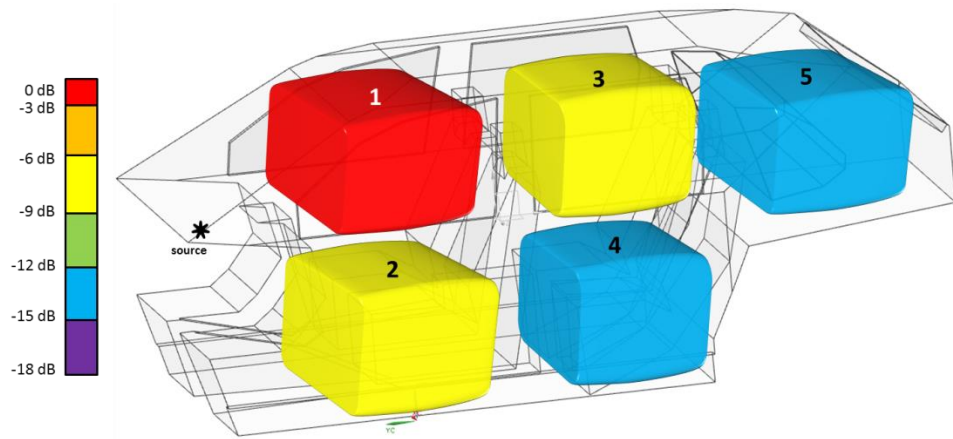


Figure 6-19. Car cabin: Five subsystem model with horizontal subdivision: Ray tracing results in terms of the sound pressure level in each subsystem relative to the source subsystem. Point source in front left subsystem.

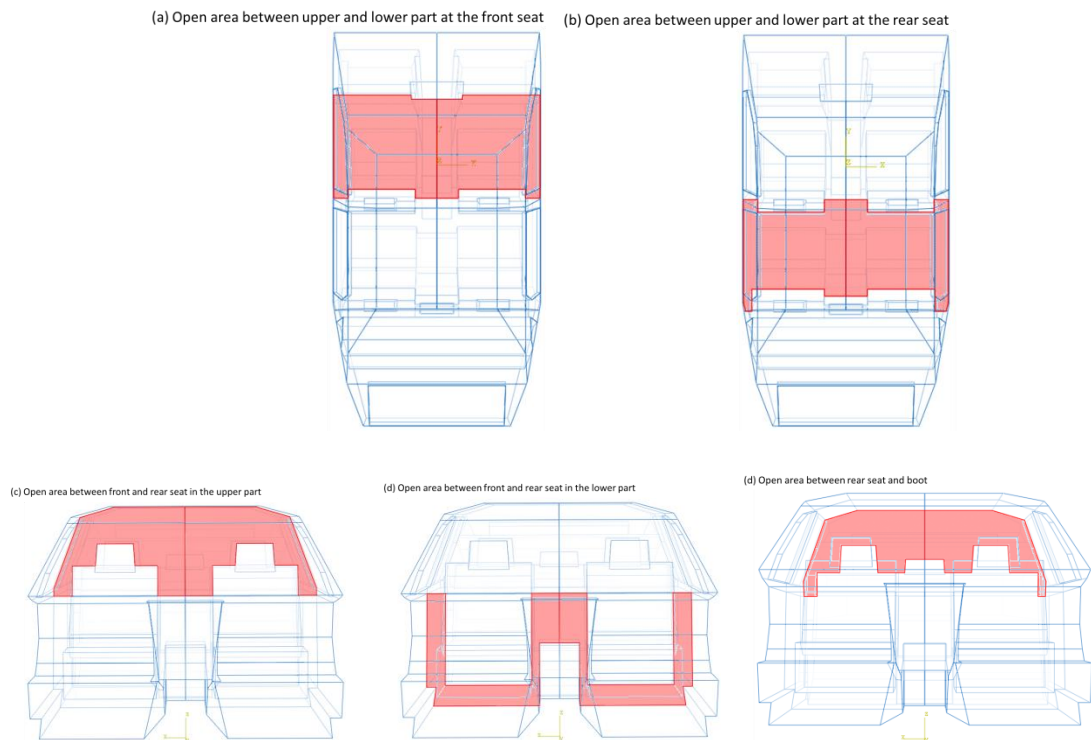


Figure 6-20. Car cabin: Open area (shaded red) between adjacent subsystems (a) Top view of front upper to lower, (b) Top view of rear upper to lower, (c) Cross-section of upper front to rear, (d) Cross-section of lower front to rear and (d) Cross-section of rear to boot.

Subsystem	SPL in each subsystem relative to the source subsystem (dB)
1	0
2	7.1
3	8.2
4	14
5	13.4

Table 6-8. Car cabin: SPL in each subsystem relative to the source subsystem

Subsystem		Volume (m ³)	Subsystems coupled by open area		Open area (m ²)
1	Front_upper	0.84	1 to 3	Upper front-rear	0.6
2	Front_lower	0.88	2 to 4	Lower front-rear	0.47
3	Rear_upper	0.69	1 to 2	Front upper-lower	1.38
4	Rear_lower	0.76	3 to 4	Rear upper-lower	1.23
5	Boot	0.8	3 to 5	Rear upper – Boot	0.53

Table 6-9. Car cabin: Five subsystem model with horizontal subdivision: subsystem volumes and open area between adjacent subsystems.

6.3.2.3 Five subsystems with vertical subdivision

In this section, the cabin is again partitioned into five subsystems, but using a vertical subdivision into front left, front right, rear left, rear right and the boot. Figure 6-21 shows the SPL in each subsystem normalised to the source subsystem. Compared to five subsystems with horizontal subdivision (refer back to Figure 6-19) it is seen that (a) the SPL difference between the two subsystems in the front of the cabin is only ≈ 3 dB rather than ≈ 6 dB and (b) there is no difference between the two subsystems in the rear of the cabin (this was previously observed with the cuboid space using vertical subdivision into five subsystems in Section 6.2.2).

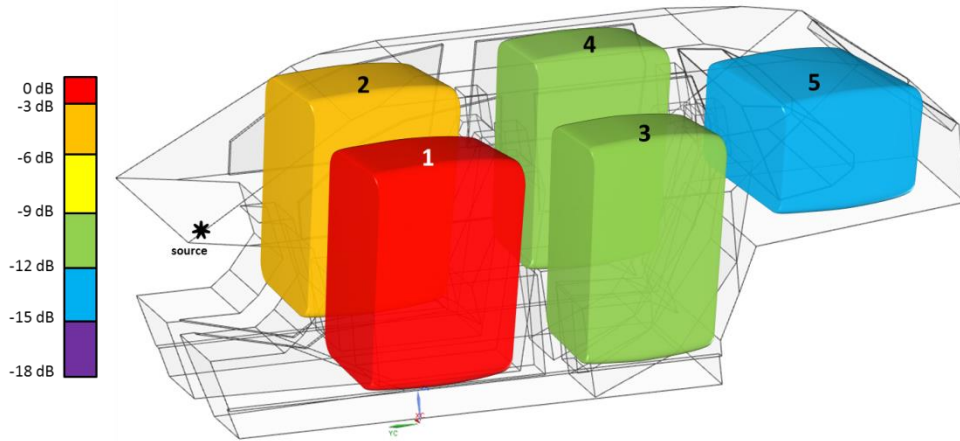


Figure 6-21. Car cabin: Five subsystem model with vertical subdivision: Ray tracing results in terms of the sound pressure level in each subsystem relative to the source subsystem. Point source in front left subsystem.

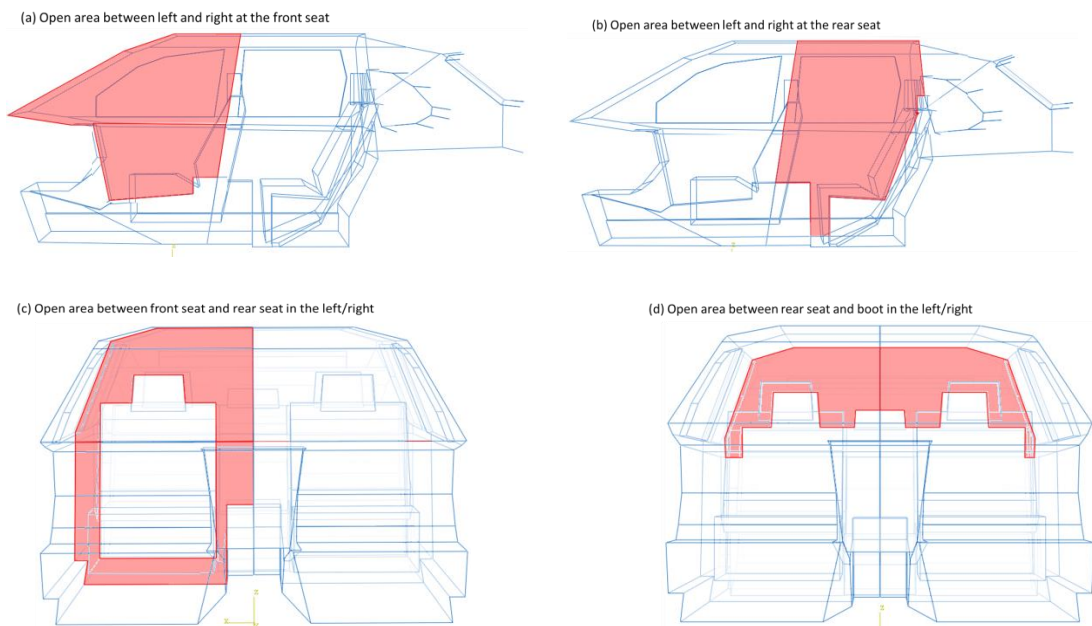


Figure 6-22. Car cabin: Open area (shaded red) between adjacent subsystems (a) front side, (b) rear side, (c) Cross-section of front to rear (left/right) and (d) Cross-section of rear to boot (left/right).

Subsystem	SPL in each subsystem relative to the source subsystem (dB)
1	0
2	5.2
3	10.9
4	9.6
5	13.7

Table 6-10. Car cabin: SPL in each subsystem relative to the source subsystem.

The combination of source positions 1, 2, 7, 8 and 9 in Figure 6-16 is used to implement ESEA. Figure 6-22 gives the open area between subsystems and Table 6-11 describes the open areas and volumes of each subsystem.

Subsystem		Volume (m ³)	Subsystems coupled by open area		Open area (m ²)
1	Front_left	0.86	1 to 2	Front side	0.86
2	Front_right	0.86	3 to 4	Rear side	0.84
3	Rear_left	0.73	1 to 3 (2 to 4)	Front – Rear (left/right)	0.53
4	Rear_right	0.73	3 to 5 (4 to 5)	Rear – Boot (left/right)	0.27
5	Boot	0.8			

Table 6-11. Car cabin: Five subsystem model with vertical subdivision: subsystem volumes and open area between adjacent subsystems.

6.3.2.4 Nine subsystems

In this section, the car cabin is modelled as nine coupled subsystems that are front left upper, front left lower, front right upper, front right lower, rear left upper, rear left lower, rear right upper, rear right lower and boot respectively. The results are shown in Figure 6-23. From the perspective of the engineer assessing noise and

sound quality, the subsystems of interest are primarily those subsystems which contain the passenger's head (i.e. subsystems 1, 3, 5, and 7). However, in order to carry out noise control it is necessary to be able to identify those regions with high sound pressure levels that contribute to the noise at the passenger's head by using path analysis. For this reason, it is potentially useful to subdivide the cabin into several subsystems.

The combination of source positions 1, 2, 3, 4, 7, 8, 5, 6 and 9 in Figure 6-16 is used for the implementation for ESEA. Figure 6-24 shows the open area between subsystems and Table 6-13 describes the open areas and volumes of each subsystem.

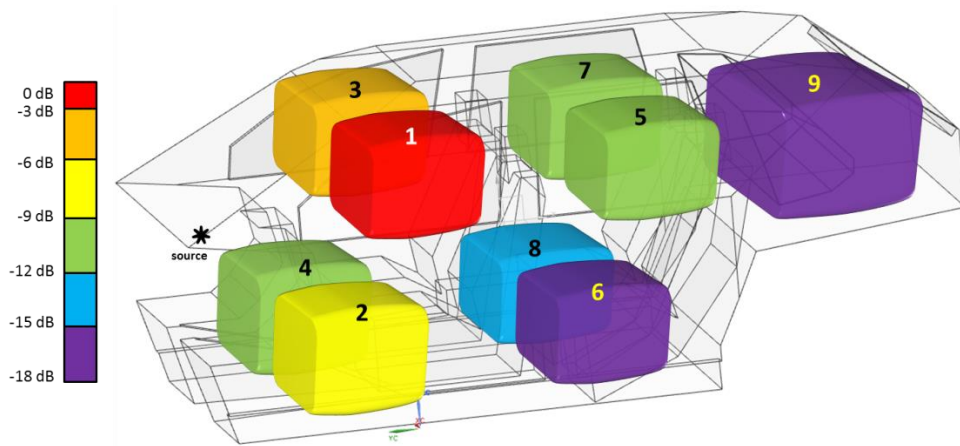


Figure 6-23. Car cabin: Nine subsystem model: Ray tracing results in terms of the sound pressure level in each subsystem relative to the source subsystem. Point source in front left subsystem.

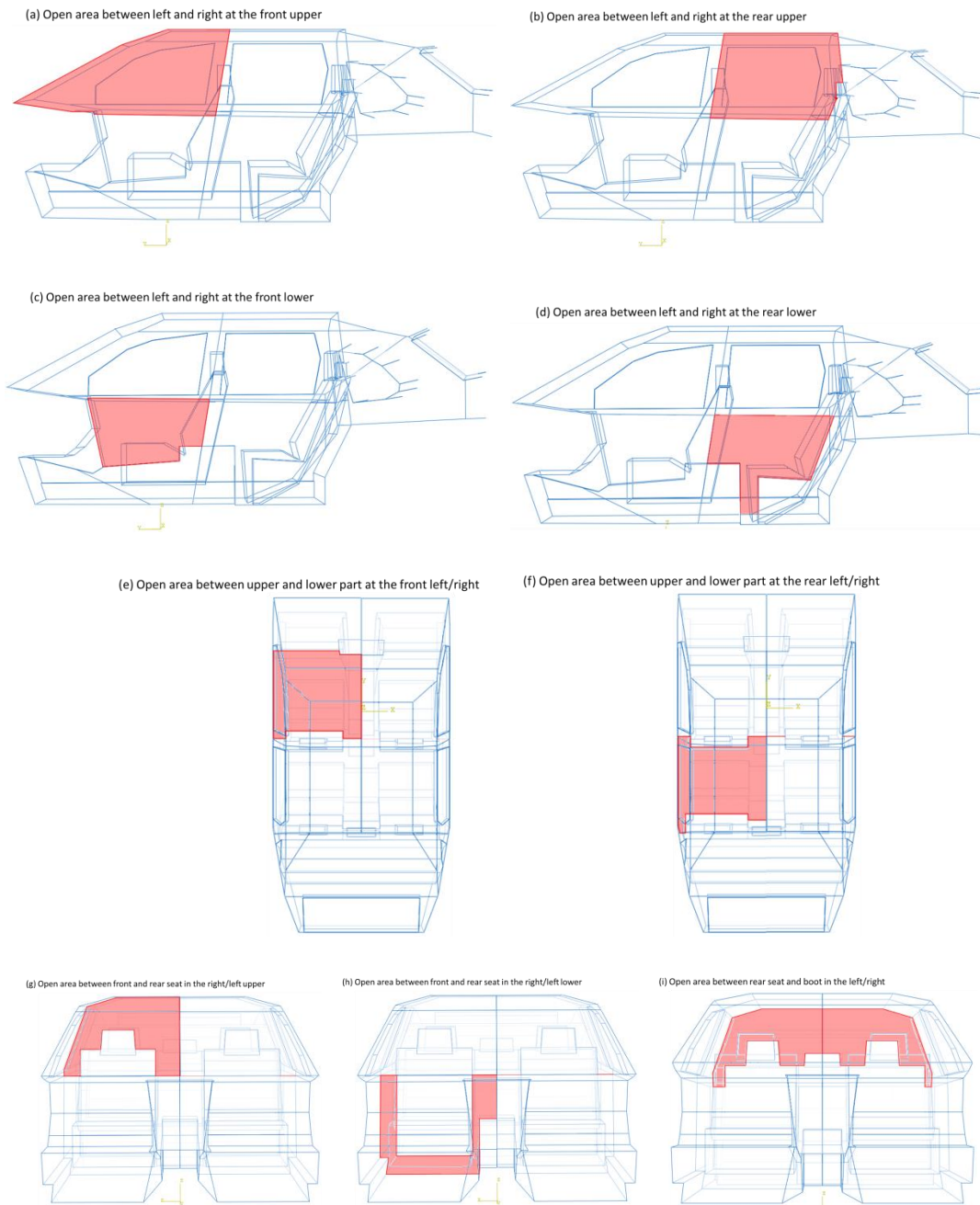


Figure 6-24. Car cabin: Open area (shaded red) between adjacent subsystems (a) front side upper, (b) rear side upper, (c) front side lower, (d) rear side lower, (e) front upper-lower (left/right), (f) rear upper-lower (left/right), (g) upper front-rear (left/right), (h) lower front-rear (left/right) and (i) rear-boot (left/right).

Subsystem	SPL in each subsystem relative to the source subsystem (dB)
1	0
2	7.8
3	5.5
4	11.4
5	10.7
6	18.3
7	9.9
8	14.6
9	15.5

Table 6-12. Car cabin: SPL in each subsystem relative to the source subsystem.

Subsystem		Volume (m ³)	Subsystems coupled by open area		Open area (m ²)
1	Front_left_upper	0.42	1 to 3	Front side upper	0.55
2	Front_left_lower	0.44	5 to 7	Rear side upper	0.49
3	Front_right_upper	0.42	2 to 4	Front side lower	0.31
4	Front_right_lower	0.44	6 to 8	Rear side lower	0.35
5	Rear_left_upper	0.34	1 to 2 (3 to 4)	Front upper-lower (left/right)	0.67
6	Rear_left_lower	0.38	5 to 6 (7 to 8)	Rear upper-lower (left/right)	0.61
7	Rear_right_upper	0.34	1 to 5 (3 to 7)	Upper front-rear (left/right)	0.3
8	Rear_right_lower	0.38	2 to 6 (4 to 8)	Lower front-rear (left/right)	0.23
9	Boot	0.8	5 to 9 (7 to 9)	Rear-boot (left/right)	0.27

Table 6-13. Car cabin: Nine subsystem model: subsystem volumes and open area between adjacent subsystems.

6.3.3 SEA using ESEA with surface source

In a real car cabin, the majority of sound is likely to come into the space through various surfaces radiation such as windscreen, windows, glazed roof, etc [52,55]. From this point of view, surface source using ray tracing is implemented to reproduce close to the realistic environment of the car cabin as described in Figure 6-25.

The radiation sources that are windscreen, front/rear side windows and floor are carried out for four SEA subsystem models described in the previous section. A radiation power of 0.01W (WS-windscreen), 0.01W (FSW-front side window left/right), 0.005W (RSW-rear side window left/right) and 0.01W (Floor) is injected in each subsystem respectively. The implementation of PIM for ESEA uses point sources as described in Sections 6.3.2.

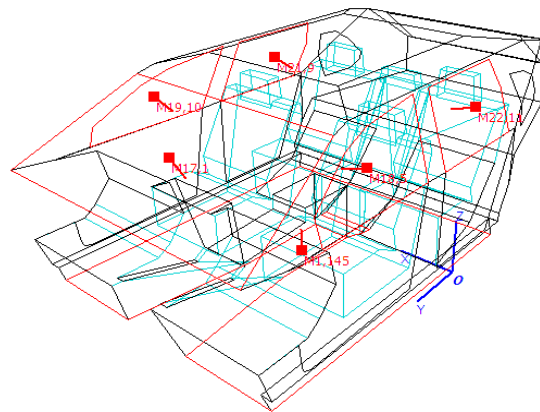


Figure 6-25. Car cabin: Red lines indicate the surface sources.

6.3.4 ESEA results

Four SEA models are implemented using FEM and ray tracing with a point source assuming diffuse reflections.

For the low- and mid-frequency range represented by octave bands from 63Hz to 1000Hz, FEM data is used as input for ESEA with. Sound pressure levels in FEM are calculated at each mesh point. The spatial average is fulfilled at each subsystem volume, also averaged into octave bands. Figure 6-26 to Figure 6-30 show the SPL in each subsystem determined from FEM for comparison with SEA using GESEA CLFs and SEA using AESEA CLFs.

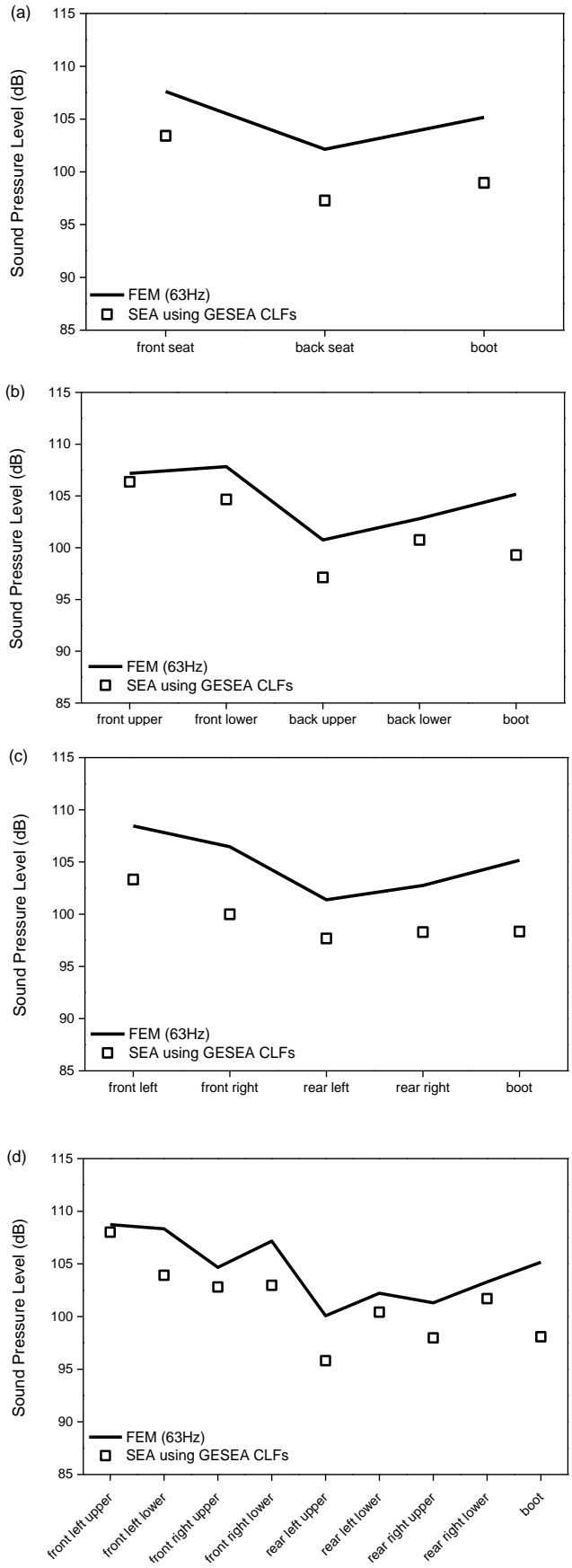


Figure 6-26. Car cabin: 63Hz octave band. Point source in front left subsystem.

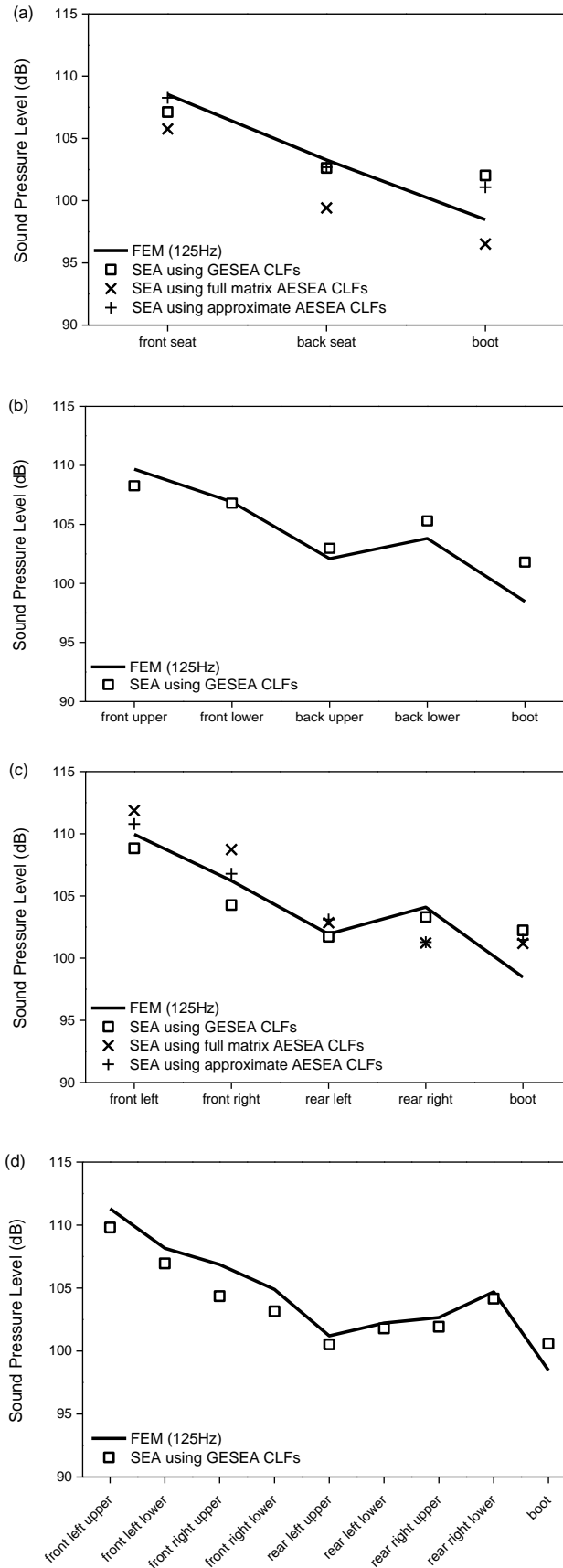


Figure 6-27. Car cabin: 125Hz octave band. Point source in front left subsystem.

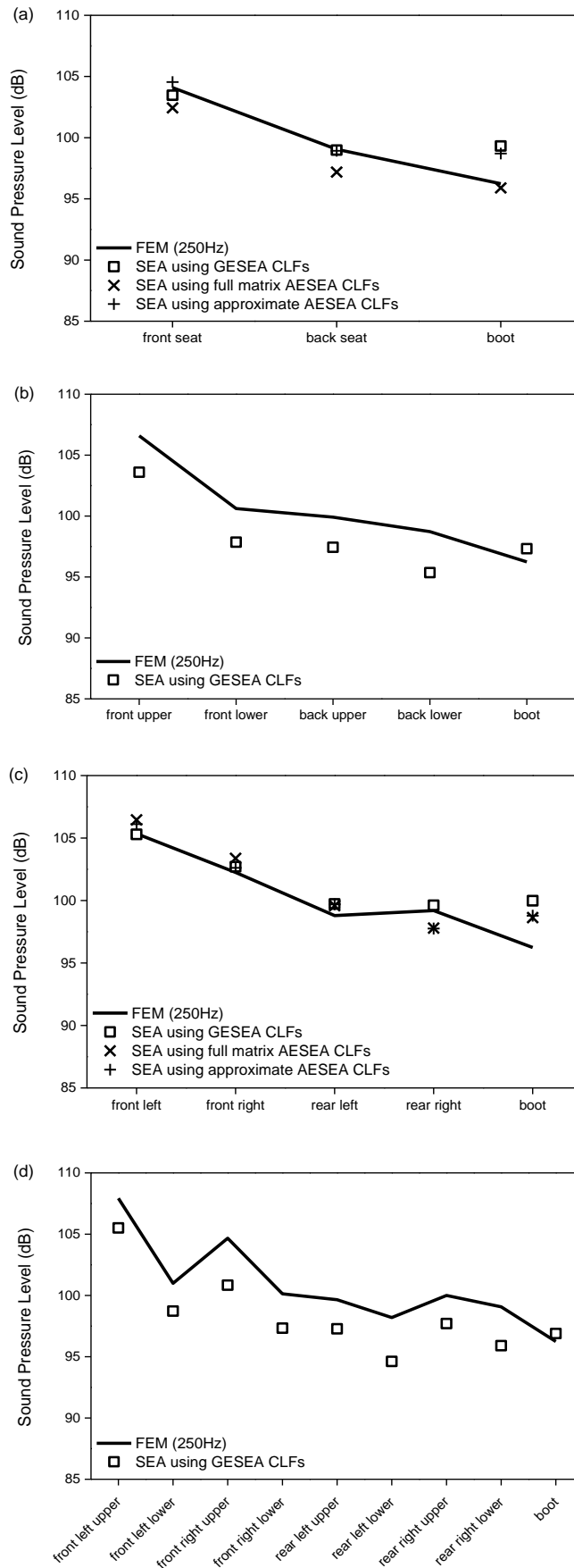


Figure 6-28. Car cabin: 250Hz octave band. Point source in front left subsystem.

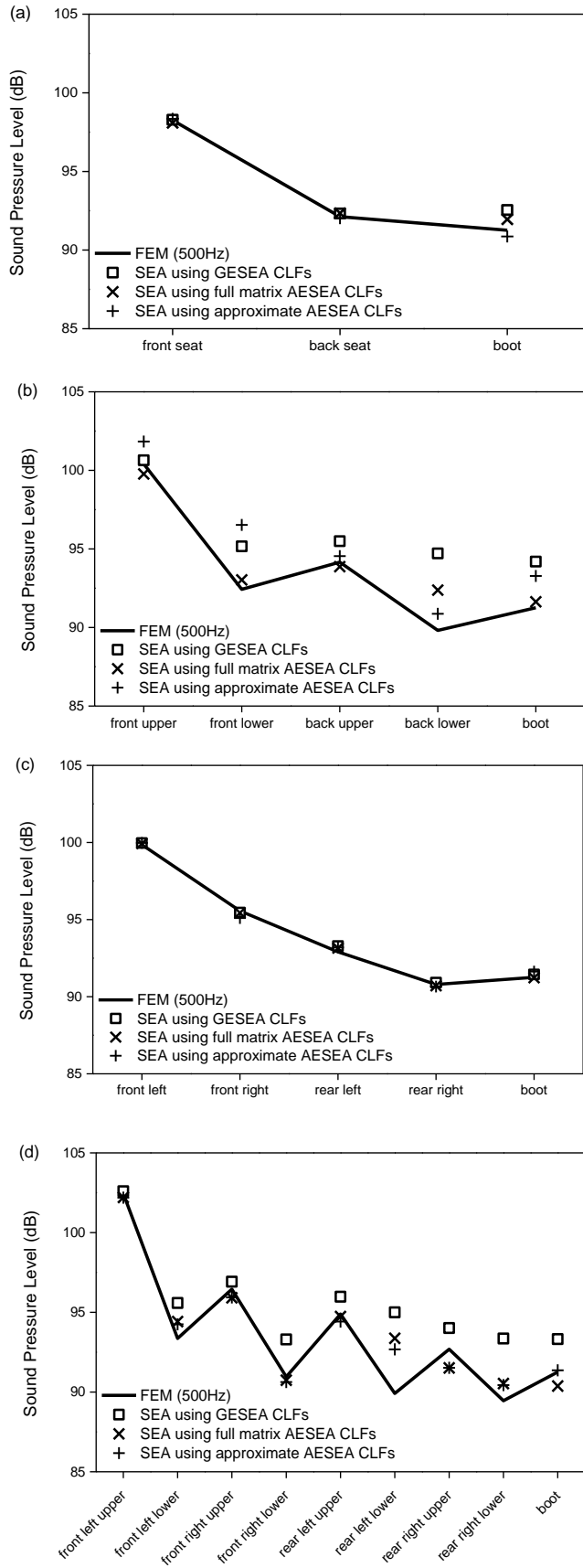


Figure 6-29. Car cabin: 500Hz octave band. Point source in front left subsystem.

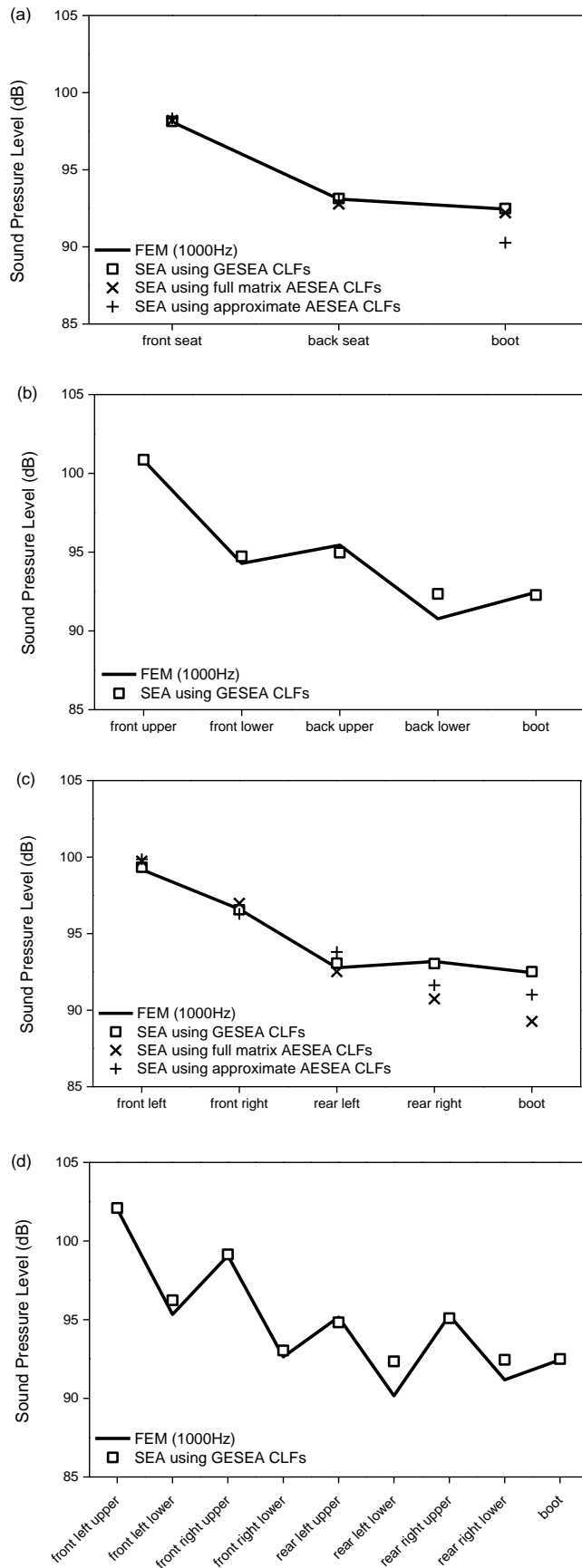


Figure 6-30. Car cabin: 1kHz octave band. Point source in front left subsystem.

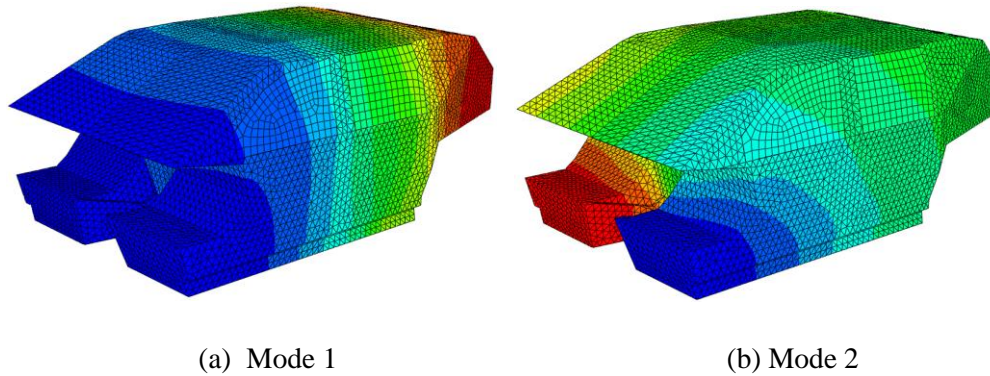


Figure 6-31. Car cabin: Eigenmodes within 63Hz octave band

When the cabin is considered as a single volume there are only two modes in the 63Hz octave band (refer back to Figure 6-15). For this reason it is expected that using SEA and ESEA CLFs could be problematic. As with the idealised cuboid space AESEA CLFs gives no data because of negative ILFs. Figure 6-26 shows SEA using GESEA CLFs gives reasonable agreement with FEM. However, it is physically implausible to divide the space into several subsystems when there are only two modes.

At and above 125Hz, the general finding for all models is that SEA using GESEA CLFs tends to be in closer agreement with FEM than SEA using two forms of AESEA CLFs. For the three- and five-subsystem models with vertical subdivision, SEA using GESEA is in closer agreement with FEM than SEA using AESEA CLFs. It is only at 500Hz that there are AESEA CLFs available for the five-subsystem model with horizontal subdivision and the nine-subsystem model. The general conclusion is that indirect coupling is usually required to provide close agreement.

To represent the high-frequency range above 1kHz, ray tracing data is used which gives a frequency-independent result because the absorption coefficients tend to be frequency-independent, as given in Table 6-5. The SPL in each subsystem determined from ray tracing is compared with SEA using GESEA and AESEA CLFs in Figure 6-32.

Figure 6-32 (a) shows the three-subsystem model for which SEA using GESEA CLFs and AESEA CLFs is in close agreement with ray tracing.

For five-subsystem model with horizontal subdivision (Figure 6-32 (b)) and nine-subsystem model (Figure 6-32 (d)), SEA using GESEA CLFs is in close agreement with ray tracing but no data is shown from SEA using AESEA CLFs due to negative ILFs.

For five-subsystem model with vertical subdivision, Figure 6-32 (c) shows that SEA using GESEA CLFs gives closer agreement with ray tracing than SEA using AESEA CLFs especially rear right seat (subsystem 4) shows a difference of ≈ 5 dB between ray tracing and SEA using AESEA CLFs. This subsystem is diagonally opposite the source subsystem; hence the direct field from the point source could affect that receiving subsystem.

Table 6-14 shows the differences between the direct CLFs determined from ESEA (GESEA and AESEA) and that predicted assuming an open area with a transmission coefficient of unity (Eq.(2.4.9)). As in Chapter 5, the standard deviation of the direct CLFs determined from ESEA is used to identify the optimal form of ESEA. Compared to the corridor, the open area differs for all coupled volumes of the car cabin.

For the three-subsystem model, Table 6-14 (a) shows that the standard deviation of the direct CLFs is the same for GESEA, approximate AESEA and full matrix AESEA, and that GESEA and AESEA give the same CLFs (within 0.1dB).

For five-subsystem with vertical subdivision, Table 6-14 (b) shows that 1) GESEA CLFs had the highest standard deviation which indicates that using the standard deviation as an indicator may not be sufficient and 2) the direct CLFs determined from GESEA and two versions of ASEA are similar to each other except for two direct CLFs, η_{13} and η_{24} . This indicates that direct CLFs determined from approximate AESEA are likely to be correct but indirect CLFs should be considered to provide more accurate values.

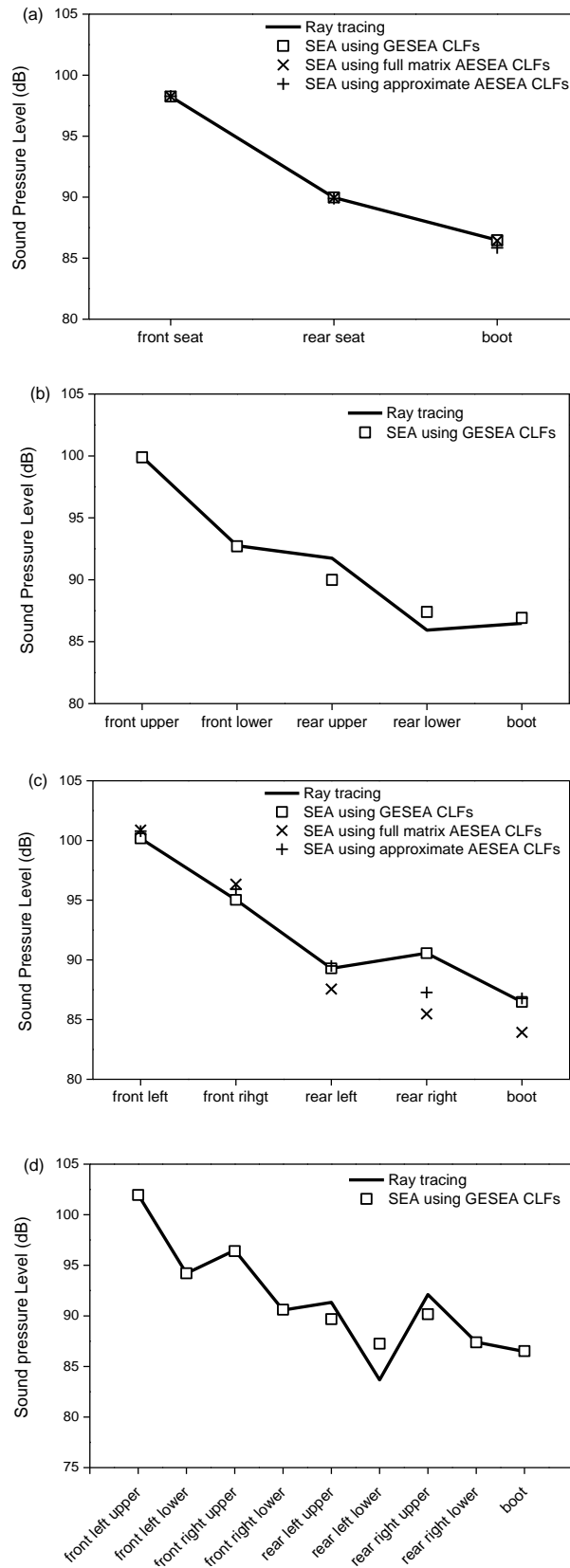


Figure 6-32. Car cabin: SPL in each subsystem estimated from SEA using ESEA and ray tracing in terms of (a) three subsystems, (b) five subsystems with horizontal subdivision, (c) five subsystems with vertical subdivision and (d) nine subsystems. Point source in front left subsystem.

(a) Three subsystems

	Difference between the ESEA CLFs and the predicted CLF		σ (dB)
	$10\lg(\eta_{\text{ESEA}} / \eta_{\text{Predicted}})$ (dB)		
	η_{12} (front-rear)	η_{23} (rear-boot)	
GESEA	-1.0	2.1	2.2
Approximate AESEA	-1.1	2.0	2.2
Full matrix AESEA	-0.9	2.1	2.2

(b) Five subsystems with vertical subdivision

	Difference between the ESEA CLFs and the predicted CLF						σ (dB)
	$10\lg(\eta_{\text{ESEA}} / \eta_{\text{Predicted}})$ (dB)						
	η_{12} (front side)	η_{34} (rear side)	η_{13} (left front- rear)	η_{24} (right front- rear)	η_{35} (left rear- boot)	η_{45} (right rear-boot)	
GESEA	1.9	3.0	-8.0	-9.3	3.5	3.0	6.0
Approximate AESEA	1.7	2.5	-2.2	-2.6	4.7	4.4	3.2
Full matrix AESEA	2.0	3.1	-4.5	-5.4	3.5	3.0	4.1

Table 6-14. Car cabin: Difference between the direct CLFs determined from ESEA and from predicted SEA in dB and standard deviation (σ) in dB for (a) three subsystems and (b) five subsystems with vertical subdivision.

Figure 6-33 to Figure 6-36 show SPL in each subsystem determined from ray tracing with surface sources, SEA using GESEA CLFs and SEA using two versions of AESEA CLFs (full matrix and approximate). However, the ESEA CLFs in the SEA models were determined using a point source. Hence, this section assesses whether this causes any issues.

Figure 6-33 shows the results with a windscreen surface source. SEA using GESEA CLFs gives closest agreement with ray tracing. Note that the point source position used for PIM was near the windscreen and therefore (similarly to the conclusion in chapter 5), better results tend to occur when the actual source position corresponds to one which is used in the PIM ESEA process. For the five-subsystem model with vertical subdivision, SEA using GESEA CLFs and SEA using approximate AESEA CLFs both show close agreement; hence inclusion of indirect coupling does not seem to be essential.

These results indicate that indirect coupling is not essential to get close agreement in the rear right subsystem (subsystem 4) for five-subsystem with vertical subdivision whereas it was essential with the point source (Figure 6-32).

SEA using AESEA CLFs did not give data due to negative ILFs with the five-subsystem model with horizontal subdivision and the nine-subsystem model but Figure 6-33 (b) and (d) shows that there is close agreement between ray tracing and SEA using GESEA CLFs.

Figure 6-34 shows the results with a floor surface source. For the three-subsystem model and the five-subsystem model with vertical subdivision, SEA using AESEA CLFs and SEA using GESEA CLFs are in less agreement with ray tracing than with the windscreen surface source. This can be attributed to the use of a point source position used in PIM which is in the upper part of each subsystem, and this seems to give CLFs that are unrepresentative of the situation where the source is near the floor. As assessed in Chapter 5 for the corridor with staggered barriers, the source position in the source subsystem is an important factor with ESEA. However, the error between ray tracing and the different ESEA models is approximately <5dB (except for the boot subsystem). In general, SEA using ESEA CLFs (GESEA and two versions of AESEA) is in reasonable agreement with the ray tracing.

Figure 6-35 and Figure 6-36 show shows the results with floor and windscreen surface sources and with windscreen, floor and front/rear side window surface sources, respectively. In both cases, SEA using CLFs estimated from GESEA and AESEA is in close agreement with ray tracing for three- and five-subsystem with vertical subdivision. For the five-subsystem model with horizontal subdivision and nine-subsystem model, SEA using GESEA CLFs is in closer agreement with ray tracing.

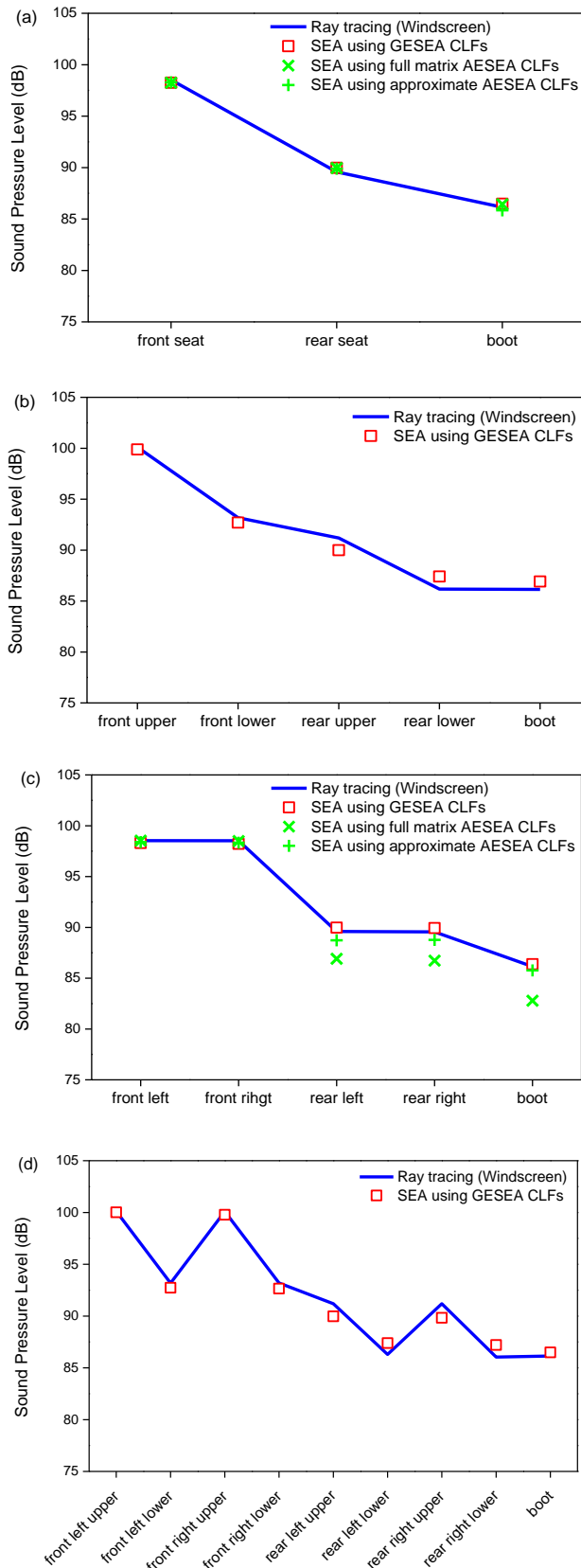


Figure 6-33. Car cabin: SPL in each subsystem estimated from SEA using ESEA and ray tracing in terms of (a) three subsystems, (b) five subsystems with horizontal subdivision, (c) five subsystems with vertical subdivision and (d) nine subsystems. WS surface source in front left and right subsystems.

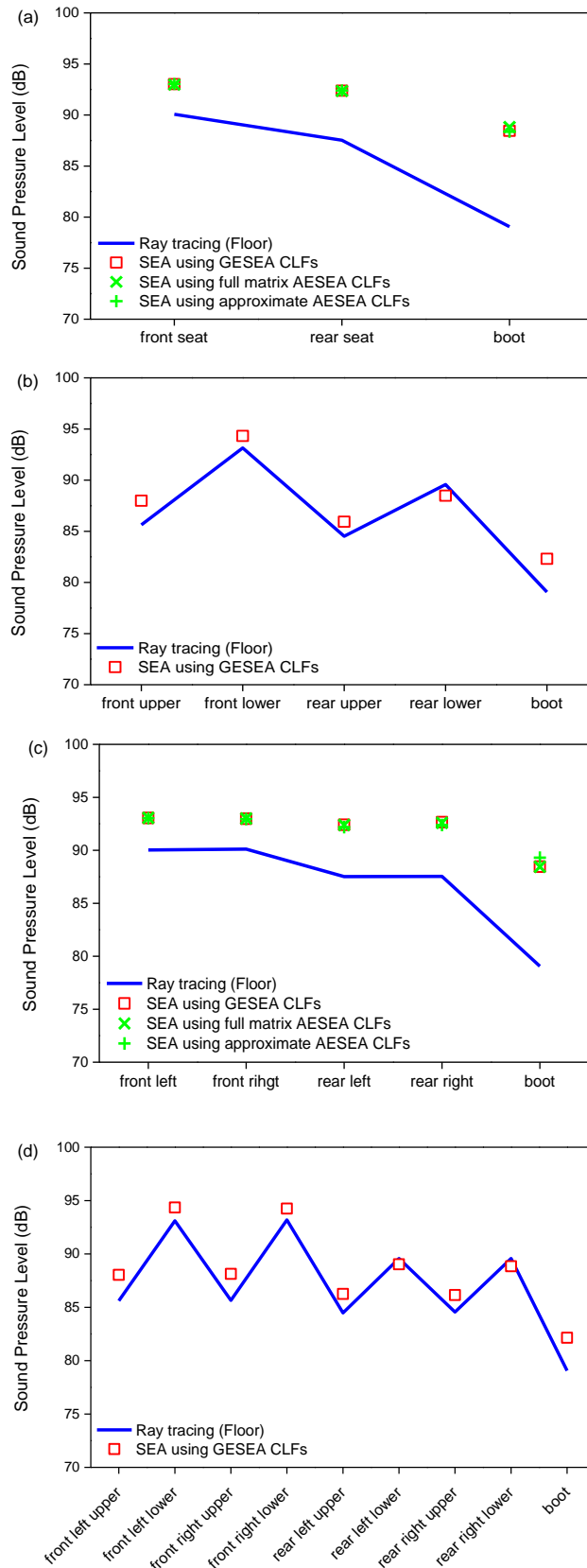


Figure 6-34. Car cabin: SPL in each subsystem estimated from SEA using ESEA and ray tracing in terms of (a) three subsystems, (b) five subsystems with horizontal subdivision, (c) five subsystems with vertical subdivision and (d) nine subsystems. Floor surface source in front left/right and rear left/right subsystems.

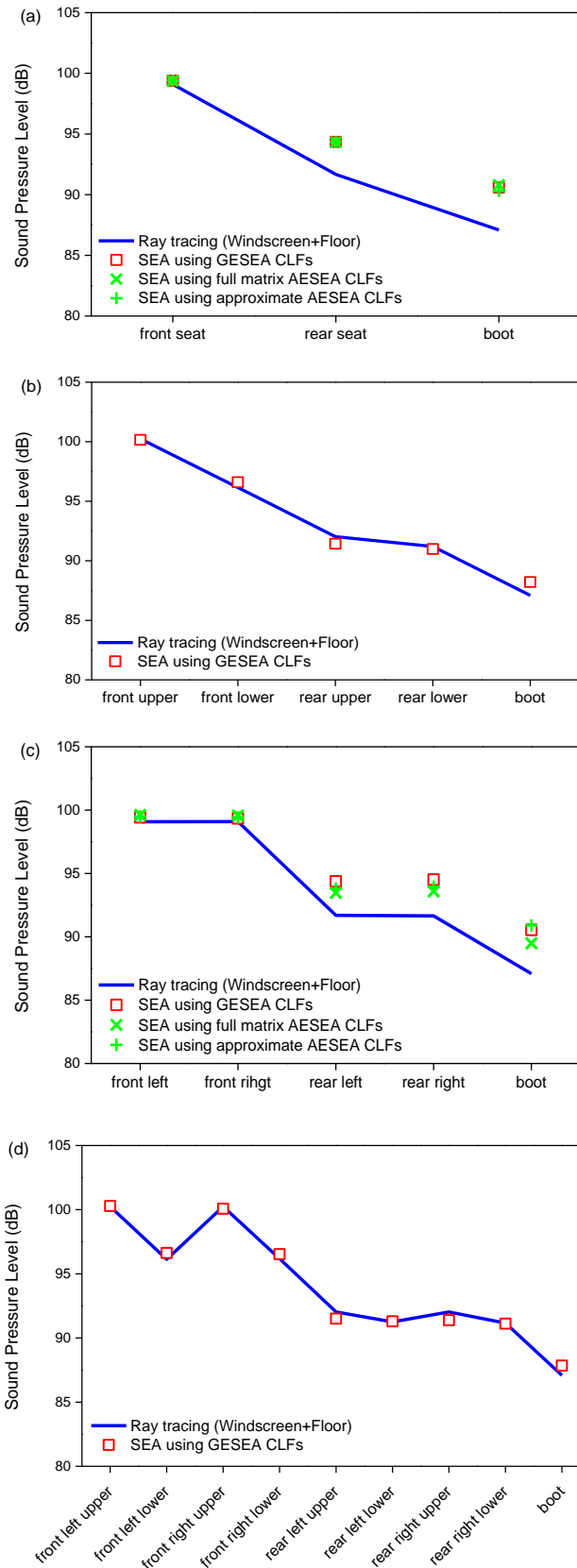


Figure 6-35. Car cabin: SPL in each subsystem estimated from SEA using ESEA and ray tracing in terms of (a) three subsystems, (b) five subsystems with horizontal subdivision, (c) five subsystems with vertical subdivision and (d) nine subsystems. WS+Floor surface sources in front left/right and rear left/right subsystems.

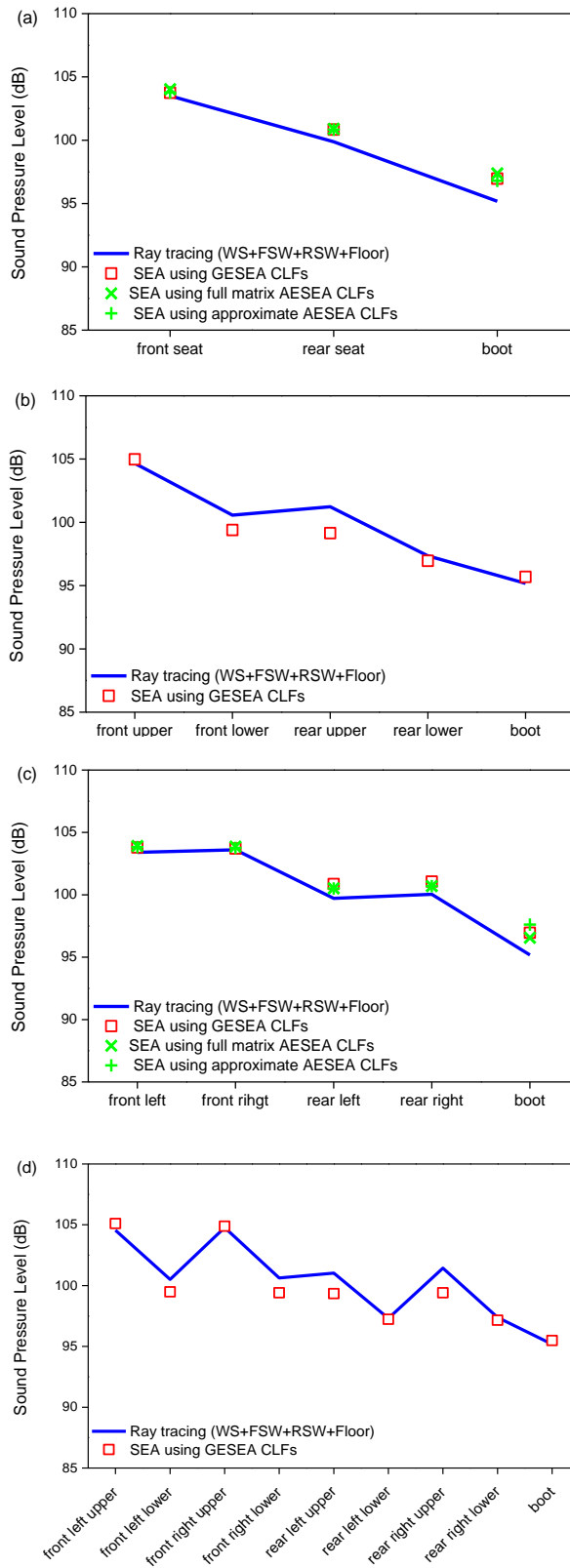


Figure 6-36. Car cabin: SPL in each subsystem estimated from SEA using ESEA and ray tracing in terms of (a) three subsystems, (b) five subsystems with horizontal subdivision, (c) five subsystems with vertical subdivision and (d) nine subsystems.

WS+FSW+RSW+Floor surface sources in front left/right and rear left/right subsystems.

6.4 Conclusions

In this chapter, ESEA has been used on a rectangular cuboid space and car cabin model which are representative of a compact and complex space. Octave band analysis was carried out for which the 63Hz band only had one or two modes for which it was not feasible to consider subdividing a single volume. However, for the 125Hz to 1000Hz octave bands there were at least six modes in each band. The general conclusion was that SEA using GESEA CLFs gives more accurate estimates than AESEA CLFs. Hence it was concluded that indirect coupling improves the accuracy of SEA models for a compact space modelled as coupled volumes.

Each compact space was subdivided into three-, five- and nine-subsystems to assess different SEA models. In contrast to the elongated cuboids considered in chapters 4 and 5, AESEA often gave negative ILFs which meant it was not possible to create an SEA model using AESEA CLFs. However, GESEA always resulted in a working model even though the errors were up to 6.7dB below 1000Hz (determined from FEM models) but they were only up to 3dB at high frequencies (determined using ray tracing).

The two different five-subsystem models (horizontal and vertical subdivision) indicate an important issue about subsystem definition by an experimenter, namely that it is not always intuitive. In this case, the vertical subdivision could be considered unintuitive because of the significantly different absorbing surfaces that are in each subsystem, whereas the horizontal subdivision seems more logical because the absorbing surfaces are more similar. However, for the five-subsystem model with horizontal subdivision (and the nine-subsystem model) AESEA gave invalid negative ILFs and therefore did not provide a working model. For this reason when carrying out ESEA it is always worth using a grid of response points that can be grouped in different ways to test different subsystem definitions (i.e. avoid carrying out spatial averages in rigidly defined subsystems where there is no scope to calculate energy average responses from slightly different volumes). However, in this thesis the results from both elongated and compact spaces suggests that GESEA will always give a working prediction model.

When a source position (point or surface) used in the PIM ESEA process is similar to the actual source position the results tend to be more accurate. However this tends

to be most apparent when there is only a single source because when there are multiple sources, the source position used in the PIM ESEA process is less critical.

Chapter 7 Conclusions

This thesis has investigated the characterisation of reverberant sound fields in terms of their diffusivity by using numerical experiments with ray tracing. The spatial correlation coefficient was calculated in reverberant rooms with low- and high-damping and compared with theory for a three-dimensional diffuse field and propagating plane waves. Three different methods were used to determine the spatial correlation coefficients based on what would be feasible in measurements or numerical models. However, these methods gave conflicting indications as to whether the sound field can be considered diffuse. Option (1) which is originally suggested by Cook et al [2] based on pairs of points formed by one fixed point at a position that is $\geq \lambda/2$ from the boundary that lies in a plane perpendicular to the measurement line, and all other points along the same line that are $\geq \lambda/2$ from the opposite boundary, can lead to conclusions that seem inappropriate. This suggests two possibilities: (i) option (1) is inappropriate for quantifying the diffusivity with ray tracing since pair of points taken into account were biased toward one boundary due to one fixed point. Individual spatial correlation coefficients tended to have different values according to measurement positions so that the data obtained from biased positions instead of random positions can affect the average R value; or (ii) the reverberation distance is not appropriate when assessing phase differences between two points because it is based only on levels. Whilst, the use of option (2) based on pairs of points with a fixed spacing, d_{ij} , along each line and option (3) based on all permutations of points with variable spacing, d_{ij} , along each line is reasonable. However it is still difficult to definitively identify sound field when a sound field in a box-shaped space can be considered as diffuse; hence it was not possible to attempt this for more complex spaces considered in this thesis, such as a long corridor and car cabin.

Sound transmission along an empty cuboid was assessed using ray tracing, direct and propagating 2D diffuse field models and SEA/ESEA model. It was found that the direct field was significant for sound propagation along a corridor with highly absorptive surfaces ($\alpha \geq 0.3$).

The propagating two-dimensional model assumed a two-dimensional diffuse sound field propagating along the corridor with the source at one end. This did not give

accurate sound transmission for low- and high-levels of surface absorptions that were $\alpha=0.1$ and $\alpha=0.6$, respectively. However, there is an intermediate level of absorption ($\alpha=0.3$) for the surfaces that gives reasonable agreement with this model. It was concluded that this model was not sufficiently flexible for practical purposes where it might be necessary to have one model for the corridor and the rooms behind the doors that face into the corridor. For this reason, SEA models were considered in detail due to their flexibility.

Comparison of ray tracing with predictive SEA models based on a transmission coefficient of unity between adjacent subsystems it was found there was closer agreement when the subsystems were assumed to support two-dimensional rather than three-dimensional sound fields. However, the assumption of a transmission coefficient of unity on the interface between adjacent subsystems tended to overestimate the decrease in sound pressure level. The direct field is unable to describe sound transmission without including reflected sound hence ray tracing model was used to determine the direct field and two types of forward propagation in each subsystem. Type 1 described rays that propagate directly from the point source to the receiver (i.e. the direct field), Type 2 described rays which only reflect from boundaries in the source subsystem before reaching the receiver and Type 3 describes rays that are reflected at least once outside the source subsystem before reaching the receiver. From these investigations, for specular reflections, all types of forward propagations were equally important but for diffuse reflections Type 3 was insignificant. These three types of forward propagations were interpreted with indirect couplings. For this reason, ESEA was considered to address the issues of (a) overestimating the coupling loss factors and (b) needing to incorporate the direct field and two types of forward propagation. SEA predictions that incorporated coupling loss factors from the general form of ESEA (GESEA) gave improved agreement with ray tracing assuming specular or diffuse reflections; this indicated the importance of indirect coupling between subsystems. For a cuboid with staggered barriers, similar trends were observed. In contrast to empty cuboid, however, it was found that the precision of SEA was strongly dependent on the source configurations for the PIM when there is obstacles between subsystems; hence the following conditions should be satisfied: (1) the source position used in the source subsystem in the actual situation should be the same as the position used in that subsystem for

the PIM; (2) source positions should preferably be (a) in a corner away from the opening and (b) in the direct line-of-sight of apertures for forward propagation rather than backward propagation; (3) when there are coupled subsystems that are adjacent to each other which should logically have the same coupling loss factor then the optimal source positions are those with the lowest standard deviation. The cuboid with staggered barriers model indicated that the consideration of indirect CLFs was recommended for a single source when it is unknown whether there are diffuse or specular reflections and the importance of indirect CLFs is magnified when the distance between the source room and the receiving room is getting closer.

Measurements on a real corridor and a real corridor with staggered partitions have been undertaken to verify the adequacy of SEA/ESEA for a practical situation. The results showed close agreement with ray tracing and SEA using GESEA CLFs. This indicated that indirect coupling loss factors are required to predict appropriate sound transmission along elongated spaces. In practice, it implies a possibility of modelling the corridor for prediction of sound transmission into and out of rooms via open doors, and for identification of the quieter and noisier area in train carriages or airplane cabins.

The use of SEA with coupled volumes then moved on to consider a car cabin because there are also problems predicting noise levels in compact acoustic cavities where surfaces have significantly different absorptions. In this work, both a point source and radiating surface source were considered. FEM and ray tracing were used to assess different subdivision of a compact space into different subsystems. The compact space was subdivided into three-, five- and nine-subsystems to assess different SEA models. In contrast to the corridor models, AESEA often returned negative internal loss factors, which meant it was not possible to create an SEA model using AESEA CLFs. However, GESEA always resulted in a working model. When a source position (point or surface) used for the PIM process is similar to the actual source position the results tend to be more accurate. However, this tends to be most apparent when there is only a single source because when there are multiple sources, the source position used in the PIM is less critical.

7.1 Future research

To try and reach a conclusion on the practical use of the spatial correlation coefficient for assessing diffusivity it would be worth using experimental work with broadband signals to assess the three different options suggested in this thesis for choosing measurement points.

For sound transmission along a corridor, experimental work has validated the use of SEA with GESEA coupling loss factors. However, it would be beneficial to repeat the validation with a corridor that had a highly-absorbent ceiling but highly reflective walls, as these also occur in buildings (i.e. uneven distribution of absorption). It also could be applicable to a large space in buildings such as airport, hospital and open plan office for estimate of sound transmission.

Where one corridor branches into other corridors at a junction it should also be possible to use SEA with GESEA coupling loss factors to describe sound transmission involving diffraction and reflection at a T- or X-junction of corridors. This would be of interest for future experimental validation.

For a compact set of coupled volumes, further numerical or experimental validations using a real car cabin would give insights into the practical applications of GESEA for the multiplicity of realistic sources that exist for a car in motion. With a powerful high-performance computing facility it would be feasible to use FEM with rain-on-the roof excitation of the various car surfaces that radiate into the car cabin such as floor, windows, windshield and sunroof.

Appendix A. Modified CLFs and TLFs

Empty cuboid

Practical subdivision				
Specular reflection (ray tracing)	Modified indirect CLFs		Modified TLFs	
	Original	Replaced	Original	Replaced
6 subsystem with equal length	$\eta_{31}, \eta_{42}, \eta_{51},$	$\eta_{13}, \eta_{24}, \eta_{15},$	$\eta_3, \eta_4, \eta_5, \eta_6$	Sum of its CLFs
	$\eta_{53}, \eta_{62}, \eta_{64}$	$\eta_{35}, \eta_{26}, \eta_{46}$		
Diffuse reflection (ray tracing)	Modified indirect CLFs		Modified TLFs	
	Original	Replaced	Original	Replaced
6 subsystem with equal length	$\eta_{31}, \eta_{42}, \eta_{51},$	$\eta_{13}, \eta_{24}, \eta_{15},$	$\eta_3, \eta_4, \eta_5, \eta_6$	Sum of its CLFs
	$\eta_{53}, \eta_{62}, \eta_{64}$	$\eta_{35}, \eta_{26}, \eta_{46}$		

Real corridor with ODEON material database				
Specular reflection (ray tracing)	Modified indirect CLFs		Modified TLFs	
	Original	Replaced	Original	Replaced
Octave band (Hz)				
500	$\eta_{31}, \eta_{42}, \eta_{51},$ $\eta_{53}, \eta_{62}, \eta_{64}$	$\eta_{13}, \eta_{24}, \eta_{15},$ $\eta_{35}, \eta_{26}, \eta_{46}$	$\eta_3, \eta_4, \eta_5, \eta_6$	Sum of its CLFs
1000	$\eta_{31}, \eta_{42}, \eta_{51},$ $\eta_{53}, \eta_{62}, \eta_{64}$	$\eta_{13}, \eta_{24}, \eta_{15},$ $\eta_{35}, \eta_{26}, \eta_{46}$	-	-
2000	$\eta_{31}, \eta_{42}, \eta_{51},$ $\eta_{53}, \eta_{62}, \eta_{64}$	$\eta_{13}, \eta_{24}, \eta_{15},$ $\eta_{35}, \eta_{26}, \eta_{46}$	-	-
4000	$\eta_{31}, \eta_{42}, \eta_{51},$ $\eta_{53}, \eta_{62}, \eta_{64}$	$\eta_{13}, \eta_{24}, \eta_{15},$ $\eta_{35}, \eta_{26}, \eta_{46}$	-	-

Diffuse reflection (ray tracing)	Modified indirect CLFs		Modified TLFs	
	Original	Replaced	Original	Replaced
8000	$\eta_{31}, \eta_{42}, \eta_{51},$ $\eta_{53}, \eta_{62}, \eta_{64}$	$\eta_{13}, \eta_{24}, \eta_{15},$ $\eta_{35}, \eta_{26}, \eta_{46}$	η_4, η_5, η_6	Sum of its CLFs

Corridor with staggered barrier

- Case A

Ideal corridor with barrier				
Specular reflection (ray tracing)	Modified indirect CLFs		Modified TLFs	
	Original	Replaced	Original	Replaced
6 subsystem	$\eta_{24}, \eta_{35}, \eta_{46}$	$\eta_{42}, \eta_{53}, \eta_{64}$	-	-
Diffuse reflection (ray tracing)	Modified CLFs		Modified TLFs	
	Original	Replaced	Original	Replaced
6 subsystem with equal length	$\eta_{13}, \eta_{15}, \eta_{24},$ $\eta_{26}, \eta_{31}, \eta_{35},$ $\eta_{42}, \eta_{46}, \eta_{51},$ $\eta_{53}, \eta_{62}, \eta_{64}$	0 (zero)	-	-

- Measurements

Real corridor				
One-third octave band measurements (Hz)	Modified indirect CLFs		Modified TLFs	
	Original	Replaced	Original	Replaced
100	$\eta_{31}, \eta_{51}, \eta_{52},$	$\eta_{13}, \eta_{15}, \eta_{25},$	η_3, η_5	Sum of its

	η_{63} $\eta_{16}, \eta_{24}, \eta_{35},$ $\eta_{42}, \eta_{53}, \eta_{61}$	η_{36} 0 (zero)		CLFs
125	$\eta_{13}, \eta_{24}, \eta_{52},$ η_{63} $\eta_{15}, \eta_{16}, \eta_{35},$ $\eta_{51}, \eta_{53}, \eta_{61}$	$\eta_{31}, \eta_{42}, \eta_{25},$ η_{36} 0 (zero)	η_2, η_3	Sum of its CLFs
160	$\eta_{13}, \eta_{24}, \eta_{35},$ $\eta_{41}, \eta_{46}, \eta_{52},$ η_{63} $\eta_{16}, \eta_{26}, \eta_{51},$ η_{62}	$\eta_{31}, \eta_{42}, \eta_{53},$ $\eta_{14}, \eta_{64}, \eta_{25},$ η_{36} 0 (zero)	η_1, η_2	Sum of its CLFs
200	η_{35}, η_{36} $\eta_{14}, \eta_{25}, \eta_{41},$ η_{62}	η_{53}, η_{63} 0 (zero)	-	-
250	$\eta_{14}, \eta_{36}, \eta_{62},$ η_{64} η_{15}, η_{51}	$\eta_{41}, \eta_{63}, \eta_{26},$ η_{46} 0 (zero)	-	-
315	$\eta_{13}, \eta_{25}, \eta_{36},$ $\eta_{41}, \eta_{53}, \eta_{64}$ η_{16}, η_{61}	$\eta_{31}, \eta_{52}, \eta_{63},$ $\eta_{14}, \eta_{35}, \eta_{46}$ 0 (zero)	-	-
400	η_{35}, η_{41} $\eta_{25}, \eta_{46}, \eta_{52},$ η_{64}	η_{53}, η_{14} 0 (zero)	-	-
500	$\eta_{14}, \eta_{25}, \eta_{31},$ $\eta_{36}, \eta_{53}, \eta_{61}$	$\eta_{41}, \eta_{52}, \eta_{13},$ $\eta_{63}, \eta_{35}, \eta_{16}$	-	-

	η_{46}, η_{64}	0 (zero)		
630	$\eta_{14}, \eta_{16}, \eta_{51}$ $\eta_{25}, \eta_{26}, \eta_{35},$ $\eta_{46}, \eta_{52}, \eta_{53},$ η_{62}, η_{64}	$\eta_{41}, \eta_{61}, \eta_{15}$ 0 (zero)	-	-
800	$\eta_{24}, \eta_{46}, \eta_{62}$ $\eta_{15}, \eta_{35}, \eta_{51},$ η_{53}	$\eta_{42}, \eta_{64}, \eta_{26}$ 0 (zero)	-	-
1000	$\eta_{25}, \eta_{36}, \eta_{51},$ η_{53}, η_{62}	$\eta_{52}, \eta_{63}, \eta_{15},$ η_{35}, η_{26}	-	-
1250	η_{53} η_{25}, η_{52}	η_{35} 0 (zero)	-	-
1600	η_{53}	η_{35}	-	-
2000	η_{53}	η_{35}	-	-
2500	-	-	-	-
3150	-	-	-	-
4000	-	-	-	-
5000	η_{26}	η_{62}	-	-
6300	η_{24}, η_{26} η_{35}, η_{53}	η_{42}, η_{62} 0 (zero)	-	-
8000	η_{24}, η_{26} η_{35}, η_{53}	η_{42}, η_{62} 0 (zero)	-	-
10000	$\eta_{24}, \eta_{26}, \eta_{64}$ η_{35}, η_{53}	$\eta_{42}, \eta_{62}, \eta_{64}$ 0 (zero)	-	-

Cuboid room

2 subsystem				
FEM Octave band (Hz)	Modified indirect CLFs		Modified TLFs	
	Original	Replaced	Original	Replaced
63	-	-	-	-
125	-	-	-	-
250	-	-	-	-
500	-	-	-	-
1000	-	-	-	-

4 subsystem with horizontal subdivision				
FEM Octave band (Hz)	Modified indirect CLFs		Modified TLFs	
	Original	Replaced	Original	Replaced
63			$\eta_1, \eta_2, \eta_3, \eta_4$ <0	invalid
125	$\eta_{14}, \eta_{23}, \eta_{32},$ η_{41}	0 (zero)	η_1, η_2, η_3	Sum of its CLFs
250	η_{12}, η_{41} η_{23}, η_{32}	η_{21}, η_{14} 0 (zero)	η_3	Sum of its CLFs
500	η_{21} $\eta_{14}, \eta_{23}, \eta_{32},$ η_{41}	η_{12} 0 (zero)	η_3, η_4	Sum of its CLFs
1000	$\eta_{14}, \eta_{23}, \eta_{32},$ η_{41}	0 (zero)	η_3, η_4	Sum of its CLFs

4 subsystem with vertical subdivision				
FEM Octave band (Hz)	Modified indirect CLFs		Modified TLFs	
	Original	Replaced	Original	Replaced
63			$\eta_1, \eta_2, \eta_3, \eta_4$ <0	invalid
125			$\eta_3, \eta_4 <0$	invalid
250	η_{31}, η_{42}	η_{13}, η_{24}	-	-
500	-	-	-	-
1000	η_{32}, η_{41}	η_{23}, η_{14}	-	-

8 subsystem				
FEM Octave band (Hz)	Modified indirect CLFs		Modified TLFs	
	Original	Replaced	Original	Replaced
63			$\eta_1, \eta_2, \eta_3, \eta_4,$ $\eta_5, \eta_6, \eta_7, \eta_8$ <0	invalid
125	$\eta_{13}, \eta_{14}, \eta_{15},$ $\eta_{17}, \eta_{24}, \eta_{26},$ $\eta_{28}, \eta_{31}, \eta_{35},$ $\eta_{37}, \eta_{42}, \eta_{46},$ $\eta_{48}, \eta_{51}, \eta_{53},$ $\eta_{57}, \eta_{62}, \eta_{64},$ $\eta_{68}, \eta_{71}, \eta_{73},$ $\eta_{75}, \eta_{82}, \eta_{84},$ η_{86}	0 (zero)	$\eta_1, \eta_2, \eta_3, \eta_4,$ η_5, η_6	Sum of its CLFs
250	$\eta_{15}, \eta_{26}, \eta_{32},$ $\eta_{36}, \eta_{41}, \eta_{45},$ $\eta_{52}, \eta_{61}, \eta_{71},$ $\eta_{74}, \eta_{76}, \eta_{82},$ η_{83}, η_{85}	$\eta_{51}, \eta_{62}, \eta_{23},$ $\eta_{63}, \eta_{14}, \eta_{54},$ $\eta_{25}, \eta_{16}, \eta_{17},$ $\eta_{47}, \eta_{67}, \eta_{28},$ η_{38}, η_{58}	$\eta_3, \eta_4, \eta_5, \eta_6,$ η_7, η_8	Sum of its CLFs

	$\eta_{35}, \eta_{46}, \eta_{53}, \eta_{64}$	0 (zero)		
500	$\eta_{52}, \eta_{61}, \eta_{74}, \eta_{83}, \eta_{14}, \eta_{17}, \eta_{18}, \eta_{23}, \eta_{27}, \eta_{28}, \eta_{32}, \eta_{35}, \eta_{36}, \eta_{41}, \eta_{45}, \eta_{46}, \eta_{53}, \eta_{54}, \eta_{58}, \eta_{63}, \eta_{64}, \eta_{67}, \eta_{71}, \eta_{72}, \eta_{76}, \eta_{81}, \eta_{82}, \eta_{85}$	$\eta_{25}, \eta_{16}, \eta_{47}, \eta_{38}$ 0 (zero)	$\eta_3, \eta_4, \eta_7, \eta_8$	Sum of its CLFs
1000	$\eta_{53}, \eta_{64}, \eta_{17}, \eta_{18}, \eta_{27}, \eta_{28}, \eta_{36}, \eta_{45}, \eta_{54}, \eta_{58}, \eta_{63}, \eta_{67}, \eta_{71}, \eta_{72}, \eta_{76}, \eta_{81}, \eta_{82}, \eta_{85}$	η_{35}, η_{46} 0 (zero)	$\eta_3, \eta_4, \eta_7, \eta_8$	Sum of its CLFs

Ray tracing (ODEON)	Modified indirect CLFs		Modified TLFs	
	Original	Replaced	Original	Replaced
2 subsystem	-	-	-	-
4 subsystem with horizontal subdivision	η_{21}, η_{41} η_{23}, η_{32}	η_{12}, η_{14} 0 (zero)	η_3, η_4	Sum of its CLFs
4 subsystem with vertical subdivision	-	-	-	-

8 subsystem	$\eta_{18}, \eta_{36}, \eta_{45},$ $\eta_{52}, \eta_{61}, \eta_{71},$ $\eta_{74}, \eta_{76}, \eta_{82},$ η_{83} $\eta_{14}, \eta_{23}, \eta_{32},$ $\eta_{35}, \eta_{41}, \eta_{46},$ $\eta_{53}, \eta_{58}, \eta_{64},$ η_{85}	$\eta_{81}, \eta_{63}, \eta_{54},$ $\eta_{25}, \eta_{16}, \eta_{17},$ $\eta_{47}, \eta_{67}, \eta_{28},$ η_{38} 0 (zero)	$\eta_3, \eta_4, \eta_7, \eta_8$	Sum of its CLFs
-------------	--	---	----------------------------------	-----------------

Car cabin

3 subsystem				
FEM	Modified indirect CLFs		Modified TLFs	
Octave band (Hz)	Original	Replaced	Original	Replaced
63	η_{13}	η_{31}	η_1, η_3	Sum of its CLFs
125	η_{13}, η_{31}	0 (zero)	η_1	Sum of its CLFs
250	η_{13}, η_{31}	0 (zero)	η_1	Sum of its CLFs
500	η_{13}	η_{31}	-	-
1000	η_{31}	η_{13}	-	-

5 subsystem with horizontal subdivision				
FEM	Modified indirect CLFs		Modified TLFs	
Octave band (Hz)	Original	Replaced	Original	Replaced
63	$\eta_{25}, \eta_{31}, \eta_{32}, \eta_{45}$	$\eta_{52}, \eta_{13}, \eta_{23}, \eta_{54}$	η_2, η_5	Sum of its CLFs
125	$\eta_{24}, \eta_{32}, \eta_{15}, \eta_{25}, \eta_{51}, \eta_{52}$	$\eta_{42}, \eta_{23}, 0$ (zero)	η_1	Sum of its CLFs
250	$\eta_{32}, \eta_{45}, \eta_{52}, \eta_{15}, \eta_{51}$	$\eta_{23}, \eta_{54}, \eta_{25}, 0$ (zero)	η_1, η_4	Sum of its CLFs
500	$\eta_{14}, \eta_{15}, \eta_{25}, \eta_{32}$	$\eta_{41}, \eta_{51}, \eta_{52}, \eta_{23}$	-	-
1000	$\eta_{14}, \eta_{23}, \eta_{25}, \eta_{32}, \eta_{41}, \eta_{52}$	0 (zero)	η_3	Sum of its CLFs

5 subsystem with vertical subdivision				
FEM Octave band (Hz)	Modified indirect CLFs		Modified TLFs	
	Original	Replaced	Original	Replaced
63	η_{15}, η_{25} $\eta_{13}, \eta_{24}, \eta_{31},$ η_{42}	η_{51}, η_{52} 0 (zero)	η_1, η_2, η_5	Sum of its CLFs
125	$\eta_{15}, \eta_{25}, \eta_{51},$ η_{52}	0 (zero)	η_1, η_2	Sum of its CLFs
250	η_{32} $\eta_{15}, \eta_{25}, \eta_{51},$ η_{52}	η_{23} 0 (zero)	η_1, η_2	Sum of its CLFs
500	η_{23} η_{14}, η_{41}	η_{32} 0 (zero)	-	-
1000	η_{51}, η_{52}	η_{15}, η_{25}	-	-

9 subsystems				
FEM Octave band (Hz)	Modified indirect CLFs		Modified TLFs	
	Original	Replaced	Original	Replaced
63	$\eta_{26}, \eta_{29}, \eta_{48},$ $\eta_{49}, \eta_{52}, \eta_{69},$ η_{74}, η_{89} $\eta_{15}, \eta_{37}, \eta_{51},$ $\eta_{68}, \eta_{73}, \eta_{86}$	$\eta_{62}, \eta_{92}, \eta_{84},$ $\eta_{94}, \eta_{25}, \eta_{96},$ η_{47}, η_{98} 0 (zero)	η_2, η_4, η_9	Sum of its CLFs
125	$\eta_{28}, \eta_{46}, \eta_{49},$ η_{52} $\eta_{19}, \eta_{24}, \eta_{29},$	$\eta_{82}, \eta_{64}, \eta_{94},$ η_{25} 0 (zero)	η_1, η_3	Sum of its CLFs

	$\eta_{39}, \eta_{42}, \eta_{68},$ $\eta_{86}, \eta_{91}, \eta_{92},$ η_{93}			
250	$\eta_{23}, \eta_{38}, \eta_{41},$ $\eta_{52}, \eta_{63}, \eta_{67},$ $\eta_{69}, \eta_{74}, \eta_{81},$ $\eta_{85}, \eta_{92}, \eta_{94}$ $\eta_{19}, \eta_{28},$ $\eta_{39}, \eta_{46}, \eta_{64},$ $\eta_{82}, \eta_{91}, \eta_{93}$	$\eta_{32}, \eta_{83}, \eta_{14},$ $\eta_{25}, \eta_{36}, \eta_{76},$ $\eta_{96}, \eta_{47}, \eta_{18},$ $\eta_{58}, \eta_{29}, \eta_{49}$ 0 (zero)	$\eta_{1}, \eta_{3}, \eta_{6}, \eta_{8}$	Sum of its CLFs
500	$\eta_{16}, \eta_{18}, \eta_{19},$ $\eta_{29}, \eta_{38}, \eta_{46},$ $\eta_{49}, \eta_{52}, \eta_{71},$ $\eta_{74}, \eta_{76}, \eta_{96}$ $\eta_{28}, \eta_{35}, \eta_{53},$ $\eta_{82}, \eta_{89}, \eta_{98}$	$\eta_{61}, \eta_{81}, \eta_{91},$ $\eta_{92}, \eta_{83}, \eta_{64},$ $\eta_{94}, \eta_{25}, \eta_{17},$ $\eta_{47}, \eta_{67}, \eta_{69}$ 0 (zero)	-	-
1000	η_{32}, η_{81} $\eta_{16}, \eta_{25}, \eta_{29},$ $\eta_{36}, \eta_{38}, \eta_{47},$ $\eta_{49}, \eta_{52}, \eta_{61},$ $\eta_{63}, \eta_{74}, \eta_{83},$ η_{92}, η_{94}	η_{23}, η_{18} 0 (zero)	η_{5}, η_{7}	Sum of its CLFs

Ray tracing (ODEON)	Modified indirect CLFs		Modified TLFs	
	Original	Replaced	Original	Replaced
3 subsystem	-	-	-	-
5 subsystem with horizontal subdivision	η_{15} $\eta_{14}, \eta_{25}, \eta_{41},$ $\eta_{45}, \eta_{52}, \eta_{54}$	η_{51} 0 (zero)	η_3	Sum of its CLFs

5 subsystem with vertical subdivision	-	-	-	-
9 subsystem	$\eta_{19}, \eta_{39}, \eta_{52},$ $\eta_{64}, \eta_{74}, \eta_{82}$ $\eta_{16}, \eta_{18}, \eta_{29},$ $\eta_{36}, \eta_{38}, \eta_{49},$ $\eta_{61}, \eta_{63}, \eta_{68},$ $\eta_{69}, \eta_{81}, \eta_{83},$ $\eta_{86}, \eta_{89}, \eta_{92},$ $\eta_{94}, \eta_{96}, \eta_{98}$	$\eta_{91}, \eta_{93}, \eta_{25},$ $\eta_{46}, \eta_{47}, \eta_{28}$ 0 (zero)	η_{5}, η_{7}	Sum of its CLFs

Appendix B. Negative ILFs

Empty cuboid

Practical subdivision		
Specular reflection (ray tracing)	Negative ILFs (subsystem)	Positive ILFs (subsystem)
6 subsystem with equal length	None	All ILFs
Diffuse reflection (ray tracing)	Negative ILFs	Positive ILFs
6 subsystem with equal length	None	All ILFs

Real corridor with ODEON material database		
Specular reflection (ray tracing)	Negative ILFs (subsystem)	Positive ILFs (subsystem)
Octave band (Hz)		
500	None	All ILFs
1000	None	All ILFs
2000	None	All ILFs
4000	None	All ILFs
Diffuse reflection (ray tracing)	Negative ILFs	Positive ILFs
Octave band (Hz)		
8000	None	All ILFs

Corridor with staggered barrier

- Case A

Ideal corridor with barrier		
Specular reflection (ray tracing)	Negative ILFs (subsystem)	Positive ILFs (subsystem)
6 subsystem	None	All ILFs
Diffuse reflection (ray tracing)	Negative ILFs (subsystem)	Positive ILFs (subsystem)
6 subsystem with equal length	None	All ILFs

- Measurements

Real corridor		
One-third octave band measurements (Hz)	Negative ILFs (subsystem)	Positive ILFs (subsystem)
100	None	All ILFs
125	None	All ILFs
160	2	1,3,4,5, 6
200	None	All ILFs
250	None	All ILFs
315	None	All ILFs
400	None	All ILFs
500	None	All ILFs
630	None	All ILFs
800	None	All ILFs
1000	None	All ILFs
1250	None	All ILFs
1600	None	All ILFs

2000	None	All ILFs
2500	None	All ILFs
3150	None	All ILFs
4000	None	All ILFs
5000	None	All ILFs
6300	None	All ILFs
8000	None	All ILFs
10000	None	All ILFs

Cuboid space

2 subsystem		
FEM Octave band (Hz)	Negative ILFs (subsystem)	Positive ILFs (subsystem)
63	None	All ILFs
125	None	All ILFs
250	None	All ILFs
500	None	All ILFs
1000	None	All ILFs

4 subsystem with horizontal subdivision		
FEM Octave band (Hz)	Negative ILFs (subsystem)	Positive ILFs (subsystem)
63	3,5	1,2
125	1	2,3,4
250	1,4	2,3
500	None	All ILFs
1000	3	1,2,4

4 subsystem with vertical subdivision		
FEM Octave band (Hz)	Negative ILFs (subsystem)	Positive ILFs (subsystem)
63	None	All ILFs
125	None	All ILFs
250	None	All ILFs
500	None	All ILFs
1000	None	All ILFs

8 subsystem		
FEM Octave band (Hz)	Negative ILFs (subsystem)	Positive ILFs (subsystem)
63	3,4,7,8	1,2,5,6
125	5,6	1,2,3,4,7,8
250	3,4	1,2,5,6,7,8
500	3,4,7,8	1,2,5,6
1000	3,4	1,2,5,6,7,8

Ray tracing (ODEON)	Negative ILFs (subsystem)	Positive ILFs (subsystem)
2 subsystem	None	All ILFs
4 subsystem with horizontal subdivision	3,4	1,2
4 subsystem with vertical subdivision	None	All ILFs
8 subsystem	3,7	1,2,4,5,6,8

Car cabin

3 subsystem		
FEM Octave band (Hz)	Negative ILFs	Positive ILFs
63	1,3	2
125	None	All ILFs
250	None	All ILFs
500	None	All ILFs
1000	None	All ILFs

5 subsystem with horizontal subdivision		
FEM Octave band (Hz)	Negative ILFs	Positive ILFs
63	3,5	1,2,4
125	1	2,3,4,5
250	1,4	2,3,5
500	None	All ILFs
1000	3	1,2,4,5

5 subsystem with vertical subdivision		
FEM Octave band (Hz)	Negative ILFs	Positive ILFs
63	1,2,5	3,6
125	None	All ILFs
250	None	All ILFs
500	None	All ILFs
1000	None	All ILFs

9 subsystem		
FEM Octave band (Hz)	Negative ILFs (subsystem)	Positive ILFs (subsystem)
63	2,4	1,3,5,6,7,8,9
125	1,3	2,4,5,6,7,8,9
250	1,3,6,8	2,4,5,7,9
500	None	All ILFs
1000	5,7	1,2,3,4,6,8,9

Ray tracing (ODEON)	Negative ILFs (subsystem)	Positive ILFs (subsystem)
3 subsystem	None	All ILFs
5 subsystem with horizontal subdivision	3	1,2,4,5
5 subsystem with vertical subdivision	None	All ILFs
9 subsystem	5,7	1,2,3,4,6,8,9

References

- [1] Eyring, C. F. (1931). Reverberation time measurements in coupled rooms. *The Journal of the Acoustical Society of America*, 3(2A), 181-206.
- [2] Cook, R. K., Waterhouse, R. V., Berendt, R. D., Edelman, S., & Thompson Jr, M. C. (1955). Measurement of correlation coefficients in reverberant sound fields. *The Journal of the Acoustical Society of America*, 27(6), 1072-1077.
- [3] Toyoda, E., Sakamoto, S., & Tachibana, H. (2004). Effects of room shape and diffusing treatment on the measurement of sound absorption coefficient in a reverberation room. *Acoustical Science and Technology*, 25(4), 255-266.
- [4] Zeng, L. J. (1992). The sound distribution in a rectangular reverberation chamber. *The Journal of the Acoustical Society of America*, 92(1), 600-603.
- [5] Bistafa, S. R., & Bradley, J. S. (1998). Comparisons of computer simulations of acoustical conditions in classrooms. *Canadian Acoustics*, 26(3), 21-22.
- [6] Atalla, N., & Sgard, F. (2015). *Finite Element and Boundary Methods in Structural Acoustics and Vibration*. CRC Press.
- [7] Herrin, D. W., Wu, T. W., & Seybert, A. F. (2003). Practical issues regarding the use of the finite and boundary element methods for acoustics. *Building Acoustics*, 10(4), 257-279.
- [8] Lyon, R. H., & Dejong, R. G. (1975). *Statistical energy analysis of dynamical systems: theory and applications*. Cambridge: MIT press.
- [9] Zeman, J.L., & Bogdanoff, J.L. (1969). A comment of the Statistical Energy Analysis. *Society of Automotive Engineers*.
- [10] Kuttruff, H. (1963). Raumakustische korrelationsmessungen mit einfachen mitteln. *Acustica*, 13, 120-122.
- [11] Morrow, C. T. (1971). Point-to-point correlation of sound pressures in reverberation chambers. *Journal of Sound and Vibration*, 16(1), 29-42.

- [12] Koyasu, M., & Yamashita, M. (1971). Evaluation of the degree of diffuseness in reverberation chambers by spatial correlation techniques (Spatial correlation techniques for evaluating diffuseness of sound field in reverberation chamber). *Nippon Onkyo Gakkaishi*,(Tokyo), 26(3), 132-143.
- [13] Chu, W. T. (1981). Comments on the coherent and incoherent nature of a reverberant sound field. *The Journal of the Acoustical Society of America*, 69(6), 1710-1715.
- [14] Chu, W. T. (1982). Note on the independent sampling of mean-square pressure in reverberant sound fields. *The Journal of the Acoustical Society of America*, 72(1), 196-199.
- [15] Néglise, H., & Nicolas, J. (1997). Characterization of a diffuse field in a reverberant room. *The Journal of the Acoustical Society of America*, 101(6), 3517-3524.
- [16] Rafaely, B. (2000). Spatial-temporal correlation of a diffuse sound field. *The Journal of the Acoustical Society of America*, 107(6), 3254-3258.
- [17] Chun, I., Rafaely, B., & Joseph, P. (2003). Experimental investigation of spatial correlation in broadband reverberant sound fields. *The Journal of the Acoustical Society of America*, 113(4), 1995-1998.
- [18] Langley, R. S. (1989). A general derivation of the statistical energy analysis equations for coupled dynamic systems. *Journal of Sound and Vibration*, 135(3), 499-508.
- [19] Mace, B. R. (2005). Statistical energy analysis: coupling loss factors, indirect coupling and system modes. *Journal of Sound and Vibration*, 279(1), 141-170.
- [20] Langley, R. S. (1990). A derivation of the coupling loss factors used in statistical energy analysis. *Journal of Sound and Vibration*, 141(2), 207-219.
- [21] Keane, A. J. (1992, March). Energy flows between arbitrary configurations of conservatively coupled multi-modal elastic subsystems. In *Proceedings*

of the Royal Society of London A: Mathematical, Physical and Engineering Sciences (Vol. 436, No. 1898, pp. 537-568). The Royal Society.

- [22] Mace, B. R. (1997). Wave coherence, coupling power and statistical energy analysis. *Journal of Sound and Vibration*, 199(3), 369-380.
- [23] Mees, P., & Vermeir, O. (1993). Structure-borne sound transmission at elastically connected plates. *Journal of Sound and Vibration*, 166(1), 55-76.
- [24] Zhang, Q. J., & Sainsbury, M. G. (1999, February). The Energy Flow Method for Strongly Coupled Systems. In *PROCEEDING OF THE INTERNATIONAL MODAL ANALYSIS CONFERENCE* (Vol. 2, pp. 1839-1845).
- [25] Bies, D., & Hamid, S. (1980). In situ determination of loss and coupling loss factors by the power injection method. *Journal of Sound and Vibration*, 70(2), 187-204.
- [26] Woodhouse, J. (1981). An introduction to statistical energy analysis of structural vibration. *Applied Acoustics*, 14(6), 455-469.
- [27] Hodges, C. H., Nash, P., & Woodhouse, J. (1987). Measurement of coupling loss factors by matrix fitting: An investigation of numerical procedures. *Applied Acoustics*, 22(1), 47-69.
- [28] Lalor N. (1990). Practical considerations for the measurement of internal and coupling loss factors on complex structures. *Technical Report No.182*, Southampton: ISVR
- [29] Hopkins, C. (2002). Statistical energy analysis of coupled plate systems with low modal density and low modal overlap. *Journal of Sound and Vibration*, 251(2), 193-214.
- [30] Mace, B. (2003). Statistical energy analysis, energy distribution models and system modes. *Journal of Sound and Vibration*, 264(2), 391-409.
- [31] Borello, G., & Gagliardini, L. (2007). Virtual SEA: towards an industrial process (No. 2007-01-2302). *SAE Technical Paper*.

- [32] Thite, A. N., & Mace, B. R. (2010). The effects of design modifications on the apparent coupling loss factors in SEA-like analysis. *Journal of Sound and Vibration*, 329(24), 5194-5208.
- [33] Gagliardini, L., Houillon, L., Borello, G., & Petrinelli, L. (2005). Virtual SEA-FEA-based modeling of mid-frequency structure-borne noise. *Sound and Vibration*, 39(1), 22.
- [34] Kovalevsky, L., & Langley, R. S. (2012, April). Automatic recognition of the components of a Hybrid FE-SEA model. In *Acoustics 2012*.
- [35] Totaro, N., & Guyader, J. L. (2006). SEA substructuring using cluster analysis: The MIR index. *Journal of Sound and Vibration*, 290(1), 264-289.
- [36] Kassem, M., Soize, C., & Gagliardini, L. (2011). Structural partitioning of complex structures in the medium-frequency range. An application to an automotive vehicle. *Journal of Sound and Vibration*, 330(5), 937-946.
- [37] Díaz-Cereceda, C., Poblet-Puig, J., & Rodríguez-Ferran, A. (2015). Automatic subsystem identification in statistical energy analysis. *Mechanical Systems and Signal Processing*, 54, 182-194.
- [38] Kuttruff, H. (2000). *Room Acoustics*, Spon Press, Abingdon, 4th Edition.
- [39] Anderson, J. S., Bratos-Anderson, M., & Doany, P. (1997). The acoustics of a large space with a repetitive pattern of coupled rooms. *Journal of Sound and Vibration*, 208(2), 313-329.
- [40] Anderson, J. S., & Bratos-Anderson, M. (2000). Acoustic coupling effects in St Paul's cathedral, London. *Journal of Sound and Vibration*, 236(2), 209-225.
- [41] Bradley, D. T., & Wang, L. M. (2007). Comparison of measured and computer-modelled objective parameters for an existing coupled volume concert hall. *Building Acoustics*, 14(2), 79-90.
- [42] Xiang, N., Jing, Y., & Bockman, A. C. (2009). Investigation of acoustically coupled enclosures using a diffusion-equation model a. *The Journal of the Acoustical Society of America*, 126(3), 1187-1198.

- [43] Cremer, L. and Müller, HA (translated by TJ Schultz, 1982). *Principles and applications of room acoustics*, Volumes 1. Barking, Essex: Applied Science Publishers, Ltd.
- [44] Nijs, L., Jansens, G., Vermeir, G., & Van der Voorden, M. (2002). Absorbing surfaces in ray-tracing programs for coupled spaces. *Applied Acoustics*, 63(6), 611-626.
- [45] *The Building Regulations 2000*. Approved Document B. Fire safety.
- [46] Kang, J. (1996). Sound attenuation in long enclosures. *Building and Environment*, 31(3), 245-253.
- [47] Yamamoto, T. (1961). On the distribution of sound energy along a corridor. *The Journal of Acoustical Society of Japan*, 17, 286-292.
- [48] Davies, H. G. (1973). Noise propagation in corridors. *The Journal of the Acoustical Society of America*, 53(5), 1253-1262.
- [49] Redmore, T.L. and Flockton, S.J. (1977). A design formula for predicting the attenuation of sound along a corridor, *Acoustic Letters*, 1, 21-24
- [50] Redmore, T. L. (1982). A method to predict the transmission of sound through corridors. *Applied Acoustics*, 15(2), 133-146.
- [51] Hopkins, C. (2012). *Sound insulation*. Routledge.
- [52] DeJong, R. G. (1985). A study of vehicle interior noise using statistical energy analysis (No. 850960). *SAE Technical Paper*.
- [53] Fahy, F.J. A note on the subdivision of a volume of air in a vehicle enclosure into sea subsystems, *Journal of Sound and Vibration*, Volume 271, Issues 3–5, 6 April 2004, Pages 1170-1174
- [54] Musser, C., Manning, J., & Peng, G. C. (2011). Prediction of Vehicle Interior Sound Pressure Distribution with SEA (No. 2011-01-1705). *SAE Technical Paper*.
- [55] Manning, P., Manning, J., Musser, C., & Peng, G. (2013). Evaluation of Ground Vehicle Wind Noise Transmission through Glasses Using

Statistical Energy Analysis. *SAE International Journal of Materials and Manufacturing*, 6(2013-01-1930), 589-598.

- [56] Charpentier, A., Birkett, C., Sanchez, M., & Dias, V. (2007). Modeling airborne noise transmission in a truck using statistical energy analysis (No. 2007-01-2432). *SAE Technical Paper*.
- [57] Wang, T., & Maxon, J. (2008, October). Application of statistical energy analysis and optimization in the design of Gulfstream large-cabin aircraft interior thermal/acoustic package. In *INTER-NOISE and NOISE-CON Congress and Conference Proceedings* (Vol. 2008, No. 7, pp. 2073-2084). Institute of Noise Control Engineering.
- [58] Forssén, J., Tober, S., Corakci, A. C., Frid, A., & Kropp, W. (2012). Modelling the interior sound field of a railway vehicle using statistical energy analysis. *Applied Acoustics*, 73(4), 307-311.
- [59] San Martin, R., Vela, A., San Martin, M. L., & Arana, M. (2002). Comparative analysis of two acoustic simulation software. In *Proceedings of Forum Acusticum*. Seville, Spain.
- [60] RAYNOISE Rev 3.0 *User's Manual*. (1998). LMS international.
- [61] ODEON 14.01 *Room Acoustic Software User Manual*, (2017). The Department of Acoustic Technology, Technical University of Denmark.
- [62] Rindel, J.H., (1995). Computer simulation techniques for acoustical design of rooms. *Acoustics Australia*, 23, 81-86.
- [63] Sheng, M. P., Wang, M. Q., & Sun, J. C. (1998). Effective internal loss factors and coupling loss factors for non-conservatively coupled systems. *Journal of Sound and Vibration*, 209(4), 685-694.
- [64] Morse, P. M. (1981). *Vibration and Sound*, Acoustical Society of America : American Institute of Physics, ISBN 0-88318-876-7.
- [65] Brüel & Kjær *Instruction Manual* (1976). Reference sound source Type 4204.

- [66] Waterhouse, R. V. (1955). Interference patterns in reverberant sound fields. *The Journal of the Acoustical Society of America*, 27(2), 247-258.
- [67] Schroeder, M. R. (1996). The “Schroeder frequency” revisited. *The Journal of the Acoustical Society of America*, 99(2), 3240-3241.
- [68] Davies, H. G. (1973). Noise propagation in corridors. *The Journal of the Acoustical Society of America*, 53(5), 1253-1262.
- [69] Kang, J. (2002). Comparison of sound fields in regularly-shaped, long and flat enclosures with diffusely reflecting boundaries. *International Journal of Acoustics and Vibration*, 7, 165-171.
- [70] Kang, J. (2002). *Acoustics of Long Spaces: theory and design guidance*. Thomas Telford.
- [71] Redmore, T. L. (1982). A theoretical analysis and experimental study of the behaviour of sound in corridors. *Applied Acoustics*, 15(3), 161-170.
- [72] Kang, J. (2002). Reverberation in rectangular long enclosures with diffusely reflecting boundaries. *Acta Acustica United with Acustica*, 88(1), 77-87.
- [73] Tachibana, H., Yoshihisa, K., Hidaka, Y., & Ishii, K. (1984, December). Correction method for the effect of air absorption on sound absorption coefficients measured in reverberation rooms. In *INTER-NOISE and NOISE-CON Congress and Conference Proceedings* (Vol. 1984, No. 1, pp. 1225-1228). Institute of Noise Control Engineering.
- [74] Cox, T. J., & D'antonio, P. (2009). *Acoustic absorbers and diffusers: theory, design and application*. CRC Press.
- [75] Sadri, M., Brunskog, J., & Younesian, D. (2016). Application of a Bayesian algorithm for the Statistical Energy model updating of a railway coach. *Applied Acoustics*, 112, 84-107.
- [76] Cordioli, J. A., Gerges, S. N., Pererira, A. K., Carmo, M., & Grandi, C. (2004). Vibro-Acoustic Modeling of Aircrafts Using Statistical Energy Analysis (No. 2004-01-3337). *SAE Technical Paper*.

- [77] Craik, R. J. (1996). *Sound transmission through buildings: using statistical energy analysis*. Gower Publishing Company.
- [78] Schroeder, M. R. (1969). Effect of frequency and space averaging on the transmission responses of multimode media. *The Journal of the Acoustical Society of America*, 46(2A), 277-283.
- [79] Jain, S. K., Joshi, M. P., Shrivage, P. G., Yadav, P. S., & Karanth, N. V. (2013). Evaluation of Acoustic Performance of Automotive Seats by Experimental and Simulation Techniques (No. 2013-26-0105). *SAE Technical Paper*.
- [80] Pan, J., Saha, P., & Veen, J. R. (2007). Random Incidence Sound Absorption Measurement of Automotive Seats in Small Size Reverberation Rooms (No. 2007-01-2194). *SAE Technical Paper*.
- [81] McMullan, A., & Mealman, M. (2001). An Investigation of Automotive Seat Fabric Sound Absorption (No. 2001-01-1454). *SAE Technical Paper*.
- [82] 3D CAD BROWSER. (2001-2007). <http://www.3dcadbrowser.com>, Assessed on 26/05/2015.
- [83] Parrett, A. V., Hicks, J. K., Burton, T. E., & Hermans, L. (1997). Statistical energy analysis of airborne and structure-borne automobile interior noise (No. 971970). *SAE Technical Paper*.